Politecnico di Bari

Repository Istituzionale dei Prodotti della Ricerca del Politecnico di Bari

Application of co-flow jet methodology for rear wing flow control in high-performance vehicles

This is a PhD Thesis

Original Citation:
Application of co-flow jet methodology for rear wing flow control in high-performance vehicles / Herberg, M.R.. - ELETTRONICO. - (2026).

Availability:
This version is available at http://hdl.handle.net/11589/307440 since: 2026-09-24

Published version
DOI:

Publisher: Politecnico di Bari

Terms of use:

(Article begins on next page)

23 November 2026

Politecnico di Bari

Department of Mechanics, Mathematics and Management

Ph.D. Program (Cycle XXXVII)

SSD: ING-IND/06 Fluid-Dynamics

Final Dissertation

Application of Co-Flow Jet Methodology for Rear Wing Flow Control in High-Performance Vehicles

---

by

Marco Robert Herberg

Academic Supervisor:

Prof. Giuseppe Pascazio

Prof. Marco Donato de Tullio

Industrial Supervisor

Dr. Stefano de Pinto

Coordinator of Ph.D Program:

Prof.ssa Caterina Ciminelli

Date 23/09/2026

Course n°37, 01/11/2021-31/10/2024

Department of Mechanics, Mathematics and Management
Ph.D. Program (Cycle XXXVII)
SSD: ING-IND/06 Fluid-Dynamics
Final Dissertation

Application of Co-Flow Jet Methodology for Rear Wing Flow Control in High-Performance Vehicles

by
Marco Robert Herberg

Signature of PhD student

Academic Supervisors:
Prof. Giuseppe Pascazio
Prof. Marco Donato de Tullio

Industrial Supervisor:
Dr. Stefano de Pinto

Coordinator of Ph.D Program:
Prof.ssa Caterina Ciminelli

Date 23/09/2026
Course n°37, 01/11/2021-31/10/2024

Abstract

This thesis investigates the application of the Co-Flow Jet (CFJ) active flow-control methodology to an automotive rear wing through a combined CFD and experimental campaign conducted on a modified McLaren 765LT. The work evaluates the aerodynamic response, energy performance, and practical integration of embedded Co-Flow systems under representative on−track conditions. An extensive CFD design campaign assessed multiple Co-Flow architectures, from which three representative configurations incorporating ducted axial fans were selected for experimental testing. The results indicate that aerodynamic performance is strongly influenced by the interaction between momentum injection, vehicle conditions, and duct architecture. The most effective configuration achieved drag reductions of up to 9.6% together with downforce increases of 17.7% under highly loaded conditions, significantly exceeding the repeatability levels of the measurements. The efficiency analysis further showed that, under selected operating conditions, the aerodynamic benefits obtained from the Co−Flow system can exceed the electrical power required by the actuation system. However, increased mass-flow capability alone was not found to guarantee improved aerodynamic performance or efficiency. The results demonstrate the successful integration and operation of a fan-driven Co-Flow system on a production-based vehicle and highlight the importance of momentum injection level and duct design. The findings should be interpreted within the scope of the investigated vehicle and operating envelope. Due to confidentiality constraints, part of the absolute aerodynamic data could not be disclosed, and the results are therefore presented primarily as relative variations.

Keywords: Co-Flow Jet; active flow control; boundary-layer energization; drag reduction; rear wing aerodynamics; RANS CFD; experimental validation; aerodynamic efficiency; flow separation control; high-performance automotive

Acknowledgements

Ed eccoci qua.

Non avrei mai pensato che, dopo tutti questi anni lontano dall'università, mi sarei ritrovato nuovamente davanti a una commissione per discutere una tesi. Per me questo rappresenta il completamento di un percorso che desideravo intraprendere già molto tempo fa, ma che, a causa di diverse circostanze, non avevo mai avuto la possibilità di portare avanti. È stato un pensiero rimasto sopito negli anni, ma mai davvero scomparso.
Questa vuole essere una piccola dedica fatta a coloro che mi sono stati vicini e mi hanno permesso di conseguire i risultati ottenuti.
Desidero ringraziare i miei tutor Dr Stefano De Pinto, Prof Giuseppe Pascazio e Prof Marco Donato de Tullio per la loro disponibilità nell'aiutarmi a risolvere i problemi che si sono posti in itinere e il continuo supporto.
Un ringraziamento particolare a Michael, per avermi supportato (e sopportato) con le mie infinite questioni di CFD e per aver resuscitato *"Loki"* innumerevoli volte, molte delle quali, spero, con un bicchiere di vino spagnolo in mano.
A Vincenzo, che mi ha fatto fare pace con Catia, aiutandomi in un task impossibile nel tempo a mia disposizione.
A Josè, che a causa del mio banco, ho fatto litigare coi vicini per i rumori molesti delle mie ventole da caratterizzare.
A "Goffredo", che se gli vado appresso qualcosa me tira fuori dal cappello, mi sa che dovevo offrirti un po' di vino pure a te.
Chiaramente, Mutti e Ste, che, come per la laurea, hanno creduto in me spronandomi a non mollare tutto (e non è stato semplice).

Per ultimo solo in ordine di scrittura ma prime nei miei pensieri ringrazio "Il Principale" per avermi concesso la presenza di tre splendide donne che mi hanno sopportato per tutti questi anni e senza le quali non avrei ottenuto questo importante risultato e tanti altri che verranno.

Micio, Ciccia e Polly, il mio grazie va a voi.

Contents

Abstract 3
Acknowledgements.....4
1 Chapter 1 - Introduction 7
1.1 Background…….....7
1.2 Research Objective and Original Contributions…….9
1.3 Thesis Structure…….....10
2 Chapter 2 - Literature Review 12
2.1 State of the Art of Active Boundary Control Techniques ……....12
2.2 Fluidic Methods…… 16
2.2.1 Steady Suction and Blowing…….....17
2.2.2 Pulsed Blowing…….....…20
2.2.3 Synthetic Jets……..……..…...22
2.2.4 Co-Flow…….....…26
2.3 Surface-Based Active Flow Control and Morphing.....27
2.3.1 Surface-Based…….....27
2.3.2 Morphing…..…….....28
2.4 Plasma-Based Actuation (DBD Actuators) 32
2.5 Discussion and Generale Considerations.....…37
2.5.1 Fluidic Blowing and/or Suction…….....….38
2.5.2 Profile…….....….39
2.5.3 Plasma.....……..……..40
2.5.4 Comparative Assessment…….....……...41
2.6 Conclusions and Future Trends…….....……..……...43
3 Chapter 3 - Baseline CFD vs Real World Testing…….....46
3.1 Turbulence Modelling Strategy, Limitations and CFD Baseline Setup…….....46
3.2 Vehicle Baseline Setup 56
3.3 CFD vs Experimental Results…….....61
3.4.1 C_d Comparison 63
3.4.2 C_l Comparison 66
3.4.3 C_p Comparison 70
3.4.4 Assessment of CFD Predictive Capability.....72
4 Chapter 4 - Fan Characterization Rig……..…….....73
4.1 Rig Hardware Setup 73
4.2 Rig Electronic Set …….....75
4.3 Fan Characterization Data Analysis……..…….....78
5 Chapter 5 - Co-Flow CFD Performance Analysis.....83
5.1 Front Suction Concept……..85

5.2 Front Blowing Concept……88
5.3 Combined Front Suction and Rear Blowing Concepts…….....……...91
5.4 Final Co-Flow Design and CFD Performance Assessment …….……... 94
6 Chapter 6 - Experimental Validation and Performance Assessment….....115
6.1 Wing Preparation 115
6.2 Experimental Results 119
6.2.1 Drag Coefficient 120
6.2.2 Lift Coefficient …….....123
6.2.3 Pressure Coefficient 131
6.2.4 Efficiency …….....138
7 Chapter 7 – Conclusions…….....143
Appendices 145
References 166

Chapter 1 – Introduction

1.1 Background

Aerodynamic forces play a fundamental role in determining the performance, efficiency, and dynamic behaviour of modern road vehicles. In particular, aerodynamic drag directly affects fuel or energy consumption and maximum speed, whereas lift (or downforce in high-performance vehicles) strongly influences vehicle stability, handling, and cornering capability. Since these aerodynamic requirements are often conflicting, considerable research has been devoted to the development of technologies capable of actively manipulating the flow field to improve overall vehicle performance. Flow-control methodologies are generally classified into two categories:

- Passive flow control, where aerodynamic improvements are achieved without external energy input.

- Active flow control, where an external energy source is employed to manipulate the flow field.

Passive devices, such as vortex generators, have been extensively adopted because of their simplicity and robustness. However, their aerodynamic effect is permanent and cannot be adapted to changing operating conditions, often resulting in unnecessary drag penalties when flow control is not required. Consequently, increasing attention has been devoted to active aerodynamic systems capable of adapting their behaviour according to the instantaneous driving conditions. Among the various approaches investigated, active flow control (AFC) has emerged as one of the most promising aerodynamic technologies. By introducing controlled perturbations into the flow through moving surfaces, wall jets, or travelling-wave excitations, AFC systems can modify boundary-layer behaviour, delay flow separation, and alter wake structures. In recent years, several studies have successfully demonstrated the application of these concepts to automotive configurations. Harinaldi et al. [1] investigated active blowing on a family-van model derived from the classical Ahmed body, reporting drag reductions of approximately 14% through boundary-layer re-energization and delayed flow separation. Similarly, Cerutti et al. [2] indicated that distributed slot jets applied to a square-back vehicle achieved drag reductions of up to 12% while maintaining a stable wake structure. More recently, Phan et al. [3] numerically investigated multiple suction and blowing configurations on a square-back Ahmed body, showing that the combined use of suction and blowing further improves flow attachment, wake symmetry, and overall aerodynamic efficiency. Collectively, these studies demonstrate that active flow control has the potential to significantly improve vehicle aerodynamic performance and energy efficiency. One of the most representative

examples in the automotive field is the Aerodinamica Lamborghini Attiva (ALA) system developed by Lamborghini [4]. By actively controlling the airflow through internal ducts integrated into the front splitter and rear wing, the ALA system performs a function conceptually similar to the Drag Reduction System (DRS) employed in Formula 1. During straight-line driving, the system reduces aerodynamic drag by promoting controlled rear-wing stall, whereas during cornering it maximizes downforce to improve grip and vehicle stability. This adaptive aerodynamic concept enabled the Huracán Performante to substantially increase aerodynamic loading while simultaneously improving straight-line performance, demonstrating the advantages of actively controlled aerodynamic devices. Despite these achievements, systems such as ALA remain strongly dependent on vehicle speed, since their effectiveness is directly related to the available dynamic pressure. Alternative active flow-control strategies based on tangential wall jets have therefore attracted considerable interest because they directly energize the boundary layer and delay flow separation. Although highly effective from an aerodynamic perspective, these systems generally require relatively large mass flow rates and significant energy input, limiting their practical application in energy-sensitive automotive systems. A promising evolution of this concept is represented by the Co-Flow Jet (CFJ) methodology. Unlike conventional blowing systems, CFJ combines suction and blowing within a closed-loop configuration in which low-momentum boundary-layer fluid is extracted, re-energized, and re-injected through a downstream blowing slot (Danò et al. [5]). This approach enhances momentum transfer within the boundary layer while reducing the mass-flow requirements associated with conventional blowing techniques, offering the potential to improve aerodynamic performance with lower energy consumption. Furthermore, unlike adaptive systems such as ALA or DRS, whose effectiveness primarily depends on the vehicle operating conditions, the Co-Flow Jet provides direct control of the boundary layer through momentum injection, introducing an additional degree of freedom for aerodynamic optimization. Despite the considerable progress achieved in active flow-control research, several challenges remain before these technologies can be effectively transferred to production-derived high-performance vehicles. Most published investigations have been performed on simplified aerodynamic models, such as airfoils or Ahmed-body configurations, through numerical simulations or controlled laboratory experiments. Consequently, limited information is available regarding the practical integration of active flow-control systems into real vehicles, where geometric constraints, actuator packaging, electrical power consumption, structural modifications, instrumentation, and measurement uncertainty must all be considered simultaneously. Moreover, previous studies have predominantly focused on aerodynamic performance, while comparatively little attention has been devoted to the interaction between aerodynamic effectiveness, actuator operating conditions, and overall energetic efficiency.

The present research addresses these limitations through the development and experimental validation of a fan-driven Co-Flow Jet system integrated into the rear wing of a production-

derived high-performance vehicle. Unlike previous investigations, this work combines CFD-based aerodynamic design, laboratory fan characterization, additive manufacturing, full-scale vehicle instrumentation, and on-track experimental testing within a single integrated engineering methodology. Particular emphasis is placed not only on the achievable aerodynamic benefits but also on the relationship between aerodynamic performance, fan operating conditions, electrical power consumption, and overall system efficiency under representative operating conditions.

1.2 Research Objectives and Original Contributions

The primary objective of this PhD research is to develop and experimentally validate a practical methodology for the implementation of fan-driven Co-Flow Jet technology in high-performance automotive applications. The main original contributions of this work can be summarized as follows:

- Development of an integrated methodology for the design, implementation, and assessment of active aerodynamic systems under realistic automotive constraints, combining CFD analysis, laboratory fan characterization, vehicle instrumentation, and full-scale experimental testing.

- Experimental implementation and validation of a fan-driven Co-Flow Jet system integrated into the rear wing of a production-derived high-performance vehicle, supported by a comprehensive aerodynamic database including pressure distributions, aerodynamic loads, fan operating characteristics, and vehicle-level performance measurements.

- Comprehensive assessment of the interaction between active flow control, aerodynamic performance, electrical power consumption, and overall energetic efficiency, providing a practical framework for evaluating both aerodynamic effectiveness and actuation efficiency under realistic operating conditions.

The remainder of this thesis describes the methodology adopted to achieve these objectives, presents the numerical and experimental investigations performed throughout the research, and discusses the potential of fan-driven Co-Flow Jet technology for future high-performance automotive applications.

1.3 Thesis Outline

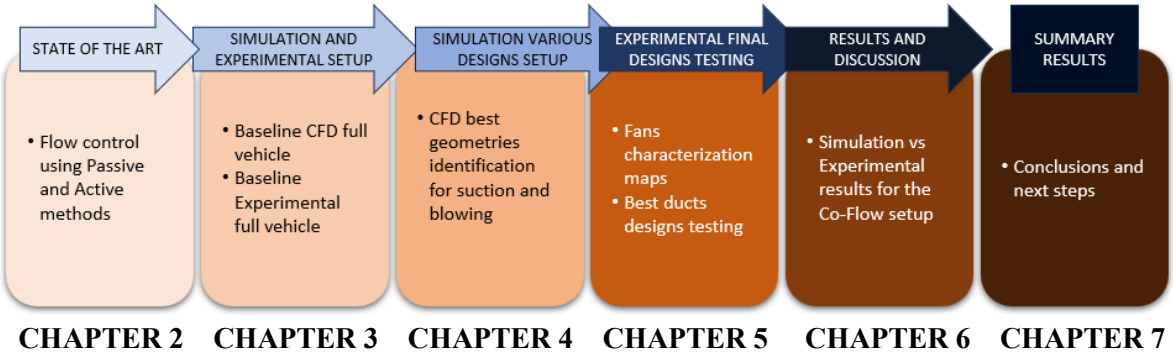

Figure 1.1: Workflow of the research methodology adopted throughout the thesis.

Figure 1.1 illustrates the logical progression of the research, from the literature review and baseline vehicle characterization to CFD design, experimental validation, and the assessment of aerodynamic and energetic performance:

- Chapter 2 provides a theoretical in-depth analysis of fluid dynamics and a comprehensive review of the state of the art in active flow control technologies developed over recent decades in the aerospace field, with a particular focus on their application to the automotive sector.

- Chapter 3 focuses on the evaluation of the baseline aerodynamic configuration of the McLaren 765LT rear wing, combining both computational fluid dynamics (CFD) simulations and experimental on-track testing. This stage establishes a robust reference framework for subsequent comparisons once the proposed Co-Flow Jet configurations are developed and tested. Data are obtained through a combination of direct and indirect measurement techniques, including:
  - Static pressure ports positioned along the extrados wing surface at multiple spanwise sections
  - Suspension displacement sensors on all four corners to quantify downforce via vertical movement
  - Vehicle coast-down tests, used to determine the drag coefficient under various configurations and speeds.

- Chapter 4 describes the fan selection and characterization process, mapping the performance of available ducted fans in the laboratory based on the geometric constraints of the wing. The resulting fan performance maps, relating static pressure differential and mass flow rate, serve as a reference for validating the boundary

conditions used in CFD simulations and for ensuring compatibility with real-world components.

- Chapter 5 presents the design, modelling, and simulation of multiple Co-Flow Jet configurations. Several duct geometries are proposed and assessed through CFD analysis to identify the most promising designs to be physically fabricated and tested. The McLaren 765LT vehicle test platform is then modified to accommodate the selected Co-Flow ducts, allowing for experimental validation of the computational predictions.

- Chapter 6 discusses the results and correlations between CFD predictions and experimental data, comparing the baseline configuration with the various Co-Flow geometries. The chapter concludes with a critical analysis of the aerodynamic, energetic, and practical implications of Co-Flow technology for high-performance automotive applications.
- Chapter 7 summarizes the results of the research, drawing the main conclusions and outlining possible future developments, including limitations of the current findings and next recommended steps.

Due to confidentiality and intellectual property restrictions imposed by McLaren Automotive Ltd., certain detailed numerical data, CFD parameters, and geometric information are normalized or, where necessary, not disclosed; however, all relevant findings are presented in a consistent and technically representative manner, ensuring full scientific validity.

Chapter 2 - Literature Review

2.1 State of the Art of Boundary Control Techniques

In the continuous pursuit of improved vehicle performance, automotive engineers are exploring a wide range of strategies to meet increasingly demanding targets. Among these, aerodynamic optimization plays a central role, encompassing both lift (or downforce) enhancement and aerodynamic drag reduction [6,7]. For instance, given the high annual mileage of long-haul trucks (approximately 160,000 km/year), even modest reductions in aerodynamic drag can lead to significant savings in fuel consumption and operating costs [8]. In high-performance vehicles, high cornering speeds require high-lift aerodynamic configurations capable of generating the necessary downforce to maximize tire grip. However, high-lift surfaces inherently lead to increased induced drag, which compromises straight-line performance. Consequently, an optimal balance between downforce generation and drag minimization must be achieved [9]. Different methods to generate downforce such as inverted wings, diffusers, and vortex generators have been studied, with complex geometry involving aerodynamic interaction between the various body components [10]. Moreover, and particularly in the case of high-speed road cars, the aerodynamics should be properly taken into account so as to achieve safety, which is a primary factor [11]. Various strategies have been developed to reduce aerodynamic drag, all based on altering the flow field around the vehicle; these approaches generally fall into two main categories: passive and active flow control methods. Passive methods rely exclusively on geometric modifications of the vehicle body, such as tailored surface profiles, external aerodynamic appendages, or flow-guiding devices, to manipulate airflow. These solutions do not require any additional energy input during operation and are inherently robust. However, each passive configuration is optimized for a specific operating condition and cannot adapt to changing flow regimes. As a result, passive solutions may lead to degraded performance or even flow instabilities when operating outside their optimal range [12,13]. Active flow control (AFC) techniques overcome these limitations by enabling real-time manipulation of the flow field based on operating conditions; unlike passive solutions, AFC systems can be activated or deactivated on demand, allowing the aerodynamic response of the vehicle to adapt dynamically [14]. These strategies are primarily applied to modify boundary layer behaviour, delay separation, alter wake structures, or control vortex formation. However, this adaptability comes at the cost of additional system complexity and increased energy consumption [15]. In automotive aerodynamics, the evaluation of flow behaviour is often carried out using simplified geometries that capture the essential physics of vehicle wakes while remaining computationally and experimentally manageable. One of the most widely adopted models is the Ahmed body, introduced by Ahmed et al. [16] through an extensive experimental campaign aimed at understanding flow structures around bluff bodies. Their work demonstrated that the rear slant angle is the

dominant parameter affecting wake topology and aerodynamic drag. Further experimental studies by Brunn et al. [17] illustrated the major wake flow regimes as a function of the rear slant angle. Results showed that the drag coefficient reaches a maximum at a slant angle of approximately 30°. For larger angles, the longitudinal vortices break down, and the wake becomes dominated by spanwise structures, leading to a reduction in pressure drag. Over the past decade, a growing number of review papers have investigated active and passive flow control techniques aimed at improving aerodynamic performance. While these studies provide valuable overviews, they often remain descriptive and primarily focus on cataloguing available actuation concepts rather than critically assessing their applicability under realistic operating conditions. Jahanmiri [18] provided an early classification of major AFC techniques based on their actuation mechanisms, including a distinction between feedforward (open) and feedback (closed) control strategies. Although comprehensive at the time, this review is mainly oriented toward aerospace applications and does not account for several technological developments that have emerged in recent years, such as plasma-based actuators and hybrid control strategies. Maine et al. [19] reviewed experimental and numerical studies published between 2010 and 2018, focusing on drag reduction levels exceeding 3%. Their findings are consistent with those reported by Mukuk et al. [20], indicating maximum drag reductions of approximately 20%; however, numerical investigations suggest that Coandă-based flow control applied to the rear of bluff bodies could further enhance performance, potentially enabling drag reductions of up to 50%. The Ahmed body remains the canonical benchmark for studying wake dynamics and aerodynamic drag in ground vehicles due to its simplified geometry, which enables controlled and reproducible investigations of flow separation and vortex structures; however, its lack of realism, particularly the absence of rotating wheels, detailed underbody geometry, and complex front-end features, limits its applicability to real vehicles. To address these limitations, more advanced generic models such as the DrivAer configuration have been introduced [21–23]. Initially developed through a collaboration between the Technical University of Munich (TUM) and BMW, the DrivAer model represents a realistic vehicle geometry while remaining suitable for both experimental and numerical investigations. Unlike the Ahmed body, it comprises a family of configurations (fastback, notchback, and estate) and can incorporate additional features such as rotating wheels and detailed underbody geometries, enabling a more accurate representation of real aerodynamic conditions. Although these models capture complex flow interactions more effectively, the Ahmed body remains the dominant reference in drag reduction and AFC studies due to its simplicity, comparability, and widespread use in the literature; consequently, while the present review primarily focuses on Ahmed-based studies, the inclusion of DrivAer demonstrates the ongoing transition toward more realistic aerodynamic analyses. Cho et al. [24] investigated the aerodynamic performance of various drag reduction devices applied to the DrivAer model, providing one of the first systematic comparisons on a realistic passenger-car geometry. Their

study showed that passive devices such as rear spoilers and horizontal and vertical planes located on C-pillar or on the rear trunk can achieve drag reductions on the order of 3–5.1%, depending on the configuration and flow conditions; the results also demonstrated how these devices interact with complex flow features, including rotating wheels and underbody structures, which significantly influence overall effectiveness. Ashton et al. [25–27] conducted comprehensive experimental and numerical investigations of the DrivAer model, reporting drag coefficient values typically in the range of Cd ≈ 0.25–0.30, depending on the configuration. Their work emphasized the increased flow complexity compared to simplified models, including strong wheel–wake interactions and three-dimensional separation structures, making the DrivAer model particularly suitable for evaluating advanced flow control techniques under realistic conditions. Wang et al. [28] analysed the aerodynamic behaviour of the DrivAer model, Estate variant, under moving-ground conditions, demonstrating that the inclusion of a moving ground and rotating wheels can alter drag values by approximately 5–15% compared to fixed-ground simulations with a Cd ≈ 0.28, in line with Ashton et al.'s [25] results range. Their results showed significant modifications in wake structure and underbody flow, affecting both separation regions and pressure distribution. These findings demonstrate the importance of realistic boundary conditions when assessing flow control strategies. Therefore, while the Ahmed body remains a valuable benchmark for fundamental investigations and is widely used in this review, more realistic models such as DrivAer are essential for accurately assessing the effectiveness of AFC techniques under real operating conditions. However, this state-of-art review does not include a detailed assessment of vehicle dynamics integration; instead, it focuses on the aerodynamic performance and feasibility of each method; here, "performance" refers to the achievable drag reduction and/or downforce generation, while "aerodynamic feasibility" denotes the practical applicability of the method in real-world conditions, including aspects such as implementation complexity, scalability, and compatibility with production vehicles.
The active flow control methods discussed are categorized as follows:

- Fluidic techniques, involving jet injection and/or suction.
- Surface-based techniques, based on mechanical modification of geometry.
- Plasma actuators, which alter the boundary layer through ionization and electrical forcing.

Figure 2.1 provides a visual overview of the different variants of active flow control (AFC). The primary aerodynamic objectives of these techniques include drag reduction and downforce enhancement, both of which are critical to improving overall vehicle performance. Drag reduction aims to decrease aerodynamic resistance, thereby improving straight-line speed, fuel efficiency, and overall energy consumption. In contrast, downforce enhancement

improves vehicle stability, handling, and tire grip, particularly at high speeds and during cornering. Achieving an optimal balance between these objectives is essential, as excessive downforce generation may lead to increased aerodynamic drag, negatively impacting performance under certain operating conditions. Therefore, a detailed aerodynamic design employing an adaptive aerodynamic concept is required, allowing an optimal compromise to be achieved between fuel consumption and performance, e.g., [29].

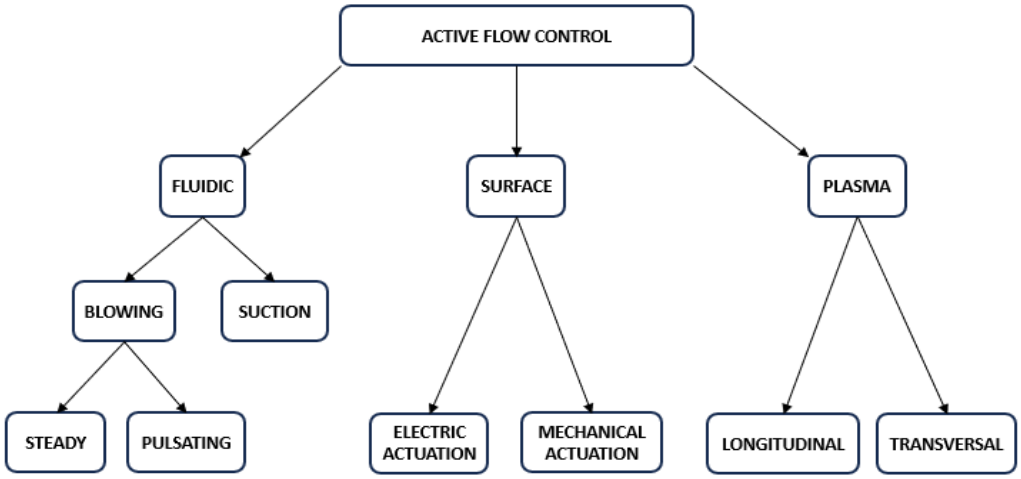

Figure 2.1 Overview of active flow control (AFC) methodologies and their main categories.

While the previous sections classify active flow control (AFC) techniques according to their actuation mechanisms, their practical applicability strongly depends on the specific automotive context. In particular, different application domains, ranging from simplified benchmark models to passenger vehicles, high-performance cars, and heavy-duty transport, are characterized by distinct aerodynamic objectives, flow features, and design constraints. As a result, the effectiveness and feasibility of each AFC approach cannot be assessed independently of its intended application. In simplified configurations, AFC techniques are primarily used to investigate fundamental flow mechanisms under controlled conditions. In contrast, real vehicle applications introduce additional constraints such as packaging, system efficiency, and robustness, which significantly affect the achievable performance. Moreover, the aerodynamic objectives may vary across applications: drag reduction is typically dominant in passenger and heavy-duty vehicles, whereas high-performance applications often prioritize aerodynamic balance and downforce generation. For this reason, the discussion presented in the following section is interpreted with reference to these different application domains, highlighting how the suitability of each AFC technique varies depending on the specific use case.

2.2 Fluidic Methods

Fluidic techniques rely on the injection or removal of air from the main flow field in either steady or unsteady conditions, with jets oriented tangentially or orthogonally to the surface [30]. The effectiveness of these strategies is evaluated using specific performance metrics. Danò et al. [5] proposed the jet momentum coefficient C_μ, defined as

$$C_\mu = \frac{\dot{m} V_j}{1/2 \rho_\infty V_\infty^2 A_{ref}} \tag{2.1}$$

where $\dot{m}$ is the mass flow rate, ρ_∞ is free-stream density, V_∞ is free-stream velocity, and A_{ref} is the reference area; the jet velocity (V_j) reported in the study refers to averaged value at the injection slot. Brunet et al. [31] share the same coefficient as per Danò [5] for steady blowing but propose for pulsed blowing (squared signal) the following jet momentum coefficient C_μ

$$C_\mu = \frac{1}{DC} \frac{<q_m>_t * <V_j>_t}{1/2 \rho_\infty V_\infty^2 A_{ref}} \tag{2.2}$$

where $<q_m>_t$ is the time-averaged mass flow rate, $<V_j>_t$ is the time-averaged output velocity, DC is the duty cycle, and the rest of the parameters are as above. In the context of active flow control, the introduction of the duty cycle (DC) enables temporal modulation of the actuation, making it intermittent rather than continuous; this parameter, defined as the fraction of time during which the actuator is active within a given cycle, allows for precise control of the energy input into the flow. However, although formulations explicitly accounting for the duty cycle have been proposed [31], in many studies, the jet velocity is still expressed as a time-averaged quantity, consistent with the definition adopted in Equation (2.1), as discussed later. Rouméas et al. [32] further introduced a power efficiency metric η, originally proposed for steady suction and here extended to steady blowing that can be defined as well for steady blowing as

$$\eta = \frac{P_{ec}}{P_c};\ P_{ec} = \Delta F_x V_0 \ and \ P_c = 1/2\ k\rho\ V_j^3 S_j \tag{2.3}$$

where P_{ec} represents the power saved through the aerodynamic improvements and P_c is the actuation power, k represents a coefficient accounting for total pressure losses in the actuation system, S_j is the suction/blowing area, V_j is the speed in that area and ΔF_x is the drag reduction induced by the fluidic method. The actuation power is estimated from the time-averaged kinetic energy flux of the jet, representing the fluid mechanical power input, while additional system-level losses (e.g., compression and electrical inefficiencies) are not accounted for. Density requires clarification depending on the actuation method; for steady suction, the freestream air density is considered, as the control power is estimated from the kinetic energy flux of the entrained ambient fluid. For steady blowing, assuming the jet is low in velocity and near-ambient temperature, the freestream density represents a reasonable approximation.

However, for high-speed or thermally altered jets, the density at the jet exit should be used to accurately evaluate both the kinetic energy flux and the mass flow rate. In the present review, the freestream density is assumed unless otherwise specified. For pulsed blowing, in line with Brunet et al. [31], the actuation power is evaluated as the time-averaged kinetic energy flux of the jet. Assuming a duty cycle DC, this leads $P_c = DC \cdot \frac{1}{2}\rho A_j V_{jet,on}^3$, highlighting the potential for reduced power consumption compared to steady blowing. The control is considered efficient when the value η is equal to or greater than 1. Fluidic methods are subdivided into:

- Steady suction and blowing
- Pulsed blowing
- Synthetic jets
- Co-Flow Jets (CFJ)

2.2.1 Steady Suction and Blowing

Suction has long been used in aerospace to stabilize boundary layers, delay transition, and suppress separation. Rouméas et al. [32] demonstrated a 17% drag reduction on an Ahmed body using a suction slot located at the rear slant, resulting from the elimination of the separated flow region on the rear slant when suction was active. Harinaldi et al. [1] explored a reversed Ahmed body to simulate a family van, using suction on the rear; numerical and experimental data align well, showing a drag reduction of approximately 16%, which is close to the results of Rouméas et al.'s [32] study (Figure 2.2). Tarakka et al. [33] conducted a similar setup but, instead of using slots, employed cylindrical holes, achieving a lower drag reduction of about 11% compared to Harinaldi et al.'s [1] setup.

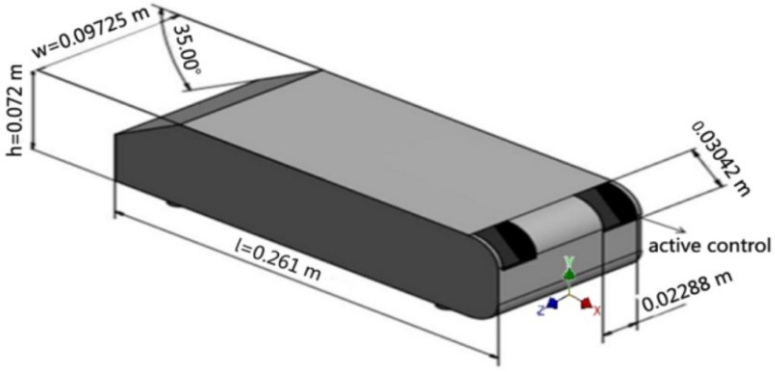

Figure 2.2 Harinaldi et al. [1] van model of a type of reversed Ahmed body.

Blowing techniques, either steady or unsteady, are commonly classified according to jet orientation relative to the surface as tangential, normal (orthogonal), or inclined, each influencing the flow through distinct mechanisms and levels of control authority. Although many active flow control (AFC) strategies in automotive aerodynamics have been developed for specific vehicle geometries, their effectiveness relies on physical mechanisms originally identified in canonical boundary layer studies, primarily within an aeronautical context. In this framework, the work of Gilles Godard et al. [34–36] provides a comprehensive investigation of flow separation control using both passive and active vortex generators, including slotted and round jets. Their results show that streamwise vortices enhance near-wall momentum transfer, reducing boundary layer thickness and shape factor (by up to ~20–25%) and delaying separation. Although developed for aeronautical applications, these mechanisms are directly relevant to bluff-body aerodynamics, where similar separation occurs at the rear of ground vehicles. Consistently, Radespiel et al. [37] reviewed steady blowing for high-lift configurations, demonstrating how momentum injection via tangential and inclined jets effectively delays separation. Their work further demonstrates boundary layer energization and vortex generation as the key mechanisms underlying active flow control and reinforces their applicability to bluff-body flows, where separation control and momentum transfer are central to wake manipulation and drag reduction. High-lift configurations based on steady blowing and Coandă flaps can achieve maximum lift coefficients up to $C_l \approx 5$, which can be further increased to $C_l \approx$ 6-7 through leading-edge optimization and suction. In extreme conditions, values approaching $C_l \approx 8$ have been reported. Among these approaches, tangential blowing, where the jet is aligned with the surface, is primarily used to energize the near-wall flow and counteract viscous losses. It is important to distinguish between classical boundary layer control (BLC) obtained through tangential or inclined blowing and the Coandă effect, as these mechanisms rely on different physical principles. In BLC, the injected momentum is primarily used to compensate viscous losses within the boundary layer, thereby delaying or preventing flow separation, and this mechanism can be applied to both flat and curved surfaces. In contrast, the Coandă effect occurs when a high-momentum jet is tangentially injected over a curved surface, causing the jet to remain attached to the surface due to entrainment and centrifugal effects, generating a low-pressure region and a significant deflection of the external flow. Although high-momentum blowing over curved geometries may involve both mechanisms, the distinction remains important when interpreting aerodynamic performance and actuator efficiency. This blowing technique has been widely applied both to airfoils, through slot injection at the leading or trailing edge, and to automotive configurations such as the Ahmed body. For example, Mestiri et al. [38] investigated steady tangential blowing on an Ahmed body, reporting drag reductions between 6% and 10.4% depending on the Reynolds number. Their flow visualizations indicate that tangential blowing enlarges the separated region over the rear window, thereby disrupting the formation of

counter-rotating longitudinal vortices along its lateral edges. On the other hand, orthogonal blowing, where the jet is injected perpendicular to the surface, primarily enhances mixing and disrupts coherent wake structures; this configuration is commonly used in bluff body wake control and in automotive applications through microjets or jet arrays positioned at the rear of the vehicle. Aubrun et al. [39] demonstrated that orthogonal microjet injection on a 25° Ahmed body slant can reduce drag by approximately 9–14% while also significantly modifying lift characteristics due to strong wake interaction. Inclined blowing represents an intermediate configuration that combines the advantages of both tangential and orthogonal injection, simultaneously energizing the boundary layer and promoting mixing in the outer flow. In automotive aerodynamics, inclined jets are frequently applied on the rear slant of the Ahmed body on diffusers and spoilers to optimize flow attachment and wake development. Similarly, Littlewood et al. [40] suggested that steady blowing on a simplified square-back vehicle can achieve drag reductions of up to approximately 8–10%, depending on the blowing momentum coefficient and the jet orientation. McNally et al. [41] showed that combining tangential and orthogonal blowing on a modified Ahmed body can yield drag reductions of approximately 2–3%, while more aggressive configurations, such as the distributed actuators proposed by Zhang et al. [42], have shown drag reductions up to 29%, albeit with relatively low overall efficiency (0.36) according to Equation (3) due to a large energy consumption to obtain the maximum drag reduction. Furthermore, CFD studies by Wassen et al. [43,44] were consisted with the fact that combined blowing and suction strategies applied on the rear slant can achieve drag reductions of approximately 9.4%, emphasizing the importance of jet orientation and system integration. A drag reduction of 9.4% corresponds to an equivalent decrease in propulsion power. However, as the control strategy is active, additional energy input is required. The propulsion power to overcome the aerodynamic drag for natural flow is defined by

$$P_D = F_D U_0 = \frac{1}{2} C_d \rho B H U_0^3 \tag{2.4}$$

and the blowing fluid power proposed as

$$P_{act} = \frac{1}{2} \dot{m}_{slit} v_{slit}^2 \tag{2.5}$$

where “B” is the vehicle’s width, “H” is the vehicle’s height, “U_0” is the average tunnel air velocity, “ρ” is the tunnel density, “$\dot{m}_{slit}$” actuation’s mass flow rate and “v_{slit}” is the actuation speed. A simplified estimation shows that the actuation power amounts to only 0.6% of the baseline propulsion power (P_{act}/P_D=0.006), resulting in a net energy saving of approximately 8.8%; it should be noted that this estimate does not account for potential losses in practical implementations. Overall, these studies demonstrate that jet orientation plays a critical role in determining the balance between boundary layer energization and wake manipulation, with tangential blowing being more efficient for separation delay, orthogonal blowing more

effective for wake disruption, and inclined blowing offering a balanced and often optimal solution between the two mechanisms. Blowing can be effectively used on aerodynamic devices such as wings to enhance downforce ($\Delta C_l = 0.105$) with only a minor drag penalty ($\Delta C_d = 0.01$) [45]. When implemented through a Coandă-based flow control system, the injected jet remains attached to the curved surface, energizing the boundary layer and suppressing trailing-edge separation. This results in a more favourable pressure distribution along the airfoil, effectively increasing its aerodynamic camber and lift capability. Unlike conventional lift augmentation, the drag increase remains limited because the flow stays attached and the wake structure is improved, making Coandă blowing a highly efficient active flow control strategy. Building on the previously discussed steady blowing strategies, pneumatic active flow control has been extensively investigated for heavy vehicles, showing significant aerodynamic benefits. Early studies on pneumatic configurations demonstrated that tangential blowing applied at the trailer curved edges can achieve drag reductions of up to 31%, mainly through enhanced entrainment and increased base pressure, which suppress large-scale separation and even allow additional functionalities such as aerodynamic braking and crosswind stabilization [46]. More recent investigations on European-type truck models confirm these mechanisms, demonstrating that blowing to curved rear geometries effectively keeps the flow attached by generating a low-pressure region that attracts external flow toward the surface (Coandă effect). This results in a clear reduction in the wake recirculation zone, as evidenced by PIV measurements, and leads to drag reductions up to about 12.6% compared to the baseline configuration [47]. Overall, these studies demonstrate that steady Coandă-based blowing modifies the wake topology by reducing separation and recirculation, thereby improving aerodynamic efficiency, with performance strongly dependent on actuator placement, jet momentum, and interaction with underbody flow structures.

2.2.2 Pulsed Blowing

Steady blowing has been shown to improve aerodynamic performance of both slender bodies such as airfoil profiles and bluff bodies such as simplified vehicle models by altering wake characteristics and reducing separation; however, excessive steady blowing can unfavourably alter the boundary layer thickness and wake dynamics, potentially increasing total drag under certain conditions [48]. In this context, unsteady actuation techniques such as pulsed blowing have emerged as a more efficient alternative, particularly in aerospace applications where flow control authority must be achieved with minimal energy input. In high-lift configurations, experimental studies conducted by Brunet et al. [31] have demonstrated that pulsed blowing can significantly delay flow separation and increase lift, extending the operational angle-of-attack range before stalling. These improvements are especially relevant for modern aircraft, where enhanced lift-to-drag ratios directly translate into better fuel efficiency and reduced emissions. The underlying physical mechanisms were

established by Greenblatt et al. [49], who confirmed that periodic excitation interacts with the natural instabilities of the shear layer, promoting the formation and organization of large-scale coherent vortical structures; these structures play a dominant role in momentum transfer and entrainment, enhancing the exchange of high-momentum fluid toward the wall and thereby re-energizing the boundary layer. In the context of pulsed blowing, this mechanism is achieved through the periodic injection of momentum via intermittent jets, which effectively trigger and control these instabilities; as a result, boundary layer separation can be delayed or even suppressed with momentum input levels one to two orders of magnitude lower than those required for steady blowing, making the technique highly attractive for practical implementation. The effectiveness of pulsed blowing has also been validated in flight-relevant conditions. Whalen et al. [50] conducted both wind tunnel and full-scale flight tests on a vertical tail equipped with active flow control actuators based on pulsed blowing. The system, installed near the leading edge of the vertical stabilizer, was shown to significantly enhance side-force generation at high sideslip angles, where baseline configurations typically experience massive flow separation. Quantitatively, the results indicated increases in effective side-force of up to a maximum of 14%, along with a marked improvement in yaw control authority. Additionally, the technology enabled similar control performance at reduced rudder deflection angles, showing the potential for smaller tail sizing, reduced structural loads, and overall drag reduction in off-design flight conditions. Building upon these aerospace developments, the application of pulsed blowing has been extensively extended to bluff-body flows, particularly in the automotive sector. Closed-loop flow control of bluff bodies has been extensively investigated in the literature, particularly in the context of wake stabilization and drag reduction [51–53], where reductions in drag on the order of 10–20% and a significant attenuation of wake fluctuations have been reported, depending on the actuation strategy and flow conditions. A central contribution of Pfeiffer's work [54] lies in the identification of LPV models for the actuated flow and the transient crosswind gust response, capturing the dependence of the aerodynamic dynamics on parameters such as free-stream velocity and crosswind angle. The approach relies on feedback-controlled Coanda actuation at the trailing edges, combined with multivariable control strategies based on both robust H∞ and linear parameter-varying (LPV) frameworks. These models enable the synthesis of gain-scheduled controllers with improved performance compared to conventional robust designs. Wind tunnel experiments on 2D and 3D bluff bodies demonstrate significant drag reduction (up to 35% for the 2D case and about 15% for the 3D configuration) and effective attenuation of unsteady aerodynamic loads, particularly in terms of yaw moment and side-force fluctuations, leading to enhanced lateral stability under realistic gust conditions. Unsteady flow control using pulsed jets has also been widely investigated on the Ahmed body, a canonical model for ground vehicle aerodynamics. Joseph et al. [55,56] reported drag reductions of up to approximately 8% for the 25° slant configuration using both pulsed jets and MEMS-based

micro-jets. Optimal performance was achieved when the actuation frequency matched the natural shear-layer instabilities, leading to enhanced mixing, reduced recirculation, and increased base pressure. Further improvements have been verified by He et al. [57], who achieved drag reductions of up to approximately 9.2% on a notchback Ahmed body through the combined use of pulsed jets and a genetically inspired optimization strategy. Their results demonstrate the importance of tuning actuation parameters to effectively control the three-dimensional wake, promoting partial flow reattachment and suppressing large-scale separation. This results in a more compact and stabilized wake, reduced recirculation, and a significant increase in base pressure, ultimately improving aerodynamic efficiency. Even larger drag reductions have been reported by Bideaux et al. [58], who applied pulsating flow control to an Ahmed body and observed reductions of up to 20% at an actuation frequency of 500 Hz compared to uncontrolled conditions. In their study, a solenoid valve was used to modulate the airflow issuing from the rear slant, demonstrating the strong sensitivity of the control effectiveness to actuation frequency. Gillièron [59] subsequently confirmed the repeatability of these results and provided additional insight into the wake topology, showing how pulsed actuation modifies the large-scale flow structures behind the bluff body. Overall, these studies confirm that pulsed blowing represents a highly effective and versatile active flow control strategy. Compared to steady blowing, periodic actuation enables a significant reduction in the required mass flow rate for a given control authority, thereby improving overall efficiency. The effectiveness of the technique is strongly linked to the actuation frequency, with optimal performance typically achieved when the forcing is tuned to the natural instabilities of the shear layer. This highlights a fundamental advantage of unsteady forcing: rather than relying solely on continuous momentum injection, pulsed blowing exploits intrinsic flow instabilities to enhance mixing, accelerate momentum transfer, and promote flow reattachment. These characteristics make it particularly attractive for real-world applications, where efficiency, robustness, and reduced energy consumption are critical design constraints.

2.2.3 Synthetic Jets

To complete the overview of pulsating flow methodologies, it is relevant to introduce synthetic jets. A synthetic jet actuator (SJA) is a fluidic device that generates a quasi-steady jet through cyclic suction and blowing of fluid into and out of a cavity via an orifice or slot, resulting in zero net mass flow over one actuation cycle. This oscillatory process produces a train of vortical structures that interact with the external flow [60]. The effectiveness of synthetic jets arises from the alternating blowing and suction phases: momentum is injected into the external flow during blowing, while the suction phase perturbs and restructures the shear layer. This leads to enhanced mixing, reduced recirculation, and increased base pressure, promoting flow reattachment. Despite the zero-net-mass-flux condition, a net momentum

transfer is achieved through vortex shedding and entrainment, allowing synthetic jets to reproduce many of the benefits of steady or pulsed blowing with significantly lower momentum input. Accordingly, their effectiveness is governed by the momentum coefficient rather than the mass flow rate. The key advantages of SJAs include fast response time, high jet velocity, no requirement for external air supply, absence of complex piping, and compactness, which have attracted significant attention in recent years. A relevant design approach relies on Helmholtz-resonator-type cavities, enabling efficient coupling between actuator dynamics and the fluidic response. Schueller et al. [61] investigated synthetic jet actuators based on this configuration combined with a dual-transducer concept. Their results showed that operating near the resonant frequency significantly enhances actuator efficiency and jet momentum. In particular, the use of two transducers led to an increase in jet exit velocity of up to 50% compared to a single-transducer setup, with peak velocities approaching 90m/s under certain actuation conditions.

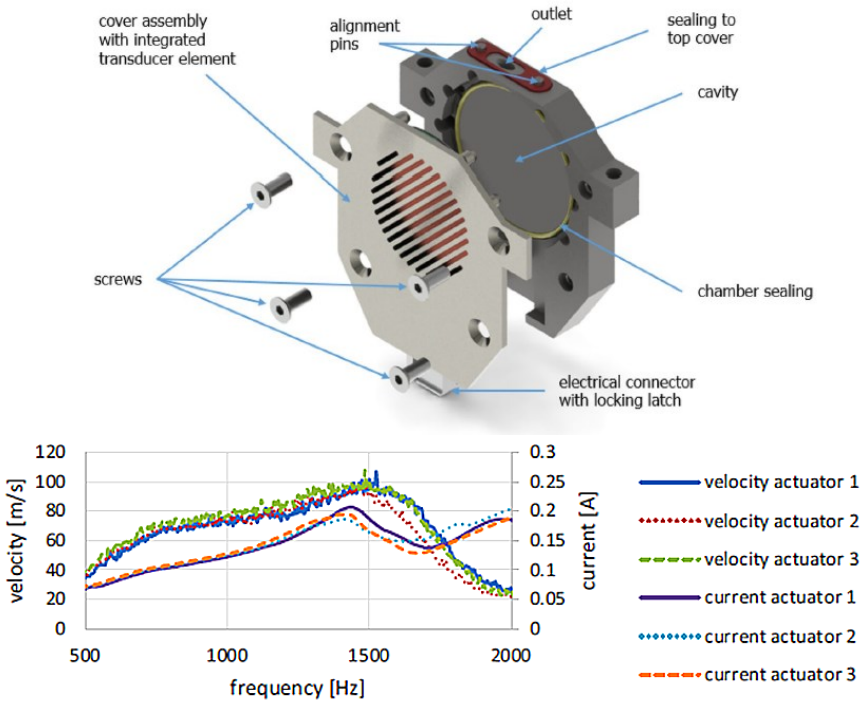

Figure 2.3. Weigel et al. [62]: synthetic jet actuator (top), actuator velocity and current versus frequency (bottom).

This demonstrates the strong potential of resonant, multi-actuator configurations for applications requiring high momentum injection and efficient energy conversion. Recent studies further highlight both the performance potential and the design challenges of these

devices. In particular, Weigel et al. [62] developed a compact synthetic jet actuator specifically designed for flow separation control, based on a cavity–orifice configuration driven by a piezoelectric diaphragm. Their design focuses on achieving high jet velocities while maintaining low power consumption and structural simplicity. The actuator integrates a carefully optimized cavity geometry and slot configuration to maximize the expelled momentum, resulting in jet velocities almost exceeding 100 m/s (Figure 2.3). These actuators operate under a zero-net-mass-flux condition, meaning that the mass flow rate averaged over one cycle is zero (i.e., c_q=0), while a finite momentum flux is still generated. Accordingly, the appropriate parameter to characterize their intensity is the momentum coefficient c_μ, rather than the mass flow rate coefficient.

For synthetic jets, Kourta et al. [63] defined c_μ based on the cycle-averaged momentum flux as

$$C_\mu = \frac{\rho_j U_j^2 \Sigma_j}{\rho_\infty V_\infty^2 S_\infty} \tag{2.6}$$

where U_{jm} is the speed's amplitude of the synthetic jet, $\sum_j$ is the slot synthetic area and S_∞ is the reference body surface. Kourta et al. [63] applied this methodology to the Ahmed body by integrating an array of synthetic jets on the rear slant, reporting drag reductions of up to 8.5% at Re=1.2×10^6. Their results demonstrate the strong dependence of the drag coefficient on the momentum coefficient: the drag reduction increases with C_μ up to a maximum of approximately 8.5%, after which a plateau is reached, indicating a saturation of the control effect (Figure 2.4).

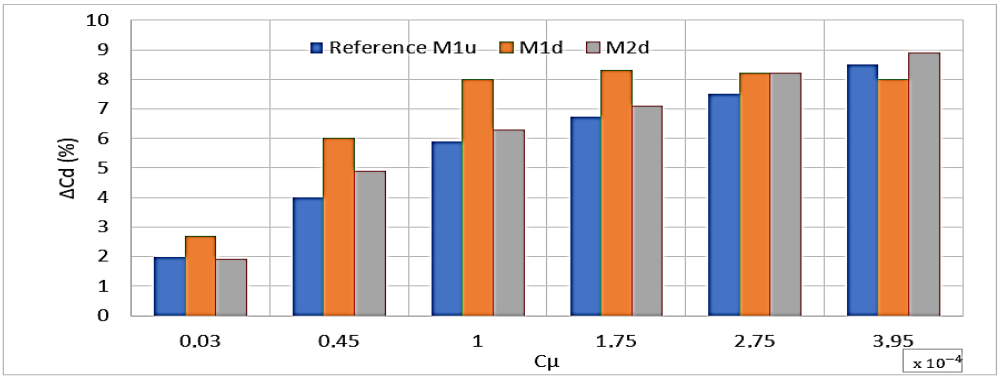

Figure 2.4. Adapted from Kourta et al. [63]: drag reduction vs. momentum flux.

Furthermore, the effectiveness of the control is strongly influenced by the actuator location. While downstream configurations can yield slightly higher peak drag reductions under specific actuation conditions (M2d), the actuator positioned near the onset of separation (M1d) provides more robust and consistent performance, reaching optimal efficiency at lower

momentum coefficients and over a broader range of operating parameters. Flow visualizations further show that, in the uncontrolled case, a large recirculation region develops over approximately 86% of the rear slant, characterized by a saddle point located at z/H_A≈0.74. When control is applied, the flow becomes significantly more organized and fully reattached along the slant. Park et al. [64] extended this analysis by investigating different slant angles (25° and 35°) and jet orientations, confirming drag reduction for the 25° configuration and an increase in drag for the 35° case, in agreement with the classical findings of Ahmed. This behaviour is associated with the formation of streamwise vortices that alter the wake structure. Similarly, Tounsi et al. [65] confirmed these trends and provided detailed wake topology measurements using Particle Image Velocimetry (PIV), showing that the recirculation bubble can be completely suppressed when flow control is applied (Figure 2.5) with a drag reduction

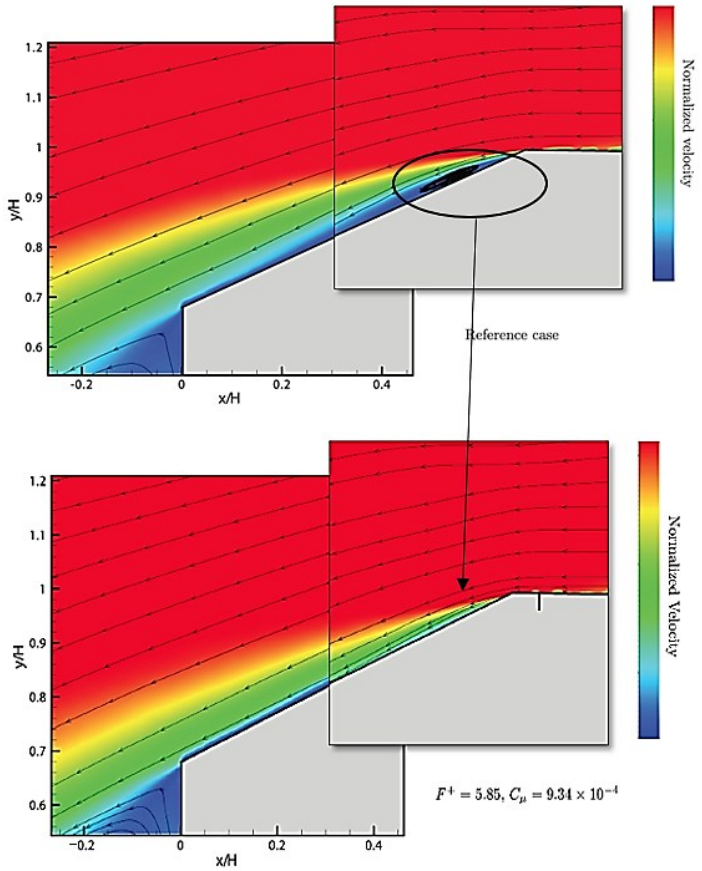

Figure 2.5. Tounsi et al. [65], rear slant flow topology, reference (top) and controlled flow (bottom).

of almost 10%.

To complete the overview of steady and unsteady flow control methods, it is worth mentioning the numerical investigation carried out by Edwige et al. [66] on the square-back Ahmed body;

the authors performed a comparative analysis of steady blowing, pulsed blowing/suction, and synthetic jets using Large Eddy Simulations (LESs). The results confirm the effectiveness of active flow control, with comparable drag reductions across the different techniques, although unsteady actuation demonstrates superior performance. In particular, synthetic jets achieved drag reductions of up to 8% at an actuation frequency of 400 Hz. Moreover, this technique offers a practical advantage, as it does not require a continuous external air supply, making it especially attractive for real-world applications. Moreover, it should be noted that piezoelectric-driven synthetic jets can offer high efficiency; although they require relatively high driving voltages, their predominantly capacitive behaviour results in low current levels and limited power consumption. However, electromagnetic compatibility (EMC) issues may arise, particularly at high operating frequencies.

2.2.4 Co-Flow

In the automotive field, there is a growing interest in the application of the Co-Flow Jet (CFJ) technique, as shown by the computational study of Derghal et al. [67]. Their work investigates the effect of coupled suction and blowing slots arranged along the rear slant of an Ahmed body, varying key parameters such as the streamwise positions of the suction (L_a) and blowing (L_b) slots, the jet angle (Φ), and the jet velocity (V_j), at a freestream velocity of 40 obtained when changing the position of the suction and blowing slots.

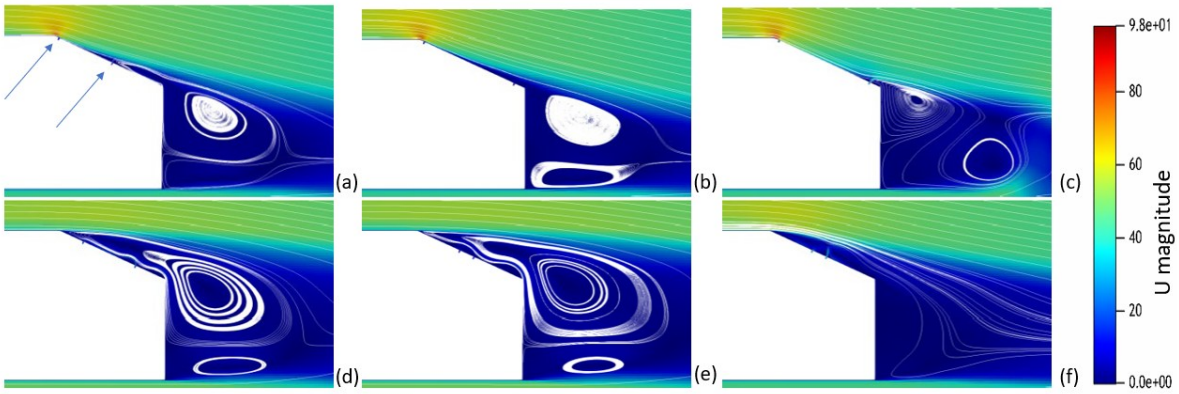

Figure 2.6. Adapted from Derghal et al. [67]: time-average velocity magnitude (m/s) at different locations of blowing and suction slots: (a) CFJ1V10, (b) CFJ3V10, (c) CFJ3V40, (d) CFJ5V25, (e) CFJ7V10, and (f) CFJ7V40.

m/s corresponding to a Reynolds number of 4.29×10^6. Figure 2.6 illustrates some of the results The results demonstrate a strong sensitivity of the flow control performance to the relative positioning of the suction and blowing slots. In particular, the configuration denoted as CFJ14 yielded the best aerodynamic performance, corresponding to the maximum separation distance between the two slots (Figure 2.7). Under these conditions, and for a jet velocity of

40 m/s, a drag reduction of approximately 7% was achieved compared to the baseline configuration. This improvement is attributed to the enhanced momentum exchange induced by the co-flow jet, which delays flow separation and promotes a more attached flow over the rear slant, thereby increasing base pressure and reducing pressure drag. A complementary experimental investigation was conducted by Jahanmiri et al. [68], where an Ahmed body was equipped with a suction slot on the upper rear slant and a blowing slot at the base. The study reported drag reductions of up to approximately 4%, with good agreement between experimental measurements and numerical predictions. The results indicate that increasing

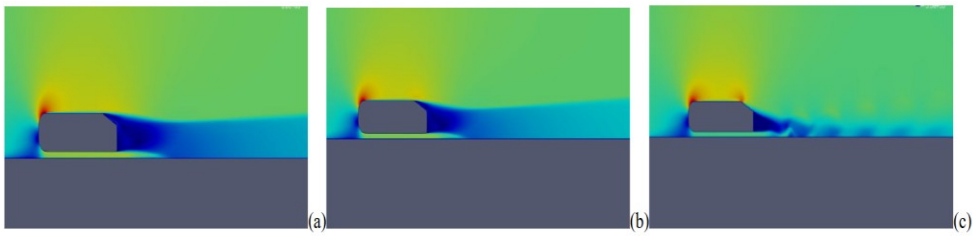

Figure 2.7. Derghal et al. [67]: instantaneous velocity contour of CFJ14 cases (a) 10 m/s; (b) 25 m/s; (c) 40 m/s.

suction strength enhances drag reduction, particularly when combined with base blowing. Moreover, for a fixed-control flow rate, improved performance is achieved by reducing the suction slot area while increasing the base blowing area, highlighting the importance of properly distributing the injected and extracted mass flow.

2.3 Surface-Based Active Flow Control and Morphing

Up to this point, aerodynamic performance has been discussed mainly in relation to fluidic-based techniques involving jet injection and suction.

2.3.1 Surface-Based

Comparable results in reduction in drag can also be achieved using mechanically actuated surfaces capable of injecting momentum directly into the boundary layer. This class of techniques is generally referred to as Moving Surface Boundary-Layer Control (MSBC). Modi et al. [69,70] conducted extensive experimental investigations on rotating-cylinder actuators applied to airfoils, flat plates, and bluff bodies, with particular emphasis on heavy-duty vehicle configurations. Their results showed that operating the cylinders significantly altered the near-wall momentum distribution, leading to an impressive drag reduction of up to 22% in truck-like geometries (Figure 2.8).

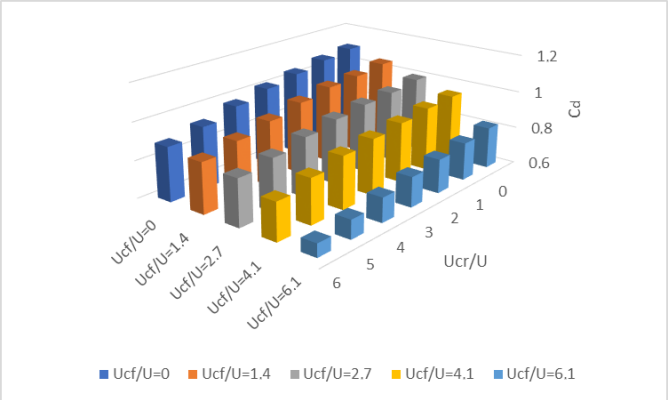

Figure 2.8. Adapted from Modi et al. [69]: Cd variation due to the cylinder speeds.

Complementary computational analyses carried out by Singh et al. [71] confirmed these findings, reporting drag reductions of approximately 35%, with a strong dependence on the linear velocity of the rotating cylinders relative to the incoming flow, as found by Modi et al. [70].

2.3.2 Morphing

Morphing technologies represent an advanced evolution of surface-based flow control, enabling adaptive aerodynamic shapes under varying operating conditions. Originally developed in the aerospace field, early research focused on compliant mechanisms and adaptive structures capable of achieving smooth geometric variations without introducing aerodynamic discontinuities, as shown by Kota et al. [72]. These concepts were further consolidated through comprehensive studies demonstrating the potential of morphing aircraft to enhance lift-to-drag performance, delay flow separation, and improve operational flexibility. In particular, Sofla et al. [73] and Barbarino et al. [74] provided systematic classifications of morphing technologies and their aerodynamic benefits. The development of compliant and adaptive structures has also been investigated in European research, particularly through the work of Monner [75], who showed the feasibility of form-variable trailing edge structures capable of achieving smooth camber variation while maintaining structural integrity. These results highlight the potential of distributed structural compliance for aerodynamic load control and performance enhancement. These concepts have been further consolidated through more recent studies on morphing wing modelling and analysis. Li et al. [76] provided a comprehensive review of modelling strategies for morphing wings, highlighting the importance of multidisciplinary approaches combining structural mechanics, aerodynamics, and control. Their work emphasized the role of aeroelastic coupling and numerical methods in enabling accurate prediction and optimization of morphing configurations. More recent developments have extended these concepts to leading-edge morphing configurations. Wang et al. [77] presented the design optimization and experimental

validation of a seamless morphing leading edge for large civil aircraft, demonstrating the feasibility of continuous surface deformation in high-lift devices. Their results confirm that morphing concepts can be effectively applied to both trailing and leading-edge regions, enabling continuous surface adaptation across the wing. Subsequent developments introduced structurally integrated actuation and smart materials, enabling more compact and efficient morphing solutions. Sun et al. [78] emphasized the role of smart materials in distributed actuation, reporting actuation strains up to approximately 8% for Shape Memory Alloys, with lower values typically adopted in cyclic applications to ensure durability. Chu et al. [79] and Zhu et al. [80] further incorporated advanced design methodologies, numerical modelling, and control strategies, showing that morphing configurations can improve aerodynamic efficiency and delay flow separation under off-design conditions. A significant step toward practical implementation is represented by the Adaptive Compliant Trailing Edge (ACTE) program, developed by NASA in collaboration with Air Force Research Laboratory and FlexSys. Flight-test campaigns reported by Cumming et al. [81] demonstrated operation under realistic conditions, including Mach numbers up to approximately 0.75–0.85 and altitudes up to 40,000 ft, with trailing-edge deflections ranging from −2° to +30°. Experimental results showed good agreement between predicted and measured aerodynamic loads, with discrepancies on the order of a few percent depending on operating conditions. Additional investigations by Herrera et al. [82] confirmed structural integrity and airworthiness, while Cruz et al. [83] and Miller et al. [84] validated load predictions and hinge moment estimations, reporting deviations as low as a few percent in flight conditions. Modern control-oriented frameworks have further improved the feasibility of morphing systems by enabling stable and adaptive operation under varying flight conditions [85]. Overall, these developments reflect the evolution from mechanically driven concepts to integrated morphing systems based on distributed actuation and structural compliance. Despite their extensive development in aerospace engineering, morphing technologies remain relatively uncommon in the automotive sector. This is primarily due to the effectiveness and simplicity of passive aerodynamic devices, such as vortex generators and fixed appendages, which provide satisfactory drag reduction without introducing additional mechanical complexity. It should be noted that most automotive implementations rely on discrete movable components rather than continuous surface deformation and therefore differ from strict morphing concepts. Various notable automotive applications have been reported. Kang et al. [86] investigated a movable rear diffuser applied to a sedan vehicle (Hyundai Sonata), testing multiple configurations across a speed range between 70 and 160 km/h using CFD. The arc-plate diffuser geometry resulted in a drag reduction of approximately 7% in simulations and 5.2% in full-scale road testing for the arc plate shape, along with a significant improvement in vehicle stability due to increased downforce generation. Active aerodynamics have found broader application in the supercar and hypercar segments, where performance optimization outweighs cost and complexity

considerations. Meder et al. [87] presented the Porsche Active Aerodynamics (PAA) system, designed to maintain an optimal aerodynamic balance between the front and rear axles under varying driving conditions. The system operates in two primary modes: a low-drag "Speed" mode, characterized by nearly neutral downforce (~9 kg), and a high-downforce "Performance" mode, delivering over 130 kg of vertical load. Experimental data indicate a lap-time improvement of approximately 2 s on the North Loop Nürburgring Nordschleife, highlighting the tangible impact of active aerodynamic control. Similarly, Estrada [88] reported the application of advanced active aerodynamic devices in Mercedes-AMG vehicles, combining dynamic front and rear surfaces to enhance handling, braking stability, and cornering performance, where a combination of aerodynamics solutions again helps to push the boundaries of their sports vehicles with a similar approach made by Meder et al. [87]. Figure 2.9 shows the changes in vehicle drag, front and rear axle downforce depending on the

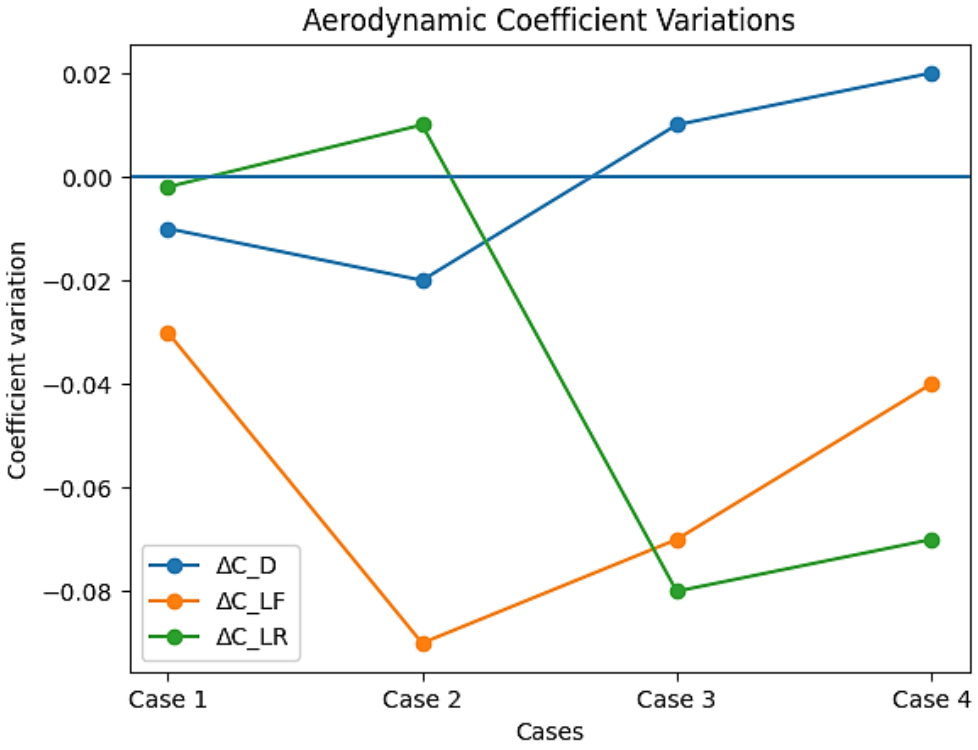

Figure 2.9. Adapted from Estrada [88]: Influence of active aerodynamic configurations on performance coefficients.

geometric setup of the vehicle in various driving conditions.

The results show that deployment of the active underbody profile leads to an improvement in drag performance; however, it also alters the aerodynamic balance by inducing lift on the rear axle. When the rear wing is deployed, the rear downforce is recovered and further increased, as expected, at the expense of a moderate drag penalty. Finally, opening the frontal louvers

results in an additional increase in drag accompanied by a reduction in overall downforce capability, making this configuration aerodynamically inefficient. Based on the data presented, the baseline configuration appears to be the most suitable for road usage, whereas Configuration “C” represents the most promising setup for track-oriented driving. An interesting example is the McLaren P1, where active aerodynamics are integrated with adaptive suspension systems to dynamically control ride height, aerodynamic balance, and overall vehicle performance. The rear wing, a two-axis hydraulically actuated device, is capable of multiple configurations, including partial deployment, full deployment for high-downforce conditions, and forward rotation to function as an aerodynamic brake during deceleration. In parallel, the front aerodynamic elements actively redirect the airflow to enhance underbody suction, further contributing to vehicle stability and performance [89]. The McLaren P1 is reported by McLaren to generate approximately 600 kg of downforce through its active aerodynamic system. Although the manufacturer has not published an exact Nürburgring Nordschleife time, it claims a lap below seven minutes, while the Porsche 918 Spyder has set a documented production-car lap of 6 min 57 s on the same circuit. The P1’s hybrid powertrain produces approximately 916 PS compared to 887 PS for the 918 Spyder [89,90]. In automotive applications, vehicles are typically designed to be aerodynamically efficient, with the option to utilize flow control to enhance aerodynamic performance when needed. However, Lamborghini [4] took a different approach with their ALA system (Active Lamborghini Aerodynamics); the ALA system is inspired by the Drag Reduction System (DRS) used in Formula 1 cars, where a movable flap switches between open and closed positions to actively control downforce and drag. In Lamborghini’s implementation, the system manages airflow, specifically at the front splitter and rear wing area, allowing for impressive cornering speeds by increasing lateral grip without compromising straight-line performance (i.e., top speed). In the standard Huracán, total downforce is estimated at around 200 kg, whereas in the Performante version, it reaches approximately 1500 kg, over seven times higher. This significant increase in downforce drastically improves cornering speed; however, without the ALA system, the car would suffer a reduction in straight-line speed. To address this, the ALA system modifies airflow beneath the car via the front splitter and stalls the rear wing, reducing its circulation and, consequently, the induced drag. This innovative system enabled Lamborghini to achieve a Nürburgring lap time of 6:52 with the Huracán Performante (640 PS), beating the Porsche 918 Spyder (887 PS) by five seconds, despite having 247 PS less power than the Porsche [91]. In contrast to these discrete systems, true morphing approaches in the automotive field are still at an early stage of development. One promising direction involves the use of smart materials, such as Shape Memory Alloys (SMAs), which enable continuous surface deformation as a function of temperature. As widely discussed by Jani et al. [92], SMAs exhibit a reversible martensitic phase transformation, allowing the material to recover its original shape upon heating after

deformation. Han et al. [93] proposed an adaptive spoiler concept based on SMA wires embedded within a compliant polymer matrix, enabling smooth and continuous modification of the aerodynamic profile without discrete mechanical components; in this configuration, thermally induced phase transformation generates axial contraction forces, which, when applied eccentrically within the structure, produce bending moments and thus continuous shape deformation. Experimental results demonstrated a significant aerodynamic impact, with the system enabling a transition from lift to downforce and an increase in vertical force exceeding one order of magnitude compared to the undeformed configuration. For instance, at a freestream velocity of 23 m/s, the aerodynamic force varied from approximately +0.3 N (lift) to −4.2 N (downforce), while in a vehicle-mounted configuration at 15 m/s it changed from +1.8 N to −1.75 N. However, this improvement in downforce was accompanied by an increase in drag of approximately 40–50%, highlighting the inherent trade-off between enhanced vehicle stability and overall aerodynamic efficiency. More recent studies have further explored SMA-based morphing concepts for automotive applications, highlighting their potential for compact integration and adaptive aerodynamic control while also emphasizing challenges related to response time, thermal management, and energy efficiency. Within this context, Rodinò et al. [94] proposed an SMA–polymer composite solution that enhances structural compliance and enables more distributed and controlled deformation, achieving recoverable strains on the order of a few percent (up to ~5%) and deflections up to 20 mm, with good agreement between numerical predictions and experimental results. This approach allows for smooth camber variation and improved aerodynamic adaptability compared to purely discrete actuation systems. A more application-oriented implementation is presented by Battaglia et al. [95], where SMAs are integrated into automotive aerodynamic devices through a bistable actuation system, focusing on robust actuation and system-level integration. In this case, SMA activation produces a linear stroke of about 5 mm, resulting in an angular variation of approximately 12° and a corresponding displacement of about 40–45 mm. The system enables reliable configuration switching and maintains stable positions without continuous energy input, improving aerodynamic adaptability while minimizing power consumption. Overall, while true morphing concepts based on continuous surface deformation remain limited in automotive applications, the increasing integration of active aerodynamic systems and smart materials shows a growing interest in adaptive flow control strategies for road vehicles.

2.4 Plasma-Based Active Flow Control

After discussing fluidic and surface-based techniques for modifying aerodynamic performance, we present a relatively recent class of active flow control methods that involves the use of plasma actuators. These devices generate weakly ionized air near the surface to induce momentum into the boundary layer without mechanical moving parts. Early

experimental work by Post et al. [96] clearly established the potential of plasma actuation for separation control at high angles of attack, providing the foundation for subsequent developments in both aerospace and automotive applications. The most widely adopted configuration is the Dielectric Barrier Discharge (DBD) actuator, consisting of two electrodes separated by a dielectric material and embedded flush with the surface. Plasma actuators operate by ionizing air in proximity to the wall, producing an electrohydrodynamic body force that accelerates near-wall fluid, as described by Zhang et al. [97] and Iranshahi et al. [98]. However, it is important to note that the induced ionic wind velocity is typically of the order of a few meters per second, which is significantly lower than the typical freestream velocity in most aerodynamic applications. As a result, plasma actuation does not represent a direct substitute for conventional blowing but rather modifies the near-wall flow structure through relatively weak momentum addition. Several actuator layouts can be employed to influence flow topology. Among them, two dominant configurations are widely discussed in the literature, including by Choi et al. [99]:

- A longitudinal orientation, where electrodes are aligned with the freestream to directly accelerate the near-wall flow.
- An orthogonal orientation, in which electrodes are arranged transversely to the external flow to generate streamwise vortices acting similarly to vortex generators.

Overall, AC-DBD plasma actuators either introduce additional momentum into the lower boundary layer or promote mixing through the generation of streamwise vortices that entrain high-momentum fluid toward the wall (Figure 2.10).

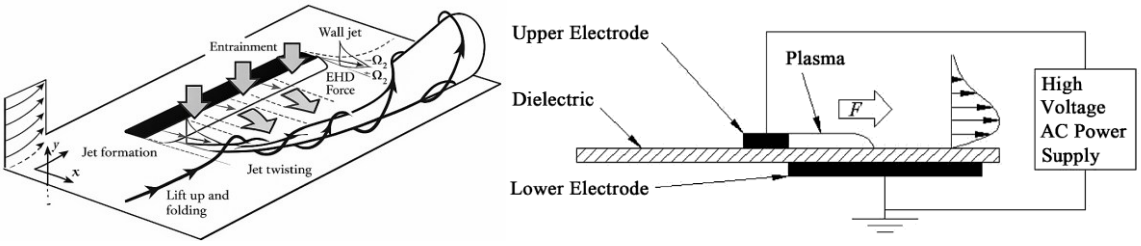

Figure 2.10. Choi et al. [99]: DBD plasma vortex generator setup for orthogonal (left) or longitudinal (right) design.

In automotive applications, several studies have investigated the use of AC-DBD actuators for drag reduction and wake control. Boucinha et al. [100] were among the first to conduct a comprehensive investigation of plasma-based flow control on an Ahmed body. Multiple DBD actuator arrays were installed at different locations on the rear slant and edges to assess their

influence on separation and wake formation. Their results showed that activating only the top actuator strip led to a drag reduction of approximately 8%, primarily due to improved flow reattachment on the rear slant. Conversely, activating additional actuators along the sides and edges increased wake unsteadiness and turbulence intensity, ultimately negating drag benefits. These results highlight the strong sensitivity of plasma actuation to actuator placement and configuration. Flow visualizations confirmed a clear downward deflection of the separated shear layer when actuation was active, resulting in a reduced recirculation region and improved pressure recovery. Subsequent studies by Shadmani et al. [101,102] extended this work by comparing steady and unsteady actuation. Their experiments showed a drag reduction of approximately 7% under steady forcing, while pulsed operation achieved around 5%. Further analysis based on pressure distributions indicated that the majority of the drag reduction originated from altered pressure recovery on the rear slanted surface, rather than from modifications of skin friction. Smoke visualization confirmed a significant reduction in the separation bubble under steady forcing, with improved flow attachment along the rear slant. In contrast, unsteady actuation produced weaker effects, particularly at higher freestream velocities, where the control authority of plasma actuation decreased.
However, when the actuator location was shifted toward the centre of the rear slant, the drag reduction effect became negligible, emphasizing the high sensitivity of plasma actuation to geometric placement. Moreover, increasing the flow speed reduces the drag-reduction effectiveness of the control methods and leads to increasingly similar results between steady

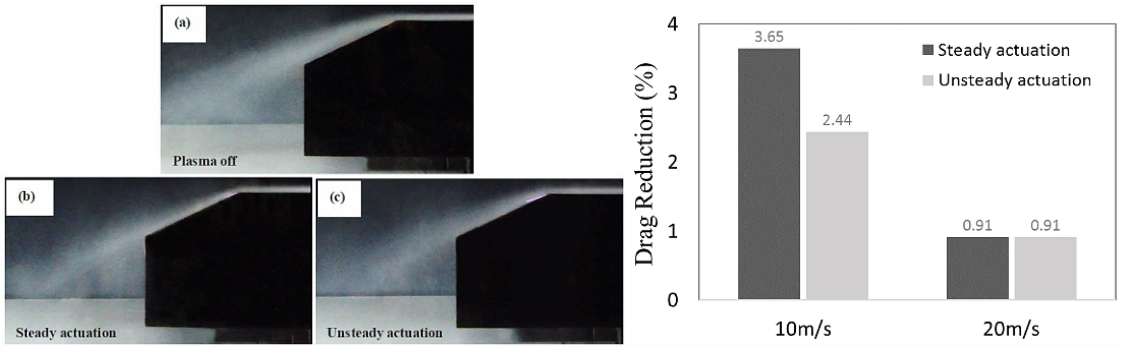

Figure 2.11. Shadmani et al. [101]: smoke wake visualization, plasma off (a), steady (b), unsteady (c) on the top, adapted drag reduction on the bottom.

and unsteady actuation, as shown in Figure 2.11.
Khalighi et al. [103] explored actuator arrangements on the vertical side edges of the rear surface and reported a drag reduction of up to 21% at 10 m/s. This benefit decreased rapidly with increasing freestream velocity, highlighting an important limitation: as speed increases, the electrohydrodynamic body force becomes insufficient to meaningfully affect the flow field. Similarly, Roy et al. [104] evaluated serpentine and linear electrode designs on a model-scale truck and measured drag reductions of approximately 15% at 60 mph and over 10% at

70 mph. However, when extrapolated to full-scale configurations, the electrical power demand exceeded the vehicular energy savings, raising significant concerns about industrial feasibility. Vernet et al. [105,106] further investigated plasma actuation on a truck model, including configurations on both the tractor and trailer. A particularly relevant result was obtained under crosswind conditions: at a yaw angle of 9° and a wind speed of 10 m/s, drag reductions of up to 20% were measured (Figure 2.12). Nonetheless, these experiments were conducted at Reynolds numbers far below full-scale conditions, and further validation is required to assess real-world applicability.

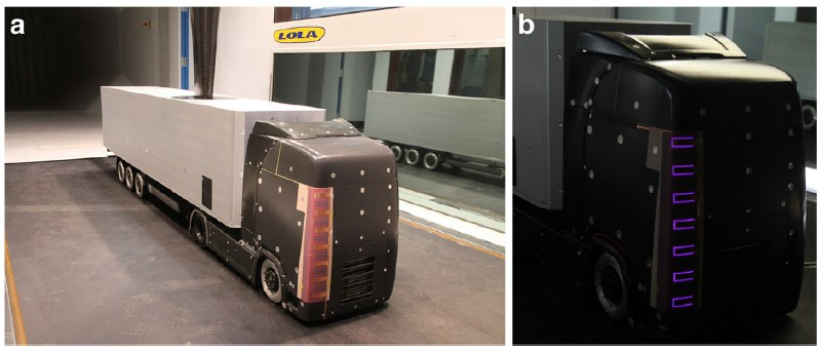

Figure 2.12. Vernet et al. [105]: installation of the truck in the wind tunnel (a) with the actuators ON (b).

Additional studies [107] have explored variations in actuation frequency, electrode geometry, slant angle, and discharge mode (wire-to-plate vs. embedded electrodes). Despite these innovations, the gains obtained were generally comparable to or inferior to those reported by Boucinha et al. [100]. As a result, the practical adoption of plasma actuators in automotive or freight transport remains limited, despite their excellent controllability under laboratory conditions. This limitation is fundamentally linked to the weak scaling of electrohydrodynamic forcing in conventional AC-DBD actuators, which rapidly lose effectiveness as the Reynolds number increases and are therefore unable to significantly alter the global flow field. These limitations have motivated the development of alternative plasma actuation strategies, among which nanosecond-pulsed DBD (NS-DBD) actuators represent one of the most promising approaches. Instead of generating a quasi-steady ionic wind through electrohydrodynamic forcing, NS-DBD actuation is characterized by rapid energy deposition on nanosecond timescales, leading to localized heating, pressure waves, and strong unsteady perturbations of the flow. Roupassov et al. [108] demonstrated that pulsed nanosecond discharges can effectively control flow separation, achieving significant modifications of the separated shear layer structure and reattachment under conditions where steady forcing is ineffective. Similarly, Little et al. [109] reported substantial aerodynamic improvements in high-lift configurations, including a marked delay of leading-edge separation and lift

coefficient increases on the order of 10–20%, depending on actuation conditions. These findings were further supported by Correale et al. [110], who observed enhanced flow attachment and increased mixing in separated regions through pulsed plasma excitation. The underlying physical mechanisms have been extensively discussed by Adamovich et al. [111], who showed that nanosecond surface discharges generate localized temperature rises of several tens of Kelvin and produce compression waves capable of propagating into the outer flow. This leads to a significantly stronger flow response compared to conventional AC-DBD actuators, whose induced velocities are typically limited to a few meters per second. Consequently, NS-DBD actuation is not primarily based on mean momentum addition, but rather on the excitation of natural flow instabilities and the generation of coherent vortical structures that enhance momentum transfer across the shear layer. While the application of NS-DBD actuators in automotive aerodynamics remains limited, recent reviews (e.g., Saemian et al. [112]) indicate that their ability to interact with separated and wake-dominated flows makes them a promising candidate for bluff-body flow control. In particular, the capability of NS-DBD actuation to influence large-scale unsteady structures shows a potential advantage in automotive configurations, where drag is largely governed by wake dynamics and separation phenomena. This suggests that NS-DBD actuation could partially overcome the intrinsic scaling limitations of AC-DBD actuators in high-Reynolds-number applications. Given the fundamentally different operating principles of AC-DBD and NS-DBD actuators, their key differences in flow control mechanisms are summarized in Table 2.1.

Feature	AC-DBD Actuators	NS-DBD Actuators
Power supply	AC high voltage (kHz range)	Nanosecond high-voltage pulses
Dominant mechanism	Electrohydrodynamic (EHD) body force	Rapid energy deposition and thermal expansion
Characteristic timescale	O(μs–ms) (quasi-steady)	O(10 ns) (impulsive)
Induced velocity	~1–10 m/s (ionic wind)	Not characterized by mean velocity (impulsive forcing)
Temperature effects	Negligible	Significant localized heating and pressure waves
Forcing type	Quasi-steady	Highly unsteady / impulsive
Flow interaction	Primarily boundary-layer modification	Affects both boundary layer and outer flow
Effectiveness in separated flows	Limited at high Reynolds numbers	Effective in separated and unsteady flows
Primary control mechanism	Mean momentum addition (ionic wind)	Excitation of flow instabilities (unsteady forcing)
Typical applications	Low-speed boundary-layer control	High-speed and separated flow control

Table 2.1. Comparison of operating principles and flow control mechanisms between AC-DBD and NS-DBD plasma actuators.

2.5 Discussion and General Considerations

Although active flow control (AFC) techniques offer significant aerodynamic benefits, they inevitably require external energy input. Therefore, a method can be considered viable only when the aerodynamic gain exceeds the associated energy cost under representative operating conditions. However, efficiency alone does not fully determine suitability. In the automotive context, practical implementation must also account for a number of engineering constraints. To assess the feasibility of each AFC technology, the following criteria are adopted:

- Packaging: ability to integrate the system within the limited available vehicle volume without compromising layout or safety;
- Ease of operation: simplicity of control logic, robustness, durability, and adaptability to varying operating conditions;
- Cost: investment and operational costs associated with implementation;
- Weight: additional mass and its impact on fuel consumption, handling, and braking performance.

These constraints differ significantly between application domains, particularly when comparing automotive and aerospace systems. Table 2.2 provides a comparison between these two fields, highlighting the more restrictive conditions typical of road vehicles. Automotive flows are typically characterized by lower Reynolds numbers, strong ground effects, and highly transient operating conditions. As a result, AFC systems must operate effectively across a wide range of flow regimes while maintaining robustness and low system complexity. The progressive electrification of vehicles is reshaping the feasibility landscape of AFC technologies. Electrically driven solutions benefit from the increasing availability of onboard power and high-voltage architectures, which facilitate their integration and control. Nevertheless, this technological shift does not uniformly benefit all AFC approaches. More fundamentally, AFC techniques are based on different physical mechanisms, which inherently determine their scalability, efficiency, and integration requirements.

Parameter	Automotive Applications	Aerospace Applications	Implications for AFC Design
Reynolds Number Regime	(10^5– 10^7) (moderate, often transitional)	(10^6– 10^8) (predominantly turbulent)	Limited scalability of AFC strategies; flow control authority and actuation frequency must be adapted to lower Reynolds regimes
Ground Effect Influence	Strong (persistent proximity to ground)	Negligible (except during take-off/landing)	Significant modification of wake topology and pressure distribution; AFC must account for highly asymmetric and unsteady flow structures

Operating Conditions	Highly transient and stochastic (urban driving, maneuvers)	Relatively steady with controlled perturbations	Necessity for real-time, adaptive, and robust control strategies
Geometric Integration (Packaging Constraints)	Severe spatial constraints	Relatively relaxed constraints	Limited integration of actuators and sensors; requires compact, low-profile AFC devices
Environmental Exposure & Durability	Harsh (rain, dust, debris, thermal cycling)	Moderately controlled (but includes icing, pressure variations)	Increased robustness and reliability requirements; protection of sensing/actuation systems
Mass Constraints	Stringent	Critical but with higher allowable margins	Trade-off between control effectiveness and added system mass
Cost Constraints	Highly restrictive (mass production)	Less restrictive (low production volume, high value systems)	Strong limitations on system complexity and scalability of AFC technologies

Table 2.2 Comparison of key design constraints affecting active flow control implementation in automotive and aerospace applications.

Consequently, the evaluation of each technology must extend beyond aerodynamic effectiveness to include system-level considerations such as power demand, safety, and implementation complexity. From a system-level perspective, packaging, durability, cost, and safety therefore remain the dominant constraints for AFC implementation in production vehicles. These factors, combined with the need for reliable operation under highly variable conditions, strongly differentiate automotive applications from aerospace scenarios, where operating environments are generally more stable and less constrained.

2.5.1. Fluidic Blowing and/or Suction

Fluidic actuation based on non-zero mass flow, such as steady blowing and suction, represents one of the most established active flow-control (AFC) approaches. These techniques are relatively simple to implement and control, and they do not raise significant regulatory concerns. However, their applicability in automotive systems is fundamentally constrained by low overall efficiency. Energy losses associated with compressors, ducting, and flow distribution considerably reduce the net aerodynamic benefit [113,114], while the need for auxiliary hardware introduces additional penalties in terms of packaging and weight. Consequently, despite their demonstrated effectiveness, steady blowing and suction are unlikely to constitute a scalable solution for production vehicles. The ongoing electrification of vehicles may partially alleviate these limitations, for instance, through the adoption of localized small electric compressors, reducing the need for large, centralized compressors, reservoirs, and extensive piping. Nevertheless, system-level efficiency remains a critical issue. Zero-net-mass-flow devices, such as synthetic jets, overcome several of these limitations by eliminating the need for continuous mass injection and complex pneumatic systems, thus enabling more compact and potentially more efficient implementations. Their main drawback lies in the cost and complexity of the required power electronics, particularly to achieve the relatively high actuation voltages required by piezoelectric actuators, typically in the range of

100–300 V and potentially higher depending on performance requirements. However, this constraint is progressively diminishing with the widespread adoption of hybrid and fully electric vehicle platforms, where high-voltage architectures are becoming standard. This technological shift makes synthetic jets inherently well suited for integration into modern vehicle systems. For these reasons, synthetic jets can be regarded as one of the most promising fluidic AFC technologies for automotive applications, offering a favourable balance between aerodynamic performance and system-level feasibility [100,115].

2.5.2. Profile

Rotating surfaces have proven to be an effective approach for improving aerodynamic performance while requiring limited installation volume and only electrical wiring for operation. Nevertheless, the presence of high-speed rotating components on exposed vehicle surfaces raises substantial safety concerns, making their adoption unlikely in production vehicles due to regulatory constraints associated with the risk of accidental contact. Morphing surface technologies can be broadly classified into two main categories, depending on the actuation mechanism: mechanically actuated and electrically actuated systems. Mechanical morphing relies on linkages and actuators to physically deform aerodynamic surfaces [95]. This solution is efficient and relatively simple to control, and it does not introduce significant regulatory issues, as the moving components are comparable to conventional automotive mechanisms. However, mechanical morphing systems require considerable packaging volume due to internal kinematic assemblies, resulting in increased weight, structural complexity, and cost. Active aerodynamic devices fall within this category and include real-world implementations such as the adaptive rear wing of the McLaren P1. These systems provide high effectiveness and reliable controllability, enabling real-time optimization of aerodynamic balance, but at the expense of additional actuators, electric motors, and mechanical interfaces, which negatively impact vehicle mass, cost, and integration effort. In contrast, electrically actuated morphing systems induce surface deformation through electric fields or smart materials [116], offering a compact and lightweight solution with reduced mechanical complexity. Depending on the specific actuation technology, these systems can also provide fast response, as in the case of piezoelectric actuators. Their main limitation lies in the cost and complexity of the required power electronics, particularly to achieve relatively high actuation voltages (on the order of ~400 V, depending on the technology). This aspect is especially relevant for smart-material-based solutions such as Shape Memory Alloys (SMAs), where efficient actuation relies on controlled electrical heating. In addition, SMA-based systems may present further challenges related to response time, thermal management, and material fatigue under repeated actuation cycles, which can limit their applicability in high-frequency or long-term operation scenarios. In this context, similarly to what was discussed for synthetic jets, the ongoing transition toward hybrid and fully electric vehicle platforms

represents a key enabling factor, as the increasing availability of high-voltage architectures facilitates system integration and reduces the relative impact of power electronics constraints. Consequently, electrically actuated morphing surfaces, particularly those based on smart materials, represent a promising direction for future automotive aerodynamic control, as they offer a favourable compromise between integration, weight reduction, and functional adaptability, especially in applications where continuous surface deformation can provide aerodynamic advantages over discrete actuation systems.

2.5.3. Plasma

Plasma-based actuation represents a relatively recent active flow control (AFC) approach that enables boundary layer manipulation without moving parts and with minimal integration volume, as actuators are typically embedded flush with the surface. The most widely adopted configuration is the Dielectric Barrier Discharge (DBD or AC-DBD) actuator, which operates by ionizing the air near the wall and generating an electrohydrodynamic body force that accelerates the near-wall flow. However, the induced ionic wind is typically limited to a few meters per second, making plasma actuation significantly weaker than conventional blowing. As a result, its effect is primarily confined to near-wall flow structures, with limited influence on the outer flow. Experimental studies on simplified automotive geometries have demonstrated measurable drag reductions, mainly associated with improved flow reattachment and wake modification. Nevertheless, these benefits are highly sensitive to actuator placement, configuration, and operating conditions, and may deteriorate or even become detrimental if not properly optimized. From a system-level perspective, plasma actuation presents several limitations. When extrapolated to full-scale applications, the electrical power required for actuation can offset or exceed the aerodynamic gains, reducing overall efficiency. Furthermore, the effectiveness of conventional AC-DBD actuators decreases rapidly with increasing Reynolds number and freestream velocity, making them poorly suited for typical automotive operating conditions. To address these limitations, more advanced concepts such as nanosecond-pulsed DBD (NS-DBD) actuators have been proposed. These systems rely on rapid energy deposition and strong unsteady perturbations, rather than steady momentum addition, enabling improved interaction with separated flows. However, despite their promising performance, their application in automotive systems remains at an early stage, and plasma-based AFC is currently considered limited in terms of large-scale industrial feasibility. In addition, plasma actuators require high-voltage power electronics, typically operating at kilovolt levels, leading to significant cost and integration challenges. Although the ongoing transition toward hybrid and fully electric vehicles partially mitigates this issue through the availability of onboard high-voltage architectures, concerns related to safety, durability, and certification remain, particularly due to the presence of plasma discharges on exposed surfaces.

2.5.4. Comparative Assessment

Having analysed both the physical mechanisms and system-level constraints, a comparative assessment is now required to identify the most suitable technologies for automotive applications. Table 2.4 provides a comparative assessment of the main active flow control (AFC) techniques based on key performance and implementation criteria, including drag reduction, power consumption, response time, technological readiness level (TRL), and integration constraints. The qualitative "Overall Assessment" is derived from trends reported in the literature and reflects the relative trade-off between aerodynamic performance and practical feasibility, rather than absolute quantitative values. While Table 2.3 presents a qualitative overview derived from trends in the literature, Table 2.4 introduces a decision-oriented assessment, enabling a more direct comparison of the relative suitability of each technology for automotive applications. The results consistently indicate that synthetic jet actuators and morphing-based solutions offer the most favourable balance between aerodynamic performance and practical feasibility. Synthetic jets combine relatively high efficiency, compactness, and compatibility with electrified vehicle architectures, making them particularly suitable for integration in modern platforms. Similarly, morphing systems, especially electrically actuated configurations, provide effective aerodynamic control with manageable integration constraints, and their feasibility is expected to improve further with the increasing availability of high-voltage systems. In contrast, fluidic techniques based on steady or pulsed blowing, although capable of achieving significant drag reductions, remain penalized by low system-level efficiency, as well as packaging complexity and additional weight associated with auxiliary components. Plasma-based approaches, on the other hand, offer unique advantages in terms of actuation speed and flow responsiveness, particularly for advanced concepts such as NS-DBD actuators. However, their applicability is currently limited by high voltage requirements, integration challenges, and reduced effectiveness at high Reynolds numbers. In automotive applications, the primary aerodynamic performance indicator is typically the drag coefficient, as fuel efficiency and energy consumption are strongly influenced by drag reduction. However, a review of the literature considered in this work reveals that several studies also report meaningful variations in lift (in aerospace contexts) or downforce (in automotive applications). Although these quantities are not consistently reported across all technologies, they provide valuable insight into vehicle stability, handling, and aerodynamic balance.

AFC Technique	Drag Reduction Potential	Power Consumption	Response Time	TRL	Packaging	Cost	Weight	Overall Assessment
Steady Blowing/Suction	High	High	Medium	Medium–High	Poor	Medium	High	Limited by low system efficiency and integration complexity

Pulsed Blowing	Medium–High	Medium	Medium–Fast	Medium	Poor	Medium	High	Improved efficiency over steady blowing but still limited by hardware requirements
Synthetic Jets	Medium	Low–Medium	Fast	Medium	Good	Medium–High	Low	Promising balance between efficiency, compactness, and controllability
Co-Flow Jet (CFJ)	Medium	High	Medium	Low–Medium	Poor	High	High	Effective but complex and difficult to integrate
Rotating Surfaces (MSBC)	High	Medium	Fast	Medium	Good	Medium	Medium	High performance but limited by safety concerns
Mechanical Morphing	High	Medium	Medium	High	Medium	High	High	Mature and effective but penalized by weight and complexity
Electrical Morphing (SMA / Piezo)	Medium–High	Medium	Medium–Fast	Medium	Good	High	Low	One of the most promising solutions for future applications
Plasma (AC-DBD)	Low–Medium	High	Very Fast	Low–Medium	Very Good	High	Very Low	Limited by poor scaling at high Reynolds and energy efficiency
Plasma (NS-DBD)	Medium	High	Very Fast	Low	Very Good	High	Very Low	Promising physics but still at early research stage

Table 2.3. Comparative assessment of active flow control techniques based on aerodynamic performance, energy consumption, response time, and integration constraints.

For this reason, a complementary summary of lift and downforce effects is presented, in a format analogous to the drag comparison (Table 2.4), allowing a more comprehensive assessment of the aerodynamic impact of the investigated techniques.

Technology	Application	Downforce
Steady Blowing/Suction	Aerospace (airfoil/wing)	$C_L \approx 6$-8
	Automotive (Ahmed body)	-42%
	Automotive (Ahmed body)	ΔC_L=0.105
Pulsed Blowing	Aerospace (vertical tail)	+14% side force
Co-Flow Jet (CFJ)	Aerospace (airfoil)	$C_L \approx 3$, +80%
Mechanical Morphing	Aerospace (airfoil/wing)	10-25%
	Automotive (diffuser/spoiler)	10-20%
	Automotive (McLaren P1)	~600 kg
	Automotive (Mercedes AMG)	ΔC_L=0.08
	Automotive (Lamborghini ALA)	~200 → 1500 kg

Electrical Morphing (SMA / Piezo)	Automotive (SMA spoiler)	Spoiler max $C_L \approx 1.1$
Plasma (AC-DBD)	Aerospace / Automotive	Negligible
Plasma (NS-DBD)	Aerospace	10-40%

Table 2.4. Summary of lift and downforce effects for the investigated aerodynamic control techniques in aerospace and automotive applications.

The decision matrix (Table 2.5) further highlights that high-performance solutions such as mechanical morphing or rotating surfaces, while aerodynamically effective, are often constrained by integration, safety, and system complexity considerations.

AFC Technique	Performance	Efficiency	Integration	Maturity	Robustness	Final Score	Rank
Mechanical Morphing	5	3	2	5	4	3.8	1
Electrical Morphing	4	3	4	3	4	3.6	2
Synthetic Jets	3	4	4	3	4	3.6	3
Rotating Surfaces	5	3	2	3	2	3.0	4
Pulsed Blowing	4	2	2	3	3	2.8	5
Steady Blowing/Suction	4	1	1	4	3	2.6	6
Plasma (NS-DBD)	3	2	4	1	2	2.4	7
Plasma (AC-DBD)	2	1	5	2	2	2.4	8
Co-Flow Jet (CFJ)	3	2	1	2	2	2.0	9

Table 2.5. Decision matrix evaluating the suitability of AFC techniques for automotive applications, (1 = poor, 5 = excellent).

This table represents one of the key contributions of the present work, as it translates qualitative literature trends into a decision-oriented engineering tool. Overall, the comparison demonstrates that no single AFC technology maximizes all performance metrics simultaneously; instead, the most promising solutions are those that achieve the best compromise between aerodynamic benefits, energy efficiency, and implementation feasibility.

2.6. Conclusions and Future Trends

This review has examined the most relevant active flow control (AFC) techniques originally developed for aerospace applications and their subsequent adaptation to the automotive sector. Each methodology was assessed in terms of aerodynamic effectiveness, implementation challenges, and technological maturity, supported by a structured comparative framework and a decision-oriented analysis (Tables 2.3–2.5). The results consistently indicate that morphing aerodynamic systems and synthetic jet actuators represent the most promising solutions currently available for automotive applications, as they provide

the most favourable balance between aerodynamic performance, energy efficiency, and integration feasibility. Morphing technologies, already partially implemented in high-performance vehicles, offer reliable and effective aerodynamic control, while electrically actuated solutions are expected to benefit from the increasing availability of high-voltage architectures. In parallel, synthetic jets emerge as a particularly attractive technology due to their compactness, absence of external air supply, and relatively high efficiency, making them well suited for integration into modern electrified platforms. Fluidic techniques based on steady or pulsed blowing, although capable of achieving significant drag reductions, remain limited by system-level inefficiencies, as well as packaging and weight penalties associated with compressors, ducting, and auxiliary components. As a result, their large-scale implementation in production vehicles remains unlikely without substantial improvements in overall system efficiency. Plasma-based techniques present a contrasting scenario; conventional AC-DBD actuators are fundamentally limited by the weak scaling of electrohydrodynamic forcing, which results in a rapid loss of effectiveness at increasing Reynolds numbers and freestream velocities. In contrast, nanosecond-pulsed DBD (NS-DBD) actuators rely on a different physical mechanism based on rapid energy deposition, generating pressure waves and strong unsteady perturbations capable of interacting with large-scale flow structures. This enables more effective control of separated and wake-dominated flows, potentially overcoming some of the intrinsic limitations of steady plasma actuation. However, despite their promising aerodynamic performance, NS-DBD systems remain at an early stage of development and are still constrained by high energy requirements, system complexity, and limited experimental validation under full-scale automotive conditions. More broadly, the evolution of AFC technologies is strongly influenced by the ongoing electrification of vehicles, which facilitates the integration of electrically driven systems and reduces the relative impact of high-voltage power electronics. At the same time, research is progressively shifting from fundamental flow physics toward system-level optimization and real-world applicability, supported by increasing collaboration between academia, industry, and research institutions. In this context, emerging approaches based on Artificial Intelligence, particularly Reinforcement Learning, are receiving increasing attention for real-time closed-loop flow control. These methods enable adaptive optimization of actuation strategies under highly transient operating conditions and have demonstrated promising results in fluid mechanics applications [117,118]. The combination of AFC technologies with advanced control strategies, together with multidisciplinary integration involving aerodynamics, vehicle dynamics, and control engineering, is expected to play a key role in improving robustness, energy efficiency, and scalability. Overall, while several AFC techniques demonstrate strong aerodynamic potential, only a limited subset currently satisfy the combined requirements of performance, efficiency, and feasibility necessary for large-scale implementation in production vehicles. Future developments are likely to focus on hybrid approaches, combining

complementary actuation mechanisms with intelligent control strategies, to fully exploit the potential of active flow control in next-generation automotive systems.

Published Review

Herberg, M.R.; De Pinto, S.; de Tullio, M.D.; Pascazio, G. Active Flow Control Techniques: Classification, Analysis, and Future Trends for Automotive Applications. *Fluids* **2026**, *11*, 106. DOI: 10.3390/fluids11050106

Chapter 3 – Baseline CFD vs Real World Testing

To establish a reliable benchmark for evaluating the proposed technical solution, it is essential to define a robust aerodynamic baseline. This involves performing full-vehicle simulations under a range of operating conditions, followed by an experimental testing campaign replicating the same test conditions. By directly comparing the numerical and experimental datasets, it becomes possible to assess the accuracy and predictive capability of the CFD model in reproducing real-world aerodynamic behaviour.

3.1 Turbulence Modelling Strategy, Limitations and CFD Baseline Setup

Before introducing the numerical tools used to simulate the vehicle's flow field, it is important to recall the fundamental concept of turbulence. Turbulence is characterized by chaotic and irregular fluctuations in pressure and velocity within the fluid motion, in contrast to laminar flow, where fluid layers move smoothly and parallel to each other without significant interaction [120]. The onset of turbulence can be predicted by the Reynolds number (Re), which represents the ratio between inertial and viscous forces. To sustain a turbulent flow, a continuous energy input is required, since part of the kinetic energy is dissipated rapidly due to viscous shear stresses. Large turbulent eddies extract energy from the mean flow through vortex stretching. Their characteristic dimensions are comparable to those of the global flow field; they exhibit anisotropic behaviour and are only weakly affected by viscosity. Conversely, according to Kolmogorov's hypothesis, small eddies are nearly isotropic and exhibit universal statistical properties. Energy is transferred from larger to smaller scales through the so-called energy cascade, with negligible dissipation until the eddy size becomes sufficiently small for viscous effects to dominate. Between these two extremes exists an intermediate scale, known as the Taylor microscale, which is independent of both outer and inner turbulence scales. This intermediate region can be characterized by the eddy size l (or its corresponding wavenumber k) and the turbulent dissipation rate (ε). From dimensional analysis, the spectral energy distribution $E(k)$ can be expressed as:

$$E\,(k) = C_k\, k^{\frac{-5}{3}}\, \epsilon^{\frac{2}{3}} \tag{3.1}$$

where

$C_k = 1.5$ is the Kolmogorov constant, and $k = \frac{2\pi}{l}$ is the wavenumber (Figure 3.1).

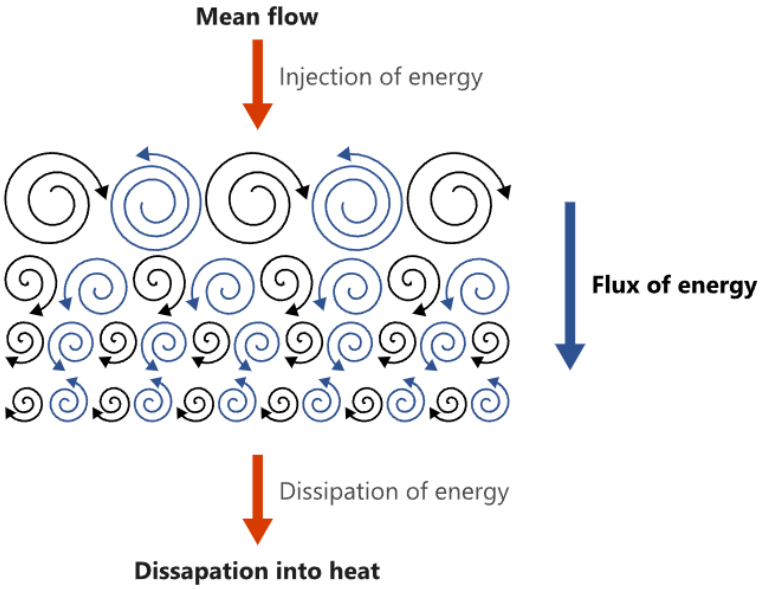

Figure 3.1 Schematic representation of the turbulent energy cascade, illustrating the transfer of kinetic energy from large-scale eddies to progressively smaller turbulent structures until viscous dissipation into heat.

This relationship describes the characteristic −5/3 slope observed in the inertial subrange of the turbulent energy spectrum, confirming that the energy transfer between eddy scales is self-similar and independent of viscosity (Figure 3.2).

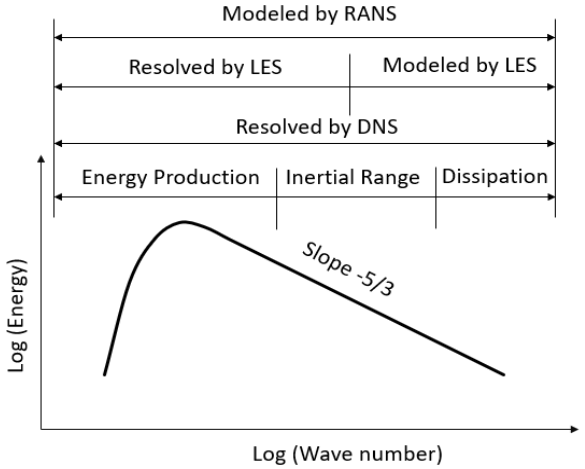

Figure 3.2 Schematic representation of the turbulent energy spectrum according to Kolmogorov theory, highlighting the range of turbulent scales resolved and modelled by DNS, LES, and RANS approaches.

This brief introduction provides the foundation for understanding how different computational fluid dynamics (CFD) tools operate when solving complex fluid flow problems.

Depending on the range of turbulence scales that need to be resolved, three major numerical approaches are commonly employed in fluid dynamics:

- DNS (Direct Numerical Simulation)
- LES (Large Eddy Simulation)
- RANS (Reynolds-Averaged Navier–Stokes)

Direct Numerical Simulation (DNS) solves the Navier–Stokes equations without any turbulence modelling, resolving all spatial and temporal turbulent scales directly. Although DNS provides the highest level of physical accuracy, its computational requirements increase rapidly with Reynolds number, making it impractical for full-scale automotive applications, where Reynolds numbers are typically of the order of 10^6–10^7 [119,120,121]. Large Eddy Simulation (LES) resolves the large energy-containing turbulent structures while modelling only the smallest scales through sub-grid scale (SGS) formulations. LES generally provides improved predictions of transient flow structures, wake dynamics, and separation phenomena compared to steady RANS approaches [122]. However, the computational cost remains extremely high for full-vehicle external aerodynamic simulations, especially when multiple geometric configurations must be investigated within reasonable turnaround times. For industrial automotive aerodynamic applications, Reynolds-Averaged Navier–Stokes (RANS) approaches remain the most widely adopted methodology due to their favourable compromise between computational cost, numerical robustness, and predictive capability [120,121]. In vehicle aerodynamics, the primary engineering objective often consists in comparing the aerodynamic behaviour of multiple design configurations under identical operating conditions rather than resolving all transient turbulent structures in detail [123]. RANS methods are based on the time-averaging of the instantaneous Navier–Stokes equations. This averaging process introduces additional unknown terms, known as Reynolds stresses, representing the effects of turbulent fluctuations on the mean flow field. Consequently, additional turbulence closure models are required to relate these stresses to the mean flow quantities [124]:

$$\frac{\partial(\rho U_i)}{\partial t} + \frac{\partial}{\partial x_j}\left(\rho U_i U_j\right) = -\frac{\partial(P)}{\partial x_i} + \frac{\partial}{\partial x_j}\left[\mu\left(\frac{\partial(U_i)}{\partial x_j} + \frac{\partial(U_j)}{\partial x_i}\right) - \rho\overline{u_i u_j}\right] \tag{3.2}$$

Several turbulence closure formulations are available for RANS simulations, including the *k*–*ε*, *k*–*ω*, or *SST* models. The selection of the turbulence model significantly affects the prediction of separation regions, pressure gradients, and wake development in external aerodynamic flows [125, 126]. Numerical simulations were performed using Simcenter STAR−CCM+ by solving the steady Reynolds−Averaged Navier–Stokes (RANS) equations. The CFD methodology was intended to support the evaluation and optimization of multiple Co−Flow Jet configurations rather than to resolve all turbulent flow structures associated with large−scale separation

phenomena. The simulations employed the Realizable k–ε turbulence model in combination with the Two−Layer All y+ wall−treatment approach. This modelling strategy was selected as a compromise between computational efficiency, numerical robustness, and consistency with the industrial aerodynamic−development methodology routinely adopted across related vehicle−development projects. The use of a common modelling framework enabled the investigation of a large number of candidate configurations while maintaining a consistent basis for comparison. Due to the geometric symmetry of the vehicle, only half of the model was simulated, reducing computational cost while preserving the dominant aerodynamic features (Figure 3.3). The computational domain was defined to ensure adequate development of the external flow field and wake structures while maintaining a computational cost compatible with the large number of configurations investigated during the design campaign. A symmetry (slip−wall) boundary condition was ap-plied at the longitudinal centre-plane. A moving ground plane and rotating wheels were employed to reproduce the relative motion between the vehicle and the road surface, while no−slip wall conditions were imposed on all vehicle surfaces.

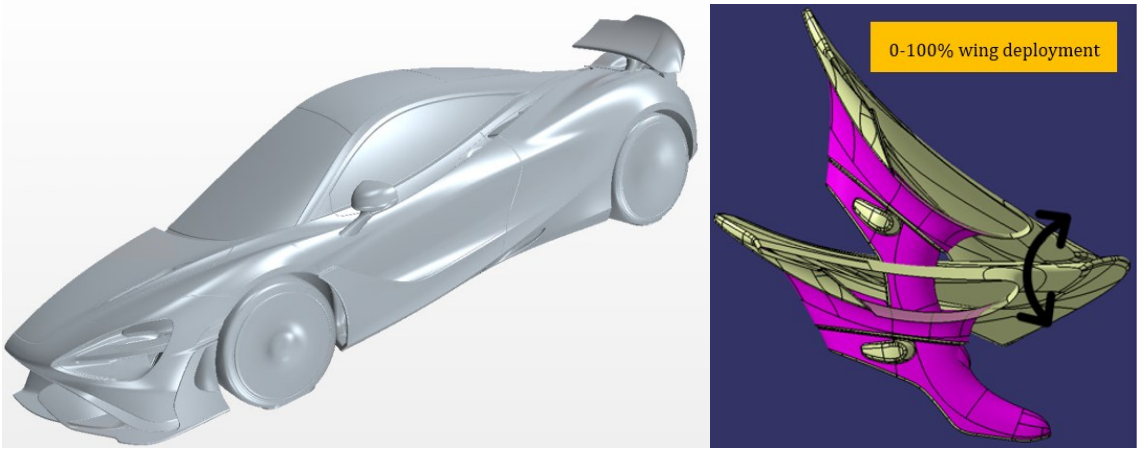

Figure 3.3 Half–vehicle CFD model of the McLaren 765LT and investigated rear−wing deployment range (0−100%). The rear wing was used as the primary aerodynamic device for the implementation and assessment of the Co−Flow configurations.

In comparison with higher-fidelity approaches such as LES or DES, the *k–ε* formulation provides substantially lower computational cost and improved numerical stability, making it particularly suitable for extensive parametric analyses involving multiple rear-wing duct configurations [122, 125]. Although more advanced models such as the SST or *k–ω* formulation generally improve the prediction of highly separated flows and strong adverse pressure gradients [123], several studies in automotive aerodynamics have shown that the standard *k–ε* model remains capable of providing reliable predictions of global aerodynamic coefficients and comparative aerodynamic trends for external vehicle flows [123, 126].

Furthermore, previous in-house validation activities performed on similar vehicle configurations showed satisfactory agreement between numerical predictions and experimental measurements when adopting the same modelling strategy. The adoption of the k–ε model therefore ensured:

- acceptable accuracy for comparative aerodynamic assessments;
- stable numerical convergence behaviour;
- reduced computational cost;
- methodological consistency with historical datasets and previously validated simulation procedures.

This choice allowed the efficient evaluation of multiple design configurations while maintaining direct comparability with existing experimental and numerical results available within the research group. Moreover, the objective of the present CFD campaign was not the absolute prediction of all separated flow phenomena, but rather the identification and ranking of promising Co−Flow Jet configurations prior to experimental validation. For this reason, a turbulence−model sensitivity study was considered beyond the scope of the present work. All vehicle simulations were performed using a consistent computational domain, boundary conditions, meshing strategy, and solver settings throughout the investigation, ensuring the consistency of the comparative analysis. Simulations were performed under International Standard Atmosphere (ISA) conditions, assuming an air temperature of 288.15 K, a pressure of 101,325 Pa, and an air density of 1.225 kg/m^3. The full-vehicle computational mesh consisted of more than 120 million cells and employed a polyhedral discretization combined with prism layer refinement in proximity to solid surfaces. A total of 15 prism layers were adopted, with a first cell height of approximately 0.055 mm, a total prism layer thickness of 4 mm, and a growth rate of 1.2. Dedicated local mesh refinements were applied in the vicinity of the rear wing. The prism-layer mesh was designed to target wall y^+ values close to unity under the nominal operating conditions. Owing to the variation in local flow conditions with vehicle speed and aerodynamic loading, the resulting wall y^+ values varied across the investigated cases but remained below 10 over the aerodynamic surfaces of interest. Mesh quality diagnostics confirmed a topologically valid mesh with no negative volume cells, a minimum face validity of 0.98, a minimum cell quality of 0.015, and a maximum skewness angle of less than 80° within the refined rear wing region. Due to industrial confidentiality constraints imposed by McLaren Automotive Ltd., the complete full-vehicle mesh topology and specific geometric features cannot be disclosed. To verify that the baseline surface discretization already implemented in the full-vehicle model was sufficiently accurate and insensitive to further grid refinement for configuration ranking, a dedicated mesh sensitivity study was conducted. The rear wing was selected as the reference geometry for this verification because it contains the

dominant flow features governing the vehicle's rear aerodynamic performance, including strong adverse pressure gradients, boundary-layer development, and wake formation, which are highly sensitive to spatial discretization (Figure 3.4).

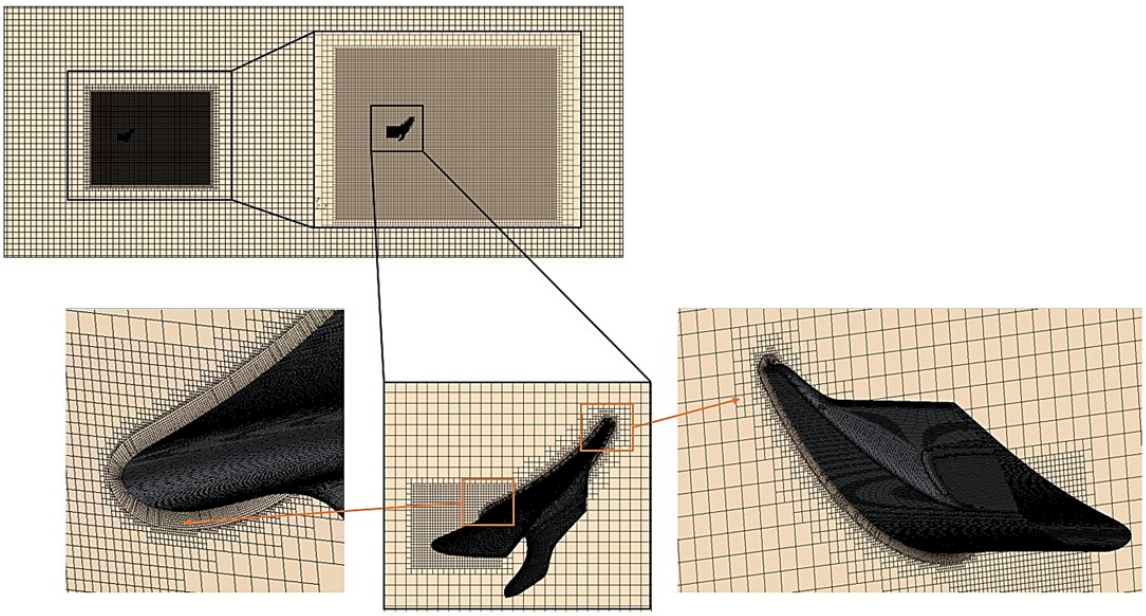

Figure 3.4 Computational mesh of the numerical domain showing the global mesh, local refinement regions around the vehicle, and prism-layer inflation adopted to accurately resolve near-wall boundary-layer effects.

These flow characteristics are particularly sensitive to spatial discretization and therefore provide a representative benchmark for assessing the influence of mesh refinement on the predicted aerodynamic quantities. The baseline mesh adopted for the isolated rear-wing study was derived from the surface discretization already employed in the full-vehicle simulations, thereby ensuring consistency between the mesh-sensitivity assessment and the complete-vehicle CFD model. The mesh-sensitivity study comprised one baseline mesh and three progressively refined meshes. Each refinement level was generated using a geometric refinement factor of 0.8 with respect to the previous mesh, preserving the same meshing strategy and numerical setup.

Wing %	Model	Mesh	$C_{d,wing}$	$C_{l,wing}$	Delta $C_{d,wing}$	Delta $C_{l,wing}$	Cells Count
100%	k−ε	Baseline	0.1035	−0.3101	–	–	6.16E+06
100%	k−ε	Finer 1	0.1024	−0.3074	−0.99%	−0.85%	1.05E+07
100%	k−ε	Finer 2	0.0997	−0.3048	−2.68%	−0.87%	2.09E+07
100%	k−ε	Finer 3	0.0983	−0.3005	−1.41%	−1.40%	3.58E+07

Table 3.1 Mesh−sensitivity assessment performed on the isolated rear−wing configuration at 100% deployment. Variations are reported relative to the baseline mesh.

The mesh refinement study showed progressively smaller variations in the predicted aerodynamic coefficients with increasing mesh density. In particular, the differences between the two finest mesh levels remained below approximately 2.7% for the drag coefficient and 1.4% for the lift coefficient, indicating that further refinement produced only marginal improvements while substantially increasing the computational cost (Table 3.1).

The results suggest that the baseline surface discretization adopted in the full-vehicle model provided an appropriate compromise between numerical accuracy and computational cost for the intended comparative aerodynamic analysis. The same surface discretization was retained through dedicated local mesh controls for the rear-wing region in all full-vehicle simulations. The near-wall prism-layer mesh was subsequently refined independently to satisfy the wall-resolution requirements of the complete-vehicle simulations, targeting wall y^+values close to unity under the nominal operating conditions. Owing to the variation in local flow conditions with vehicle speed and aerodynamic loading, the resulting wall y^+values varied across the investigated cases but remained below 10 over the aerodynamic surfaces of interest.

The objective of the mesh-sensitivity study was not to obtain a fully asymptotic mesh-independent solution for the complete vehicle, but rather to verify that the surface discretization already adopted in the full-vehicle model was sufficiently insensitive to further mesh refinement for the aerodynamic quantities used for configuration ranking. This approach is consistent with the use of the CFD model as a comparative design tool prior to experimental validation. To reduce the computational cost of the grid-convergence assessment, the isolated rear-wing model employed a coarser near-wall prism-layer discretization, resulting in representative wall y^+values of approximately 40–60. Since the objective of the assessment was to evaluate the influence of surface discretization on the predicted aerodynamic loads and pressure distributions, rather than to reproduce the final near-wall resolution adopted in the complete-vehicle simulations, this wall resolution was considered appropriate for the mesh-sensitivity analysis. The prism-layer mesh was subsequently refined only in the complete-vehicle model to satisfy the near-wall resolution requirements of the final CFD simulations while preserving the selected surface discretization of the rear-wing region. The interaction between the main wing and the supporting structure generates complex three-dimensional pressure gradients (Figure 3.5). The resulting flow field is illustrated through contours of skin friction coefficient (C_f), pressure coefficient (C_p), and velocity magnitude. The C_f distribution highlights regions of strong shear near the leading edge and along the suction side, while localized reductions indicate areas susceptible to flow separation or adverse pressure gradients, particularly in the junction region. The C_p contours reveal a pronounced suction peak on the leading edge, followed by a gradual pressure recovery toward the trailing edge, consistent with lifting aerodynamic behaviour. In Figure 3.6, the velocity field further confirms these features, showing acceleration over the suction surface and a well-defined wake downstream of the profile.

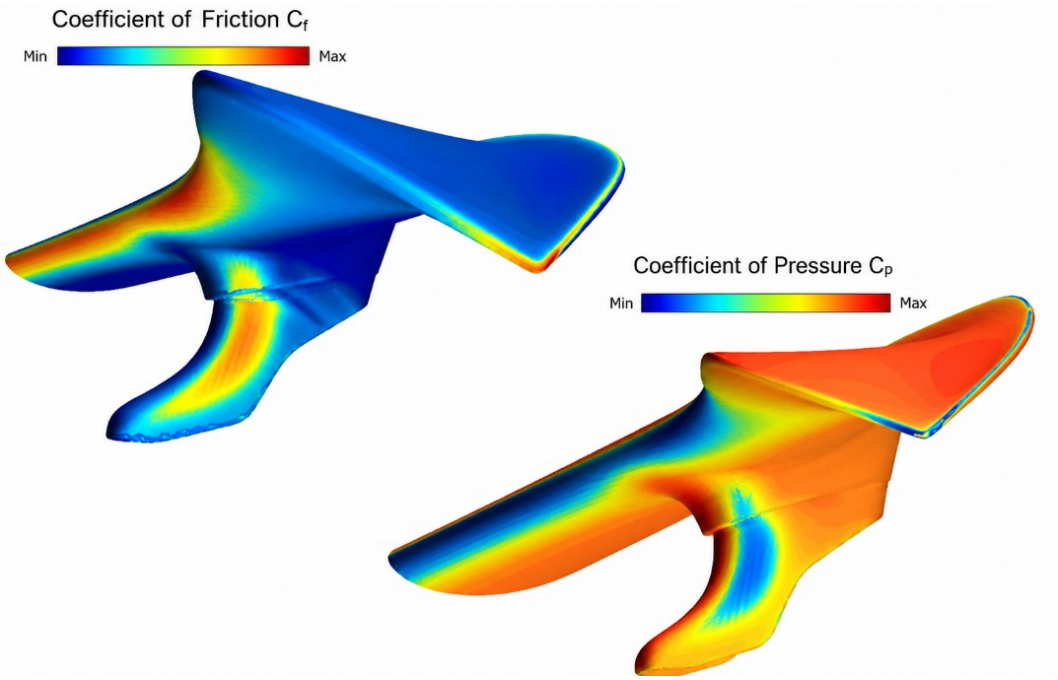

Figure 3.5 Representative CFD distributions of skin–friction coefficient (C_f) and pressure coefficient (C_p) on the isolated rear wing. The results illustrate the main flow–acceleration and pressure–loading regions governing aerodynamic performance.

Regions of low velocity and recirculation are observed in the near-wake and in the junction area, indicating potential sources of aerodynamic losses.

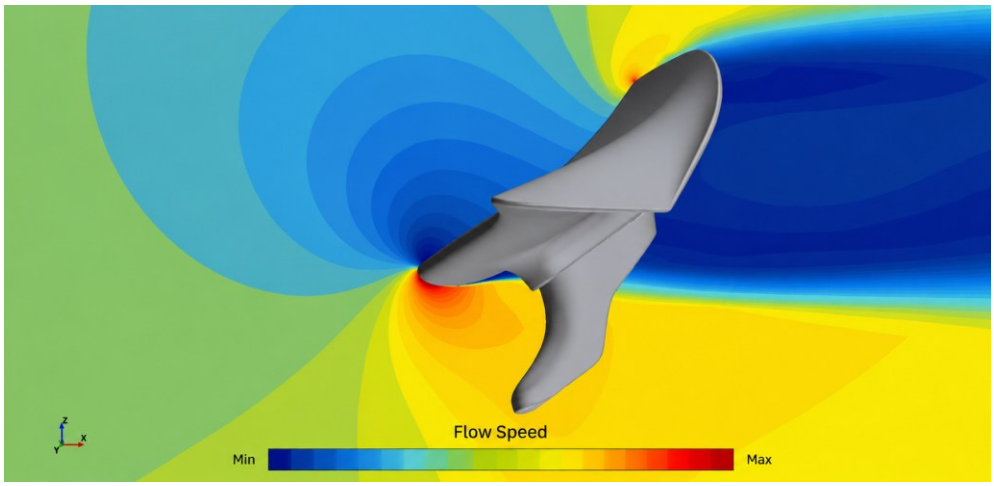

Figure 3.6 Velocity contours around the isolated rear–wing section. The accelerated flow over the suction side and the associated pressure gradients are clearly visible.

The CFD results provide a coherent representation of the flow physics, capturing the interaction between pressure distribution, boundary-layer development, and wake formation, and serving

as a robust reference for the subsequent analysis of the Co-Flow configurations. As in any CFD study, one of the primary indicators of simulation quality and convergence is the residual. In computational fluid dynamics, residuals represent the imbalance or error in the governing equations (continuity, momentum, and energy) at a given iteration. They quantify the difference between the left-hand side and right-hand side of each discretized equation at every control volume or grid node. Several types of residuals exist, however, for this investigation, absolute residuals were employed; these provide a direct measure of how well the numerical solution satisfies the governing equations. A steady and monotonic decrease of residuals over iterations indicates that the solution is progressing toward convergence, while persistent oscillations may suggest problems such as poor mesh quality, inappropriate boundary conditions, or numerical instability. In general, a solution is considered converged when the residuals fall below typical engineering thresholds, commonly in the range of 10^{-6} to 10^{-3}. Lower residuals correspond to a higher degree of numerical accuracy and ensure that the computed flow field reliably represents the physical behaviour of the system.

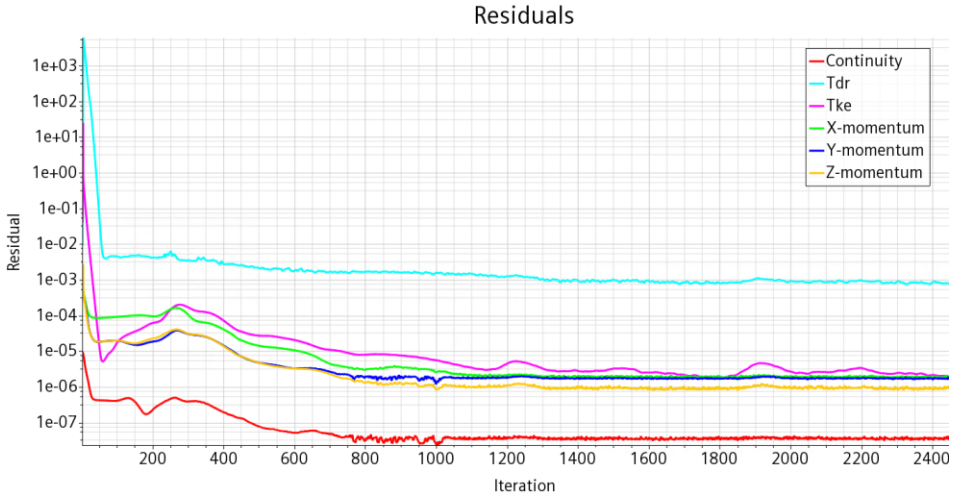

Figure 3.7 Convergence history of the unnormalized residuals for the governing equations.

In Figure 3.7, an example of the residual evolution for a single simulation run is presented. Convergence was assumed when the monitored aerodynamic coefficients remained effectively constant over successive iterations and the residuals stabilized at values of the order of 10^{-4} or lower. This confirms that the solver successfully reached a numerically converged solution, ensuring the reliability of the aerodynamic coefficients extracted from the simulation.
For each CFD run, the following key data were recorded:

- Global coefficients such C_l and C_d for both the rear wing and the full vehicle.
- The pressure coefficient (C_p) distributions extracted across nine spanwise sections of the rear wing.

These simulated results constitute the baseline reference dataset, essential for comparison against the experimental measurements collected in the subsequent testing phase.
Figures 3.8 and 3.9 show the CFD results for the non-dimensional drag (C_d) and lift (C_l) coefficients as functions of rear wing deployment and vehicle speed; all values were normalized with respect to the baseline configuration, defined as 0% wing deployment at the lowest vehicle speed, allowing a direct comparison between the different cases. The results highlight the evolution of the aerodynamic performance across the tested configurations. In theory, aerodynamic coefficients mainly depend on geometry and should remain constant for a fixed configuration when Reynolds number effects are negligible. This assumption is generally valid in high-Reynolds-number applications ($Re > 10^7$), such as aircraft cruise conditions. However, in automotive aerodynamics, where Reynolds numbers are lower and flow separation effects are more significant, both C_l and C_d vary with vehicle speed due to changes in boundary layer behaviour and flow transition.

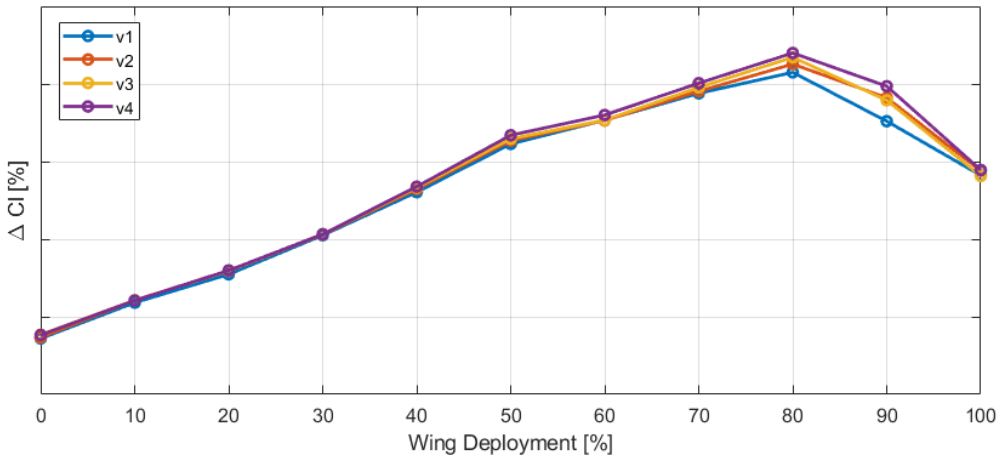

Figure 3.8 Relative variation of the lift coefficient predicted by CFD for the investigated wing design configurations at various vehicle speed (v1-v4, v1<v4).

As expected, both aerodynamic coefficients exhibited a clear dependence on rear-wing deployment and freestream velocity. The lift coefficient increased with wing angle up to a peak value, after which a reduction was observed due to the onset of flow separation on the suction side of the wing. A progressive clustering of the curves can also be observed at higher wing deployment angles with increasing Reynolds number. This behaviour suggests a reduced sensitivity of the aerodynamic response to velocity variations under highly separated flow conditions. At the same time, the drag coefficient increases progressively with wing deployment, mainly due to higher pressure and induced drag associated with increased downforce generation.

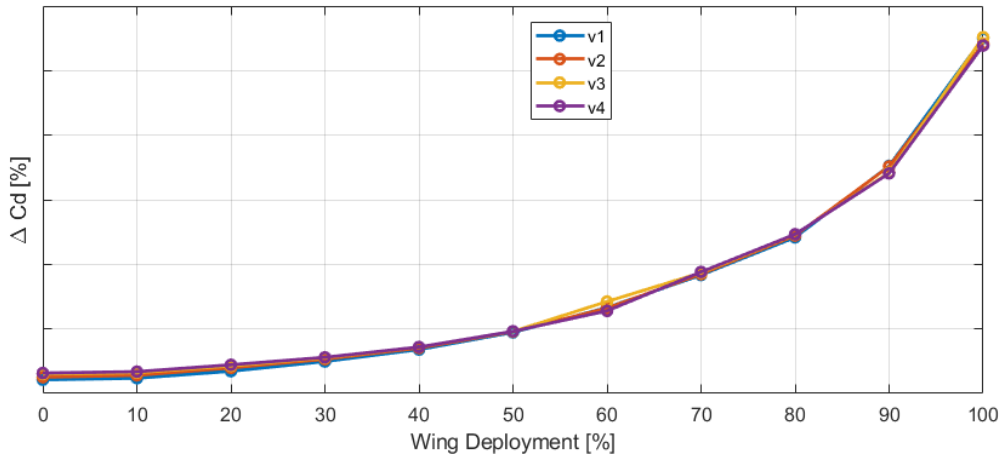

Figure 3.9 Relative variation of the drag coefficient predicted by CFD for the investigated wing design configurations at various vehicle speed (v1-v4, v1<v4).

The combined analysis of Figures 3.8 and 3.9 indicates that increasing wing deployment beyond approximately 80% provides limited additional lift while producing a comparatively larger increase in drag, highlighting the existence of an aerodynamic trade-off. In addition to global coefficients, the local pressure coefficient (C_p) distribution on the rear wing was also computed for all simulated combinations of speed and wing deployment. To ensure direct correlation with the experimental campaign, nine spanwise sections of the wing were extracted from the CFD results, corresponding to the same probe locations used in the physical tests. These datasets form the basis for the CFD-to-experiment comparison, which will be discussed in detail in the following sections.

3.2 Vehicle Baseline Setup

To verify the numerical data obtained from the internal McLaren CFD mainframe, a physical test campaign was conducted using a fully instrumented vehicle configured to match the same geometrical setup and operating conditions as those simulated. This approach ensures direct comparability between the computational and experimental datasets, allowing the assessment of the CFD model's predictive accuracy under real-world aerodynamic conditions. The test vehicle selected for this activity was a McLaren 765LT, a high-performance supercar characterized by an advanced active aerodynamic package and a lightweight carbon-fiber monocoque chassis. The vehicle was used in its production configuration, with only minor modifications introduced for instrumentation purposes. The main vehicle specifications are summarized in Table 3.2. Although wind tunnel testing would represent the ideal solution for aerodynamic characterization, it was not considered in the present work due to budget limitations. Experimental validation was therefore carried out at the Applus+ IDIADA proving ground in Spain (Figure 3.10), which provides suitable facilities for full-scale aerodynamic testing under controlled outdoor conditions. The tests were conducted on the high-speed circuit,

featuring two straight sections of approximately two kilometres each connected by parabolic bends. This configuration allows for both steady-state and coastdown runs, providing a consistent flow environment for data acquisition.
During the tests, the following measurements were performed:

- Drag estimation from the longitudinal acceleration (g_{long}) signal measured by the Racelogic VBOX VB2SX10 GPS ECU during coastdown runs.
- Downforce estimation from suspension displacement sensors installed at all four vehicle corners, allowing the estimation of vertical load transfer.
- Pressure coefficient (C_p) distributions through static pressure ports installed on the rear wing, arranged along nine spanwise sections corresponding to the CFD model.

Engine	M840T	-
Engine Format	90° V8, 4.0L Biturbo	-
Valvetrain	32 Valve, DOHC, VVT	-
Max RPM	8500	rpm
Power	765	PS
Torque	800	Nm
Transmission	7-Speed + Revers Seamleass Shift Gearbox (SSG)	-
Max Speed	330	kph
0-100 kph	2,8	s
0-200 kph	7,0	s
0-400 mt	9,9	s
100-0 kph	29,5	mt
200-0 kph	108	mt
DIN Kerb Weight	1339	kg
Body Structure	Carbon Fibre Monocage II	-
Vehicle Lenght	4600	mm
Vehicle Width	2161	mm
Vehicle Height	1193	mm

Table 3.2 Technical specifications of the experimental vehicle used in this study.

This experimental setup enables the comprehensive validation of the aerodynamic performance predicted by CFD, ensuring that both local flow behaviour (via C_p) and global aerodynamic forces (C_l and C_d) are consistently evaluated under real-world operating conditions.

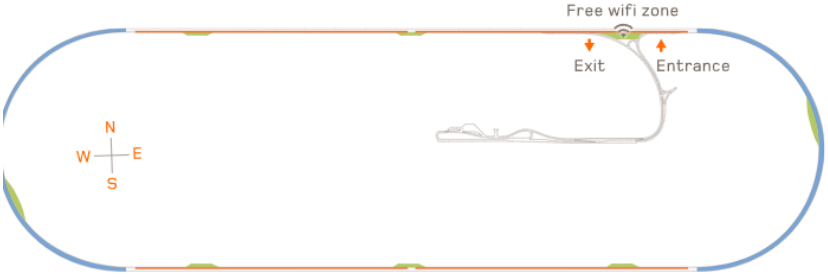

Figure 3.10 High-speed circuit section of the IDIADA Applus+ Proving Ground used during the experimental campaign.

A total of sixty-four static pressure ports were drilled on the suction side of the rear wing, following the CAD layout. Their positions were defined consistently with the CFD geometry to enable a direct comparison between experimental and numerical pressure distributions and to verify the predicted flow separation regions. The pressure taps were distributed along the wing chord from the leading edge to the trailing edge, allowing the evolution of the pressure gradient and separation point to be identified. In the Co−Flow configurations, the internal ducting reduced the number of available probes to 46 while preserving the spanwise distribution (Figure 3.11).

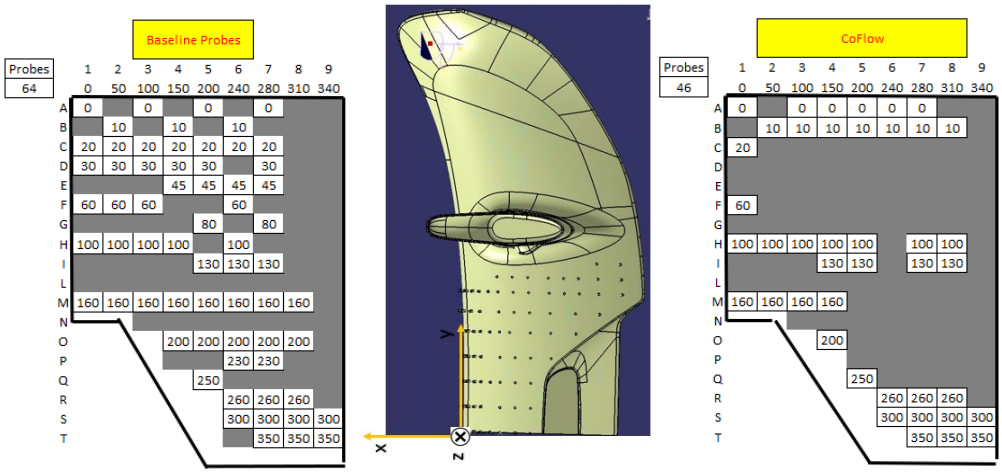

Figure 3.11 Static pressure measurement layout adopted for the experimental campaign. The central image shows the probe locations on the rear wing, while the left and right panels report the pressure−tap distributions for the baseline and Co−Flow configurations, respectively.

The pressure ports were connected to four 16-channel pressure modules integrated inside the wing structure (Figure 3.12, 3.13).



Manufacture	McLaren Applied Technologies	-
Model	Pin 16	-
Comunication	CAN - 1Mbit/s	-
Range	0-(-150)	mbar
Resolution	11	bit
Samplig rate	1	kHz
Accuracy	<±1,5%	-
Temp compensated	Yes	-

Figure 3.12 McLaren Applied Technologies 16-channel Pitot pressure sensor used in the experimental campaign, together with its main technical specifications.

A dedicated CAN communication line (CAN2) transmitted the pressure data from the four acquisition modules to the main onboard data acquisition system, ensuring synchronized and low-noise acquisition together with the vehicle dynamic signals. Each module acquires pressure measurements at a sampling rate of 1 kHz, synchronizing the data from all 64 pressure

measurement channels with the remaining measurements acquired from the other data sources within the experimental platform. This setup requires the installation of a Pitot tube at the front of the vehicle (Figure 3.14) to measure the total (stagnation) pressure of the incoming airflow. The total pressure pipe is connected to the reference port of the pressure measurement modules. Consequently, each sensor channel measures the pressure difference between the local static pressure at the corresponding wing pressure tap and the reference total pressure. In this configuration, any variation in local static pressure relative to the reference pressure produces a proportional change in the sensor output voltage.

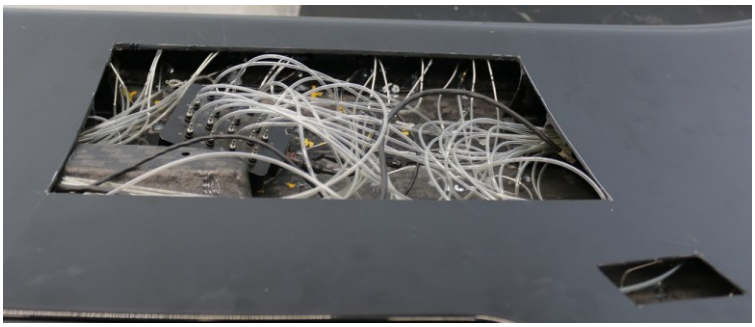

Figure 3.13 Installation of the 64 static pressure port sensors (4 × 16 channels) inside the experimental vehicle.

The Pitot tube was mounted on the front bonnet of the vehicle in a region of undisturbed airflow to ensure an accurate measurement of the free-stream total pressure. Owing to the installation geometry, the probe operated with an inclination of approximately 5° relative to the incoming flow. Although this orientation may introduce a systematic bias in the measured total pressure, the resulting error was estimated to be below 1% of the dynamic pressure and was considered constant for all tested configurations. Consequently, it does not affect the comparative analyses presented in this work. The Pitot tube was connected to a differential pressure sensor (model DPS-90-2.5, manufactured by Texense Electronics), featuring a full-scale measurement range of ±90 mbar. The sensor converts the pressure difference between the Pitot (total pressure) and static pressure references into an analogue voltage signal sampled at 1 kHz by the Arduino R4. The microcontroller performs signal acquisition, digital filtering, and synchronization with the remaining experimental measurements, ensuring consistent time alignment across all recorded data. The pressure coefficient (C_p) for each port is then calculated using the following relationship:

$$C_{Pi} = 1 + \frac{p_{pin16_i}}{p_{Pitot}} \tag{3.3}$$

where

C_{Pi} is the C_P for each generic port

p_{pin16_i} is the static pressure for each generic port

p_{Pitot} is the dynamic pressure calculated from the Pitot

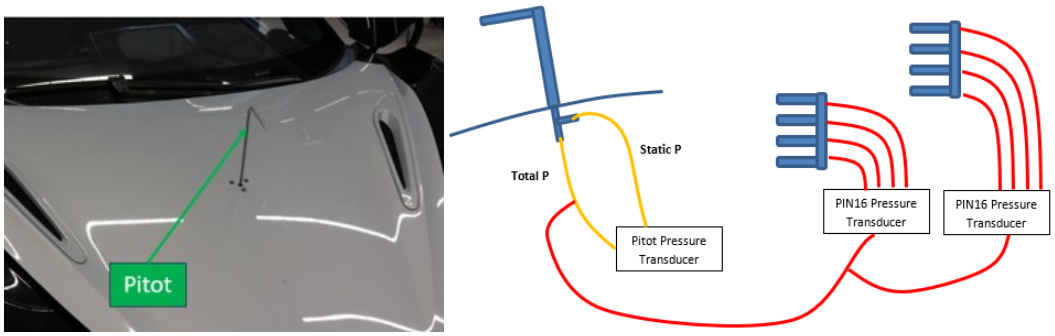

Figure 3.14 Installation of the Pitot probe on the experimental vehicle and schematic of the pressure tube plumbing to the pressure transducers.

The processed data were then broadcast over a new CAN (CAN1) network, allowing the total pressure measurement to be acquired and time-synchronized with the other aerodynamic and dynamic signals recorded by the vehicle's main data acquisition system. This configuration ensured that the total pressure reference remained consistent across all measurement channels, providing reliable input for the calculation of the pressure coefficient (C_p) at each static port location. The cabin control unit (Figure 3.15), installed next to the driver, allowed real-time monitoring of key parameters such as Pitot pressure and fan rotational speed (RPM). While active fan control was not required during the baseline tests, the system was designed to support the future integration of the rear Co-Flow fan system through the same CAN network architecture. Data acquisition was performed using CANape 17 (Vector Informatik) [128], configured to log all aerodynamic and vehicle dynamic parameters during testing. The recorded signals included Pitot total pressure, static pressures from the 64 rear wing ports, rear wing deployment, vehicle speed, suspension displacement, longitudinal acceleration, and ambient conditions for air density evaluation; vehicle data broadcasted through CAN network has a specific sample rate defined by each electronic control unit.



Figure 3.15 In-cabin control unit developed for the experimental campaign, used to control the Co-Flow system operating conditions, including fan rotational speed and actuation settings during vehicle testing.

Figure 3.16 presents an example of the acquired dataset.

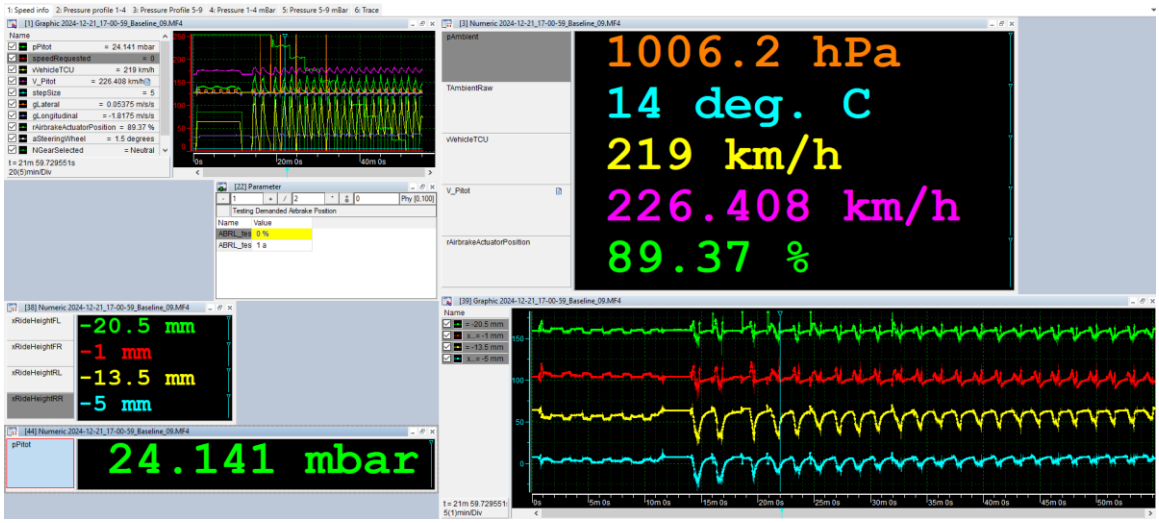

Figure 3.16 CANAPE17 data acquisition interface used to monitor and record synchronized signals from the vehicle instrumentation, including suspension displacements, pressure sensors, vehicle speed, and environmental conditions during the experimental campaign [128].

3.3 CFD vs Experimental Results

This section presents the comparison between the CFD predictions and the experimental measurements obtained during the vehicle testing campaign. The objective is to assess the capability of the numerical model to reproduce the real aerodynamic behaviour of the vehicle under different operating conditions. Particular attention is given to the comparison of pressure distributions, drag, and downforce coefficients for the investigated rear wing deployment configurations and vehicle speeds. To ensure consistency and reliability, the experimental data were processed following a standardized workflow. Raw data were initially acquired in proprietary MF4 format and subsequently converted into MATLAB-compatible MAT files. Since the measurement signals originated from multiple electronic control units operating at different native sampling rates, all channels were initially processed individually prior to time-base synchronization. A multi-stage post-processing procedure was applied before the aerodynamic analysis. First, a symmetric moving-average filter was applied to the measured quantities to attenuate high-frequency fluctuations associated with sensor noise and vehicle vibrations while preserving the low-frequency dynamics relevant to the aerodynamic response. The filter window length was selected according to the dynamic characteristics of each

experimental procedure: a window length of 50 samples was adopted for the steady-state aerodynamic analyses (C_l and C_p), whereas a longer window of 500 samples was employed for the coast-down tests used for C_d estimation, providing increased attenuation of measurement noise during the slower deceleration manoeuvres. Control and state signals, including vehicle speed, steering angle, airbrake position, fan speed, and engaged gear, were intentionally excluded from this filtering stage to preserve the original operating conditions required for the subsequent identification of valid operating conditions. For the steady-state aerodynamic analyses, suspension displacement measurements were additionally corrected through an automatic zeroing procedure based on a dedicated reference condition. Subsequently, all measurement channels were synchronized onto a common temporal basis through linear interpolation. A common time base of 1 kHz was adopted for the steady-state aerodynamic analyses (C_l and C_p), whereas a 100 Hz time base was used for the coast-down analysis (C_d). Following the signal conditioning procedure described above, steady-state operating conditions were automatically identified by applying threshold criteria to the vehicle speed, longitudinal acceleration, steering angle, fan operating condition, and minimum segment duration. Specifically, the vehicle speed was required to remain within ±1 km/h of the target value, while the steering angle was constrained within ±2° from the neutral position to exclude transient manoeuvres and cornering effects. For each rear-wing deployment and fan setting, measurements were collected over a sequence of six steady-state operating conditions corresponding to progressively increasing vehicle speeds. To eliminate residual transient behaviour following changes in operating conditions, an initial settling period of 5 s was discarded from each valid measurement segment. Depending on the target vehicle speed, the retained steady-state acquisition window ranged from 30 s to 60 s, while segments that did not satisfy the prescribed selection criteria were automatically rejected. The filtered suspension displacement signals were averaged over the retained steady-state portion of each valid operating segment. The resulting mean filtered suspension displacements were subsequently used in the Segers methodology to determine the aerodynamic loads, from which the pressure coefficient (C_p) and lift coefficient (C_l) were calculated for each operating condition. During coast-down tests for drag coefficient estimation, six back-and-forth runs in opposite driving directions were performed to minimize the influence of ambient wind and road gradient. The tests covered the deceleration interval from 200 km/h to 80 km/h, with the transmission in neutral and the clutches fully disengaged to eliminate drivetrain drag contributions. Valid coast-down events were automatically identified by applying selection criteria based on vehicle speed, longitudinal acceleration, steering angle, brake pressure, transmission state, and fan operating condition. Individual coast-down manoeuvres were separated according to temporal discontinuities and grouped into consecutive pairs to improve measurement repeatability. For each pair, the measured drag force was interpolated onto a common speed vector and averaged. A third-order polynomial regression was subsequently applied to obtain a smooth

representation of the total resistive force. The mechanical resistance model was then subtracted from the fitted curve to isolate the aerodynamic drag component. Finally, the drag coefficient was calculated over the analysed speed range, and the resulting values were averaged to obtain a representative C_d for each operating condition.

3.4.1 C_d Comparison

Vehicle drag represents one of the main aerodynamic parameters investigated in this study. Although wind tunnel testing would provide the most accurate method for measuring aerodynamic resistance under controlled conditions, its high operational cost led to the adoption of an alternative experimental approach based on coast-down testing. This methodology offers a reliable and practical means of estimating the vehicle drag under real operating conditions.
To ensure repeatability and consistency, all coast-down tests were performed following the recommendation of the SAE J1263 standard [129], which defines the environmental and operational requirements for the measurements. Testing was conducted only under suitable ambient conditions, with controlled temperature and wind limits, on a dry and smooth track characterized by minimal slope variation. Tire wear and inflation pressure were also carefully monitored to reduce the influence of rolling resistance variations on the results. According to Segers [130], the vehicle drag coefficient can be determined either by directly using the longitudinal deceleration signal measured by the GPS unit, or alternatively, by calculating the speed variation between two-time instants. The relationship can be expressed as:

$$C_{d,veh} * A = \frac{T(n_{engine}) * \frac{i_{total}}{r_{rolling}} - M g_{long}}{0.5 * \rho * V^2} \tag{3.4}$$

where T_{engine} [Nm] is the engine torque, i_{total} the overall transmission ratio, $r_{rolling}$ [m] the tire rolling radius, M [kg] the vehicle mass, g_{long} $[\frac{m}{s^2}]$ the longitudinal acceleration, ρ $[\frac{kg}{m^3}]$ the air density, and V $[\frac{m}{s}]$ the vehicle speed. During coast-down conditions, when the vehicle travels at high speeds and the transmission is fully disengaged, the engine torque term in the numerator can be considered negligible. In practice, there remains a small contribution from transmission drag and tire rolling resistance, but at such high speeds, these effects are minor compared to the aerodynamic drag, which dominates the overall resistance. Therefore, the simplified form of the equation primarily represents the aerodynamic component of the total drag force, allowing direct estimation of C_D from the measured g_{long} signal. Before discussing the CFD−to−experiment correlation, the repeatability of the experimental vehicle drag measurements was assessed. Table 3.3 reports the coefficient of variation in the measured drag−coefficient values for the baseline vehicle across the investigated airbrake deployment conditions calculated as follows:

$$CV\left(C_{d,veh}\right)[\%] = \frac{\sigma_{C_d}}{\mu_{C_d}} \times 100 \quad (3.5)$$

where σ_{C_d} is the standard deviation of each set of experimental drag−coefficient measurements and μ_{C_d} is the corresponding mean value. The resulting coefficients of variation remained relatively small throughout the test campaign, indicating good consistency of the acquisition chain and experimental procedure. A global repeatability assessment yielded an average CV of the coefficient of drag of 1.89%, with a standard deviation of 0.68%, confirming the stability and robustness of the measurement methodology.

Airbrake Deployment [%]	**CV($C_{d,veh}$) [%]**
0%	1.41%
10%	1.24%
20%	1.22%
30%	1.69%
40%	2.87%
50%	1.28%
60%	2.52%
70%	1.99%
80%	1.19%
90%	2.56%
100%	2.81%
Global Repeatability Metrics	
CV($C_{d,veh}$) average [%]	1.89%
CV($C_{d,veh}$) Std. Dev. [%]	0.68%

Table 3.3 Repeatability assessment of baseline vehicle drag−coefficient measurements expressed through the coefficient of variation (CV). Global statistics are calculated considering all investigated wing−deployment conditions.

In addition to repeatability, the uncertainty associated with the drag estimation procedure was evaluated through uncertainty propagation according to the Guide to the Expression of Uncertainty in Measurement (GUM) methodology [131]. The uncertainty analysis considers the dominant measurement quantities directly involved in the drag−area calculation, namely longitudinal acceleration, vehicle speed, vehicle mass, and air−density determination. Additional sources of variability associated with road gradient and ambient wind conditions were mitigated through the experimental procedure. In particular, coastdown tests were performed in both driving directions and only under environmental conditions compliant with the SAE J1263 recommendations, with ambient wind speeds below 2 m/s. The residual influence of these factors is therefore reflected in the repeatability statistics obtained from the repeated experimental runs rather than in the analytical uncertainty propagation. The

uncertainty associated with the drag estimation was evaluated through uncertainty propagation of the coastdown formulation, considering the contributions of vehicle acceleration, velocity measurement, air–density estimation, and vehicle mass. The dominant contributions were associated with acceleration measurement and air–density estimation, while vehicle–mass uncertainty was found to be negligible.

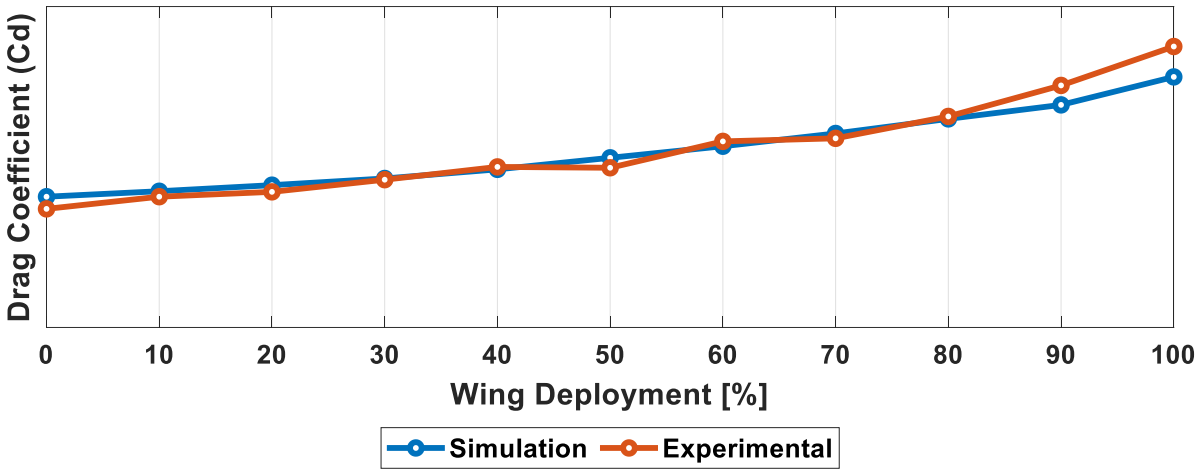

Figure 3.17 Comparison between CFD predictions and experimental measurements of the vehicle drag coefficient as a function of rear–wing deployment. The agreement supports the use of the CFD methodology as a comparative design–support tool.

The resulting expanded uncertainty was estimated to be approximately 6% (k = 2, 95% confidence); additional details are provided in the Appendix. The resulting experimental drag values were subsequently compared with the CFD predictions, as shown in Figure 3.17. The comparison showed overall good agreement in terms of global drag trends across the investigated operating conditions; however small discrepancies between the CFD predictions and the experimental measurements remain. At lower rear–wing deployment levels, CFD simulations slightly overpredicted the aerodynamic drag relative to the experimental measurements, whereas at higher deployment conditions, the trend progressively reversed and the experimentally measured drag became higher than the numerical prediction. Even under the least favourable condition, the difference remained below 10%, confirming the suitability of the numerical model for comparative aerodynamic analyses. From the experimental perspective, these differences can be attributed to the inherent variability of on-track testing. Although the vehicle speed was accurately measured, the ambient wind conditions were monitored at a single location on the circuit and therefore provide only a local estimate of the atmospheric conditions. As the vehicle travels around the closed circuit, its heading continuously changes with respect to the prevailing wind direction, resulting in continuous variations of the effective inflow conditions experienced by the vehicle. Consequently, the local

aerodynamic conditions may differ from the reference wind measurement because of changes in both wind magnitude and direction, transient wind gusts, and local atmospheric disturbances, which cannot be fully accounted for during post-processing. Additional sources of variability include interactions with surrounding traffic and driving conditions, together with the uncertainty associated with the measurement chain. From the numerical perspective, the CFD simulations were performed under steady-state conditions with uniform inlet boundary conditions, which cannot fully reproduce the continuously varying environmental conditions encountered during on-track testing. Furthermore, the numerical model neglects transient aerodynamic phenomena and other real-world factors, such as manufacturing tolerances, wheel ride-height variations, and structural deformations under aerodynamic loading, that may influence the measured aerodynamic coefficients. To minimise the influence of experimental variability, the revised test campaign included a larger number of repeated runs, providing improved statistical robustness of the measured aerodynamic coefficients, while the overall measurement uncertainty was quantified according to the GUM framework. Although absolute drag values cannot be disclosed due to confidentiality restrictions and despite the remaining local discrepancies, the CFD model successfully reproduces the overall evolution of the drag coefficient throughout the investigated deployment range. Considering the improved repeatability of the experimental campaign together with the quantified measurement uncertainty, the observed agreement supports the suitability of the numerical framework as a reliable tool for comparative aerodynamic design assessments

3.4.2 C_l Comparison

Following the comparison between CFD and experimental drag results, the second key aerodynamic parameter considered for validation was the vehicle downforce, again in the absence of wind tunnel measurements. The aerodynamic load was estimated through suspension displacement measurements obtained using four rotary potentiometer sensors, one installed at each suspension corner (Figure 3.18). Each sensor converts the rotational movement of the suspension linkage into a voltage signal proportional to wheel displacement. Through appropriate calibration procedures and geometrical transformations, the measured displacements can be converted into the corresponding vertical loads acting on each wheel, axle, and ultimately on the entire vehicle. This approach provides a reliable and repeatable method for evaluating aerodynamic load distribution and represents a fundamental element in the validation of the CFD-predicted downforce values.



Figure 3.18 Rotary displacement sensor installed on the suspension assembly.

According to Segers [130], the front and rear axle downforces can be estimated through the following relationships:

$$L_F = MR_f * SR_f * \left(x_{suspensionLF} + x_{suspensionRF}\right) + \frac{Mg_{long} * 9.81 * h_{CoG}}{WB} \quad (3.6)$$

$$L_R = MR_r * SR_r * \left(x_{suspensionLR} + x_{suspensionRR}\right) - \frac{Mg_{long} * 9.81 * h_{CoG}}{WB} \quad (3.7)$$

where MR_f and MR_r are the front and rear suspension motion ratios, SR_f and SR_r the corresponding spring rates, $x_{suspension}$ [m] the measured suspension displacements, h_{CoG} [m]the height of the centre of gravity, WB the wheelbase [m], g_{long} $[\frac{m}{s^2}]$ the longitudinal acceleration, and M [kg] the vehicle mass. These equations account for both aerodynamic loading, through suspension compression, and inertial load transfer caused by longitudinal acceleration or deceleration. Under steady-state conditions, where $g_{\text{long}} \approx 0\ \frac{m}{s^2}$, the inertial contribution becomes negligible, allowing the aerodynamic downforce to be estimated directly from the suspension displacements and suspension mechanical properties. As per C_d evaluation, and prior to the CFD−to−experiment correlation comparison, the repeatability of the experimentally estimated aero-dynamic load was assessed across all investigated operating conditions. Table 4 reports the coefficient of variation ($CV(C_{l,veh})$) of the measured lift−coefficient values for the base-line vehicle across the investigated airbrake deployment conditions calculated as follows:

$$CV\left(C_{l,veh}\right)[\%] = \frac{\sigma_{C_l}}{\mu_{C_l}} \times 100 \quad (3.8)$$

Where σ_{C_l} is the standard deviation of each set of experimental lift−coefficient measurements and μ_{C_l} is the corresponding mean value. For the sake of clarity, only the results associated with the highest airbrake deployment levels (70−100%) are reported in Table 3.4. These operating conditions correspond to the largest aerodynamic loads and therefore represent the most relevant cases from both an experimental and aerodynamic perspective. The reported global

repeatability metrics were nevertheless calculated considering the complete set of investigated operating conditions. The coefficient of variation (CV [%]) obtained from the repeated measurements remained relatively limited throughout the test matrix, with an average value of approximately 2.54% and a standard deviation of 1.64%, as shown in Table 3.5. The observed variability is higher than that reported for drag measurements, reflecting the indirect nature of the downforce evaluation procedure based on suspension−displacement measurements and calibration correlations. However, the results indicate an acceptable level of repeatability for comparative aerodynamic assessments.

vVeh Adim	Airbrake [%]	CV($C_{l,veh}$) [%]
v1	70	2.22%
v1	80	6.60%
v1	90	2.51%
v1	100	1.10%
v2	70	4.06%
v2	80	2.47%
v2	90	1.66%
v2	100	0.34%
v3	70	2.31%
v3	80	5.12%
v3	90	2.50%
v3	100	3.82%
v4	70	2.09%
v4	80	0.87%
v4	90	1.07%
v4	100	1.90%
Global Repeatability Metrics		
CV($C_{l,veh}$) average variation [%]	2.54%	
CV($C_{l,veh}$) Std. Dev. [%]	1.64%	

Table 3.4 Repeatability assessment of baseline vehicle drag−coefficient measurements expressed through the coefficient of variation (CV). Global statistics are calculated considering all investigated wing−deployment conditions.

As per drag measurements, the uncertainty associated with the aerodynamic load determination was evaluated through uncertainty propagation according to the Guide to the Expression of Uncertainty in Measurement (GUM) methodology. The uncertainty associated with the aerodynamic−load determination was evaluated considering the dominant quantities involved in the Segers methodology, namely suspension spring−rate tolerances, motion−ratio estimation, and displacement sensor accuracy. The resulting expanded uncertainty was estimated to be approximately 10% (k = 2, 95% confidence), more details in the Appendix. The resulting

experimental lift coefficient values were subsequently compared with the CFD predictions, as shown in Figure 3.19, only for the highest wing deployment values.

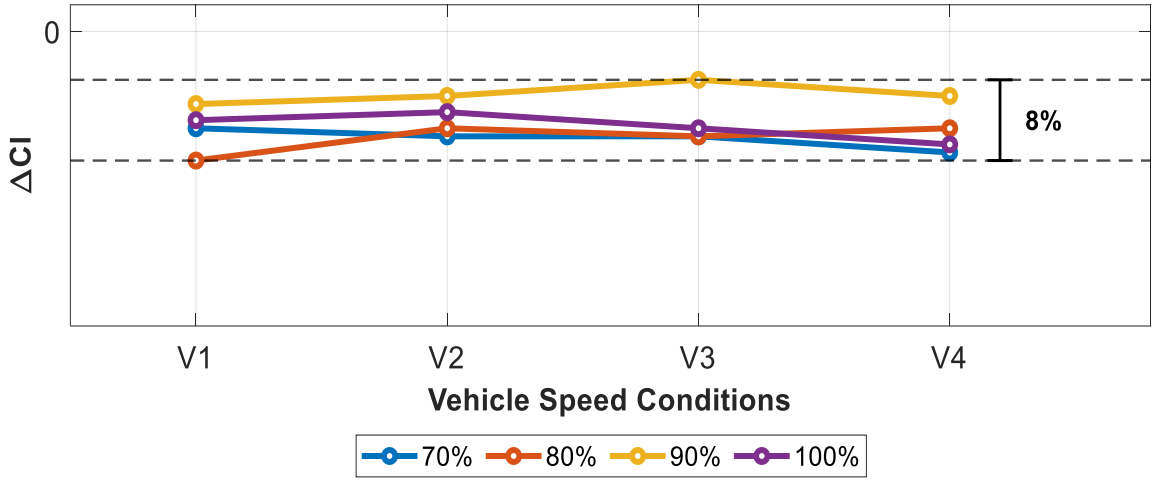

Figure 3.19 Comparison between CFD and experimental trends of rear−wing lift coefficient under high−load operating conditions (70−100% wing deployment, v1−v4).

The same limitations associated with on-track testing and the steady-state CFD approach discussed for the drag coefficient also apply to the lift coefficient comparison, since both aerodynamic coefficients were obtained during the same experimental campaign and compared against the same numerical framework. A systematic overprediction of CFD aerodynamic load was observed. This behaviour is consistent with the known limitations of steady RANS methodologies when applied to highly loaded three−dimensional flows. As aerodynamic loading increases, the influence of localized separation and unsteady flow structures may become more significant. Under these conditions, the numerical model can predict a more attached flow field than that observed experimentally, leading to a moderate overestimation of aerodynamic load. Despite this systematic bias, the CFD simulations consistently reproduced the general aerodynamic trends and relative variations across the investigated operating conditions. The experimental measurements exhibited a variation of approximately eight percentage points across the investigated operating range. The CFD results reproduced both the magnitude and progression of the measured trend, supporting the use of the numerical methodology for comparative aerodynamic assessments. Considering experimental repeatability, the estimated uncertainty associated with the load determination methodology, and the complexity of the investigated flow field, the level of agreement obtained is considered satisfactory for comparative aerodynamic analyses and configuration assessment.

3.4.3 C_p Comparison

The comparison between numerical and experimental pressure coefficient (C_p) distributions showed generally good agreement in terms of pressure recovery and aerodynamic loading, particularly in the downstream portion of the airfoil where the pressure gradients are less severe. The CFD model successfully reproduced the dominant features of the measured pressure distributions, including the location of the suction peak, the general pressure−recovery behaviour, and the evolution of aerodynamic loading with rear−wing deployment. The largest discrepancies were observed in regions characterized by strong pressure gradients, particularly near the leading edge of the rear wing. In these areas, the CFD RANS simulations tended to predict stronger suction peaks than those measured experimentally, resulting in a moderate overestimation of aerodynamic loading.

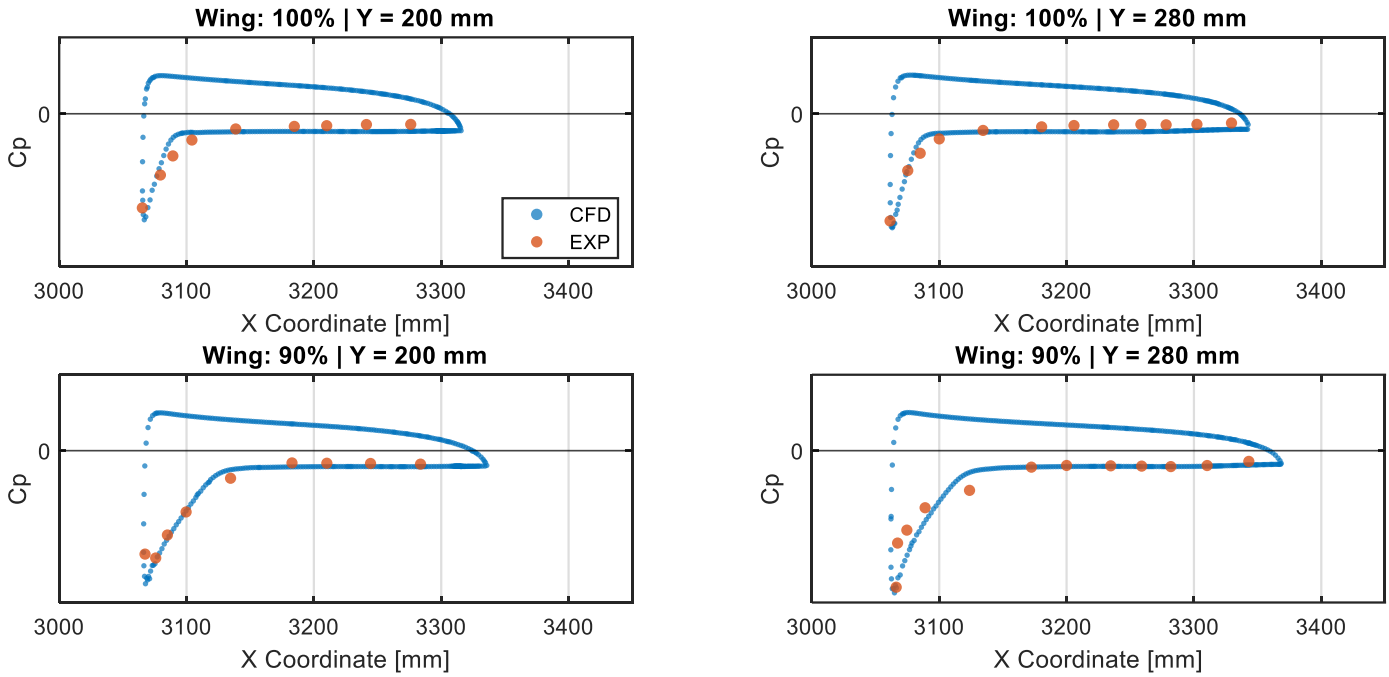

Figure 3.20 Comparison of pressure−coefficient distributions obtained from CFD and experimental measurements at the v4 operating condition for 90% and 100% rear−wing deployment. The comparison is used to assess the capability of the numerical model to reproduce the measured pressure−loading trends

This behaviour is consistent with the numerical model predicting a more attached flow in the leading-edge region, resulting in a stronger suction peak and a smoother pressure recovery than observed experimentally, as also reflected in the $\Delta C_{l,veh}$ comparison. This limitation is aligned with the well−known challenges of steady RANS methodologies in accurately predicting localized separation and unsteady flow phenomena in highly loaded aerodynamic configurations. The same limitations associated with on-track testing and the steady-state CFD

approach discussed for the drag coefficient also apply to the comparison of the pressure coefficient distributions. In addition, local discrepancies in the pressure coefficient distributions do not necessarily translate into proportional differences in the integrated aerodynamic coefficients, since the latter result from the surface integration of the pressure field over the entire aerodynamic surface. Furthermore, the experimental pressure measurements were acquired during the same on-track campaign discussed for the lift comparison and are therefore subject to the same environmental variability, including changing atmospheric conditions, local wind variations, and vehicle operating conditions. While local discrepancies are observed in regions characterized by strong pressure gradients, the objective of the present comparison was the assessment of the predictive capability of the numerical model with respect to the integrated aerodynamic quantities governing vehicle performance. For this reason, the comparison of pressure−coefficient distributions is primarily intended to support the interpretation of the underlying flow physics, whereas the quantitative validation is based on the agreement obtained for the global aerodynamic coefficients and their associated experimental uncertainty. The comparison between the Y = 200 mm and Y = 280 mm sections further demonstrates the capability of the numerical model to reproduce not only the pressure levels but also their evolution across the spanwise direction.

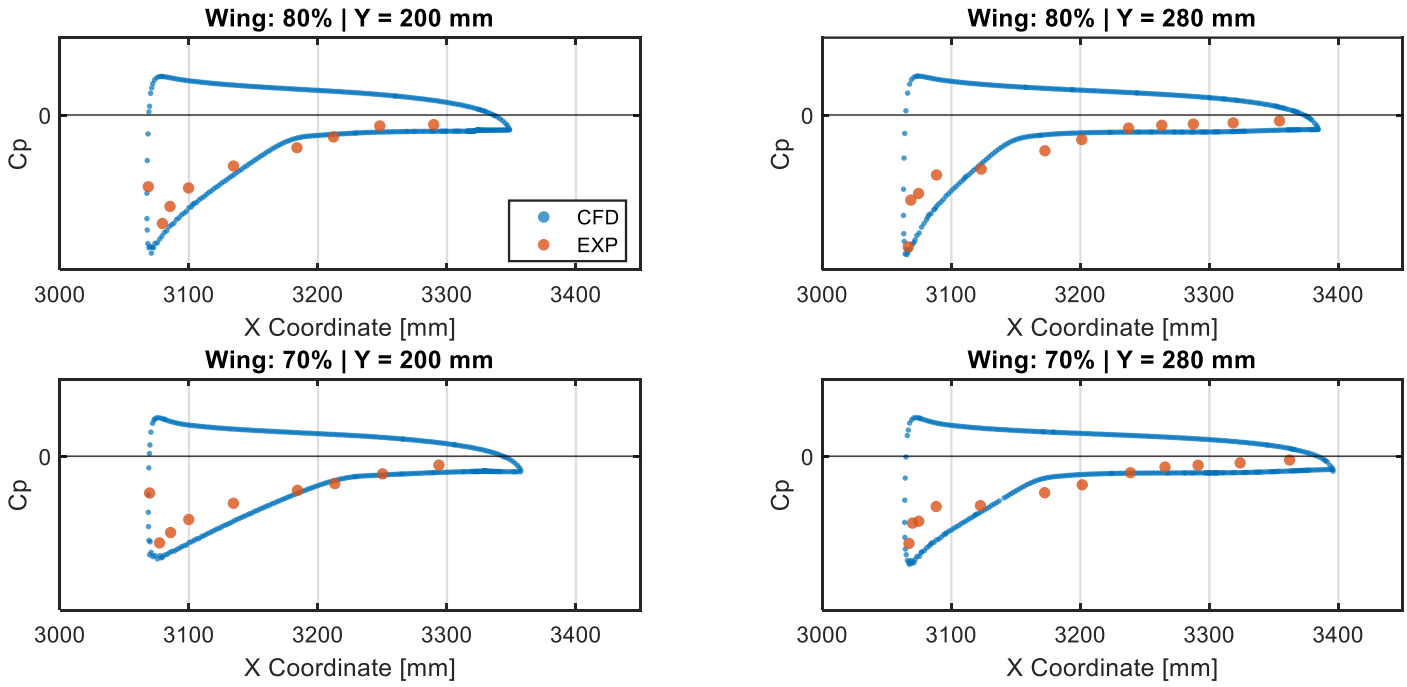

Figure 3.21 Comparison of CFD−predicted and experimentally measured pressure−coefficient distributions at the v4 operating condition for 70% and 80% rear−wing deployment. The Figure illustrates the pressure−loading distributions used to assess the agreement between numerical and experimental results.

Despite localized discrepancies near the leading edge, the CFD simulations consistently captured the general shape of the pressure distributions and their variation with rear−wing deployment, supporting the suitability of the adopted methodology for comparative aerodynamic investigations (Figures 3.20 and 3.21). While differences in suction−peak magnitude are observed, the broad distribution shape and pressure−recovery behaviour remain broadly consistent among the analysed sections. In contrast, rear−wing deployment produces substantially larger variations in the pressure distributions than the spanwise position itself, indicating that deployment angle remains the dominant parameter governing the local aerodynamic loading within the analysed region. The uncertainty associated with the pressure-coefficient measurements was estimated through uncertainty propagation of the differential-pressure measurements and the Pitot reference pressure used for normalization. The complete uncertainty analysis is presented in Appendix B.

3.4.4 Assessment of CFD Predictive Capability

The comparison between CFD predictions and experimental measurements on the baseline rear-wing configuration highlights both the capabilities and limitations of the numerical framework adopted in the present work. The RANS-based CFD methodology was able to correctly capture the overall aerodynamic trends, including the evolution of pressure distribution and the general variation of aerodynamic coefficients with wing deployment. However, quantitative discrepancies were observed under highly loaded conditions, mainly due to the intrinsic limitations of steady RANS approaches in resolving transient separated flows and unsteady wake structures. Additional variability may also originate from the experimental methodology itself, particularly from indirect drag and downforce estimations performed under real operating conditions. Despite these limitations, the CFD framework indicates sufficient robustness for comparative aerodynamic investigations, consistently reproducing the relative aerodynamic behaviour of the investigated configurations and operating conditions.

Chapter 4 – Fan Characterisation Rig

Several active-flow-control techniques can be adopted to manipulate the boundary layer around aerodynamic bodies, including compressed-air injection systems and ducted-fan-based solutions. Compressors are generally designed to generate significant pressure increases through gas compression, whereas fans primarily provide airflow motion with relatively limited pressure rise, as shown in Table 4.1. Since the present application requires a moderate pressure increase, approximately within the 2–6 kPa range, a ducted-fan configuration was identified as a suitable and cost-effective solution for the investigated aerodynamic concept.

Aspect	**Compressor**	**Fan**
Function	Increase gas pressure	Move air or gas
Pressure	High (significant increase)	Low (minimal increase)
Energy Use	High	Low
Applications	Compression systems	Ventilation and cooling
Design	Complex, multi-stage	Simple, single-stage

Table 4.1 Comparison between compressors and fans in terms of function, pressure rise, energy consumption, applications, and design characteristics.

Manufacturers typically provide performance maps describing the relationship between pressure rise, flow rate, efficiency, power consumption, and rotational speed. However, no detailed characterization data were available for the fans considered in this study. Consequently, a dedicated experimental rig was designed and manufactured to characterize the aerodynamic and electrical performance of the candidate fans under controlled operating conditions.

4.1 Rig Hardware Setup

The fan characterization rig was developed to measure pressure rise, mass flow rate, efficiency, and electrical power consumption of the tested fans, according to the recommendations of ISO 5801:2017 [132]. The rig structure was manufactured using Delrin®, an acetal homopolymer selected for its dimensional stability, stiffness, low friction coefficient, and ease of machining. Particular attention was dedicated to minimizing the internal surface roughness in order to reduce secondary pressure losses and improve repeatability of the airflow measurements. The fan was installed at the inlet of a straight circular duct equipped with static pressure taps located immediately upstream and downstream of the rotor, a centreline Pitot probe, and an electronically actuated throttle body used to vary the system resistance and to reproduce different operating conditions. The rig enabled the measurement of pressure rise, mass flow rate, electrical power consumption, and fan efficiency over the complete stable

operating range for each fan. A schematic representation and a photograph of the experimental setup are reported in Figure 4.1.

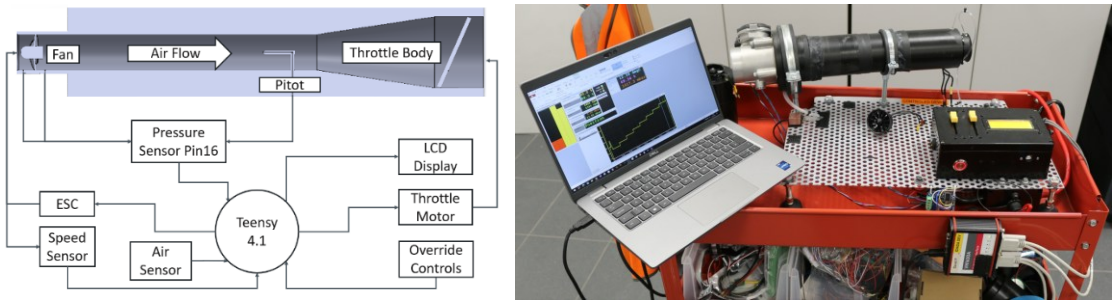

Figure 4.1 Experimental fan characterization rig, showing the system schematic (left) and the actual test setup (right).

The rig is relatively compact, and in the schematics, key components such as the fan, static pressure ports, Pitot tube, and throttle body can be easily identified. The duct incorporated static pressure ports positioned immediately upstream and downstream of the fan to minimize the influence of wall losses on the measured pressure difference. The pressure taps were connected to a McLaren® Applied Technologies PIN16 pressure acquisition module, as used in the vehicle baseline C_p measurements. Atmospheric pressure, temperature, and humidity were additionally monitored at 1Hz using a BME280 environmental sensor to allow accurate wet-air density calculation during post-processing. The test environment was maintained under controlled thermal conditions to minimize temperature-related variations during the measurements. Air density is calculated considering wet air, using the following equation:

$$\rho = \left(\frac{p_d}{R_d T}\right) + \left(\frac{p_v}{R_v T}\right) \quad \left[\frac{kg}{m^3}\right] \tag{4.1}$$

where p_d [Pa] is the dry−air partial pressure, p_v [Pa] the water−vapour partial pressure, R_d $\left[\frac{J}{kgK}\right]$ and R_v $\left[\frac{J}{kgK}\right]$ the specific gas constants for dry air and water vapour, respectively, and T [K] the absolute temperature. Airflow velocity was determined using a Pitot tube connected to a Texense DPS-190-2.5 differential pressure sensor, with a range of ±190mbar. The Pitot-tube position and duct arrangement were defined according to the recommendations provided by ISO 5801:2017 for industrial fan performance testing in standardized airways [132], ensuring improved repeatability and reduced sensitivity to local flow non-uniformities. The sensor output was processed in real time through the rig control unit. The airflow velocity was determined from the Pitot pressure measurements according to:

$$V_{center} = \sqrt{\frac{2(P_t - P_s)}{\rho}} \quad \left[\frac{m}{s}\right] \tag{4.2}$$

where P_t [Pa] and P_s [Pa] are the total and static pressures measured by the Pitot tube. Since the probe was located along the duct centerline, the measured velocity was converted into bulk velocity using a correction factor of 0.82 derived from the classical one−seventh power−law turbulent velocity profile:

$$V_{\text{mean}} = 0.82\ V_{\text{center}}\ [\tfrac{m}{s}] \tag{4.3}$$

The mass flow rate was then calculated as:

$$\dot{m} = \rho V_{\text{mean}} \text{A}_\text{p} \qquad \left[\tfrac{kg}{s}\right] \tag{4.4}$$

where A_p [m^2]is the duct cross−sectional area. Fan efficiency was evaluated as the ratio between the aerodynamic power transferred to the airflow and the electrical power absorbed by the electronic speed controller and the motor:

$$\eta = \frac{P_{air}}{P_{mot}} = \frac{q\Delta P}{VA} \tag{4.5}$$

where $q\ \left[\frac{m^3}{s}\right]$ is the volumetric flow rate, ΔP [Pa] is the pressure rise across the fan, V [V] is the electrical supply voltage, and A [I]is the absorbed current by the motor and the ESC, all acquired instantaneously.

4.2 Rig Electronic Setup

Two tested units were 40 mm brushless ducted fans sourced from the RC industry. The fan diameter was selected according to the packaging constraints imposed by the rear-wing internal geometry, which also needed to accommodate ducts and instrumentation. The tested fan's models are shown in Figure 4.2.





Model	Ref #	De mm	kV	n° Blades	Spacing	Blade Solidity
Galaxy X4 EDF	XF-DFS009	40	5000	12	7,98	0,88
AEORC	XDF40	40	8600	8	12,85	0,757

Figure 4.2 Ducted fans evaluated in this study: XFly Galaxy X4 EDF (left) and AEORC XDF40 (right), together with their main technical specifications.

The fans were controlled through a Skywalker® electronic speed controller (ESC). Fan rotational speed was measured using a dedicated Hobbywing® brushless RPM sensor, which generated train pulses processed by a Teensy® 4.1 microcontroller. The Teensy® 4.1 was also responsible for rig automation, throttle-body actuation, analogue data acquisition, signal processing, and CAN communication management. The differential pressure sensor analogue output was digitized using the integrated 12-bit analogue-to-digital converter (ADC) of the Teensy® 4.1, operating over a 0–3.3 V input range and providing a voltage resolution of 0.806 mV per least significant bit (LSB). Prior to testing, all sensors were calibrated by the instrumentation department using certified calibration procedures, and the resulting calibration curves were implemented within the data acquisition system. To ensure stable electrical operating conditions during long-duration tests, the system was powered through a combined battery and external DC power-supply setup capable of maintaining stable voltage and current delivery throughout the characterization cycle. Electrical power absorption was measured using an Isabellenhütte® IVT-S-100A-U0-I-CAN2-12 current sensor, which transmitted voltage, current, and power data directly over CAN communication. Pressure and voltage/current signals were sampled at 1 kHz and recorded through a CAN-based data acquisition system. A Bosch® electronic throttle body was installed downstream of the duct to vary the flow resistance and reproduce different operating conditions along the fan map. The throttle-body position was automatically controlled by the Teensy® microcontroller according to the predefined test sequence (Figure 4.3). All measured parameters, including pressure, RPM, voltage, current, temperature, and humidity, were transmitted through dedicated CAN buses to the data acquisition system. Data acquisition was performed using a Vector VN1630A CAN interface and processed through Vector CANape® (Figure 4.4). MATLAB scripts were subsequently used for data filtering and post-processing.

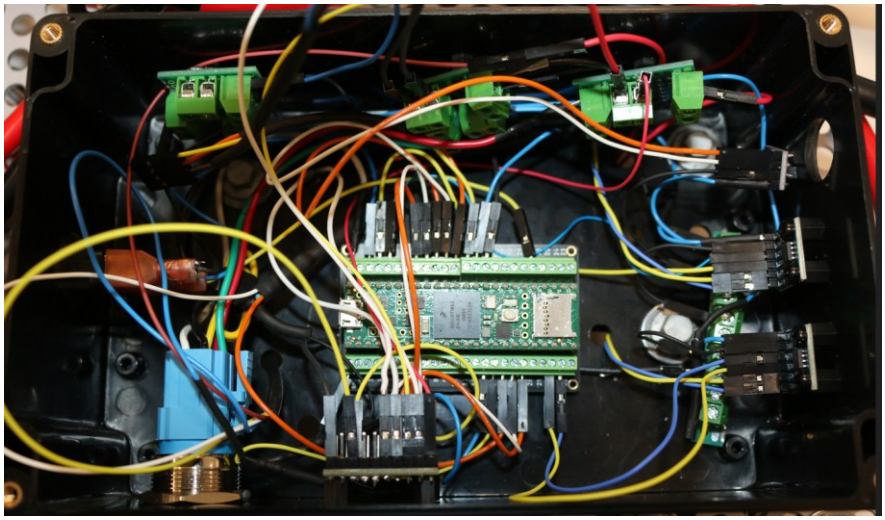

Figure 4.3 Microcontroller-based data acquisition and control system used for the fan characterization test rig.

Due to the relatively low operating Mach number ($M < 0.15$) and the limited pressure rise across the fan, compressibility effects were neglected, and the flow was treated as incompressible. All signals were recorded through a CAN−based data acquisition system. Prior to testing, all sensors were calibrated by the instrumentation department using certified calibration procedures, and the resulting calibration curves were implemented within the data acquisition system. Both automated and manual operating modes were employed to identify the stable operating envelope while avoiding surge conditions and excessive vibrations. Unstable operating conditions were observed at throttle openings below 40%; therefore, all automated measurements were performed with a safety margin of 5% above this limit to ensure stable operation and measurement repeatability. The CAN-based acquisition architecture ensured synchronized transmission of pressure, RPM, and electrical measurements, minimizing timing misalignment between channels.

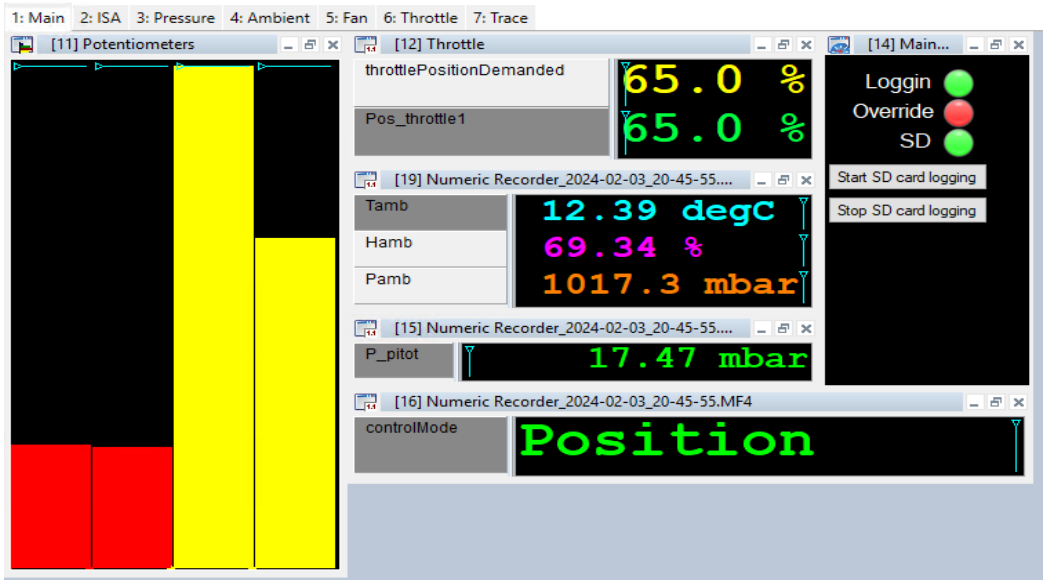

Figure 4.4 CANape® graphical user interface used for real-time data acquisition, monitoring, and logging during the experimental tests.

The repeatability of the experimental procedure was assessed through repeated acquisitions performed under identical operating conditions. For each measured quantity, the coefficient of variation (CV%) was calculated as an indicator of signal variability; Table 4.2 reports the statistics of fan rotational speed, Pitot and static pressure measurements.

Quantity	Mean CV%	Std. Dev of CV%
Fan rotational speed (RPM)	0.64	0.29
Pitot pressure measurements	3.19	0.89
Across−fan static pressure measurements	2.46	0.49

Table 4.2 Repeatability analysis of the fan–rig operating conditions based on the coefficient of variation (CV) of the measured quantities.

As shown in Table 4.2, the fan control system maintained stable operating conditions throughout the tests; steady-state conditions were isolated by discarding the initial and final transient samples. The remaining data were then characterized using the sample mean and standard deviation for each operating point. The reported power consumption refers exclusively to the ESC and motor assembly and does not include the power required by the remaining control system components. Sensor specifications are reported in the previous section, as the same instrumentation was employed for both the vehicle experiments and the fan characterization campaign. The comparatively low variability of the fan rotational speed indicates that the fan control system provided stable operating conditions throughout the experimental campaign. The larger variability observed in the aerodynamic quantities is therefore consistent with the unsteady behaviour of the generated flow field. Particular attention was also dedicated to avoiding operation within unstable surge conditions. Preliminary manual tests were therefore conducted to identify the minimum stable throttle opening for each fan configuration prior to the automated characterization procedure. Operating below this limit generated significant pressure oscillations and vibrations, potentially compromising both measurement repeatability and the mechanical integrity of the rig. Measurement uncertainty was evaluated following the GUM methodology by considering the uncertainty contributions associated with the measurement sensors, data acquisition system, and environmental conditions; additional details regarding the measurement-chain accuracy and uncertainty analysis are provided in the Appendix B.

4.3 Fan Characterization Data Analysis

Two different 40 mm ducted fans were characterized, each characterization cycle lasted approximately 3331 seconds, including stabilization, acquisition, and shutdown phases, as shown in Figure 4.5. For each target RPM, the throttle body was positioned at a predefined opening, and the system was allowed to stabilize for 5s before a 10s acquisition interval was recorded. The process was repeated for progressively lower throttle openings until the minimum stable operating condition was reached. The resulting fan pressure maps are reported in Figure 4.6. The plots show the relationship between mass flow rate and pressure rise for different rotational speeds.

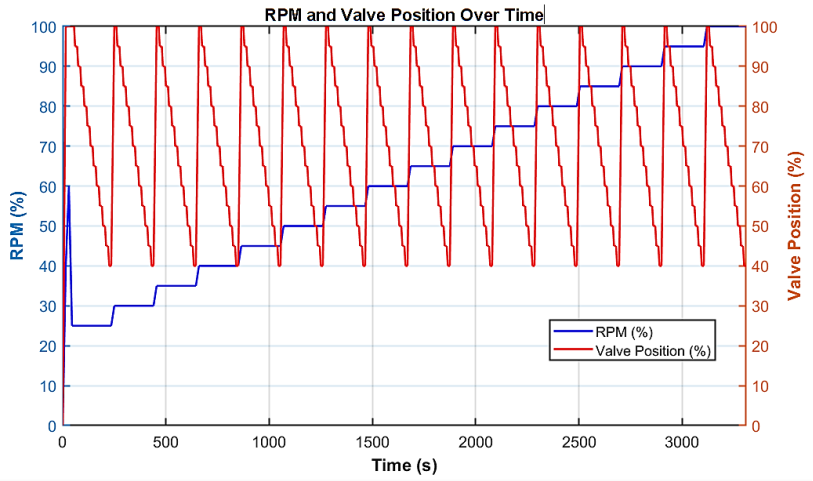

Figure 4.5 Test profile showing the commanded engine speed (blue) and cyclic valve position (red) over time. Engine speed was progressively increased from 25% to 100%, while the valve was continuously actuated between 40% and 100% opening.

Mass flow rate was preferred over volumetric flow rate in order to facilitate the subsequent integration of the fan maps into the CFD simulations. The XFLY fan exhibited a wider operating range and achieved higher pressure rise values at larger mass flow rates compared with the AEORC configuration. The maps also allow identification of the stable operating region and the proximity to surge conditions for each rotational speed. The efficiency maps presented in Figure 4.7 further confirm the improved performance of the XFLY fan. Across the investigated operating range, the XFLY configuration maintained significantly higher efficiency values, reaching almost 90% at the most favourable operating points. In contrast, the AEORC fan exhibited substantially lower efficiency levels throughout the characterization campaign.

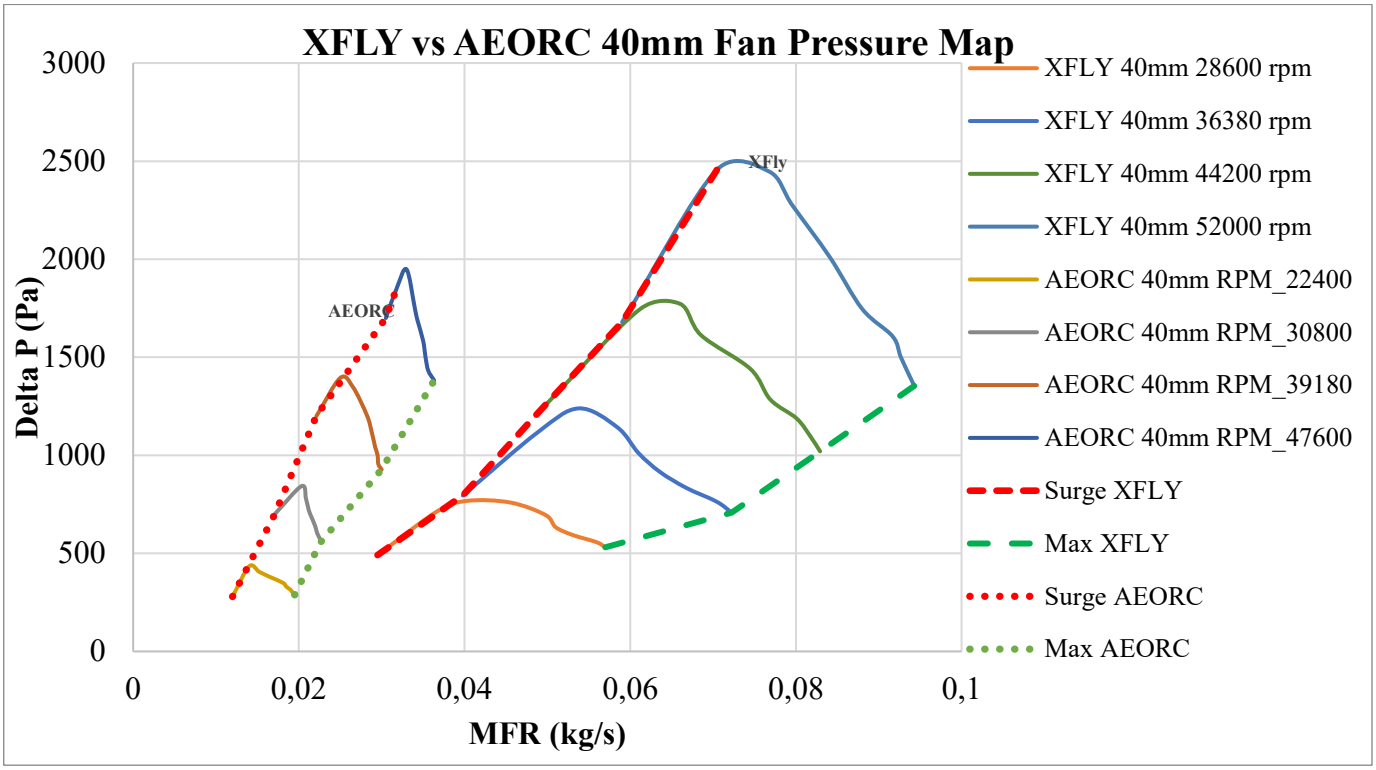

Figure 4.6 Experimentally measured pressure-rise versus mass-flow-rate characteristics of the investigated ducted fans. The curves were used to determine the operating conditions adopted in the CFD de-sign phase. The operating condition selected for the CFD simulations corresponds to the maximum XFLY fan-speed operating point (52k RPM).

The power-consumption maps shown in Figure 4.8 indicate comparable electrical power absorption between the two fan configurations under similar operating conditions; despite similar electrical input power, the XFLY fan generated higher pressure rise and mass flow rate, indicating a more effective conversion of electrical power into aerodynamic performance.

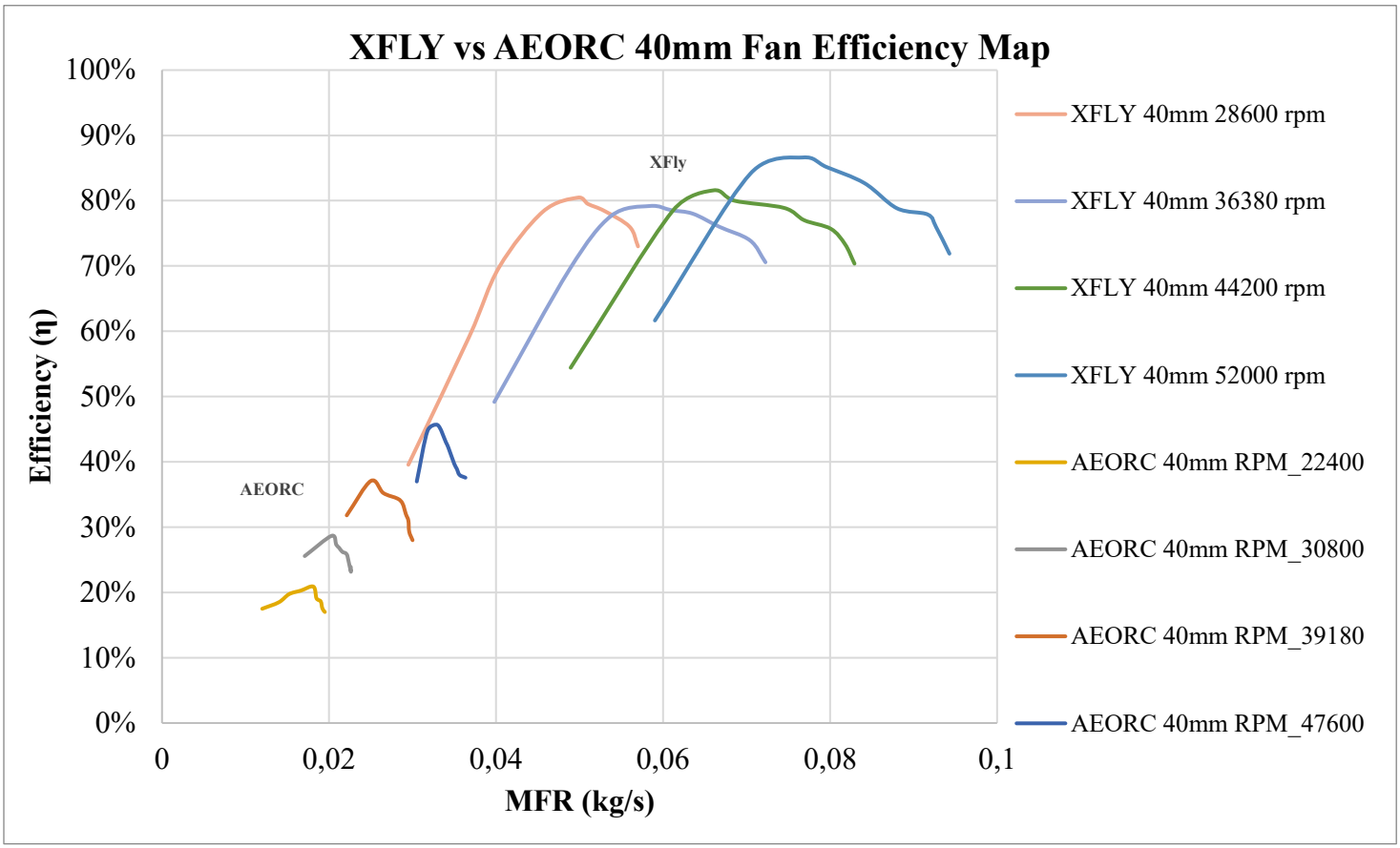

Figure 4.7 Comparison of the aerodynamic efficiency characteristics of the XFLY and AEORC 40 mm fans. Efficiency maps obtained from experimental characterization at multiple rotational speeds. The XFLY fan demonstrates significantly higher efficiency and a wider high-performance operating region, supporting its selection for the active aerodynamic system developed in this work.

During the final stages of testing, the AEORC fan exhibited increasing vibration levels at elevated rotational speed, eventually resulting in blade failure. The measurements affected by the failure were discarded and are not included in the reported performance maps. Therefore, the event did not influence the results presented in this work, although it prevented further testing. The fan characterization results high-lighted the strong sensitivity of the operating point to system resistance. This behaviour became a key consideration during the Co−Flow design process, since duct geometry, aerodynamic loading, and fan characteristics jointly determined the achievable mass flow rate and jet momentum coefficient under each operating condition.
The experimental campaign has shown that the XFLY 40 mm fan provided superior aerodynamic performance in terms of pressure rise capability, operating range, and efficiency.

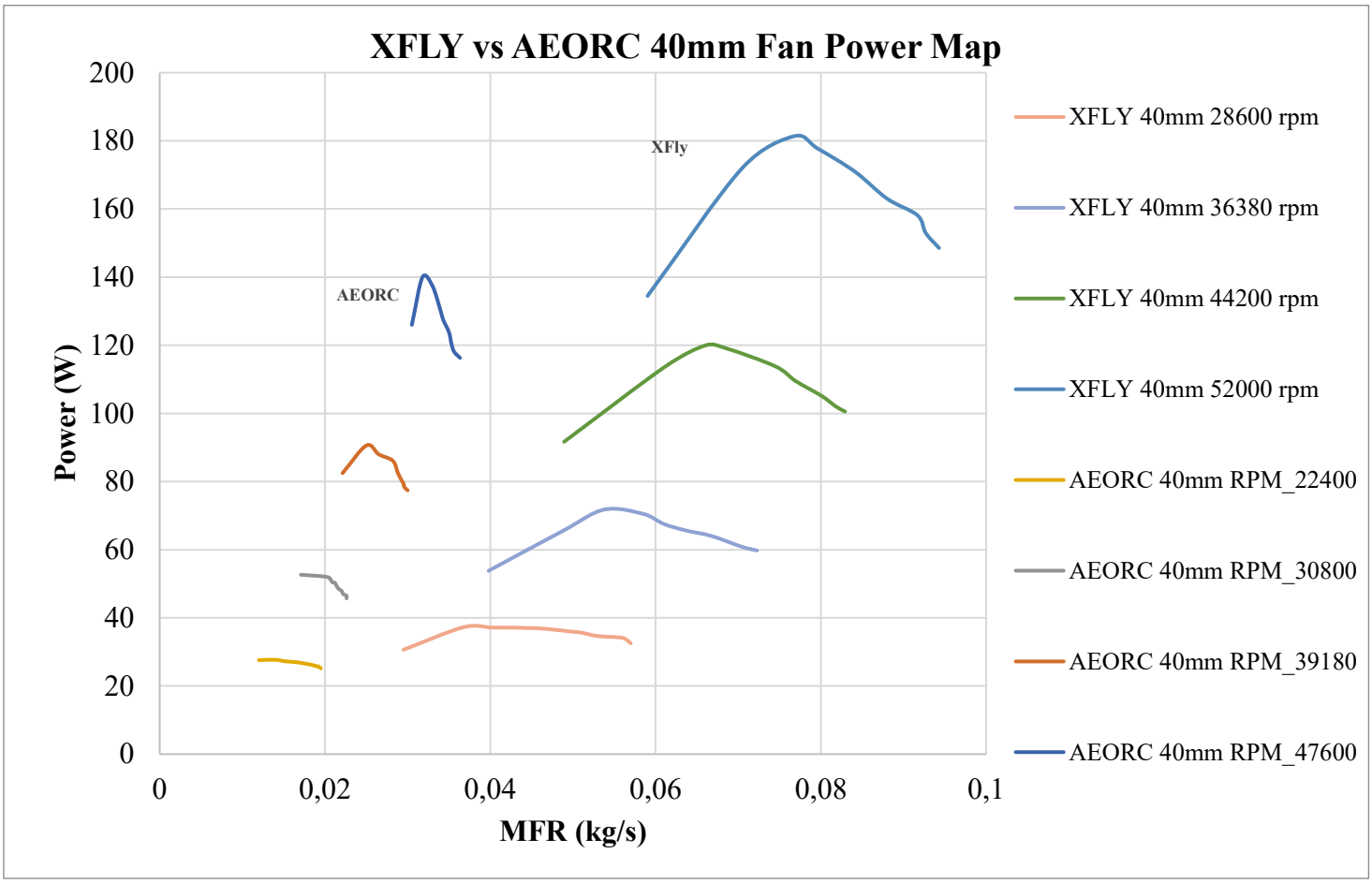

Figure 4.8 Comparison of the power consumption characteristics of the XFLY and AEORC 40 mm fans. Power maps obtained from experimental characterization at multiple rotational speeds, illustrating the operating envelope of each fan and enabling assessment of the efficiency–power trade-off relevant to active aerodynamic applications.

The experimentally derived fan maps will subsequently be integrated into the full-vehicle CFD model to evaluate the interaction between the ducted-fan system and the rear-wing aerodynamic behaviour, supporting the development and optimization of the Co-Flow configuration. A complete uncertainty assessment of the measurement chain was performed following the GUM methodology; detailed uncertainty budgets for the main measured quantities are reported in Appendix B.

Chapter 5 – Co−Flow CFD Performance Analysis

Following the validation of the baseline aerodynamic model, the rear wing was modified to integrate the Co−Flow Jet (CFJ) concept through the implementation of an embedded ducted axial fan. Since the rear−wing assembly and the Co−Flow Jet system constitute the aerodynamic components directly responsible for the investigated flow−control mechanism, the preliminary design effort focused on the aerodynamic response of this region while retaining the complete vehicle geometry to preserve realistic flow−field interactions and operating conditions. The system was designed to extract air from one region of the wing and re−inject it into another, thereby modifying the local flow field around the rear−wing assembly (Figure 5.1).

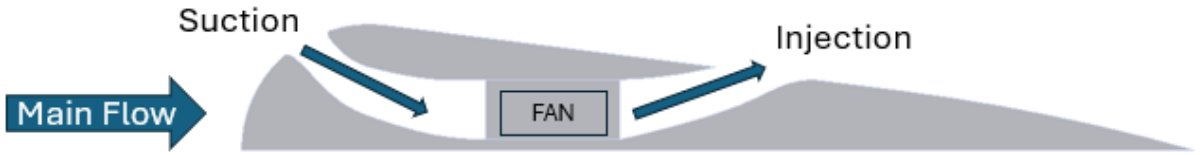

Figure 5.1 Schematic representation of the front−suction Co−Flow architecture with embedded ducted fan, suction slot, and injection slot.

Unlike most Co−Flow Jet investigations reported in the literature, where the airfoil geometry, slot locations, and internal flow−path architecture are specifically designed and optimized around the active flow−control concept [5,133–136], the present system was integrated into an existing production vehicle rear wing originally developed without consideration for Co−Flow actuation and already passed through various stages of optimization before being used for this research. While recent automotive studies have proposed the potential of active flow−control techniques for drag reduction and aerodynamic performance enhancement, most investigations remain focused on simplified geometries or generic vehicle models rather than production aerodynamic components [32,39,137]. Therefore, the present design was subject to practical constraints associated with the available internal volume, structural layout, packaging of the actuation system, and internal duct routing, which significantly limited the degree of aerodynamic optimization typically achievable in purpose-designed CFJ configurations. The available cavity inside the wing had to simultaneously accommodate the ducted axial fan, internal ducting, electronic speed controller, pressure instrumentation network, and structural mounting features while preserving the external aerodynamic profile of the wing. Consequently, the positioning of the suction and blowing slots could not be determined solely according to aerodynamic considerations. In particular, the slots could not be placed excessively close to the leading or trailing edges because of restrictions imposed by the internal duct layout. Instead, their location had to satisfy both aerodynamic objectives and the geometric, structural, manufacturability, and integration requirements dictated by the vehicle architecture. The

numerical setup adopted for both the simplified duct investigations and the final Co-Flow simulations was identical to the validated CFD framework previously presented for the baseline rear-wing configuration, including turbulence model, mesh strategy, wall treatment, and boundary conditions. This approach ensured methodological consistency between the baseline aerodynamic characterization and the subsequent comparative assessment of the investigated Co-Flow architectures. Particular attention was devoted to the aerodynamic interaction between the slot locations and the external pressure distribution over the wing profile. Regions near the leading edge are characterized by strong flow acceleration and low static pressure, making them particularly sensitive to both suction and blowing strategies. Front-suction configurations were initially considered advantageous from a packaging standpoint due to their relatively compact internal routing. However, the low-pressure conditions naturally present near the leading edge introduced significant inlet pressure losses, reducing the achievable mass flow rate through the system. Conversely, front-blowing configurations exploited the naturally accelerated flow developing along the suction side of the profile to improve boundary-layer energization and momentum injection effectiveness. Nevertheless, these configurations required more complex internal duct routing and imposed stricter geometric constraints on the positioning of the fan and downstream suction duct. Additional limitations were associated with the aerodynamic behaviour of the embedded duct system itself. Excessive duct curvature, abrupt area variations, and locally restricted sections generated additional pressure losses that directly influenced the operating point of the fan and the achievable actuation momentum. The design process therefore focused not only on maximizing aerodynamic effectiveness, but also on minimizing internal flow losses and maintaining acceptable energetic efficiency. To address these challenges, an iterative design process was adopted in which multiple duct layouts and slot arrangements were progressively evaluated through CFD simulations coupled with the experimentally characterized fan operating maps presented in Chapter 4. The CFD simulations were used to support the interpretation of the observed aerodynamic trends and to provide qualitative insight into the associated flow structures. Since no direct flow−field diagnostics such as particle image velocimetry (PIV), wake−rake surveys, or oil−film visualization were performed, the underlying flow mechanisms discussed throughout this section should be regarded as inferred from the combined experimental and numerical evidence rather than directly measured. Although the CFD simulations were conducted on the complete vehicle, the preliminary assessment of the Co−Flow concepts was based on the aerodynamic contribution of the rear−wing assembly only. The CFD−based development process was conducted in two consecutive stages. The first stage focused on the definition of the external Co−Flow architecture, including slot location, slot cross−sectional area, duct inclination, and suction/blowing arrangement. This phase comprised 797 full−vehicle simulations and was used to establish the geometric design guidelines for the Co−Flow system. Representative examples of the investigated geometries are reported in Figure 5.2. During this stage, the ducted fan was

not modelled explicitly. Instead, a uniform velocity boundary condition was imposed within the duct to generate a controlled mass flow rate through the system. The resulting flow was then allowed to develop naturally within the duct and interact with the external aerodynamic field, enabling the aerodynamic effectiveness of different suction and blowing arrangements to be assessed independently from the fan operating characteristics. The leading−edge and trailing−edge ducts were initially investigated separately un-der both suction and blowing conditions. Simulations were performed for imposed flow velocities ranging from 10 to 60 m/s, corresponding to different levels of momentum injection or extraction through the slots. As a result, the total number of simulations was determined not only by the number of investigated geometries but also by the extent of the operating conditions considered. In total, the CFD campaign comprised 885 full−vehicle simulations, 88 baseline cases, and 797 simulations performed using simplified duct configurations. This phase was intended to identify the most promising flow−control architectures and establish the design guidelines for fan−system integration. Each simulation required approximately 5 h of wall−clock time on the available high−performance computing infrastructure.

5.1 Front Suction Concept

A single construction line on the wing profile serves as the reference for all designs, with each duct using a curvilinear coordinate based on this line; in this way it was possible compare the different solutions; in figure 5.2, some examples of the position of the front slot

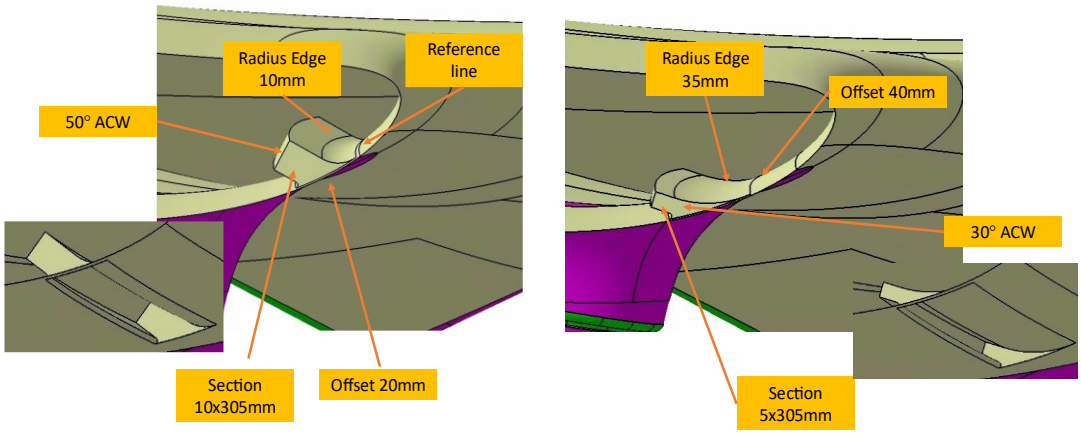

Figure 5.2 CAD models of the front slot designs considered for the front suction configuration, showing the main geometric dimensions and positioning parameters.

The preliminary assessment was intentionally conducted under highly loaded aerodynamic conditions, with the rear wing set at 100% deployment and the vehicle operating at the highest investigated speed (v4). Although additional simulations were performed at other wing deployment angles and vehicle speeds, the fully deployed configuration was selected as the primary screening condition because it represents the most demanding operating scenario in

terms of adverse pressure gradients and flow-separation tendency. Consequently, configurations demonstrating favourable behaviour under these conditions were expected to remain effective at less critical operating points. The results of the first sensitivity study on the front-suction configuration are presented in Figure 5.3, highlighting the influence of suction velocity on the aerodynamic response of the rear wing.

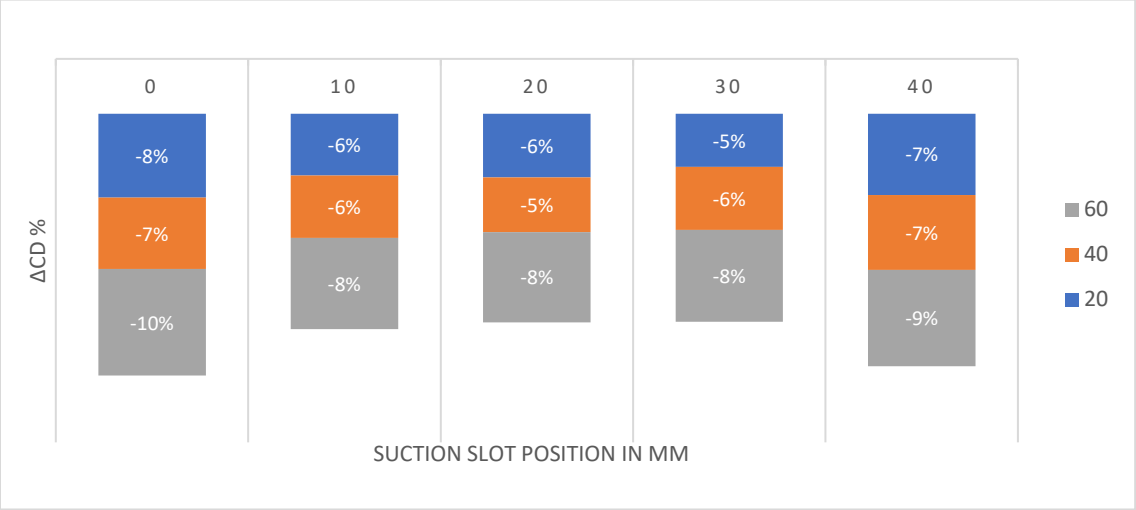

Figure 5.3 Comparison of the drag coefficient reduction (ΔC_d) obtained from CFD for different suction slot positions and suction flow velocities.

The ΔC_d has been calculate using the formula 5.1

$$\Delta C_d = \frac{C_{d,mod} - C_{d,baseline}}{C_{d,baseline}} \times 100 \quad (5.1)$$

where

$C_{d,mod}$ is the coefficient of drag of the modified flow with the ducts

$C_{d,baseline}$ is the coefficient of drag of the unmodified wing

The drag (or coefficient of it) reduction found at various front suction speed varies between 5 and 10%, best positions for slot installation seem to be or very close to the leading edge (as expected) or further back at 40mm mark. Considering that the level of wing drag reduction is similar at all slot's positions (±1%), next is to evaluate the effect on the of wing downforce (or coefficient of it) moving backward from the leading edge of the profile, as shown in Figure 5.4.

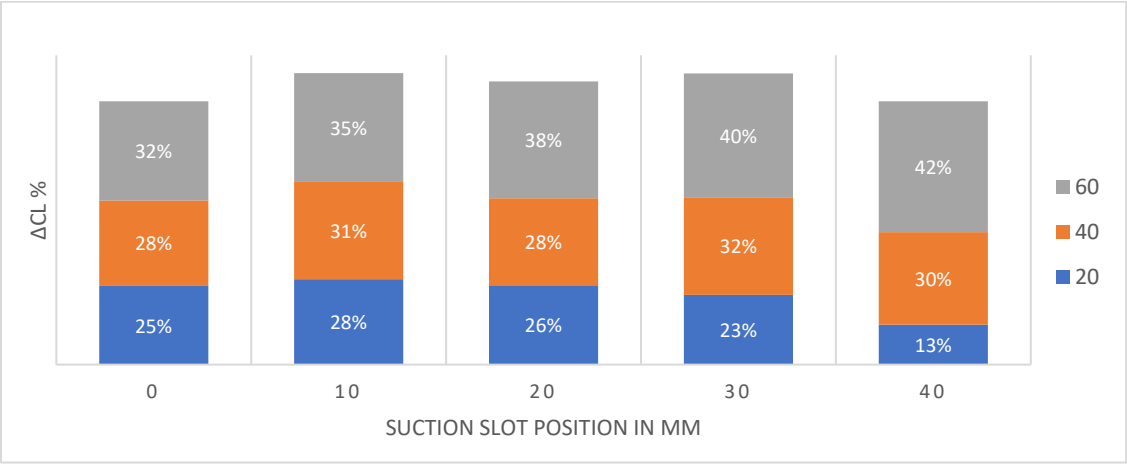

Figure 5.4 Comparison of the lift coefficient increase (ΔC_l) obtained from CFD for different suction slot positions and suction flow velocities.

The delta C_l has been calculated similarly to the C_d as per

$$\Delta C_l = \frac{C_{l,mod} - C_{l,baseline}}{C_{l,baseline}} \times 100 \tag{5.2}$$

where

$C_{l,mod}$ is the coefficient of lift of the modified flow with the ducts

$C_{l,baseline}$ is the coefficient of lift of the unmodified wing

A general increase in ΔC_l % is observed as the suction slot is shifted from the leading-edge position (0 mm) to approximately 30 mm, followed by a subsequent decline when the slot is placed further aft (40 mm). The peak lift enhancement occurs around the 30 mm position, where the overall lift reaches approximately a 95% increase compared to the reference case. This behaviour suggests that, in this configuration, the slot is located within a region where the boundary layer is sufficiently thick but still attached to the surface, allowing suction to effectively delay flow separation. Conversely, when the slot is positioned too close to the leading edge (0 mm), the extracted air is still highly energetic, and its influence on boundary layer stability is limited. Similarly, at the most rearward position (40 mm), suction occurs in a region where the flow is already partially separated, resulting in reduced system efficiency.
The observed increase in ΔC_d % with operating condition (from 20 to 60 m/s) further indicates that the suction system becomes more effective under more critical regimes, where the risk of flow separation is higher.

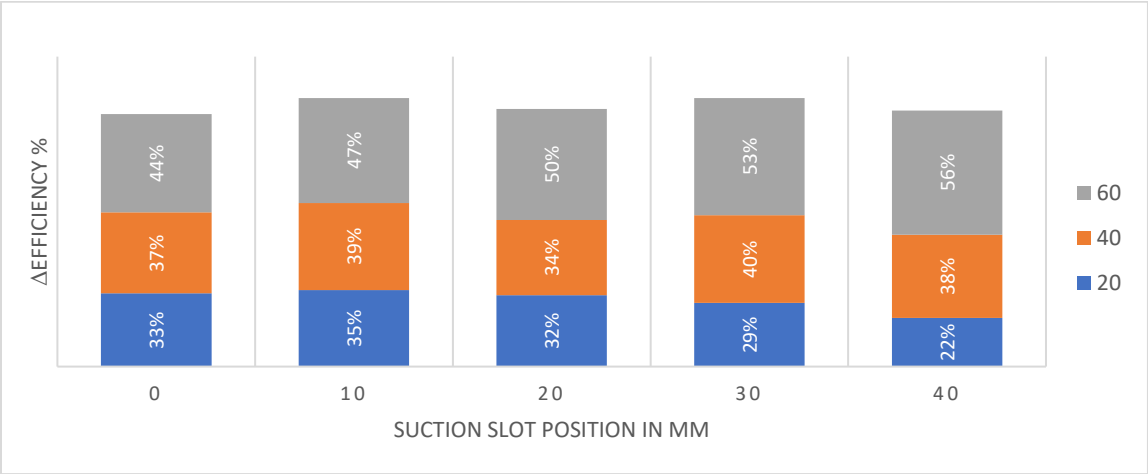

Figure 5.5 Comparison of the aerodynamic efficiency increase (ΔEfficiency) obtained from CFD for different suction slot positions and suction flow velocities.

The wing efficiency is defined as the ratio between the Lift and the Drag, or the C_l / C_d. The ΔE has been calculate using the formula 5.3

$$\Delta E = \frac{E_{mod} - E_{baseline}}{E_{baseline}} \times 100 \tag{5.3}$$

where

E_{mod} is the efficiency of the modified wing
$E_{baseline}$ is efficiency of the unmodified wing

An increase in efficiency (Figure 5.5) is observed with higher suction velocities, confirming that a greater extracted flow helps reduce viscous losses and maintain better flow attachment along the wing surface. Quantitative analysis highlights that overall, the most effective configuration occurs at a slot position of 30 mm, where the combination of location and suction intensity optimizes pressure distribution and boundary layer stability. For more rearward positions (e.g., 40 mm), efficiency tends to decline despite the high suction velocity, indicating that the system's effect is partially compromised by flow separation already occurring. After all this consideration, the suction slot was located at 30mm location.

5.2 Front Blowing Concept

Since just after the leading edge, a zone of low pressure is established, it worth verifying that blowing instead of suction would be preferable, to help the ducted fan in its job of blowing in lowest pressure region. For this reason, as per the suction in front, a blowing simplified rectangular duct has been designed and tested near the leading edge of the rear wing; same

construction line has been used to refer to the blowing duct position. In Figure 5.6 some examples of the position of the front slot for blowing purposes

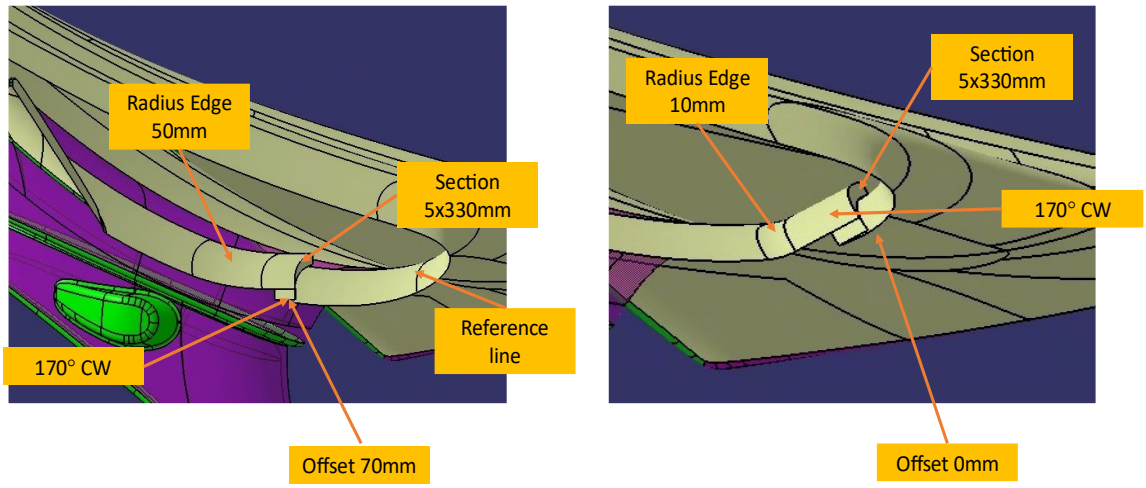

Figure 5.6 CAD models of the front slot designs considered for the front blowing configuration, showing the main geometric dimensions and positioning parameters.

Again, CFD sensitivity runs for drag evaluation have been executed and shown in Figure 5.7 Even though drag performances are close to the front suction setup, there are less CFD runs at front blowing due to the worst performance of downforce.

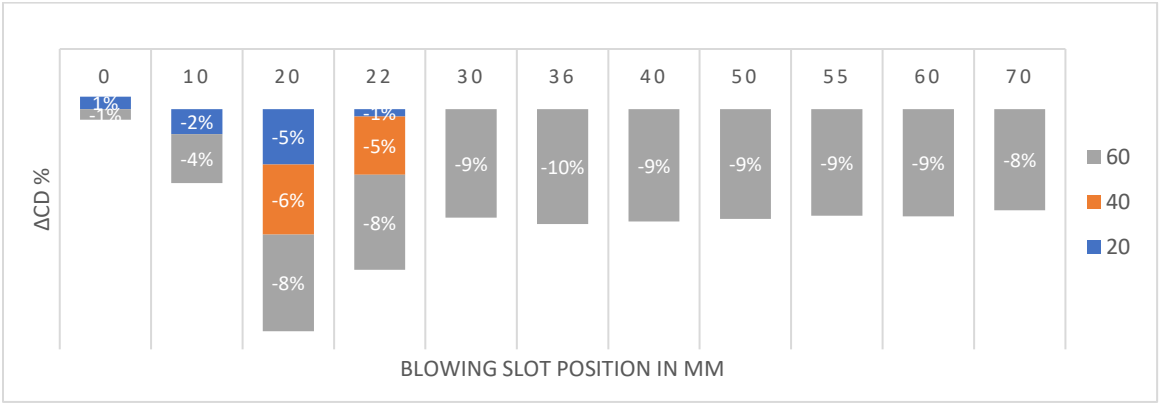

Figure 5.7 Comparison of the drag coefficient reduction (ΔC_d) obtained from CFD for different blowing slot positions and blowing flow velocities.

With the front blowing setup at 60m/s, it is possible to verify that the drag reduction is quite stable at around -9% ±1%; at 20 mm even lower blowing speeds generate an appreciable drag reduction that at 22mm starts to reduce for the lower speeds.

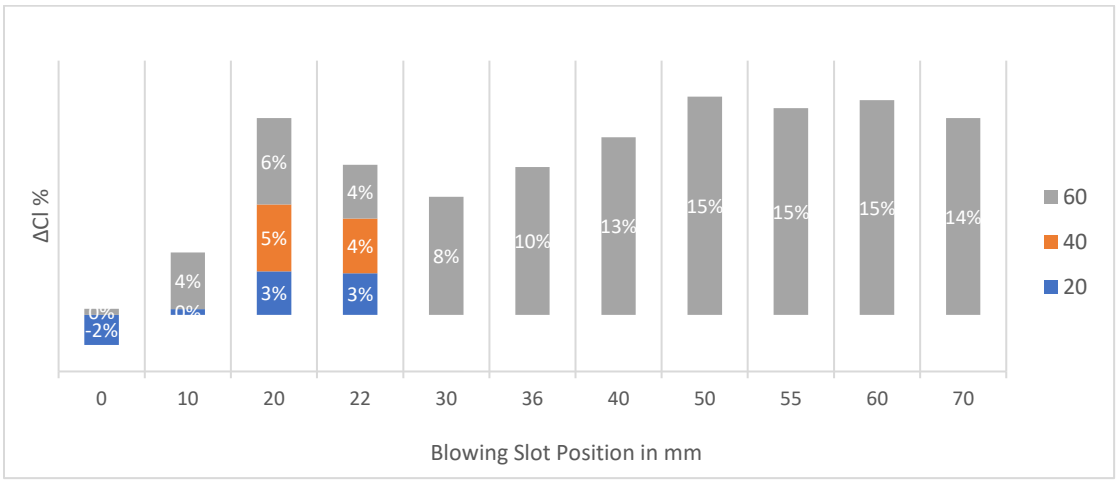

Figure 5.8 Comparison of the lift coefficient increase (ΔC_l) obtained from CFD for different blowing slot positions and blowing flow velocities.

From Figure 5.8, the application of blowing consistently leads to a notable increase in the lift coefficient compared to the baseline condition starting from the 10 mm position.
ΔC_l tends to grow with a small deep at 22mm backward until 50mm to remain stable around 15% increase, from the 30 mm position onwards, the effect of blowing speed appears to saturate or becomes less differentiated, as only the maximum value of blowing speed is reported. ΔC_l% shows a rising trend up to a 15% plateau achieved between 50 mm and 60 mm, with a slight decrease at 70 mm (14%). Even though drag performances are close to the front suction setup, as said previously, there are less CFD runs at front blowing due to the worst performance of the downforce; this technic seems, at this stage of research, not very promising to spending too many resources to investigate it in depth. However, the correct fully design ducts embedding the ducted fans are on the way and may the above consideration would be reviewed in the future.

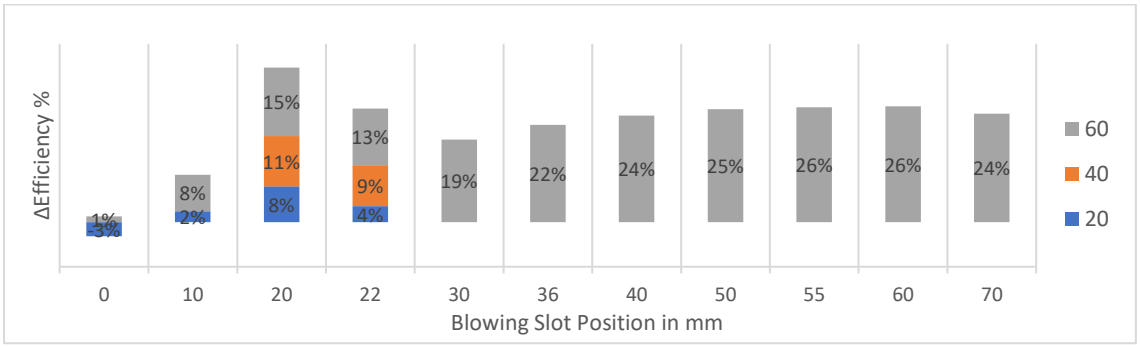

Figure 5.9 Comparison of the aerodynamic efficiency increase (ΔEfficiency) obtained from CFD for different blowing slot positions and blowing flow velocities.

Similar to ΔC_l, ΔEfficiency % also reaches a plateau for max blowing speed between 40 mm (24%) and 60 mm (26%), with a slight drop at 70 mm (24%); 50mm position decided to be used in the future front blowing setups based on the above considerations, interference between the duct and the wing skin and the limited internal wing volume (Figure 5.9).

5.3 Combined Front Suction and Rear Blowing Concepts

So far, the front slot options have been assessed, since they are expected to contribute most of the performance recovery, whether in suction or blowing configurations. However, the Co-Flow methodology is a zero-mass aerodynamic method, where the flow gets recirculated through ducts, so a rear duct was required to permit the excess flow from the front duct to be managed. First proposal was again a rectangular duct pointing backward for simplicity (limited by the volume available inside the wing and the future fan installation), combined with the best solution for front suction duct size and position. In Figure 5.10 some examples of the geometry of the rear slot for suction setup.

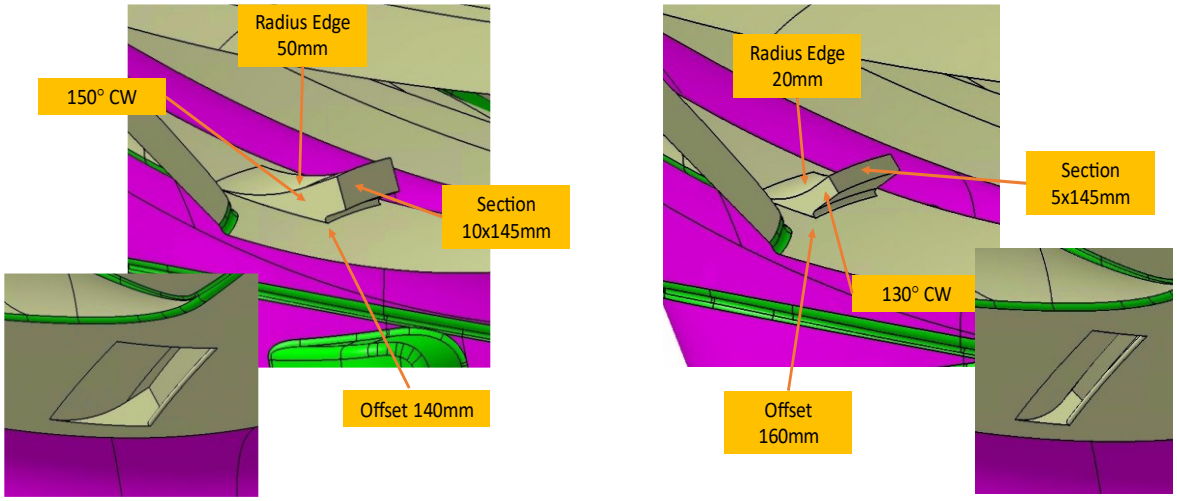

Figure 5.10 CAD models of the rear slot designs considered in this study, showing the main geometric dimensions and positioning parameters.

The only parameter that needed to be strictly maintained was the mass flow rate. Once the flow cross-section was defined, the flow velocity was adjusted accordingly to match the required mass flow rate supplied by the front duct. During this research stage, while the CFD simulations were being performed, a fan test rig was built to experimentally evaluate the actual performance of the laboratory ducted fans. The tests revealed that the fans were unable to achieve very high flow velocities, not exceeding 50 m/s at full throttle. Consequently, simulation cases were carried out at reduced Co-Flow velocities to investigate the aerodynamic behaviour under lower duct flow rates. In this configuration, the rear duct discharges the mass flow originating from the front duct, thereby injecting a blowing jet into the main flow stream directed toward the

wing's trailing edge. The chart in Figure 5.11 shows the variation of drag coefficient (ΔC_d %) with respect to the rear slot position. The 120 mm position offers a good combination of significant reduction (in total -12%) and stability across all tested intensities, safely avoiding the risk of catastrophic drag increase.

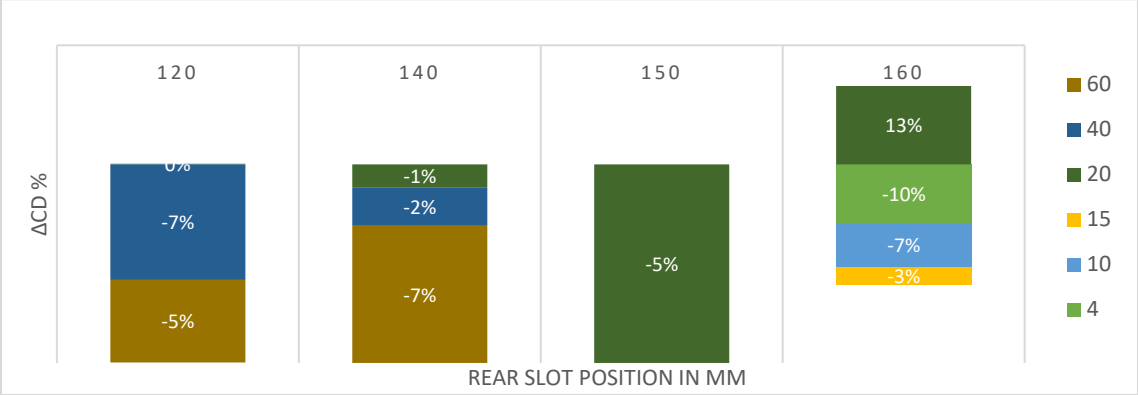

Figure 5.11 Comparison of the drag coefficient reduction (ΔC_d) obtained from CFD for different rear slot positions and suction flow velocities.

The 160 mm position is the one capable of effectively leveraging a wide range of suction flow speeds, but it is highly sensitive to the maximum flow speed with an increase of coefficient of drag of about 13%. However, to achieve maximum drag reduction with minimum required suction energy, the 160 mm position is the most promising, provided the flow control system is calibrated to ensure the suction intensity does not exceed the critical threshold for suction speed (somewhere between 40 and 60 m/s).

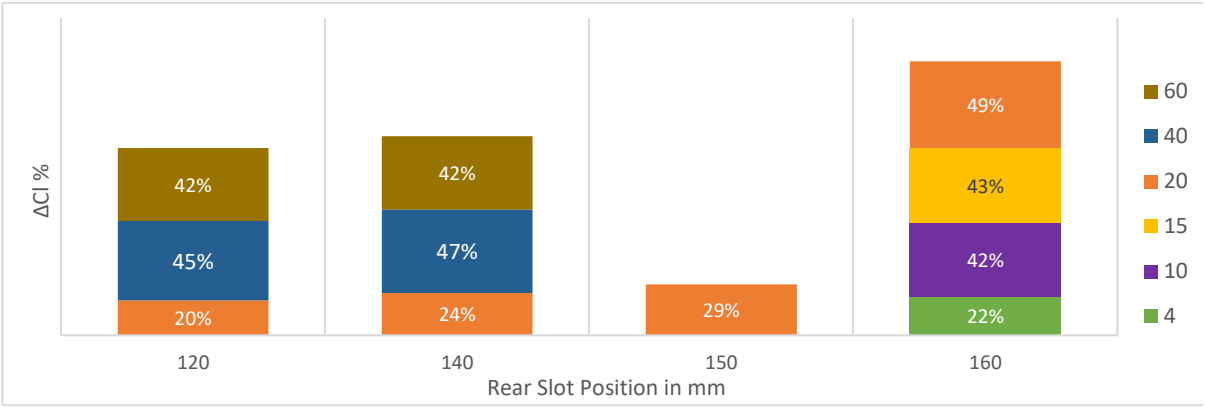

Figure 5.12 Comparison of the lift coefficient increase (ΔC_l) obtained from CFD for different rear slot positions and suction flow velocities.

The results in Figure 5.12 indicate a significant percentage increase in the lift coefficient (C_l) across all blowing slot locations; however, the improvement is neither linear nor uniform along

the chord. At higher front blowing velocities, C_l tends to increase as the blowing slot is positioned further downstream, as observed at the 120 mm and 140 mm locations. At 150 mm, data are available only for the 20 m/s condition, yet the corresponding C_l value already exceeds that of the preceding positions. This upward trend continues up to the 160 mm location, where the maximum C_l enhancement of approximately 49% is achieved. At this position, the lift coefficient is approximately 70% higher than at 150 mm under the same Co-Flow condition (20 m/s). Moreover, comparable C_l performance to that obtained at 120–140 mm can be achieved at significantly lower blowing velocities, indicating that the 160 mm location is particularly effective in enhancing lift. This suggests that, at this slot position, the blowing jet effectively energizes the boundary layer, promoting flow reattachment and consequently improving the aerodynamic performance of the wing.

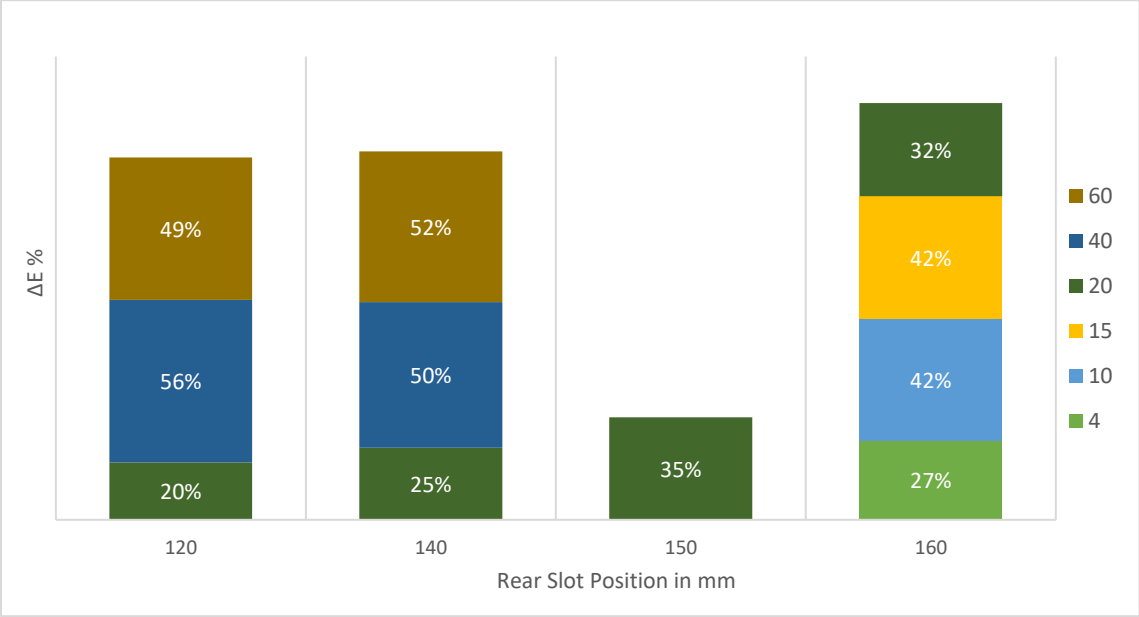

Figure 5.13 Comparison of the aerodynamic efficiency increase (ΔEfficiency) obtained from CFD for different rear slot positions and suction flow velocities.

Efficiency is a key factor in these configurations. The 120 mm and 140 mm positions perform well at higher Co-Flow velocities, improving efficiency by about 50%. At 20 m/s, the 150 mm location delivers the best result with an approximate 35% efficiency increase, and the 160 mm position performs similarly. Notably, the 160 mm setup maintains high efficiency even with lower duct mass flow, making it a strong balance between aerodynamic performance and integration feasibility, as it allows adequate space for the ducted fan and the rest of equipment within the wing (Figure 5.13). No CFD simulations were run using front blowing and rear suctioning because the complete design, introducing the ducted fan, was available for more representative simulations.

5.4 Final Co-Flow Design and CFD Performance Assessment

In the preceding paragraphs, various geometric configurations and flow scenarios were analysed to determine the optimal placement of the front and rear slots for integration within the rear wing. Following the preliminary duct investigation, the suction and blowing ducts were coupled through a 40 mm ducted fan operating in a front-suction configuration. The fan was represented within the CFD framework by means of a dedicated cylindrical volumetric region coupled with a momentum-source approach derived from the experimentally characterised fan map presented in Chapter 4 at maximum fan rotational speed. This methodology enabled the global pressure–mass flow behaviour of the actuation system to be reproduced while avoiding the computational cost associated with fully resolved rotating machinery simulations. Unlike blade-resolved CFD approaches, however, the adopted actuator-based representation does not explicitly resolve blade boundary layers, tip vortices, wake rotation (swirl), rotor-induced turbulent structures, or secondary-flow dissipation mechanisms. Consequently, part of the energy-transfer mechanisms associated with the physical rotor are inherently simplified within the numerical model. Similar actuator-based methodologies have been successfully applied by Akturk et al. [131], who suggested that simplified actuator-disk rotor models provide a computationally efficient and sufficiently accurate framework for preliminary design and parametric investigations, despite neglecting blade boundary layers, tip vortices, secondary-flow structures, and other rotor-related loss mechanisms. Their work showed that such simplified rotor representations are particularly well suited to highly iterative design and optimisation studies, where capturing the overall aerodynamic behaviour is of greater importance than resolving the detailed rotor flow physics. Consistent with these limitations, the present CFD model is expected to predict a more coherent and less dissipative jet structure than would occur in the physical ducted-fan system, as rotor-related losses and turbulent mixing mechanisms are only partially represented. Furthermore, the steady RANS formulation may not fully capture the unsteady mixing processes occurring immediately downstream of the injection slot. For these reasons, the present CFD framework should primarily be regarded as a comparative engineering tool for evaluating the relative aerodynamic influence of different Co-Flow architectures, identifying aerodynamic trends, and investigating flow-control mechanisms, rather than as an exact predictor of the detailed local flow field within the duct and injection region. The methodology is considered more reliable for identifying aerodynamic trends, relative performance variations, and flow-control mechanisms than for reproducing the detailed flow structures generated by the physical rotor. Three candidate fan positions in Figure 5.14) (D, E, and F) were evaluated using a performance index (*PI*) based on the aerodynamic response predicted by CFD. This second design phase comprised an additional 899 full−vehicle simulations and combined the assessment of fan location with the progressive refinement of the internal duct system. The analysis sought not only to identify the most favourable fan location,

but also to ensure compatibility between the predicted aerodynamic performance and the achievable operating conditions of the selected fan.

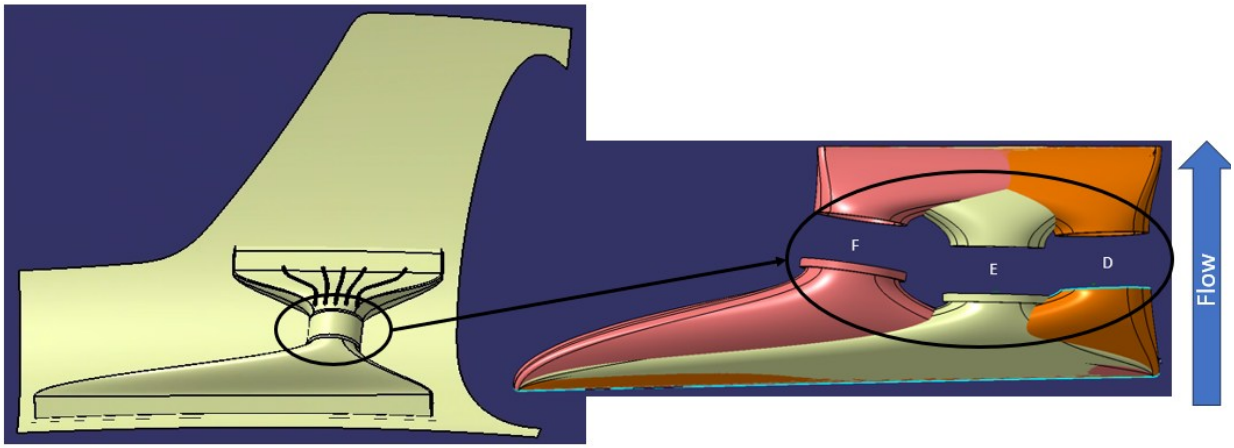

Figure 5.14 Selected position of the ducted axial fan inside the rear wing. The final location was determined through an iterative design process to balance aerodynamic performance with the packaging, structural, and manufacturability constraints associated with the available internal volume and duct routing.

All simulations were performed using the experimentally acquired fan map at maximum rotational speed to assess the upper−bound aerodynamic performance under highly loaded operating conditions. This approach allowed the effects of fan location, duct geometry, and operating conditions to be evaluated simultaneously while preserving realistic fan−performance constraints. Because drag reduction and downforce generation represent competing aerodynamic objectives, the *PI* was formulated as:

$$PI = -\Delta C_{d,wing} + \lambda \Delta C_{l,wing} \tag{5.4}$$

where λ represents the relative weighting between drag reduction and downforce increase. Three representative values (λ = 0, 0.5 and 1) were considered, corresponding respectively to a drag−driven assessment, an intermediate condition, and an equal weighting of drag and downforce contributions. The performance index is computed exclusively from CFD−predicted aerodynamic coefficients and is used as a screening metric to rank the investigated configurations. Experimental data are not directly included in the PI formulation; however, experimentally measured fan characteristics are incorporated into the CFD simulations to ensure realistic operating conditions. The performance index (PI) was introduced to rank the investigated Co−Flow configurations during the preliminary CFD screening process. Positive PI values indicate an aerodynamic improvement relative to the baseline configuration, whereas negative values indicate a deterioration. The aerodynamic variations used in the PI formulation are defined as:

$$\Delta C_{d,wing}[\%] = \frac{C_{d,CoFlow} - C_{d,Baseline}}{C_{d,Baseline}} \times 100 \quad (5.5)$$

$$\Delta C_{l,wing}[\%] = \frac{C_{l,CoFlow} - C_{l,Baseline}}{C_{l,Baseline}} \times 100 \quad (5.6)$$

The term $\Delta C_{d,wing}$ assigns a positive contribution to drag reduction, while the term $\lambda \Delta C_{l,wing}$ rewards configurations that increase aerodynamic loading. As a result, larger PI values identify more favourable configurations. Throughout this work, the lift coefficient is reported using the automotive sign convention, where positive C_l values represent downforce. Therefore, positive values of $\Delta C_{l,wing}$ correspond to an increase in aerodynamic loading. For each operating condition, all configurations were ranked according to their *PI* value, and the three best−performing solutions were identified. The occurrence frequency of each configuration within the top−three rankings was then evaluated and averaged across all operating conditions. The resulting occurrence statistics are reported in Figure 5.15. The ranking statistics indicate that the E−series configurations consistently appear among the highest−performing solutions for all investigated values of λ, demonstrating robustness with respect to the selected weighting factor. Their average occurrence within the top−three rankings is reported in Figure 5.16.

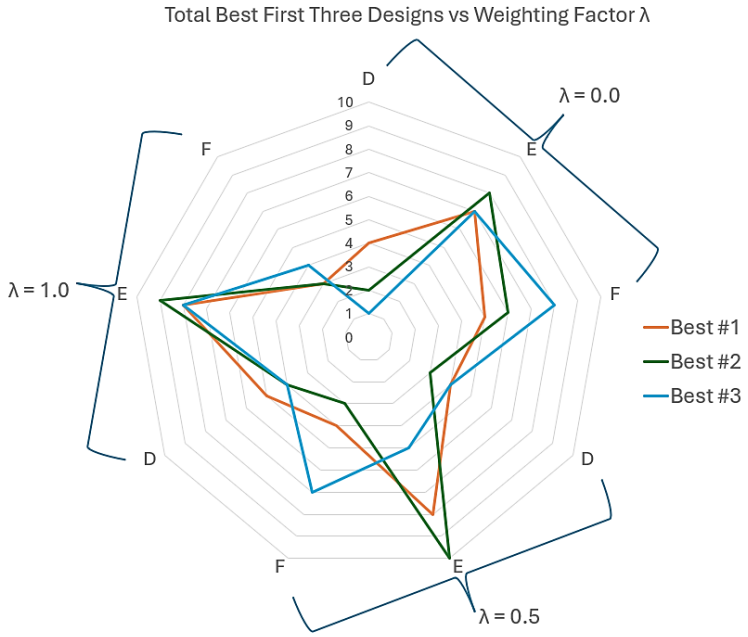

Figure 5.15 Occurrence frequency of the investigated Co−Flow configurations within the top−three rankings obtained from the performance−index analysis for different values of the weighting factor λ.

The performance−index analysis consistently identified the E−series configurations as the most effective solutions across the operating conditions investigated. Several configurations were

simulated across multiple wing−deployment conditions and vehicle speeds at the maximum mass flow rate permitted by the pressure differential across the Co−Flow ducts. Table 5.1 summarizes their geometrical details. Once the fan position was defined, several front-suction (FS) and front-blowing (FB) configurations were investigated. Suction located near the leading edge represents a particularly demanding operating condition due to the naturally occurring low-pressure region generated by flow acceleration over the wing profile. Conversely, the front-blowing configuration exploits this low-pressure region to enhance boundary-layer energization. Beyond the aerodynamic performance assessment, the integration of the experimentally characterized fan maps within the CFD framework enabled the evaluation of the actual operating point of the actuation system. This represents an important step compared with conventional Co-Flow studies, where the injected momentum is often prescribed without considering the physical limitations of the actuation device.

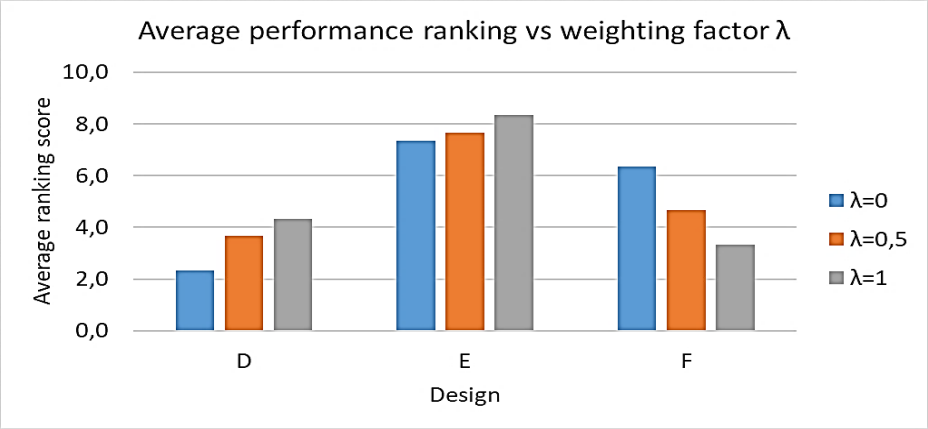

Figure 5.16 Average occurrence of each configuration within the top−three ranked solutions as a function of the weighting factor λ. For each operating condition, configurations were ranked according to the performance index (PI), and the occurrence frequency within the top three positions was evaluated.

A comprehensive simulation campaign was conducted across a range of wing deployment angles and vehicle speeds; the wing deployment was varied from 70% to 100%, while four representative vehicle speeds (v1–v4, with v1 < v2 < v3 < v4) were considered. By comparing the pressure rise and mass flow rate predicted by the CFD simulations with the experimentally measured fan characteristics, it was possible to verify whether the operating conditions imposed by the duct geometry were compatible with the achievable performance of the selected fan. Figure 5.17 presents the fan performance comparison in terms of static pressure rise across the ducted fan (ΔP) versus mass flow rate (MFR) for several front suction (FS) configurations, E3FS, E4FS, E5FS, and E6FS. The blue curve in each plot represents the experimental fan map obtained at maximum rotational speed (Max RPM), while the coloured CFD markers

correspond to the operating conditions reached in simulation at adimensional vehicle speeds and wing deployment percentage. The comparison revealed that several geometries identified as aerodynamically promising during the preliminary duct investigation could not be operated within the experimentally validated fan envelope (Table 5.1).

	Front Slot Dimensions		Rear Slot Dimensions	
Design	**a mm**	**b mm**	**a mm**	**b mm**
2FS	10	304	5	145
3FS	15	304	5	145
4FS	15	304	7	145
5FS	15	304	12	145
6FS	15	304	17	145

Table 5.1 Geometrical characteristics of the investigated Co−Flow configurations. The dimensions a and b define the front and rear slot cross−sections, from which the corresponding suction and blowing areas can be derived. The listed geometries were assessed during the CFD−based design screening prior to fan−system integration

The comparison between the CFD operating points and the experimentally measured fan characteristics reveals a clear influence of the duct geometry on the achievable operating conditions of the system (Figure 5.17). Through the progressive evolution from E3FS to E6FS, both the inlet and outlet sections were optimized to reduce flow losses and improve the aerodynamic coupling between the fan and the duct network. Configurations E3FS and E4FS are characterized by relatively low mass flow rates despite operating at pressure-rise levels comparable to those measured during fan characterization. This behaviour suggests that the combined aerodynamic resistance imposed by the duct system limits the achievable flow rate, shifting the operating point away from the experimentally characterized fan curve. A progressive improvement is observed for configurations E5FS and E6FS. The geometric modifications introduced in these layouts reduce the overall flow resistance of the system and allow higher mass flow rates to be established through the ducts. Consequently, the CFD operating points move closer to the experimentally measured fan characteristic, indicating a more realistic interaction between the fan and the aerodynamic system. The observed trend highlights the importance of considering the complete fan–duct assembly rather than the fan in isolation. Even when operating within a similar pressure-rise range, relatively small geometric modifications to the duct architecture can significantly alter the achievable mass flow rate and therefore the actual operating point of the actuation system.

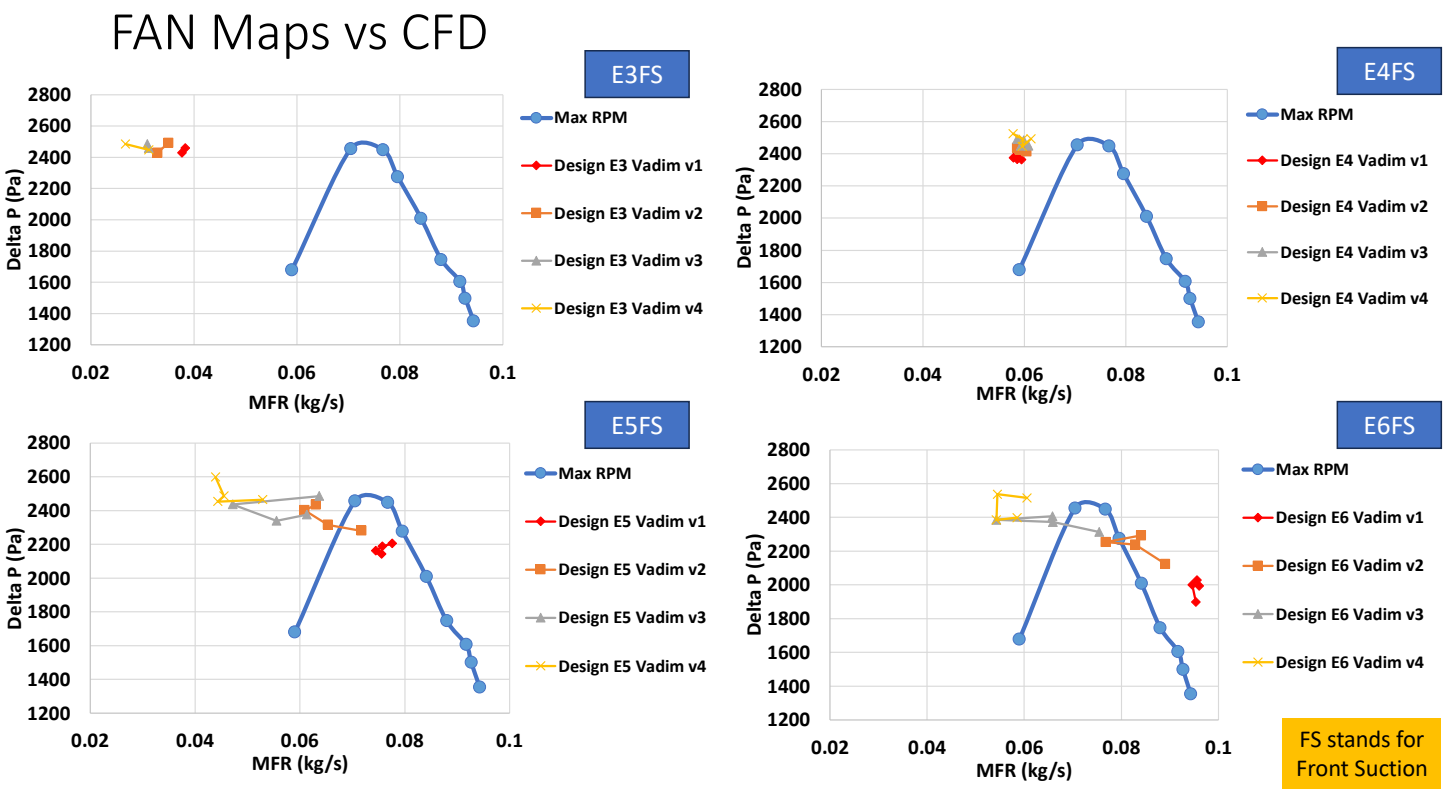

Figure 5.17 Comparison between the fan performance map at maximum rotational speed and the CFD-predicted operating points for the four investigated wing configurations (E3FS, E4FS, E5FS, and E6FS). Markers denote successive design iterations (v1–v4), illustrating the evolution of the predicted operating point toward the fan performance curve. FS denotes Front Suction

Among the investigated front-suction layouts, E6FS (Figure 5.18) has shown the best overall balance between aerodynamic performance and fan-operating feasibility.

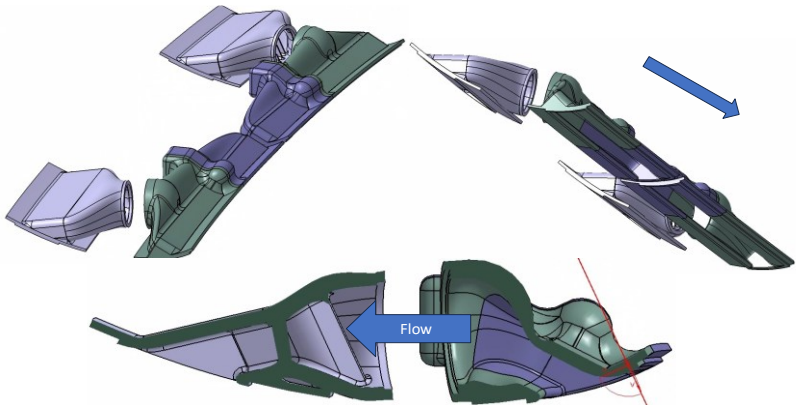

Figure 5.18 Exploded and sectional CAD views of the E6FS configuration, illustrating the internal duct layout, fan integration, and flow path. The design adopts a front suction–rear blowing configuration, with the airflow extracted through the leading-edge suction slot and discharged through the trailing-edge blowing slot.

For this reason, it was selected as the reference front-suction configuration for subsequent experimental implementation and vehicle testing, providing an opportunity to validate the numerical predictions under real operating conditions. Alongside front suction setups, a front blowing design integrated into a rear suction duct was developed to compare with the front suction proposal, aiming to minimize lamination inside the ducts and to advantage of the low-pressure bubble present close to the leading edge of the wing profile. The resulting front-blowing configurations retained the same fan integration concept previously adopted for the E-series layouts, while reversing the flow direction through the duct network, as illustrated in Figure 5.19.

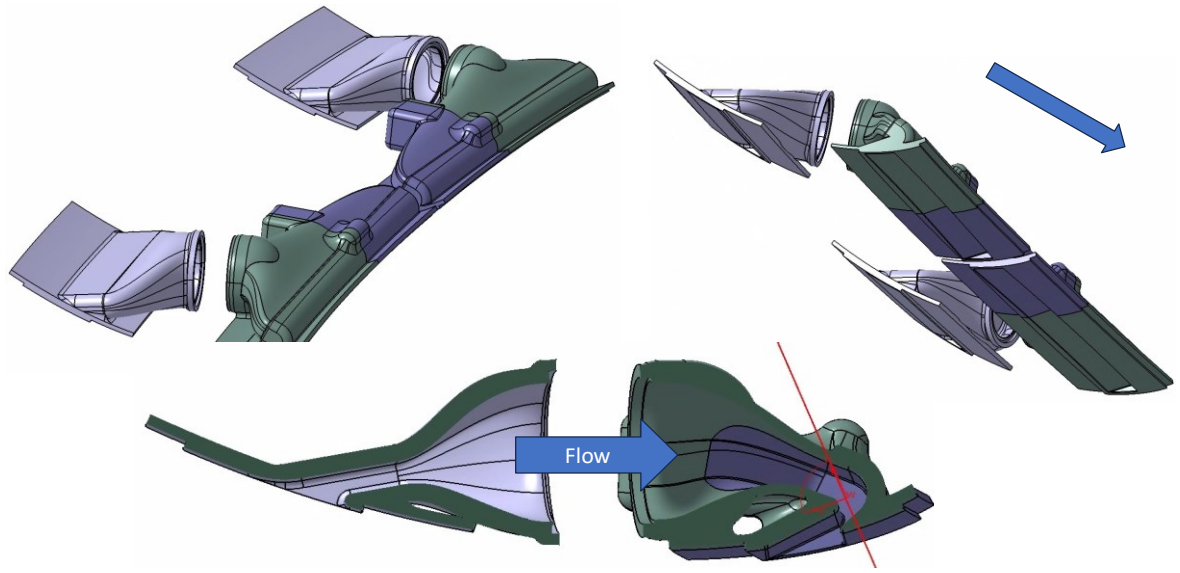

Figure 5.19 Exploded and sectional CAD views of the E8FB configuration, illustrating the internal duct layout, fan integration, and flow path. The design adopts a front blowing–rear suction configuration, with the airflow injected through the leading-edge blowing slot and extracted through the trailing-edge suction slot. The E9aFB configuration retains the same front duct layout as E8FB while incorporating an enlarged rear duct inlet section.

Figure 5.20 compares the CFD-predicted operating points for configurations E7FB, E8FB, and E9aFB with the experimentally characterized fan map. In contrast to the front-suction layouts presented previously, the front-blowing configurations exhibit substantially improved agreement with the fan characteristic curve.

	Front Slot Dimensions		Rear Slot Dimensions	
Design	**a mm**	**b mm**	**a mm**	**b mm**
7FB	4.72	304	12	145
8FB	4.72	304	7	145
9aFB	4.72	304	15	145

Table 5.2 Geometrical characteristics of the investigated Co–Flow configurations. The dimensions a and b define the front and rear slot cross–sections, from which the corresponding suction and blowing areas can be derived. The listed geometries were assessed during the CFD–based design screening prior to fan–system integration

For all three designs, the predicted operating points lie much closer to the experimentally measured fan envelope, indicating a more realistic coupling between the aerodynamic loading imposed by the duct system and the pressure–flow characteristics of the selected fan.

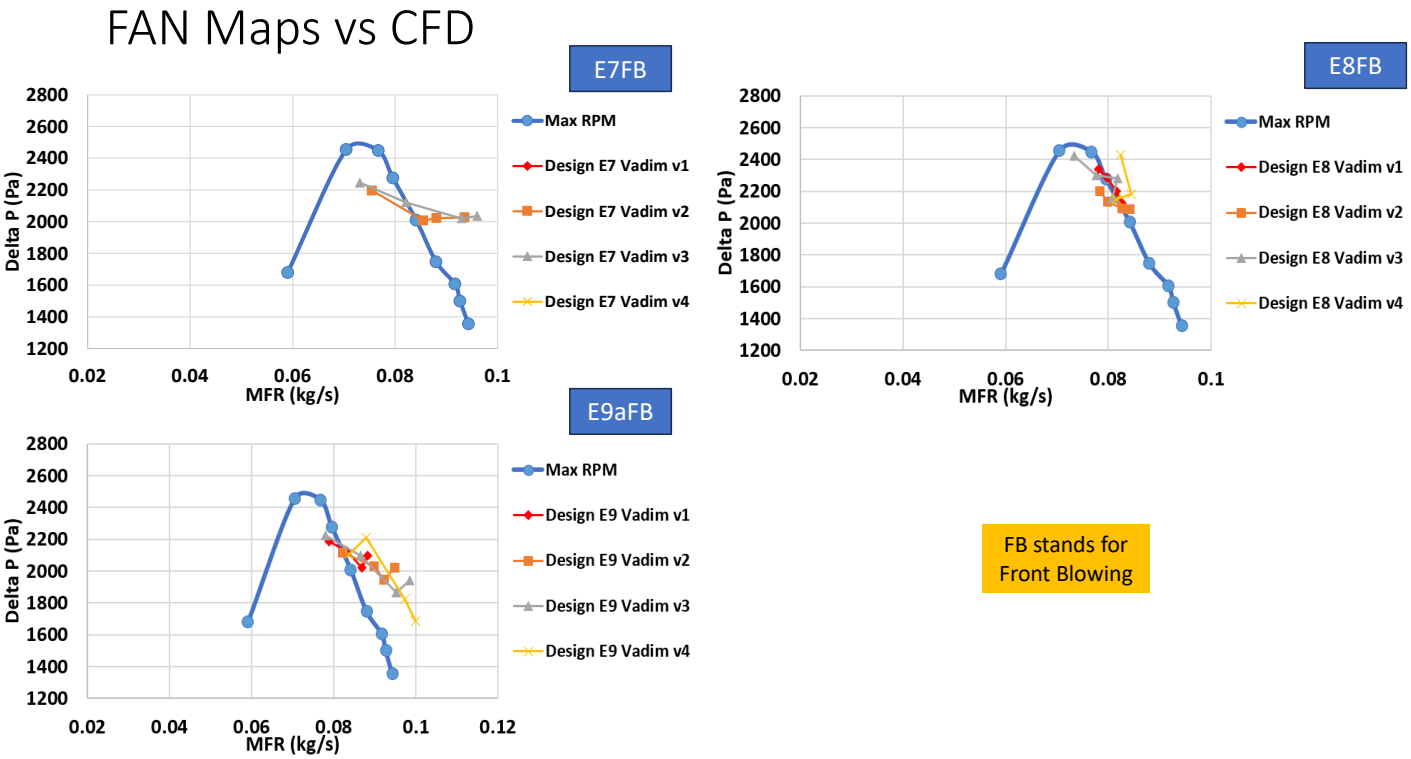

Figure 5.20 Comparison of CFD-predicted operating points with the experimentally characterized fan performance map at maximum fan speed for the E7FB, E8FB, and E9aFB configurations. Successive design iterations (v1–v4) show the refinement of the internal duct geometry, resulting in operating points that progressively approach the measured fan characteristic. FB indicates Front Blowing.

Among the investigated configurations, E8FB provides the closest overall agreement with the experimental fan characteristic over the range of vehicle speeds and wing deployment

conditions considered. The E9aFB configuration, which incorporates an enlarged suction section, enables higher mass flow rates through the system, although some operating points progressively depart from the optimum operating region of the fan map. The improvement is particularly evident in terms of the achievable mass flow rate. Whereas several front-suction configurations operated at flow rates well below those indicated by the experimental fan characteristic, the front-blowing layouts produce operating conditions that closely match the measured fan behaviour. These results show that the revised duct architecture provides a more effective fan–duct coupling, enabling the actuation system to operate under conditions that are consistent with the experimentally characterized fan performance. Based on these results, both configurations E8FB and E9aFB were selected for the subsequent aerodynamic assessment performed over the complete range of vehicle speeds and wing deployment conditions. Having verified the compatibility between the fan operating characteristics and the duct architecture, the aerodynamic mechanisms responsible for the observed performance differences were subsequently investigated through analysis of the flow field of the half vehicle model, in particular around the rear wing. The CFD assessment revealed substantial differences among the investigated configurations. Although all designs have modified the pressure and velocity fields relative to the baseline case, their aerodynamic response depended strongly on the interaction between the actuation system and the external flow.

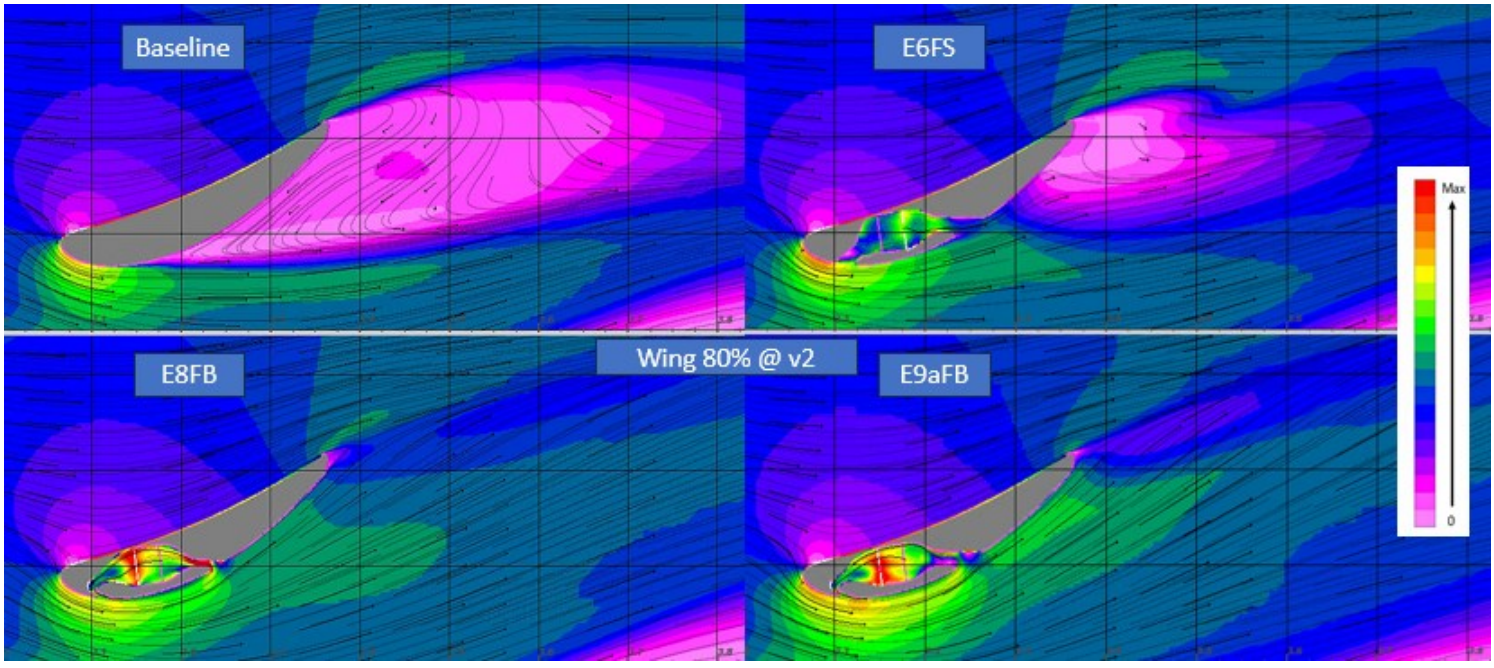

Figure 5.21 Comparison of the CFD-predicted velocity magnitude contours and streamlines around the rear wing for the baseline and the investigated Co-Flow configurations (E6FS, E8FB and E9aFB) at 80% rear-wing deployment with the fan operating at full speed and vehicle running at speed of v2.

Figure 5.21 to Figure 5.26 compare the pressure and streamline distributions for the baseline configuration and the three Co-Flow architectures at the representative operating condition corresponding to 80–100% wing deployment, vehicle speed v2, at maximum fan rotational speed. The pressure and streamline contours are shown on a cross-section passing through the fan mid-plane. The CFD results at 80% rear-wing deployment provide a comprehensive picture of the aerodynamic mechanisms associated with the different Co-Flow architectures. The velocity contours show that all active configurations modify the flow development over the suction surface with respect to the baseline, although through different mechanisms.

Among the investigated layouts, the E6FS configuration produces the most pronounced local interaction immediately downstream of the actuation device, where the suction system substantially alters the streamline topology. Conversely, the front-blowing configurations promote a smoother redistribution of the flow over the wing suction surface, with the injected momentum being progressively incorporated into the main flow rather than generating an intense local perturbation.

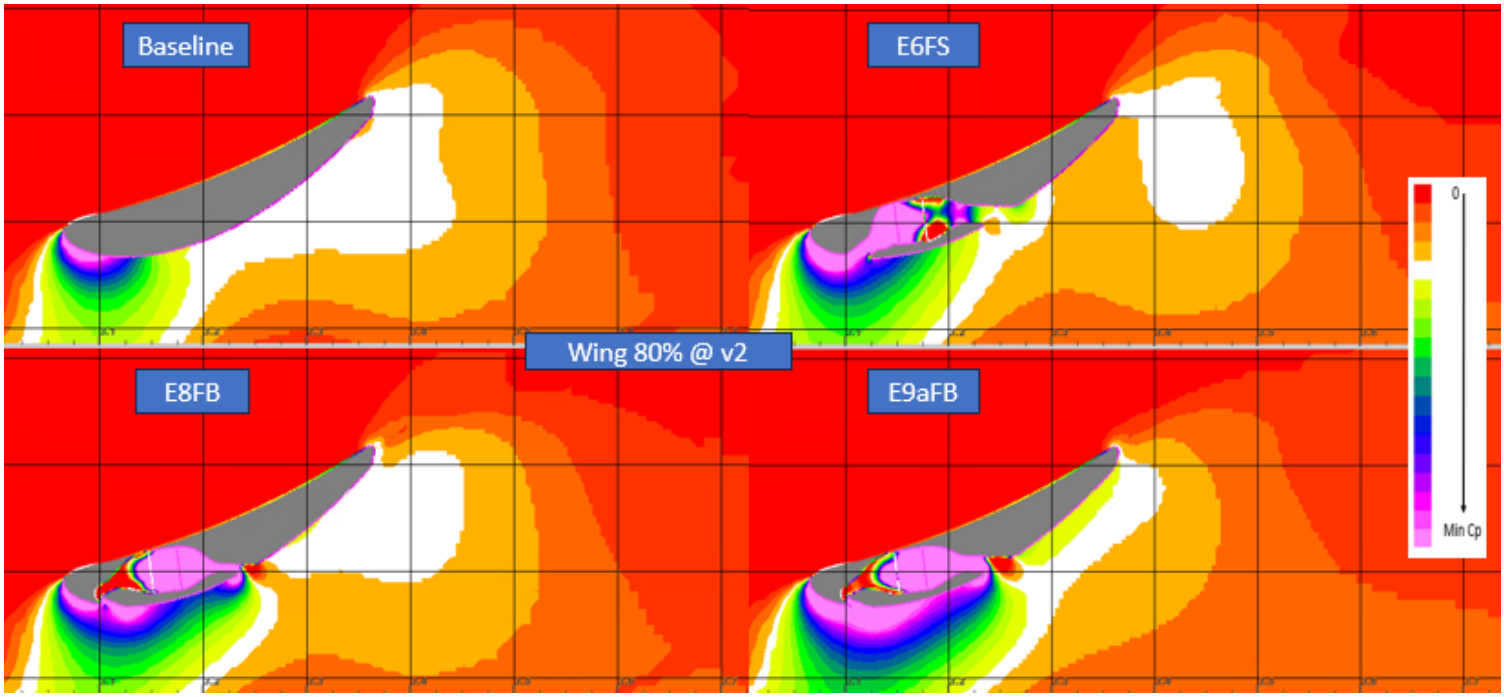

Figure 5.22 Comparison of the CFD-predicted pressure coefficient (C_P) distributions around the rear wing for the baseline and the investigated Co-Flow configurations (E6FS, E8FB and E9aFB) at 80% rear-wing deployment with the fan operating at full speed and vehicle running at speed of v2. Lower C_P values correspond to regions of increased suction.

This behaviour is further interpreted through the pressure coefficient, defined as

$$C_p = \frac{p - p_\infty}{\frac{1}{2}\rho_\infty V_\infty^2} \tag{5.7}$$

where $p\ [Pa]$ is the local static pressure, $p_\infty\ [Pa]$ is the freestream static pressure, $\rho_\infty\ [\frac{kg}{m^3}]$ is the freestream fluid density, and $V_\infty\ [\frac{m}{s}]$ is the freestream velocity. The pressure coefficient represents the local pressure difference relative to the freestream, normalized by the freestream dynamic pressure. Consequently, regions characterized by lower C_p values correspond to increased suction and generally contribute to higher aerodynamic loading on the wing. E6FS design produces a strong localized suction region close to the Co-Flow device, while E8FB and E9aFB promote a broader redistribution of the low-pressure region along the wing surface. Compared with the baseline configuration, E6FS generates a highly localized low-pressure region immediately downstream of the actuation device, whereas both E8FB and E9aFB produce a broader redistribution of the pressure field along the suction surface. Rather than intensifying the local suction, the front-blowing architectures extend the region of reduced pressure over a larger portion of the wing, indicating a more effective modification of the global pressure distribution.

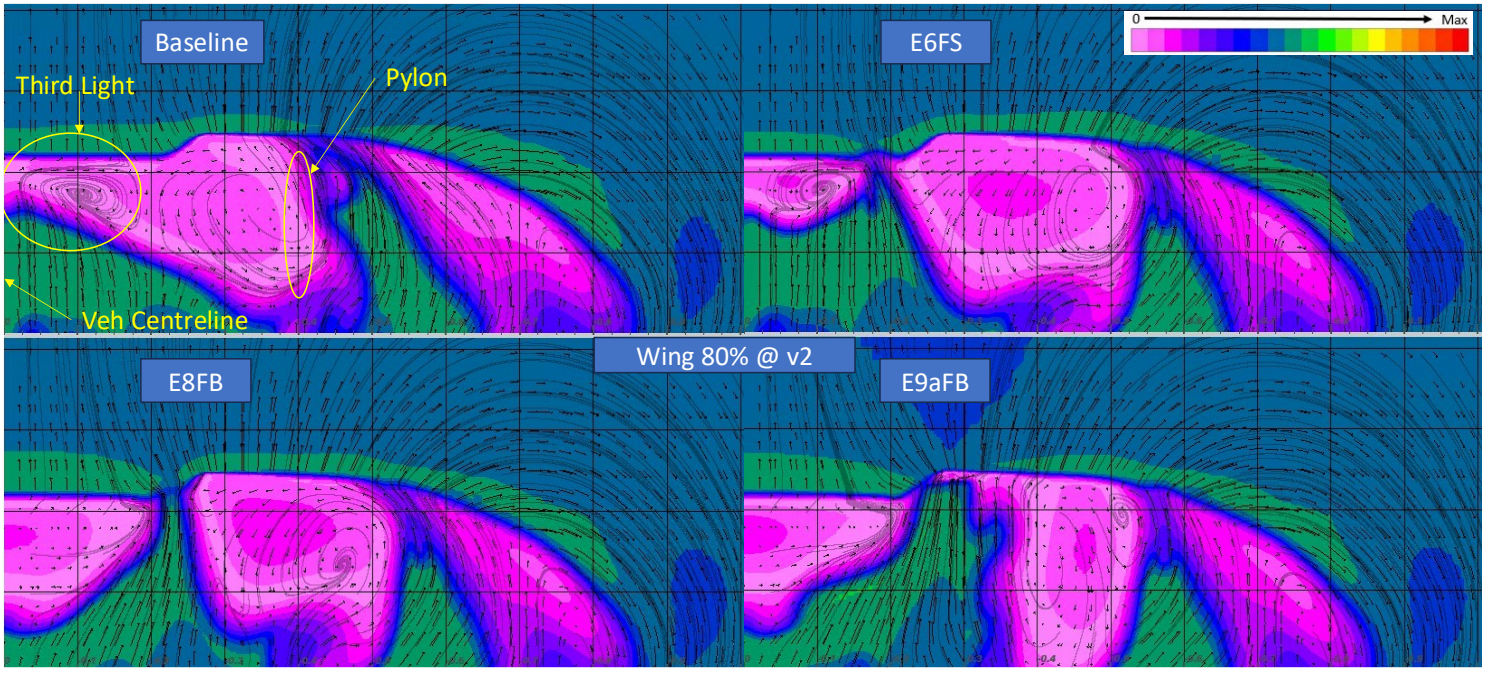

Figure 5.23 Cross-sectional CFD velocity magnitude contours and streamlines immediately downstream of the fully deployed rear wing (80% deployment at v2) for the baseline and the investigated Co-Flow configurations (E6FS, E8FB and E9aFB). The figure highlights the wake topology resulting from the interaction between the vortical structures generated by the geometric discontinuity associated with the third brake light integration, the wing pylons, and the wing-tip vortex

Although the pressure fields of E8FB and E9aFB are qualitatively similar, only E9aFB translates this pressure redistribution into an increase in aerodynamic loading, as confirmed by the CFD aerodynamic coefficients. Further insight is provided by the cross-sectional velocity

fields immediately downstream of the wing. As expected, the wake is characterized by several coherent vortical structures originating from the rear-wing geometry. A central recirculating structure develops downstream of the geometric discontinuity introduced by the integration of the third brake light, where the abrupt interruption of the wing profile forces the flow to separate. Additional vortical structures are generated by the wing pylons, while the outboard wake is dominated by the wing-tip vortex. The different Co-Flow layouts redistribute the interaction between these structures. The E6FS configuration appears to reduce the apparent extent of the recirculating region associated with the third brake light while increasing the apparent size of the pylon-induced recirculation. Conversely, both front-blowing configurations exhibit a different wake organization, characterized by a more developed central recirculating structure and a less dominant pylon-associated wake. These observations indicate that the Co-Flow architecture redistributes the flow between the principal wake structures rather than simply suppressing individual vortices, thereby modifying the three-dimensional wake topology immediately downstream of the rear wing.

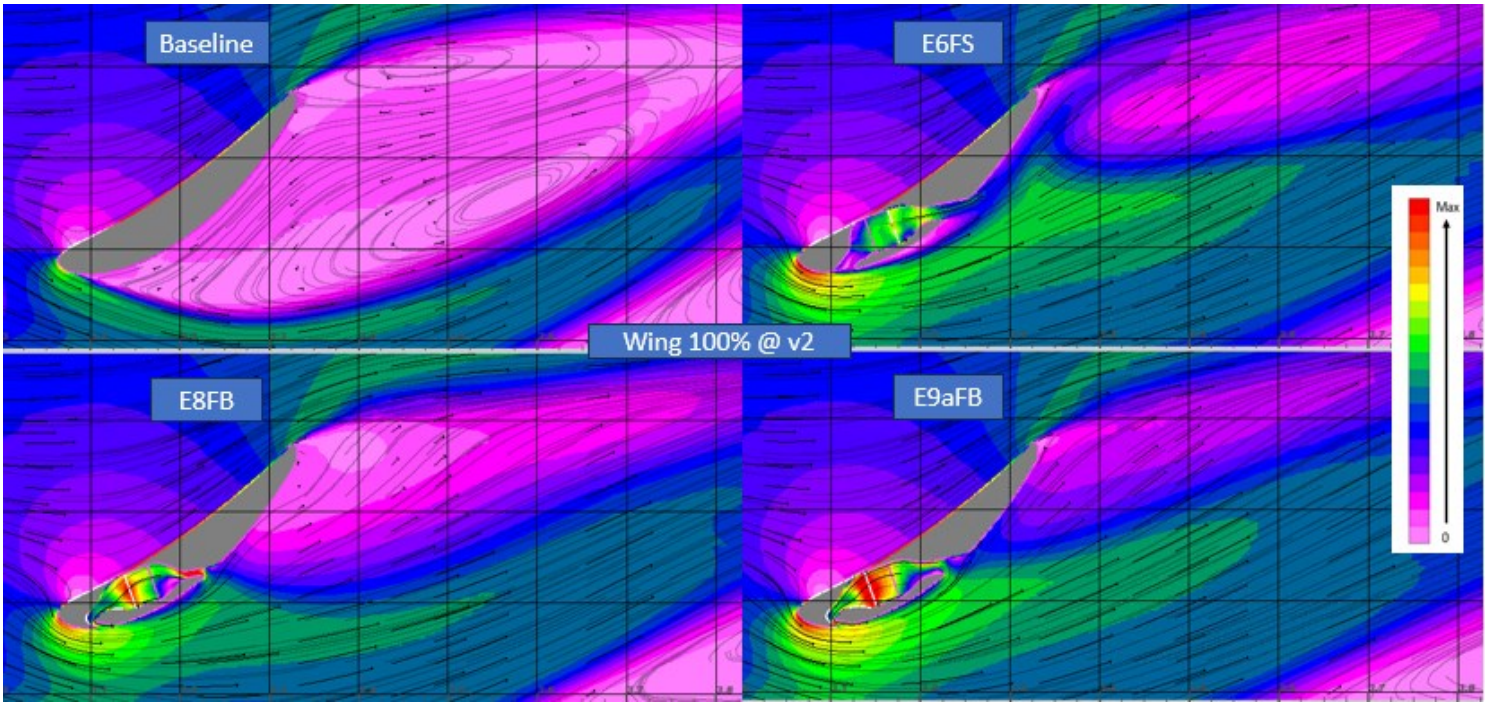

Figure 5.24 Comparison of the CFD-predicted velocity magnitude contours and streamlines around the rear wing for the baseline and the investigated Co-Flow configurations (E6FS, E8FB and E9aFB) at 80% rear-wing deployment with the fan operating at full speed and vehicle running at speed of v2.

The aerodynamic coefficients complement the qualitative observations obtained from the CFD flow visualizations. Although the E6FS configuration substantially modifies the velocity field, the pressure distribution, and the wake topology relative to the baseline, these changes translate

into an increase in wing drag ($\Delta C_{d,wing}$= +1.7%) and a slight reduction in aerodynamic loading ($\Delta C_{l,wing}$= −1.0%). Conversely, both front-blowing configurations reduce the wing drag, achieving $\Delta C_{d,wing}$ = −2.4% for E8FB and $\Delta C_{d,wing}$ = −2.2% for E9aFB. However, only E9aFB is associated with an increase in aerodynamic loading, with $\Delta C_{l,wing}$ = +6.0%, whereas E8FB still exhibits a reduction in lift ($\Delta C_{l,wing}$ −3.8%). Taken together, these results suggest that the aerodynamic effectiveness of the Co-Flow system depends not only on modifying the flow field, but also on how the specific actuation architecture redistributes momentum and pressure over the wing surface. The CFD results obtained with the rear wing fully deployed (100% deployment) reveal a substantially different aerodynamic response compared with the 80% deployment condition. The velocity contours indicate that all three Co-Flow configurations modify the flow development over the wing suction surface relative to the baseline, producing distinct velocity distributions over the flap while preserving the overall flow topology.

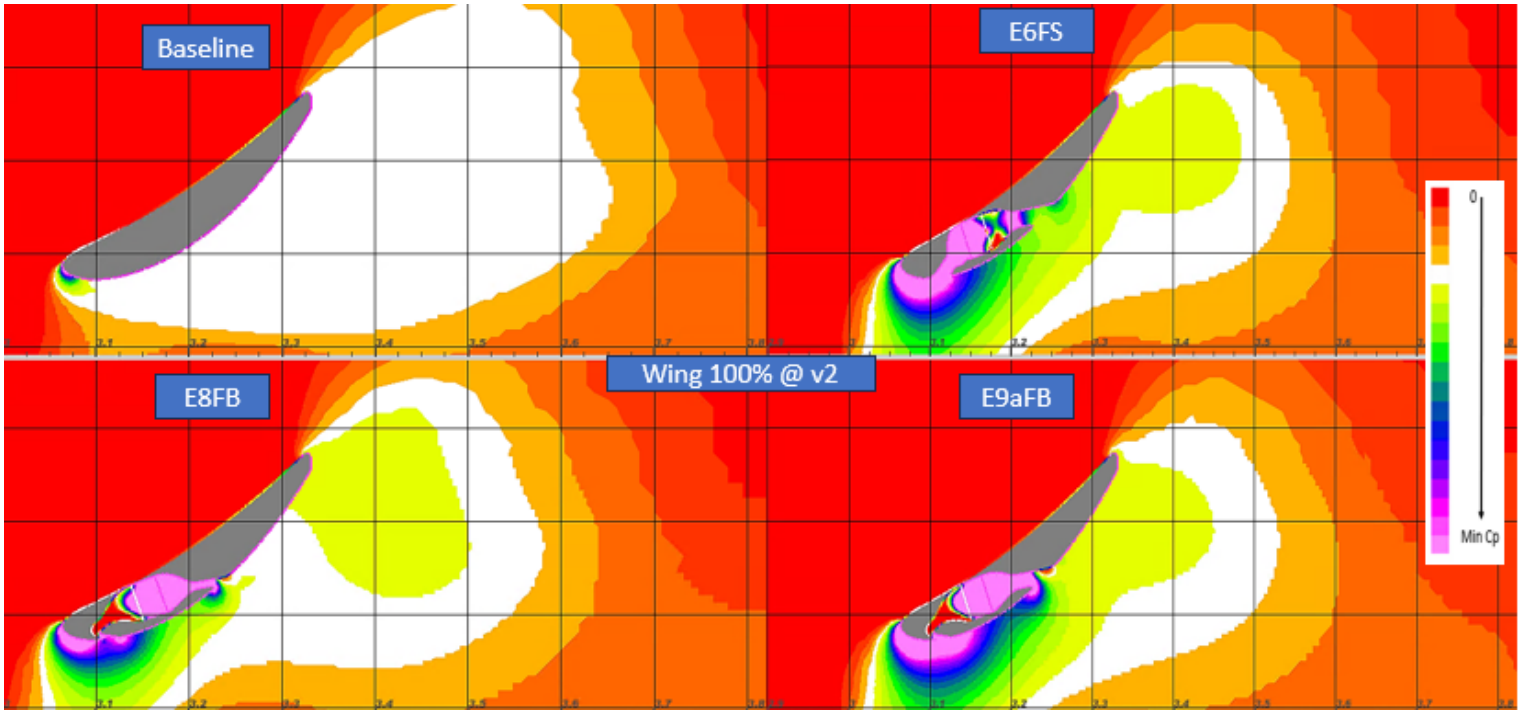

Figure 5.25 Comparison of the CFD-predicted pressure coefficient (C_P) distributions around the rear wing for the baseline and the three Co-Flow configurations (E6FS, E8FB and E9aFB) at 80% wing deployment at vehicle speed v2 (fan speed = 100%).

Compared with the 80% deployment condition, the influence of the Co-Flow system extends over a larger portion of the suction surface, indicating that the fully deployed wing provides a flow environment in which the actuation more effectively alters the near-wall flow development. The corresponding pressure coefficient distributions further support this

behaviour. The fully deployed configuration exhibits a more extensive redistribution of the low-pressure region for all three layouts compared to the 80% deployment case. The cross-sectional velocity fields immediately downstream of the wing further illustrate the influence of the Co-Flow layouts on the wake development. As in the previous operating condition, the wake is characterized by the interaction between the recirculating structure generated by the geometric discontinuity associated with the third brake light, the pylon-induced wake, and the wing-tip vortex. Although the dominant wake structures remain present in all configurations, their relative organization changes according to the selected Co-Flow architecture. Compared with the baseline configuration, all three Co-Flow architectures modify the wake generated by the geometric discontinuity associated with the third brake light. The E6FS configuration reduces the apparent extent of this central wake region while simultaneously producing a more pronounced modification of the flow in the vicinity of the wing pylon.

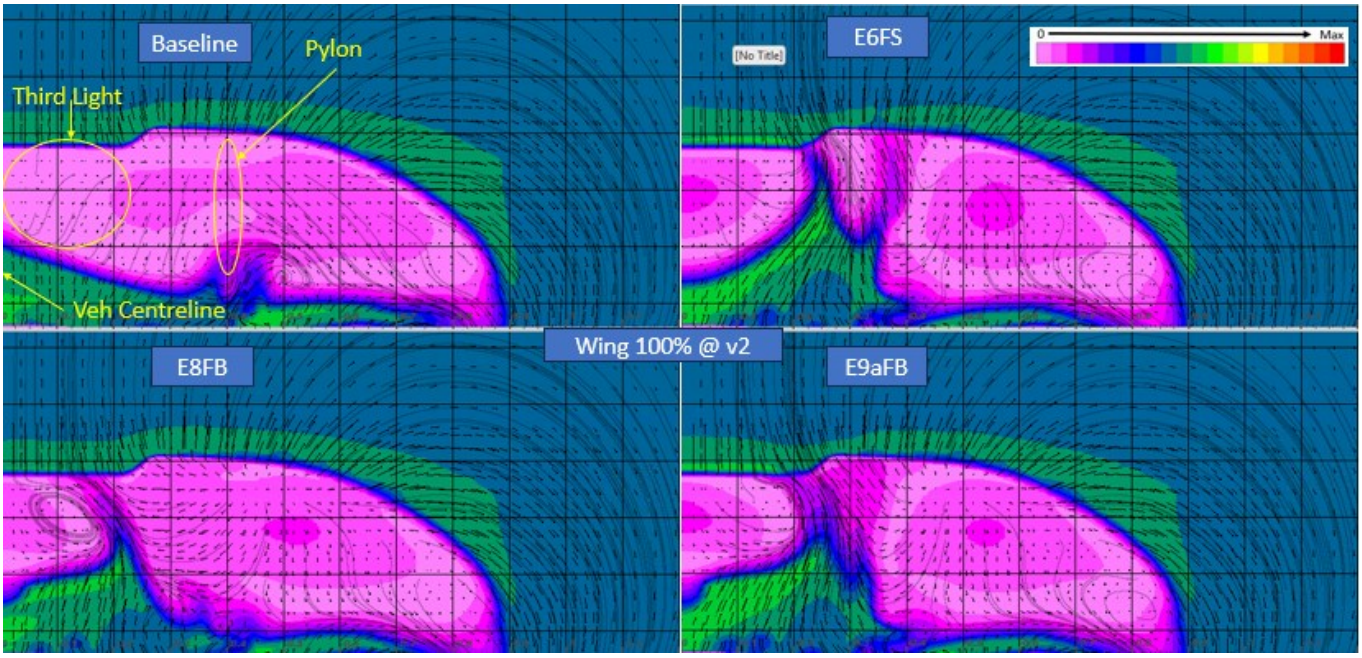

Figure 5.26 Cross-sectional CFD velocity magnitude contours and streamlines immediately downstream of the fully deployed rear wing (100% deployment at v2) for the baseline and the investigated Co-Flow configurations (E6FS, E8FB and E9aFB). The figure highlights the wake topology resulting from the interaction between the vortical structures generated by the geometric discontinuity associated with the third brake light integration, the wing pylons, and the wing-tip vortices

In contrast, the front-blowing layouts (E8FB and E9aFB) appear more effective in reducing the wake associated with the third brake light, while their influence on the pylon-induced flow remains comparatively smaller. In all configurations, the wing-tip vortex remains qualitatively unchanged, indicating that the Co-Flow system primarily affects the central portion of the wake while leaving the outer wake structures substantially unaltered. These observations suggest that

the Co-Flow architecture primarily alters the interaction between the dominant wake structures rather than suppressing individual vortices. The aerodynamic coefficients are consistent with these qualitative observations. Unlike the 80% deployment condition, all investigated configurations increase the wing aerodynamic loading relative to the baseline. The E6FS configuration achieves $\Delta C_{l,wing}$ = +23.6% while producing only a modest drag reduction ($\Delta C_{d,wing}$ = −1.0%). Both front-blowing layouts provide substantially larger drag reductions, with $\Delta C_{d,wing}$ = −8.9% for E8FB and $\Delta C_{d,wing}$ = −8.8% for E9aFB. Although the drag reductions are nearly identical, E9aFB delivers the largest increase in aerodynamic loading ($\Delta C_{l,wing}$ = +27.6%), outperforming both E8FB ($\Delta C_{l,wing}$ = +12.8%) and E6FS. To assess whether the aerodynamic behaviour observed at vehicle speed v2 is maintained under different operating conditions, the same CFD analysis was evaluated at the higher vehicle speed (v3).

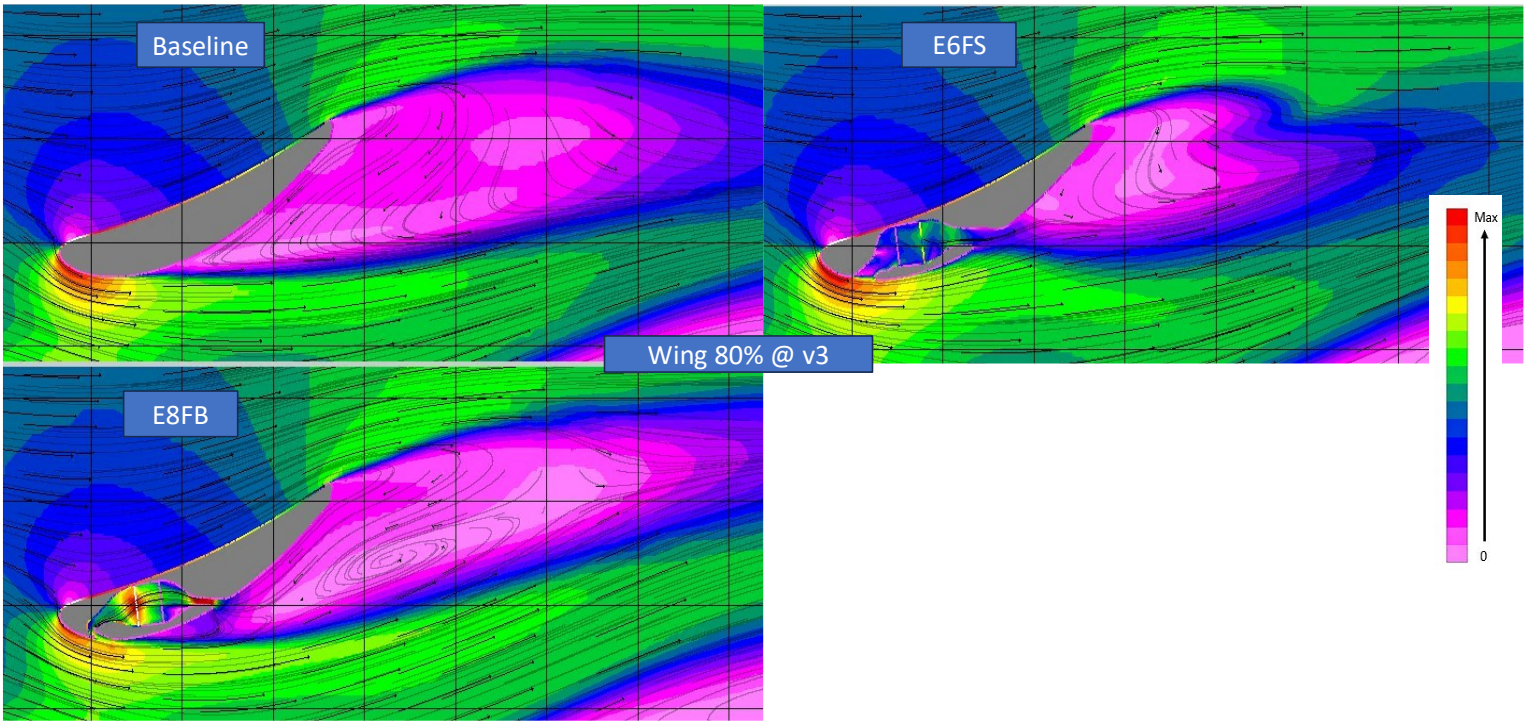

Figure 5.27 Comparison of the CFD-predicted velocity magnitude contours and streamlines around the rear wing for the baseline and the investigated Co-Flow configurations (E6FS and E8FB) at 80% rear-wing deployment with the fan operating at full speed and vehicle running at speed of v3.

This comparison allows the influence of the free-stream velocity on the Co-Flow actuation effectiveness to be evaluated and determines whether the aerodynamic trends identified at v2 remain valid under more demanding flow conditions. For 80% rear wing deployment at v3 no CFD data for E9aFB is available. The CFD results obtained at the higher vehicle speed (v3) show that the aerodynamic behaviour observed at v2 is generally preserved, although the

increased free-stream velocity modifies the relative effectiveness of the different Co-Flow architectures. Figure 5.27 to Figure 5.32 present the velocity magnitude contours, pressure coefficient distributions and wake structures for the investigated configurations under the same operating conditions considered previously. Since no CFD data are available for the E9aFB configuration at 80% rear-wing deployment, the comparison at this operating condition is limited to the Baseline, E6FS and E8FB configurations.

At 80% rear-wing deployment, the velocity contours indicate that the overall flow topology remains qualitatively similar to that observed at v2. The E6FS configuration still produces the strongest local interaction immediately downstream of the actuation device, while the E8FB architecture promotes a smoother redistribution of momentum over the suction surface. However, compared with v2, the higher incoming velocity tends to reduce the spatial extent of the Co-Flow-induced modifications, as the stronger free-stream momentum limits the penetration of the injected or extracted flow into the external aerodynamic field.

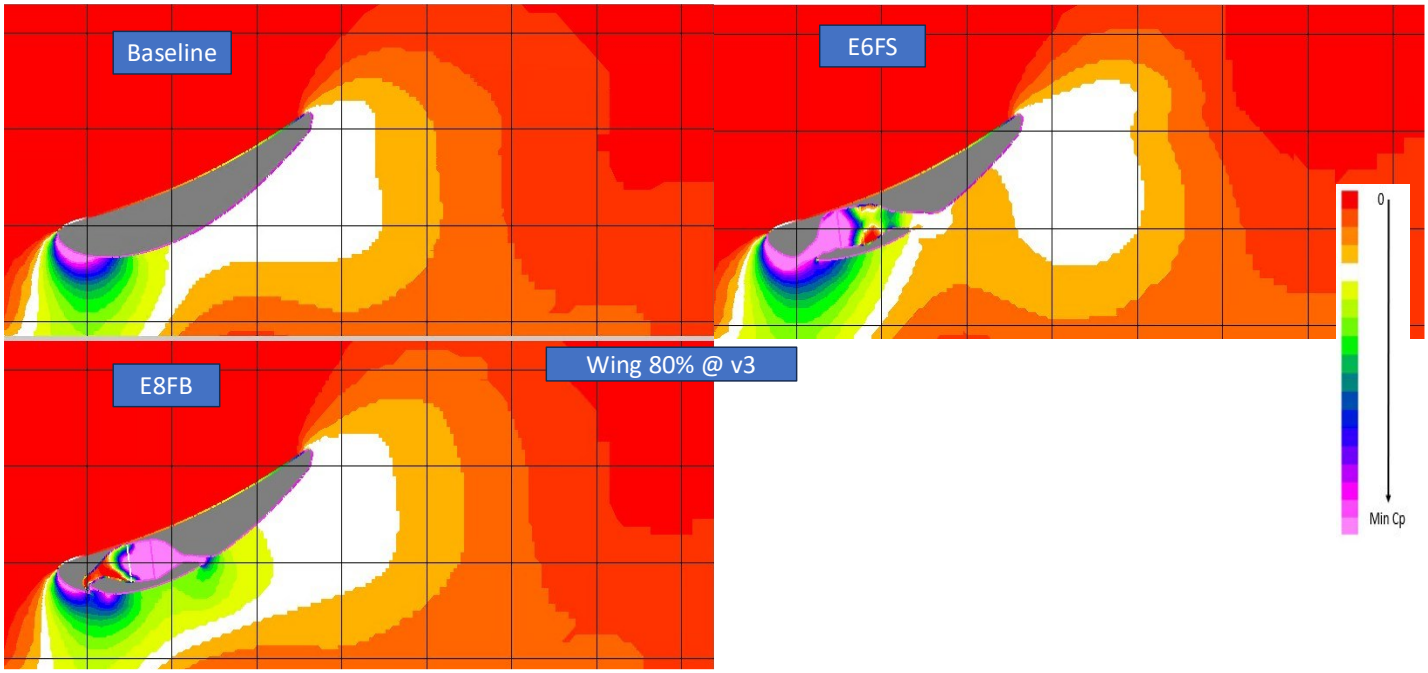

Figure 5.28 Comparison of the CFD-predicted pressure coefficient (C_p) distributions around the rear wing for the baseline and the three Co-Flow configurations (E6FS and E8FB) at 80% wing deployment at vehicle speed v3 (fan speed = 100%).

The corresponding pressure coefficient distributions confirm this behaviour. The E6FS configuration continues to generate a localized low-pressure region in the vicinity of the actuation system, whereas E8FB produces a broader but less intense redistribution of the pressure field along the suction surface.

Although the overall pressure patterns remain consistent with those observed at v2, the pressure gradients become more confined, suggesting that the aerodynamic authority of the Co-Flow system decreases as the free-stream velocity increases.

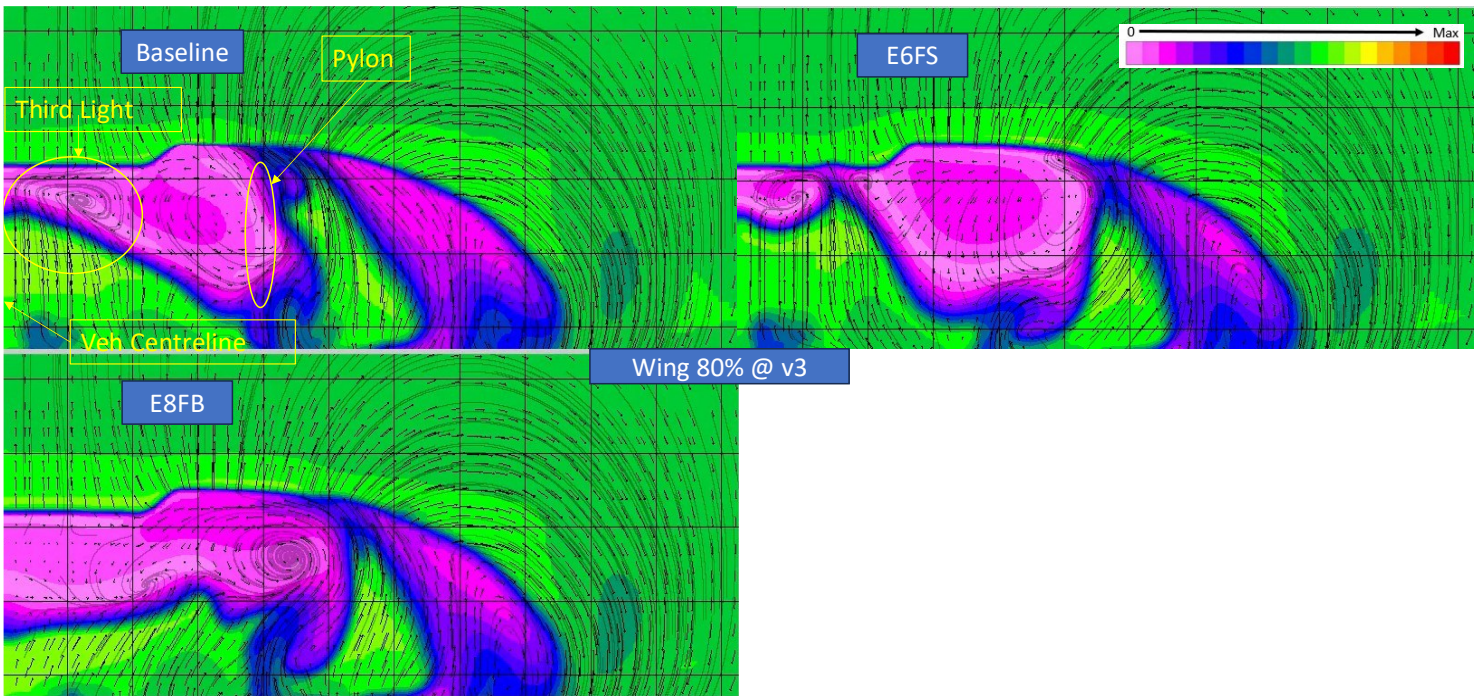

Figure 5.29 Cross-sectional CFD velocity magnitude contours and streamlines immediately downstream of the fully deployed rear wing (80% deployment at v3) for the baseline and the investigated Co-Flow configurations (E6FS and E8FB). The figure highlights the wake topology resulting from the interaction between the vortical structures generated by the geometric discontinuity associated with the third brake light integration, the wing pylons, and the wing-tip vortices

The wake structures downstream of the wing exhibit the same dominant vortical features identified at v2, namely the recirculating region associated with the third brake light integration, the pylon-induced vortices and the wing-tip vortex. The Co-Flow system continues to redistribute the interaction among these structures rather than suppressing them. Nevertheless, the stronger external flow produces a more compact wake, reducing the apparent influence of the actuation on the downstream recirculation regions. For the fully deployed rear wing (100% deployment), all investigated configurations maintain the qualitative trends previously observed at v2. The Co-Flow system continues to modify both the velocity and pressure fields over the suction surface, while the higher deployment angle allows the actuation to influence a larger portion of the wing.

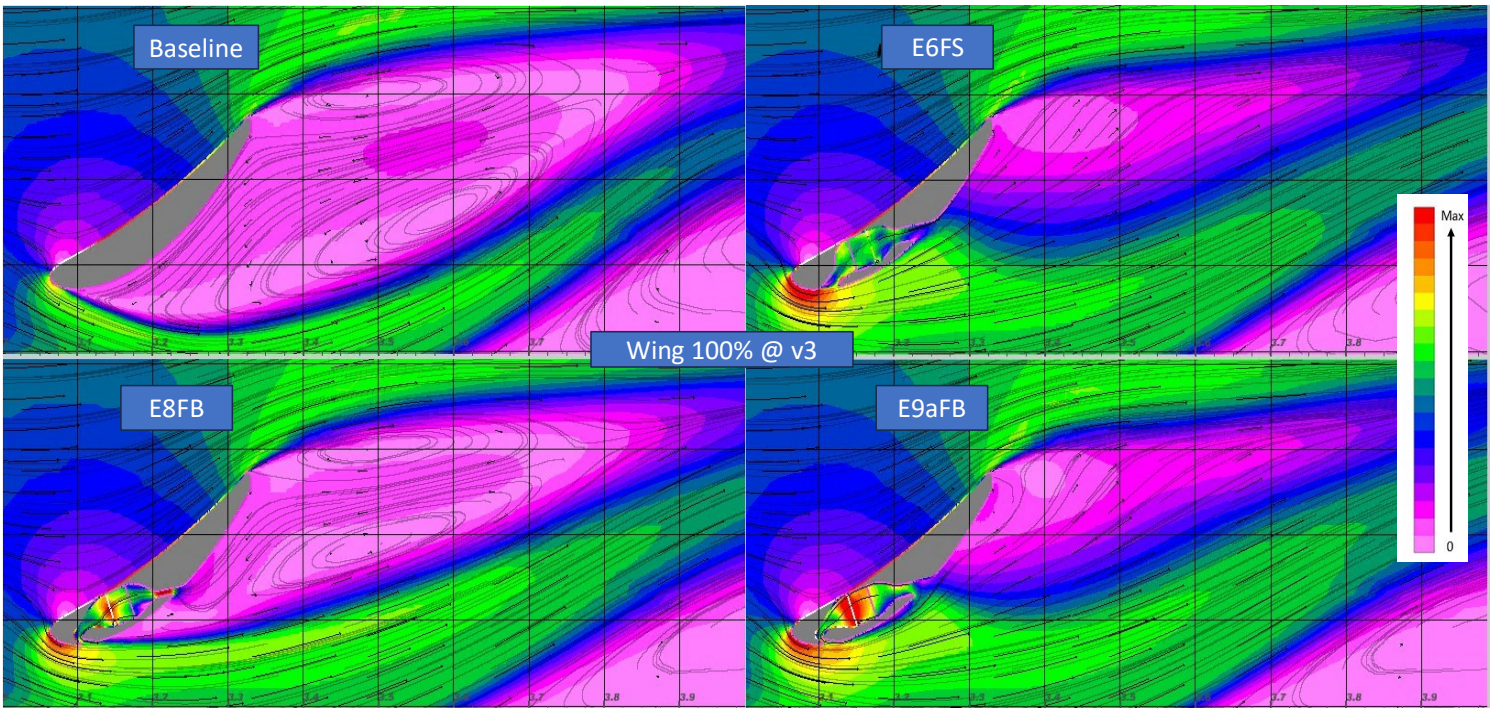

Figure 5.30 Comparison of the CFD-predicted velocity magnitude contours and streamlines around the rear wing for the baseline and the investigated Co-Flow configurations (E6FS, E8FB and E9aFB) at 100% rear-wing deployment with the fan operating at full speed and vehicle running at speed of v3.

Compared with the 80% deployment condition, the pressure redistribution remains more extensive, and the wake modifications become more evident, particularly for the front-blowing architectures. the CFD analysis suggests that the aerodynamic mechanisms identified at v2 remain valid at the higher vehicle speed (v3). Although increasing the free-stream velocity does not alter the fundamental flow physics associated with the different Co-Flow architectures, it reduces the relative extent of the local flow modifications generated by the actuation, making the aerodynamic response increasingly dependent on the balance between the Co-Flow momentum and the higher kinetic energy of the external flow. Consequently, the aerodynamic effectiveness of the Co-Flow system depends not only on the selected actuation architecture, but also on the rear-wing deployment angle and the operating vehicle speed. Among the investigated configurations, E9aFB consistently provides the most favourable aerodynamic compromise, combining the largest increase in wing aerodynamic loading with one of the largest reductions in aerodynamic drag over the investigated operating conditions. To facilitate the comparison between the investigated operating conditions, Table 5.3 summarizes the aerodynamic performance of the three Co-Flow architectures relative to the baseline configuration.

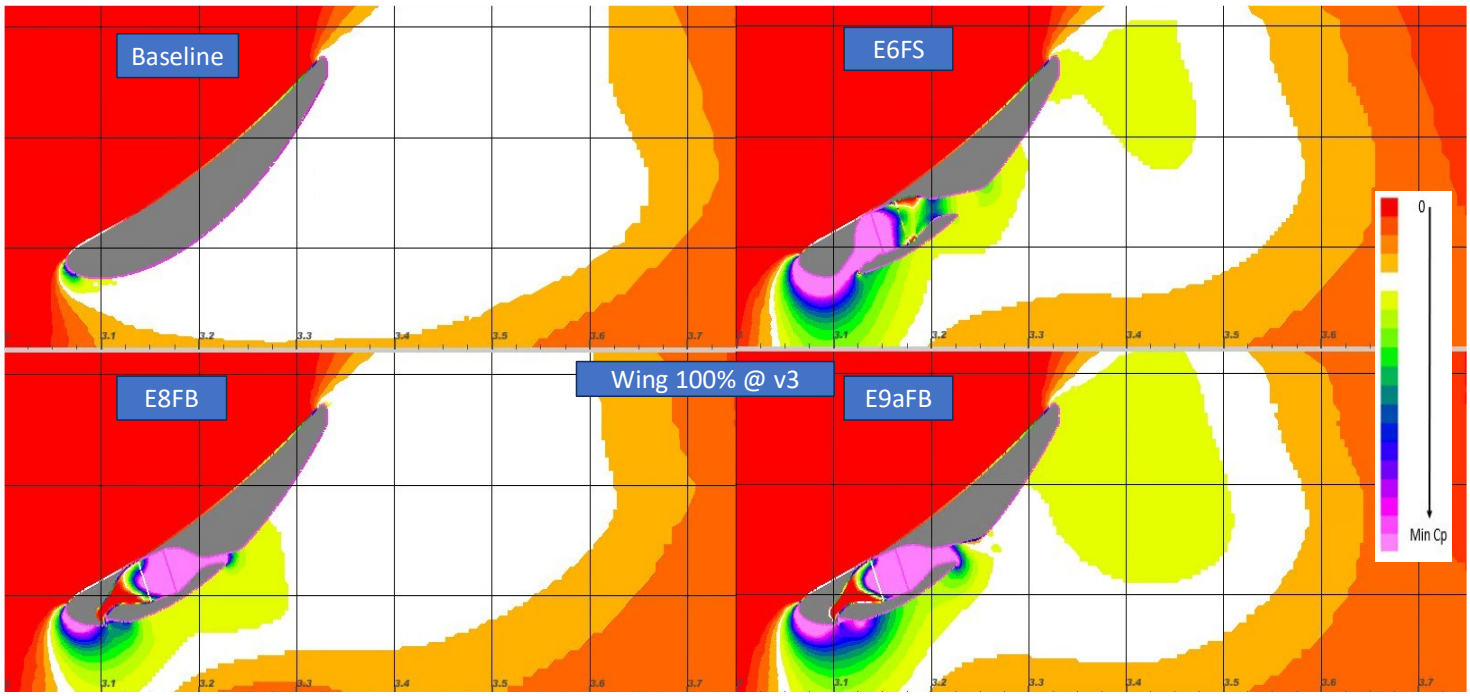

Figure 5.31 Comparison of the CFD-predicted pressure coefficient (C_P) distributions around the rear wing for the baseline and the three Co-Flow configurations (E6FS, E8FB and E9aFB) at 80% wing deployment at vehicle speed v3 (fan speed = 100%).

The results are reported for both vehicle speeds (v2 and v3) and for the two rear-wing deployment angles (80% and 100%), including the variations in wing drag coefficient (ΔC_d), in wing lift coefficient (ΔC_l), wing aerodynamic efficiency, and the corresponding wing aerodynamic efficiency improvement.

Wing Position	Configuration	ΔC_d v2 (%)	ΔC_d v3 (%)	ΔC_l v2 (%)	ΔC_l v3 (%)	Wing Aero Efficiency v2	Wing Aero Efficiency v3	Wing Aero Efficiency Improvement v2	Wing Aero Efficiency Improvement v3
80%	E6FS	1.7%	-1.5%	-1%	-4.7%	5.63	5.64	-3%	-3%
80%	E8FB	-2.4%	4.8%	-3.8%	-10.4%	5.7	4.98	-1%	-15%
80%	E9aFB	-2.2%	N/A	6%	N/A	6.26	N/A	8%	N/A
100%	E6FS	-1%	-6.5%	23.6%	16.6%	2.46	2.37	25%	25%
100%	E8FB	-8.9%	-9.6%	12.8%	7.8%	2.44	2.27	24%	19%
100%	E9aFB	-8.8%	-9%	27.6%	13.6%	2.75	2.37	40%	25%

Table 5.3 CFD comparison of the aerodynamic performance of the investigated Co-Flow configurations relative to the baseline at vehicle speeds v2 and v3 and rear-wing deployment angles of 80% and 100%.

It is worth noting that ΔCd (%) < 0 indicates a reduction in drag, while ΔCl (%) > 0 indicates an increase in downforce compared with the baseline configuration. The wing aerodynamic efficiency is defined as

$$E_{wing} = \frac{C_l}{C_d} \tag{5.8}$$

and the relative wing aerodynamic efficiency improvement with respect to the baseline configuration is calculated as

$$E_{rel,wing} = \frac{E_{wing,Co-Flow} - E_{wing,baseline}}{E_{wing,baseline}} \tag{5.9}$$

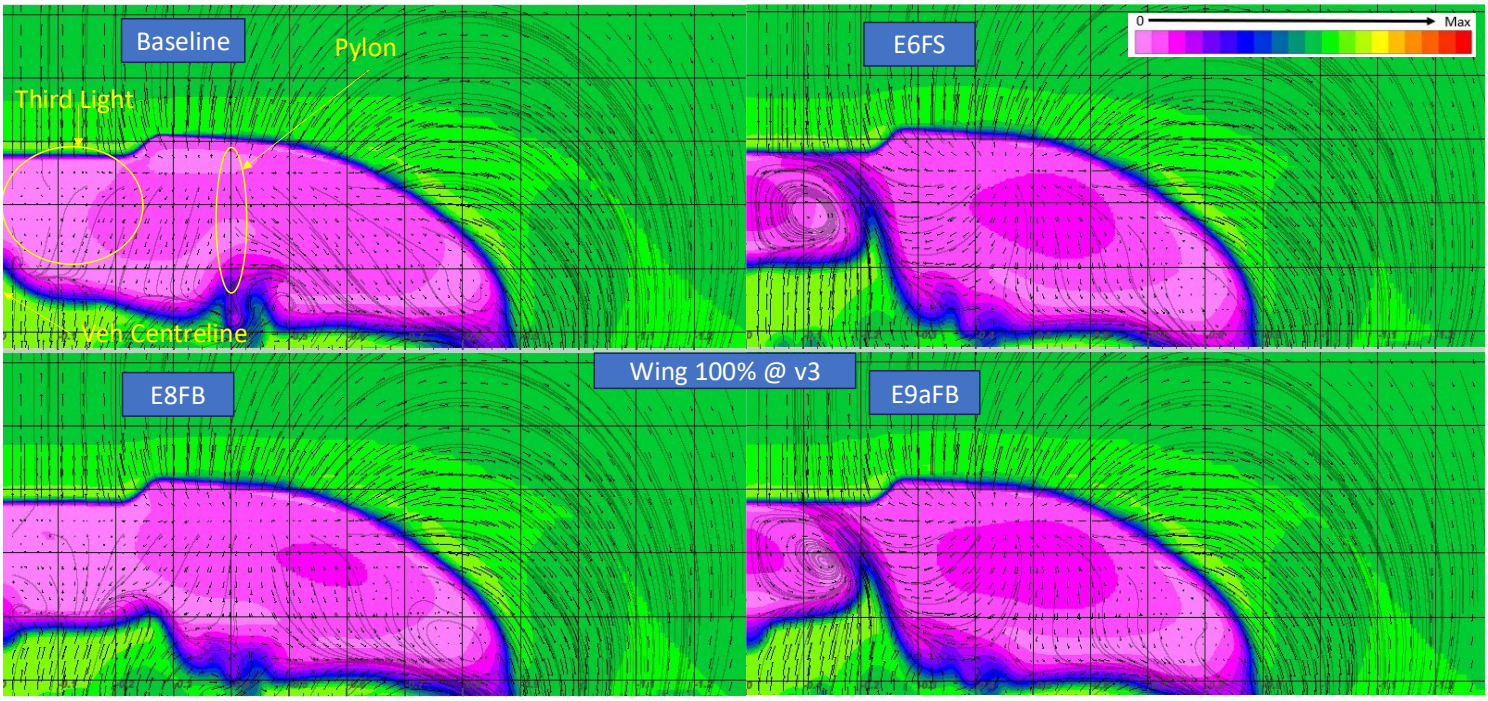

Figure 5.32 Cross-sectional CFD velocity magnitude contours and streamlines immediately downstream of the fully deployed rear wing (100% deployment at v3) for the baseline and the investigated Co-Flow configurations (E6FS, E8FB and E9aFB). The figure highlights the wake topology resulting from the interaction between the vortical structures generated by the geometric discontinuity associated with the third brake light integration, the wing pylons, and the wing-tip vortices

The results confirm that the aerodynamic performance of the Co-Flow system depends on both the actuation architecture and the operating condition. At 80% rear-wing deployment, the aerodynamic benefits are more limited and become increasingly sensitive to the vehicle speed. In contrast, at 100% rear-wing deployment all investigated configurations produce

simultaneous improvements in aerodynamic loading and drag reduction. Among the investigated layouts, the E9aFB configuration consistently provides the most favourable overall aerodynamic compromise across the analysed operating conditions, while E6FS generally exhibits the lowest sensitivity to the increase in vehicle speed. Based on these numerical results, all three Co-Flow designs were manufactured and experimentally tested. Unlike previous CFD investigations reported in the literature, the proposed design methodology ensures that every investigated aerodynamic solution remains compatible with the experimentally characterized operating envelope of the electric fan. Consequently, all numerical simulations are performed within physically achievable operating conditions, enabling a direct and meaningful comparison between CFD predictions and experimental measurements. The following chapter presents the experimental campaign and compares the measured aerodynamic performance with the CFD predictions, providing a comprehensive validation of both the numerical methodology and the proposed Co-Flow concept.

Chapter 6 – Experimental Validation and Performance Assessment

In the previous sections, the Co-Flow system has been assessed from computational perspectives, numerical analyses were carried out to identify the optimal design configurations and operating conditions capable of maximizing aerodynamic performance and flow control effectiveness. Moreover, significant effort was devoted to the development of a robust experimental baseline, intended to serve as a reliable reference for future validation activities. This baseline provides a consistent framework for comparing the future aerodynamic and energetic performance of the most promising Co-Flow setups, ensuring that the experimental verification can be accurately compared with the experimental baseline data. As defined in Section 5, three Co-Flow configurations were selected for fabrication and testing: one operating in front suction mode (E6FS) and two in front blowing mode (E8FB and E9aFB).

6.1 Rear Wing Preparation

To accommodate the installation of both the ducting system and the ducted fans, together with the required instrumentation and measurement devices, the carbon-fibre wing was sectioned. To ensure that the slot openings on the curved airfoil surface were accurately reproduced according to the CAD geometry, a set of custom 3D-printed masks was designed and manufactured; these masks were precisely contoured to match the external geometry of the wing and served as cutting templates to guide the machining process. This method guaranteed that the slots were opened as close as possible to the correct positions and orientations, while minimizing material removal and avoiding unnecessary weakening of the carbon-fibre wing.

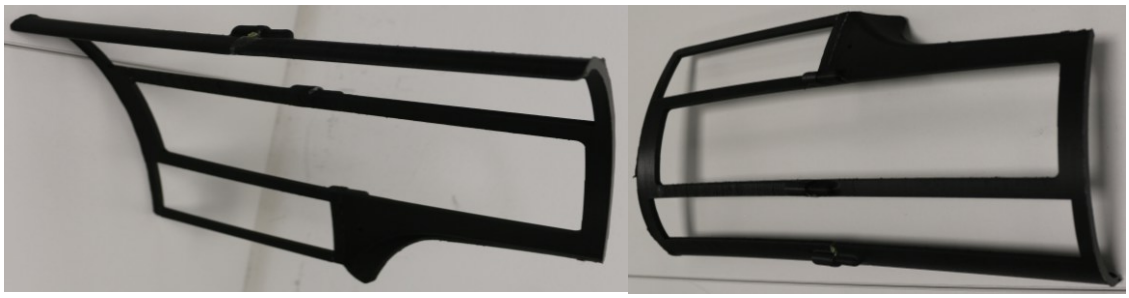

Figure 6.1 3D-printed cutting templates developed for the fabrication of the wing front and rear slots.

The internal Co-Flow duct system was fabricated by additive manufacturing (3D printing) to reproduce the complex internal duct geometry while maintaining low mass and sufficient structural stiffness. The components were printed using Creality Hyper PLA Carbon Fiber 1.75 mm filament on a Creality Ender 3 Pro printer. Compared with standard PLA, the selected

material provides improved dimensional accuracy, surface finish, and stiffness-to-weight ratio, ensuring both geometric fidelity and structural integrity of the duct assembly.
The cutting operations on the wing were carried out using an air-driven rotary tool equipped with a diamond disc, ensuring high precision and clean cuts along the curved surfaces, essential to preserve the aerodynamic integrity of the airfoil. The adopted manufacturing methodology guaranteed high geometric fidelity between the physical prototype and the digital model, enabling accurate integration of the Co-Flow system and reliable aerodynamic assessment during the subsequent experimental campaign (Figure 6.1). It worths to remind the wing experimental setup as shown in Figure 6.2, that illustrates the physical configurations of the static pressure probe arrays adopted for both the baseline and Co-Flow configurations; probes were mounted on the extrados of the rear wing element to capture the pressure distribution along the spanwise and chordwise directions.

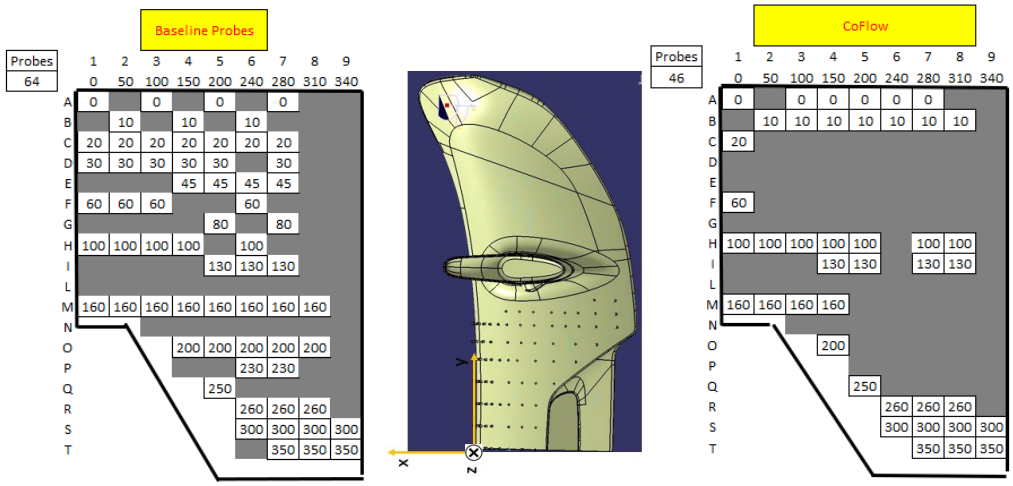

Figure 6.2 Layout of the static pressure probe distributions for the baseline (left) and CoFlow (right) configurations, with the corresponding locations on the wing.

In baseline setup as discussed in previous chapters, a total of 64 static pressure probes were installed on the convex profile of the wing, distributed across nine vertical measurement sections (identified from Section 1 to 9) extending from the vehicle centreline (Y = 0 mm) up to Y = 340 mm. Each section included multiple chordwise measurement points defined along the *X–Z* plane, following the local curvilinear coordinate of the wing surface up to X = 350 mm. This dense probe arrangement allowed for a detailed mapping of the aerodynamic pressure field over the entire lower surface, enabling accurate evaluation of local C_p measurements. For the Co-Flow configuration, the presence of internal flow ducts and their associated components imposed geometric constraints on probe positioning; consequently, the number of active probes was reduced to 46, maintaining the same spanwise distribution but with a lower chordwise resolution near the duct exit and suction regions. Probes that would have interfered with the

internal ducting or the Co-Flow outlet slots were omitted to prevent flow perturbations and ensure measurement reliability. Both configurations shared identical reference coordinate systems, with the *X*-axis aligned with the freestream direction, the *Y*-axis oriented spanwise, and the *Z*-axis normal to the wing surface. This consistent reference allowed direct comparison between the baseline pressure field and the modified pressure distribution under Co-Flow operation. Figure 6.3 illustrates the experimental setup installed on the test vehicle, used for the acquisition of aerodynamic parameters such as the pressure coefficient (C_p), drag and downforce.



Figure 6.3 Experimental installation of the Co−Flow system on the test vehicle, showing the E8FB configuration (left) and the E6FS configuration (right).

The image shows the integration of the internal duct system for the Co-Flow configuration, as well as the instrumentation layout employed to correlate experimental measurements with the results obtained from CFD simulations. In this setup, the ducted fans are governed by the same ESC controller and RPM acquisition system utilized in the previously described fan characterization rig, thereby ensuring identical control logic and measurement accuracy. The electrical power drawn by the fans was recorded using the IVC current and voltage sensor, also shared with the earlier test rig, enabling direct comparison of performance and energy efficiency under identical measurement conditions. The car configuration used to measure C_p, C_d, and C_l follows exactly the same setup as the baseline experimental campaign. It is nonetheless summarized here to remind the reader of the key instrumentation and measurement procedures relevant to the comparison with the Co-Flow configuration. For the pressure coefficient (C_p) evaluation, a set of static pressure ports was mounted along the convex (extrados) surface of the wing; these probes provide the static pressure distribution necessary to compute local and global aerodynamic loads. The downforce was estimated using displacement sensors installed on the vehicle suspension system. The vertical displacement of each suspension arm was converted into wheel load using pre-determined stiffness and calibration curves, enabling calculation of the total aerodynamic load distribution under various configurations. The drag was derived from coastdown tests, where vehicle deceleration was recorded via an onboard three-axis accelerometer under free-rolling conditions (no throttle or braking input). From the deceleration data, aerodynamic drag was isolated from rolling resistance and inertial

components, allowing estimation of total drag at each speed range. The configuration shown in Figure 6.3 represents the experimental test bench on which the baseline and Co-Flow hypotheses were verified. The system integrates aerodynamic, mechanical, and kinematic sensors to provide a comprehensive experimental dataset for direct comparison with numerical and experimental baseline predictions. A complete control and instrumentation chain was developed for the ducted fan actuation system and subsequently integrated into the test vehicle. The assembly was installed on top of the rear diffuser (see Figure 6.4), housing all electronic components required for power supply, control, and signal acquisition.

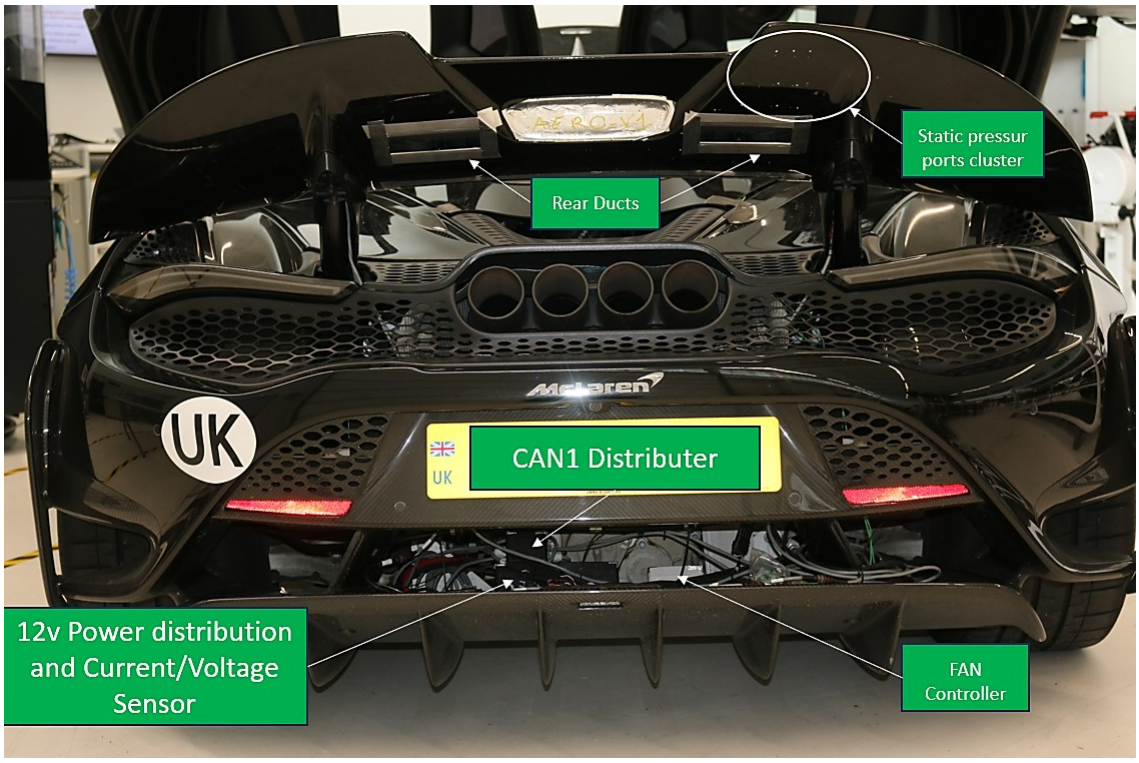

Figure 6.4 Full−scale vehicle implementation of the Co−Flow Jet system, indicating the rear duct assembly, pressure measurement instrumentation, fan controller, CAN distribution unit, and electrical power monitoring system.

Owing to the active nature of the system, the fan pressure rise, mass flow rate, rotational speed, and electrical power consumption were additionally monitored throughout the experimental campaign. These quantities were used not only to characterize the operating condition of the integrated fan–duct system, but also to assess the aerodynamic benefits achieved by the Co−Flow concept in relation to the corresponding energetic cost. Minor asymmetries between the left and right duct systems generated small differences in operating conditions, which were compensated through a master–slave fan control strategy. Vehicle roll angles were monitored to ensure consistent test conditions, showing a maxi-mum deviation of only 0.1°, well within

acceptable limits. To facilitate the interpretation of the aerodynamic response generated by the different Co−Flow configurations, the jet momentum coefficient Cμ was adopted as a non−dimensional measure of the actuation intensity. The parameter relates the jet momentum introduced by the Co−Flow system to the freestream dynamic pressure acting on the rear wing and is commonly employed in active−flow−control studies to compare operating conditions characterized by different mass flow rates and vehicle speeds, introduced by Danò [31] as shown next:

$$C_{\mu} = \frac{\dot{m} V_j}{q_{\infty} A_{ref}} \tag{6.1}$$

where $\dot{m}$ $[\frac{kg}{s}]$ is the mass flow rate (MFR) derived from the differential pressure measurements performed across two duct sections of the Co−Flow ducts, V_j $[\frac{m}{s}]$ is the slot exit velocity calculated from the MFR, duct internal density $[\frac{kg}{m^3}]$considered equivalent to external air density due to the low-pressure increase made by the fans and jet-slot area A_{jet} $[m^2]$, q_{∞} $[Pa]$ is the freestream dynamic pressure, and A_{ref} $[m^2]$ is the rear wing reference area. Since the experimental system employed two symmetrically installed fan–duct assemblies, the reported momentum coefficient accounts for the combined contribution of both actuation systems. Unlike conventional CFJ investigations, where the momentum coefficient is typically prescribed through imposed blowing and suction boundary conditions, the values obtained in the present study arise from the coupled interaction between duct geometry, fan operating characteristics, aerodynamic loading, and vehicle operating conditions. Consequently, C_{μ} should not be interpreted as an independent control parameter, but rather as a resulting system−level quantity reflecting the combined behaviour of the integrated actuation architecture. The jet momentum coefficient was used to characterize actuation intensity and to interpret the aerodynamic response across different vehicle speeds, wing−deployment angles, and Co−Flow configurations.

6.2 Experimental Results

This section discusses the aerodynamic behaviour of the investigated Co−Flow configurations through combined CFD and experimental analyses. The results are compared with the baseline configuration in terms of vehicle drag reduction, aerodynamic loading, energetic performance, and local wing pressure distributions, in order to assess the aerodynamic effectiveness and practical feasibility of the proposed active flow−control system. CFD results are used to support the interpretation of the observed aerodynamic trends, while the experimental measurements are used to quantify the resulting aerodynamic and energetic performance.

6.2.1 Drag Coefficient

This section presents the comparison between the baseline and Co−Flow experimental drag−coefficient ($C_{d,veh}$) results obtained across the investigated rear−wing deployment conditions (70-100%), including the fully stowed wing configuration (0%). The investigation was conducted to evaluate the influence of the different Co−Flow arrangements on the aerodynamic drag behaviour of the vehicle and to identify the operating conditions under which the active flow−control system provides the largest aerodynamic benefit. The vehicle drag variation relative to the baseline configuration was evaluated experimentally for all investigated Co−Flow systems. The drag variation percentage relative to the baseline was computed using:

$$\Delta C_{d,veh}[\%] = \frac{C_{d,CoFlow} - C_{d,Baseline}}{C_{d,Baseline}} \times 100 \quad (6.2)$$

where $C_{d,CoFlow}$ is the drag coefficient with the Co−Flow system installed and $C_{d,Baseline}$ corresponds to the unmodified wing. Negative values of $\Delta C_{d,veh}$ indicate drag reduction relative to the baseline configuration, whereas positive values indicate a drag penalty. The three investigated configurations exhibit markedly different drag responses across the tested operating envelope (Figure 6.5). At low wing deployment (70–80%), the observed changes remain relatively modest for all configurations. Under these conditions, the E6FS configuration generally produces a drag penalty, while E8FB and E9aFB provide limited but measurable drag reductions. At higher wing deployment levels (90−100%), larger drag reductions are observed, particularly for the front−blowing configurations E8FB and E9aFB.

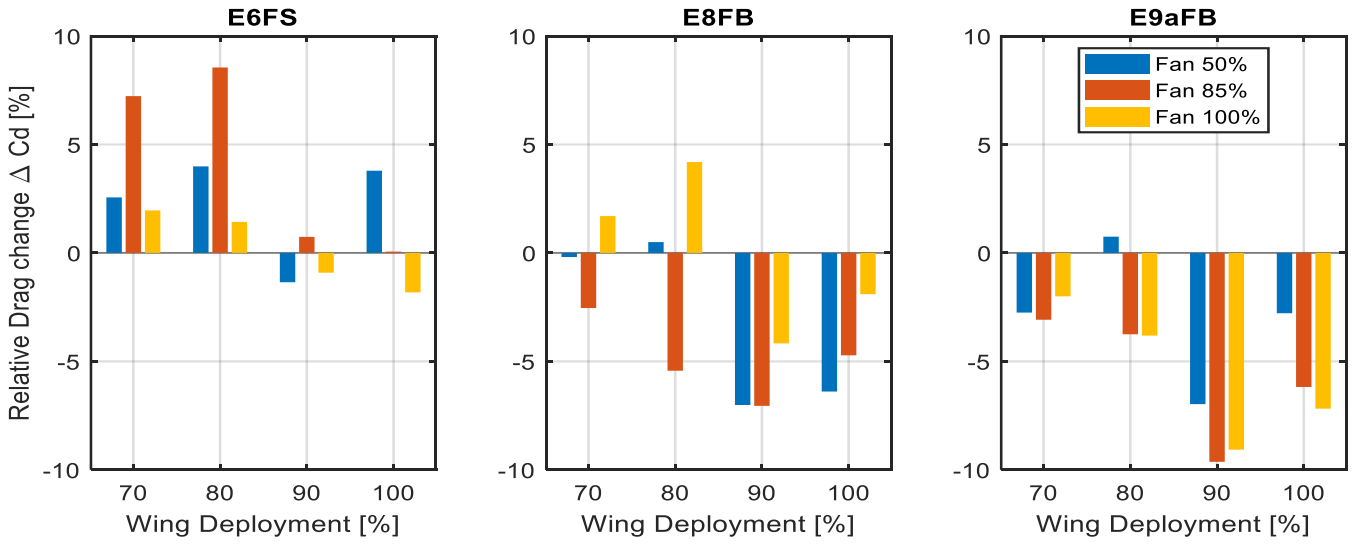

Figure 6.5 Vehicle experimental variation in drag coefficient relative to the baseline configuration for E6FS, E8FB, and E9aFB designs across different wing deployment positions and fan operating conditions.

The experimental measurements are summarized in Table 6.1, which reports the relative variation in wing drag coefficient (ΔC_d) of each Co-Flow configuration with respect to the baseline rear wing for all investigated operating conditions.

		ΔC_d Vehicle		
Fan Speed (%)	**Wing Position (%)**	**E6FS**	**E8FB**	**E9aFB**
50	70	+2.6%	-0.2%	-2.8%
	80	+4.0%	+0.5%	+0.8%
	90	-1.4%	-7.0%	-7.0%
	100	+3.8%	-6.4%	-2.8%
85	70	+7.2%	-2.5%	-3.1%
	80	+8.6%	-5.4%	-3.8%
	90	+0.7%	-7.1%	-9.6%
	100	+0.1%	-4.7%	-6.2%
100	70	+2.0%	+1.7%	-2.0%
	80	+1.4%	+4.2%	-3.8%
	90	-0.9%	-4.2%	-9.1%
	100	-1.8%	-1.9%	-7.2%

Table 6.1 Experimental relative variation in wing drag coefficient (ΔC_d %) of the investigated Co-Flow configurations with respect to the baseline vehicle for different fan operating conditions and rear-wing deployment angles.

Among the investigated solutions, E9aFB achieves the largest drag reduction, reaching approximately 9% under the most favourable operating conditions. E8FB also produces consistent drag reductions across a broad range of operating conditions. In contrast, E6FS does not consistently outperform the baseline configuration and remains characterized by less favourable drag performance throughout much of the investigated operating envelope. The influence of fan speed is not uniform across all operating conditions. Increasing fan speed does not always result in larger drag reductions, and the maximum fan speed does not systematically correspond to the largest aerodynamic benefit. This behaviour is observed for both E8FB and E9aFB, particularly at intermediate wing−deployment conditions. It should be noted that, during the coastdown tests used for drag evaluation, the momentum coefficient C_μ was not a fixed parameter but varied continuously with vehicle speed and fan operating condition throughout the deceleration process. Therefore, unlike the downforce measurements conducted under steady−state conditions, no unique C_μ value can be associated with a given drag test. For this reason, a detailed analysis of C_μ is presented in the lift assessment, where steady operating conditions allow a more rigorous interpretation of the actuation intensity. Nevertheless, the drag results clearly show that the front−blowing configurations (E8FB and E9aFB) provide the most

effective drag−reduction performance within the investigated operating range, while E6FS delivers comparatively limited aerodynamic benefits.

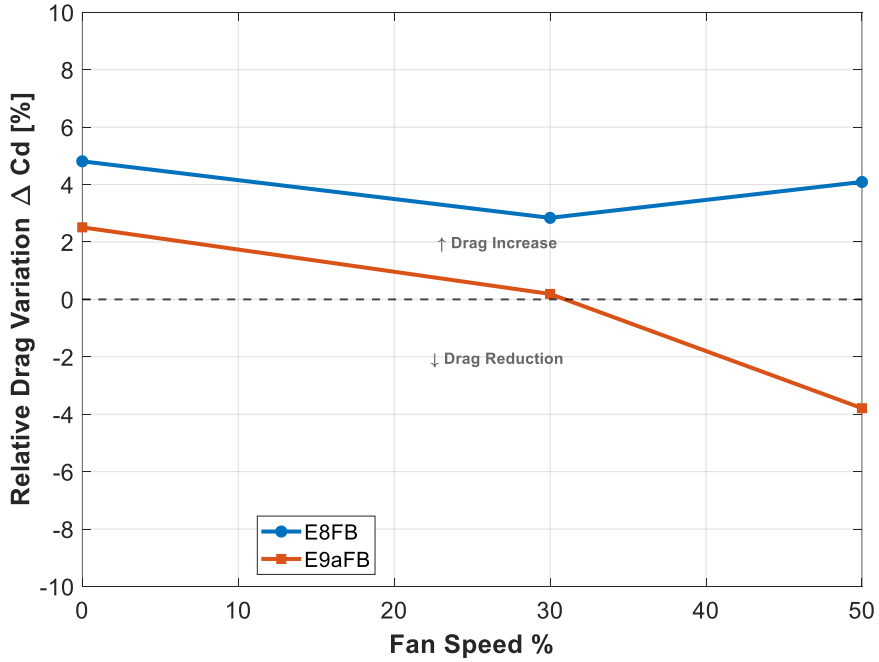

Figure 6.6 Vehicle experimental drag coefficient variation at 0% wing deployment as a function of fan speed for the E8FB and E9aFB configurations relative to the baseline case.

Additional measurements were performed with the rear wing fully stowed to evaluate the aerodynamic impact of the duct openings required by the Co−Flow system and to assess the system behaviour under conditions of minimal rear−wing loading (Figure 6.6).

Based on the results obtained for the deployed−wing configurations, E6FS exhibited limited aerodynamic benefits throughout the investigated operating range and was therefore not considered for further testing under fully stowed conditions. Consequently, the analysis was restricted to the E8FB and E9aFB configurations. To maintain consistency with the practical−feasibility objectives of the study, the investigation was limited to fan operating conditions up to 50% speed. While higher fan speeds were technically achievable, continuous operation under such conditions would inevitably increase energy consumption, acoustic emissions, and mechanical loading of the actuation system. Therefore, only the 0%, 30%, and 50% fan−speed operating points were considered for the fully stowed wing configuration. Under these conditions, the aerodynamic response differs substantially from that observed for the deployed−wing cases. The E8FB configuration consistently produces a drag penalty across the investigated fan−speed range, with drag increases be-tween approximately 3% and 5% relative to the baseline configuration. In contrast, E9aFB exhibits a progressive improvement as fan speed increases. While a drag penalty is observed at low actuation levels, the

aerodynamic response improves with increasing fan speed and transitions to a net drag reduction at 50% fan speed, reaching approximately 4% under the investigated conditions. Compared with the deployed−wing cases, the magnitude of the aerodynamic benefit is generally reduced when the wing is fully stowed. Nevertheless, the outcomes indicate that measurable drag reductions can still be achieved for selected configurations and operating conditions. Among the investigated solutions, E9aFB remains the most effective configuration, whereas E8FB does not provide a drag benefit within the tested operating range.

6.2.2 Lift Coefficient

The variation in lift coefficient relative to the baseline configuration was evaluated to determine the impact of the Co−Flow system on aerodynamic loading and computed as:

$$\Delta C_{l,veh}[\%] = \frac{C_{l,CoFlow} - C_{l,Baseline}}{C_{l,Baseline}} \times 100 \tag{6.3}$$

Where $C_{l,CoFlow}$ is the lift coefficient with the Co−Flow system active and$C_{l,Baseline}$ corresponds to the baseline configuration. Positive values of $\Delta C_{l,veh}$ indicate an increase in downforce relative to the baseline case, whereas negative values indicate a reduction. The operating points v1 to v4 correspond to increasing vehicle speed. The lift variation obtained for the three investigated Co−Flow configurations is discussed together with the corresponding jet momentum−coefficient distributions.

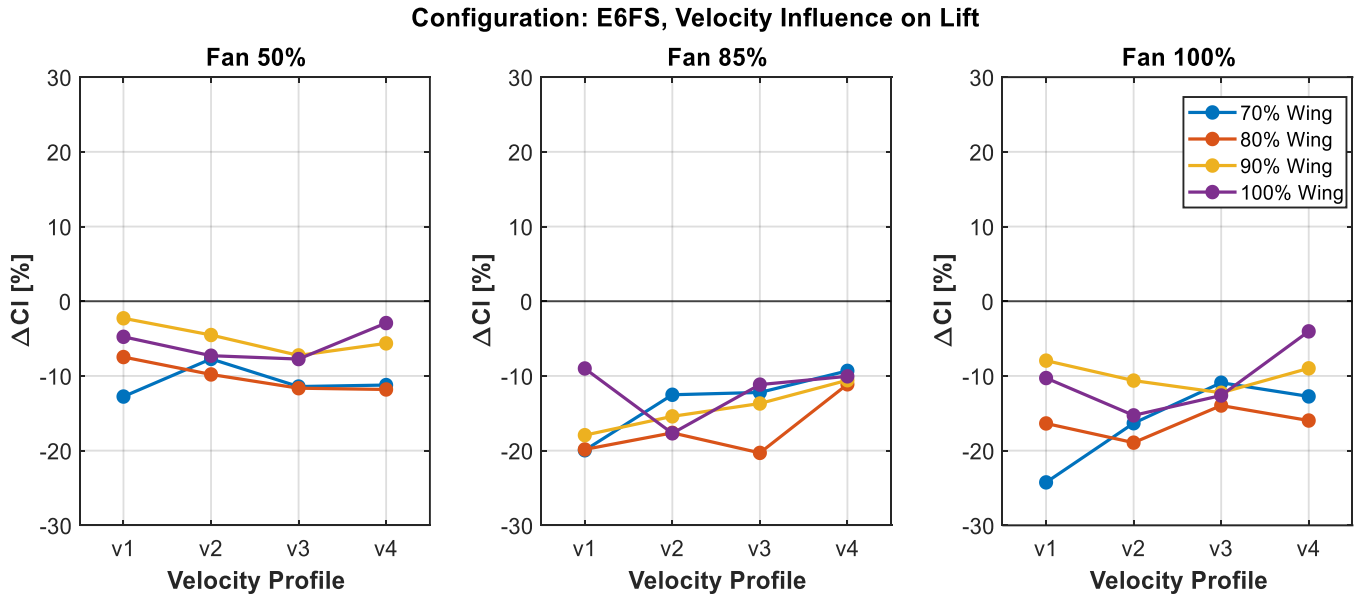

Figure 6.7 Influence of vehicle velocity profile and wing deployment position on the experimental vehicle lift coefficient variation in the E6FS configuration relative to the baseline case for different fan operating speeds.

This combined analysis provides insight into the relationship between aerodynamic performance and actuation intensity across the investigated range of wing deployments, vehicle speeds, and fan operating conditions. The E6FS configuration exhibits a reduction in aerodynamic loading across the entire investigated operating range (Figure 6.7). Negative values of $\Delta C_{l,veh}$ are observed for all tested fan speeds, wing deployments, and vehicle−speed conditions, indicating that the Co−Flow system does not provide a measurable downforce benefit for this configuration. Depending on the operating condition, downforce penalties typically range between approximately 5% and 25% relative to the baseline vehicle. To support the interpretation of these results, the corresponding jet momentum−coefficient distributions are reported in Figure 25. As expected, C_μ increases with fan speed and decreases with vehicle speed. The highest momentum−coefficient values are consistently observed at 100% wing deployment, whereas the lowest values occur at 70% deployment, reflecting the strong interaction between wing operating condition and the operating point of the integrated fan−duct system. Despite spanning more than one order of magnitude across the investigated operating envelope, the momentum coefficient does not produce corresponding improvements in aerodynamic loading. The measured values of $\Delta C_{l,veh}$ remain consistently negative, and no clear relationship between increasing C_μ and improved aerodynamic performance can be identified. In several cases, the largest aerodynamic penalties are associated with the highest momentum−coefficient conditions, particularly at low vehicle speeds. The results indicate that increasing the available actuation intensity alone is insufficient to generate a beneficial aerodynamic response for the front−suction architecture. This observation suggests that the effectiveness of the Co−Flow system depends not only on the magnitude of the injected momentum but also on how that momentum is introduced into the flow field through the duct arrangement. A markedly different behaviour is observed for the E8FB configuration (Figure 6.9). Compared with E6FS, E8FB produces measurable increases in downforce over a substantial portion of the investigated operating range. Positive values of $\Delta C_{l,veh}$ are obtained for several combinations of wing deployment, vehicle speed, and fan operating condition, with the largest improvements generally observed at 100% fan speed.

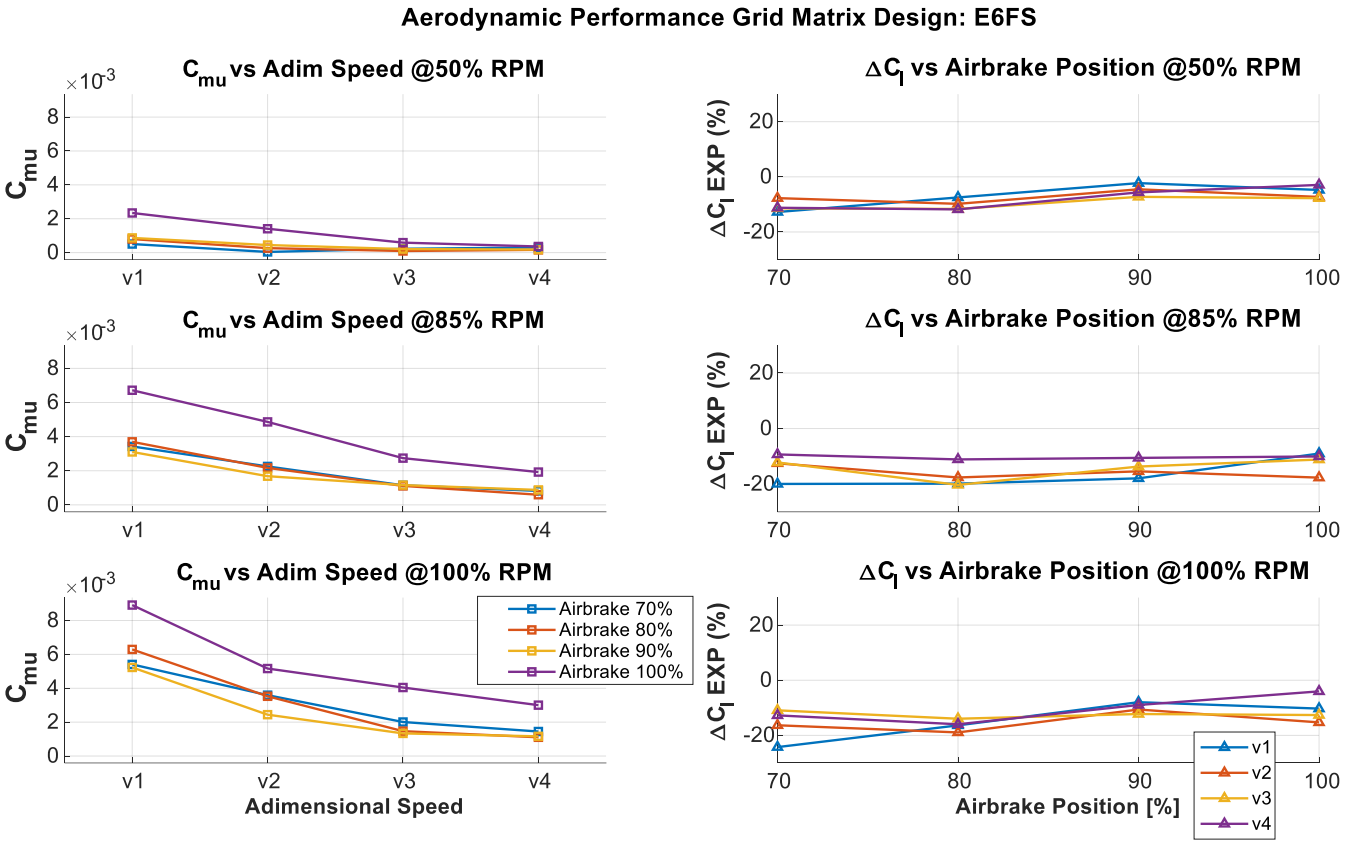

Figure 6.8 Vehicle experimental aerodynamic performance matrix for the E6FS configuration, showing mo-mentum coefficient variation with dimensionless velocity and vehicle lift coefficient variation with airbrake position at different fan speeds.

Depending on the operating condition, $\Delta C_{l,veh}$ varies from approximately −10% to +15%. To support the interpretation of these results, the corresponding jet momentum−coefficient distributions are reported in Figure 6.10. Similar to E6FS, the jet momentum coefficient increases with fan speed and decreases with vehicle speed. However, E8FB generally operates at lower C_μ levels than E6FS due to the reduced mass flow rate delivered by the integrated fan−duct system. Despite operating at lower momentum−coefficient levels than E6FS, E8FB provides substantially improved aerodynamic performance, highlighting the importance of duct architecture in determining Co−Flow effectiveness. Unlike E6FS, E8FB exhibits a progressive improvement in aerodynamic loading as the actuation level increases.

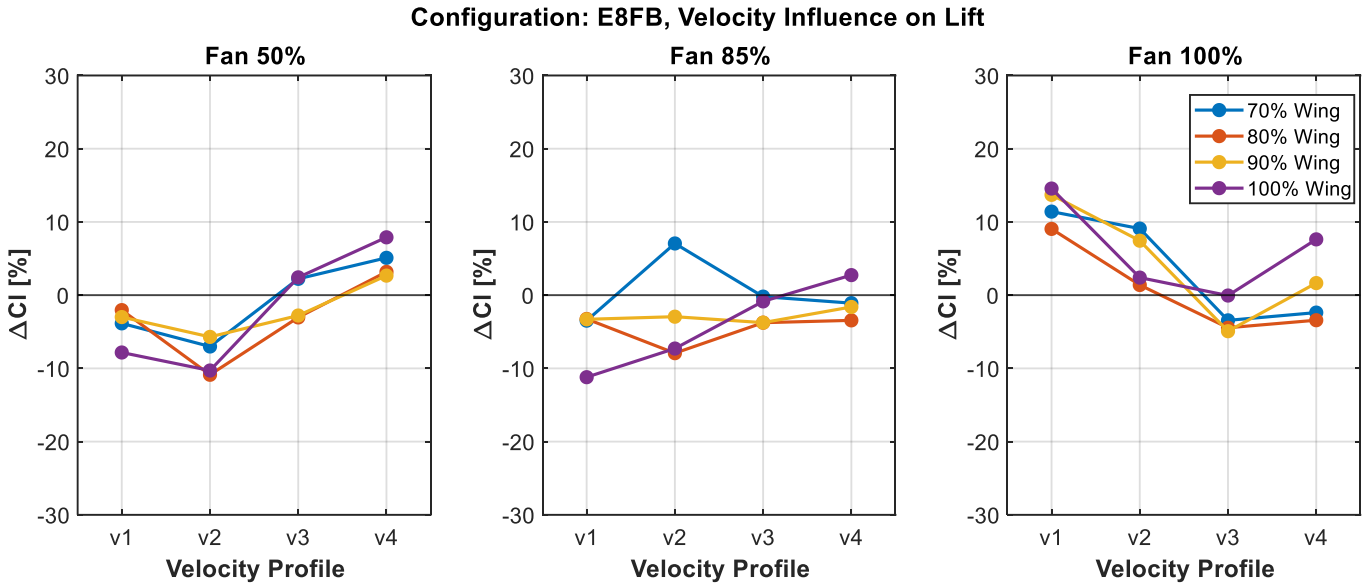

Figure 6.9 Influence of vehicle velocity profile and wing deployment position on the experimental vehicle lift coefficient variation in the E8FB configuration relative to the baseline case for different fan operating speeds.

At low fan−speed settings, the response remains mixed, whereas positive values of $\Delta C_{l,veh}$ become increasingly common as fan speed increases. As fan speed increases, positive values of $\Delta C_{l,veh}$ become increasingly common and larger improvements in downforce are achieved. This trend suggests that the available momentum injection becomes sufficiently effective only above a certain actuation level. Nevertheless, the relationship between $\Delta C_{l,veh}$ and C_μ is not monotonic. For 100% fan−speed setting, a distinct deterioration in aerodynamic performance is observed around the v3 operating condition, followed by a recovery at v4, despite the comparatively smooth variation of C_μ with vehicle speed. The presence of this local minimum suggests that the aerodynamic response cannot be explained solely by the magnitude of the injected momentum. While increasing C_μ generally improves the performance of E8FB, additional factors associated with the aerodynamic operating condition clearly influence the resulting aerodynamic benefit. The specific flow mechanisms responsible for this behaviour cannot be identified from the present dataset and would require dedicated flow−field measurements for further investigation. The analysis suggests that the E8FB configuration provides substantially better aerodynamic performance than E6FS and demonstrates the capability of generating measurable increases in vehicle downforce over a broad range of operating conditions, using a much lower flow rate.

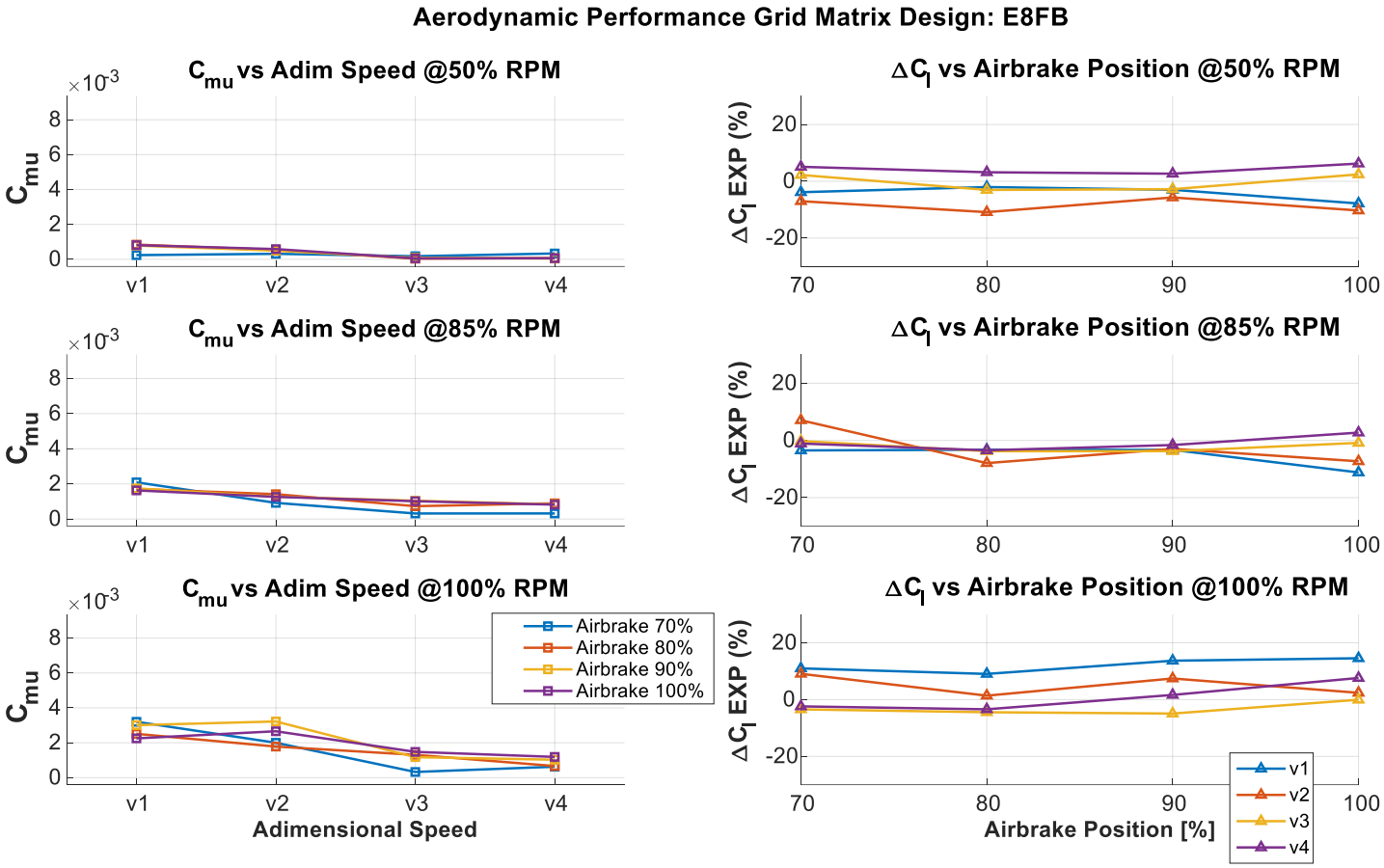

Figure 6.10 Vehicle experimental aerodynamic performance matrix for the E6FS configuration, showing momentum coefficient variation with dimensionless velocity and vehicle lift coefficient variation with airbrake position at different fan speeds.

To further increase the available actuation intensity, the E9aFB configuration was developed by enlarging the inlet section identified as a flow restriction in the previous E8FB design. The corresponding jet momentum−coefficient distributions are reported in Figure 6.11. Compared with E8FB, E9aFB consistently operates at higher C_μ levels across the investigated operating range. This behaviour reflects the increase in measured mass flow rate resulting from the enlarged inlet geometry and is consistent with the CFD predictions, which indicated reduced flow restriction for this configuration. The aerodynamic response of E9aFB differs from that observed for E8FB. Whereas E8FB generally requires higher actuation levels to achieve consistent downforce benefits, E9aFB produces positive values of $\Delta C_{l,veh}$ over a larger portion of the investigated operating envelope, including several low−actuation conditions.

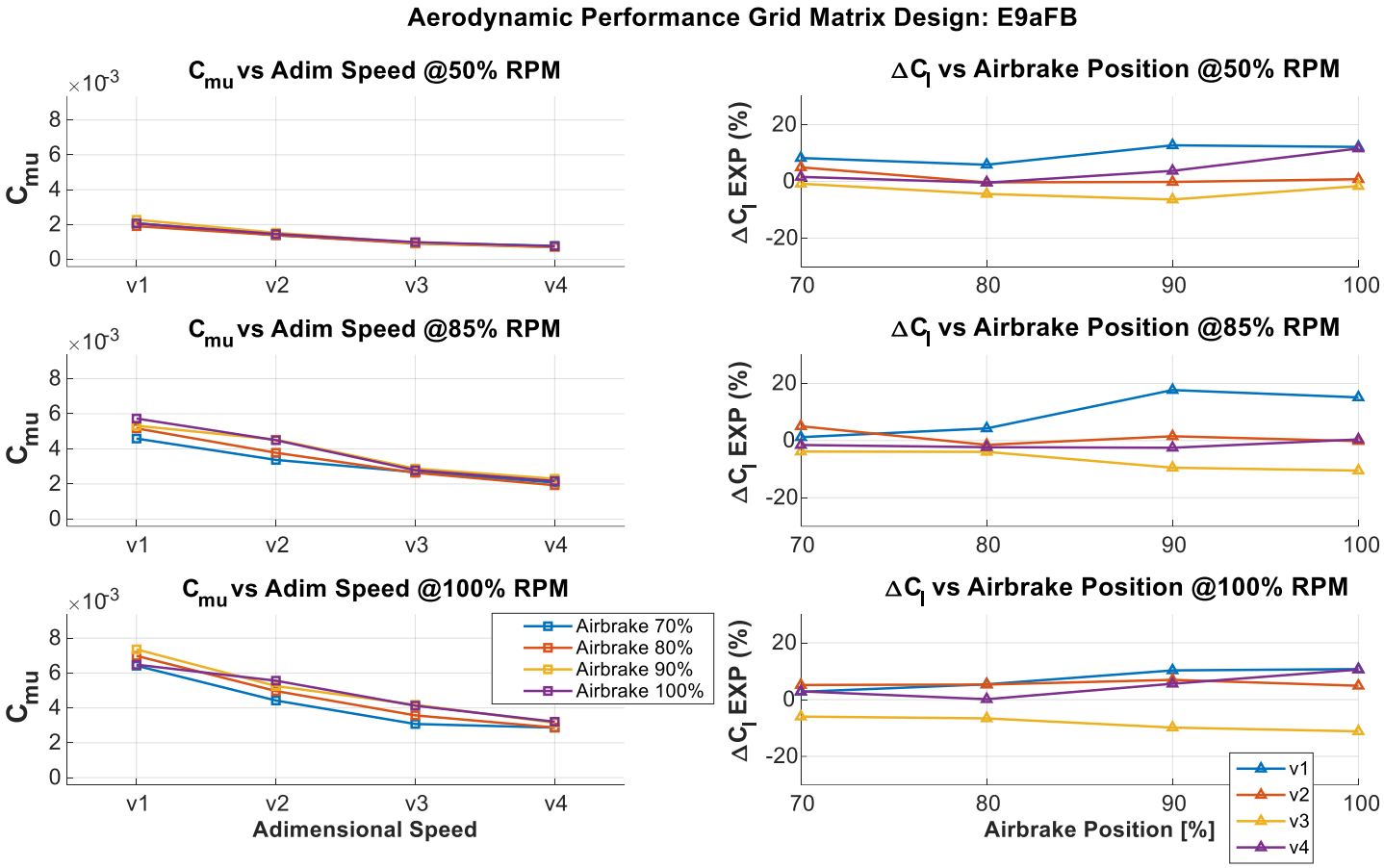

Figure 6.11 Vehicle experimental aerodynamic performance matrix for the E9aFB configuration, showing momentum coefficient variation with dimensionless velocity and vehicle lift coefficient variation with airbrake position at different fan speeds.

While C_μ remains a useful parameter for characterizing actuation intensity, no unique momentum coefficient value associated with the observed deterioration in aerodynamic performance could be identified from the present dataset. The E9aFB results indicate that the enlarged inlet geometry successfully increases the available actuation authority and broadens the range of operating conditions for which positive aerodynamic benefits can be obtained, depending on the operating condition, $\Delta C_{l,veh}$ varies from approximately −11% to +17.7%. The additional momentum is not converted into proportional increases in downforce, highlighting the complex relationship between momentum injection and aerodynamic effectiveness in integrated Co−Flow systems. A further insight emerges from the comparison between the E8FB configuration operating at 100% fan speed and the E9aFB configuration operating at 50% fan speed (Figure 6.13).

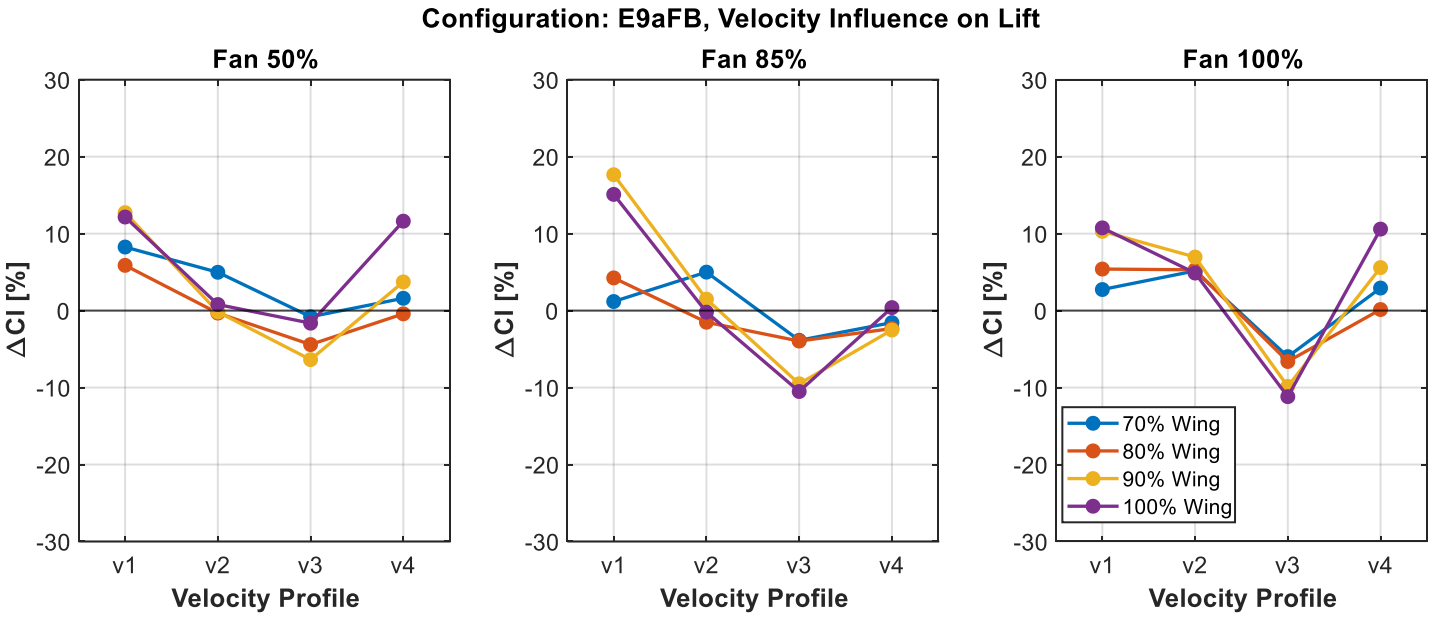

Figure 6.12 Influence of vehicle velocity profile and wing deployment position on the experimental vehicle lift coefficient variation in the E9aFB configuration relative to the baseline case for different fan operating speeds.

In both cases, positive values of $\Delta C_{l,veh}$ are obtained at the lower vehicle–speed conditions, followed by a pronounced deterioration around the v3 operating condition and a subsequent recovery at v4.

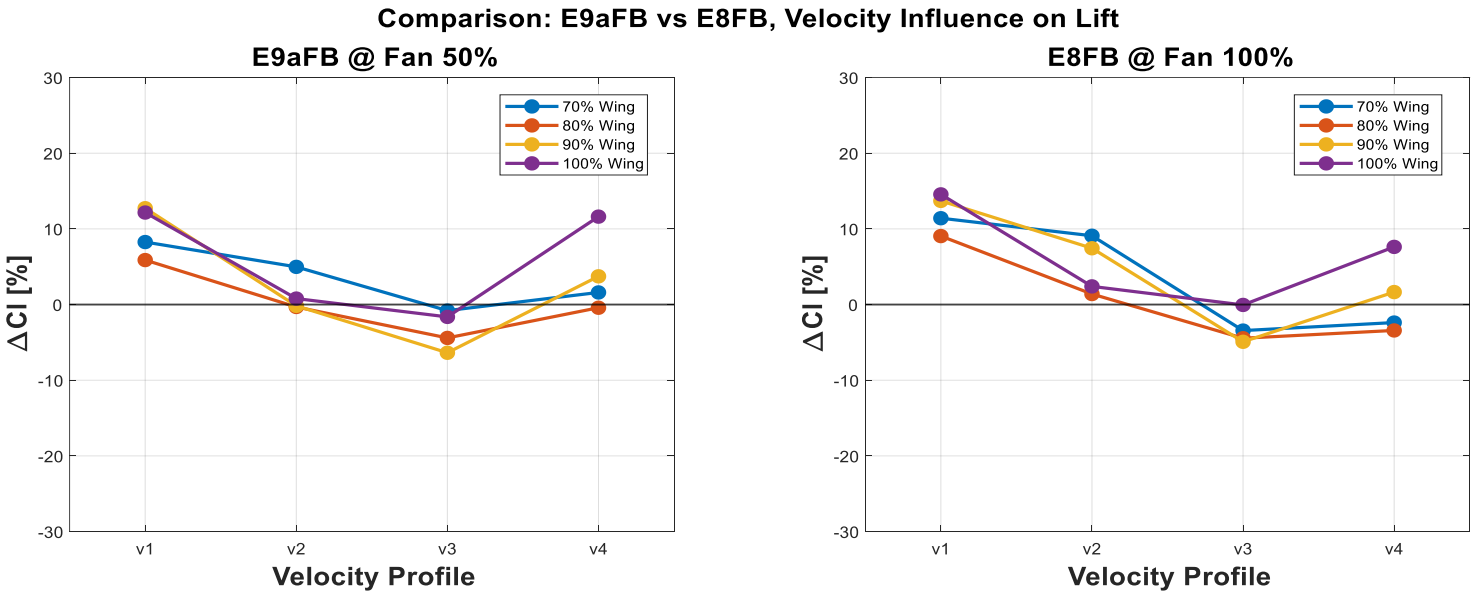

Figure 6.13 Comparison of the vehicle lift coefficient variation obtained with the E9aFB configuration at 50% fan speed and the E8FB configuration at 100% fan speed for different wing deployment positions and velocity profiles.

The similarity of the resulting aerodynamic trends is particularly noteworthy because the comparable performance is achieved using significantly different actuation strategies. This observation further indicates that fan rotational speed alone is not an adequate parameter for characterizing the aerodynamic response of the Co−Flow system. The comparison also highlights that increasing the available actuation intensity does not necessarily translate into proportional aerodynamic gains. Despite the substantially higher fan speed required by E8FB, its aerodynamic response remains comparable to that obtained by E9aFB operating at only 50% fan speed. This behaviour suggests that the improved duct architecture of E9aFB enables a more effective utilization of the available actuation authority. More importantly, the persistence of the local minimum around the v3 operating condition in both configurations indicates that the flow response cannot be described solely by either fan speed or jet momentum coefficient, as explained before. While C_μ remains a useful parameter for characterizing actuation intensity, the recurring deterioration observed at v3 across different configurations and operating conditions suggests that additional factors associated with the aerodynamic operating condition continue to play an important role in determining the effectiveness of the Co−Flow system. Results show that the lift measurements indicate a clear progression in aerodynamic performance across the investigated Co−Flow configurations. The E6FS arrangement does not provide measurable downforce benefits despite operating at relatively high momentum−coefficient levels. In contrast, both front−blowing configurations generate significant increases in aerodynamic loading over a substantial portion of the investigated operating range. The comparison between E8FB and E9aFB further indicates that improvements in aerodynamic performance are linked not only to the magnitude of the injected momentum but also to the effectiveness with which that momentum is introduced into the flow field through the duct architecture. To facilitate the comparison among the investigated Co-Flow configurations, Table 6.2 summarizes the overall ranges of the measured aerodynamic performance obtained throughout the experimental campaign. The reported values correspond to the minimum and maximum variations of the lift and drag coefficients observed over the investigated operating conditions.

Design	Maximum Drag Reduction (Best ΔCd)	Maximum Lift Improvement (Best ΔCl)
E6FS	-1.8%	-2.3%
E8FB	-7.1%	+14.6%
E9aFB	-9.6%	+17.7%

Table 6.2. Best aerodynamic performance achieved by each investigated Co-Flow configuration during the experimental campaign.

6.2.3 Pressure Coefficient

The pressure coefficient distributions were first analysed through CFD simulations on the wing section aligned with the fan centreline. This comparison enables the flow behaviour of the different Co−Flow configurations to be evaluated under identical operating conditions, including the E9aFB configuration for which complete experimental data were not available. Compared with the baseline configuration, all Co−Flow designs produce noticeable modifications of the pressure distribution within the leading−edge region and over the portion of the wing directly influenced by the actuation system (Figure 6.14).

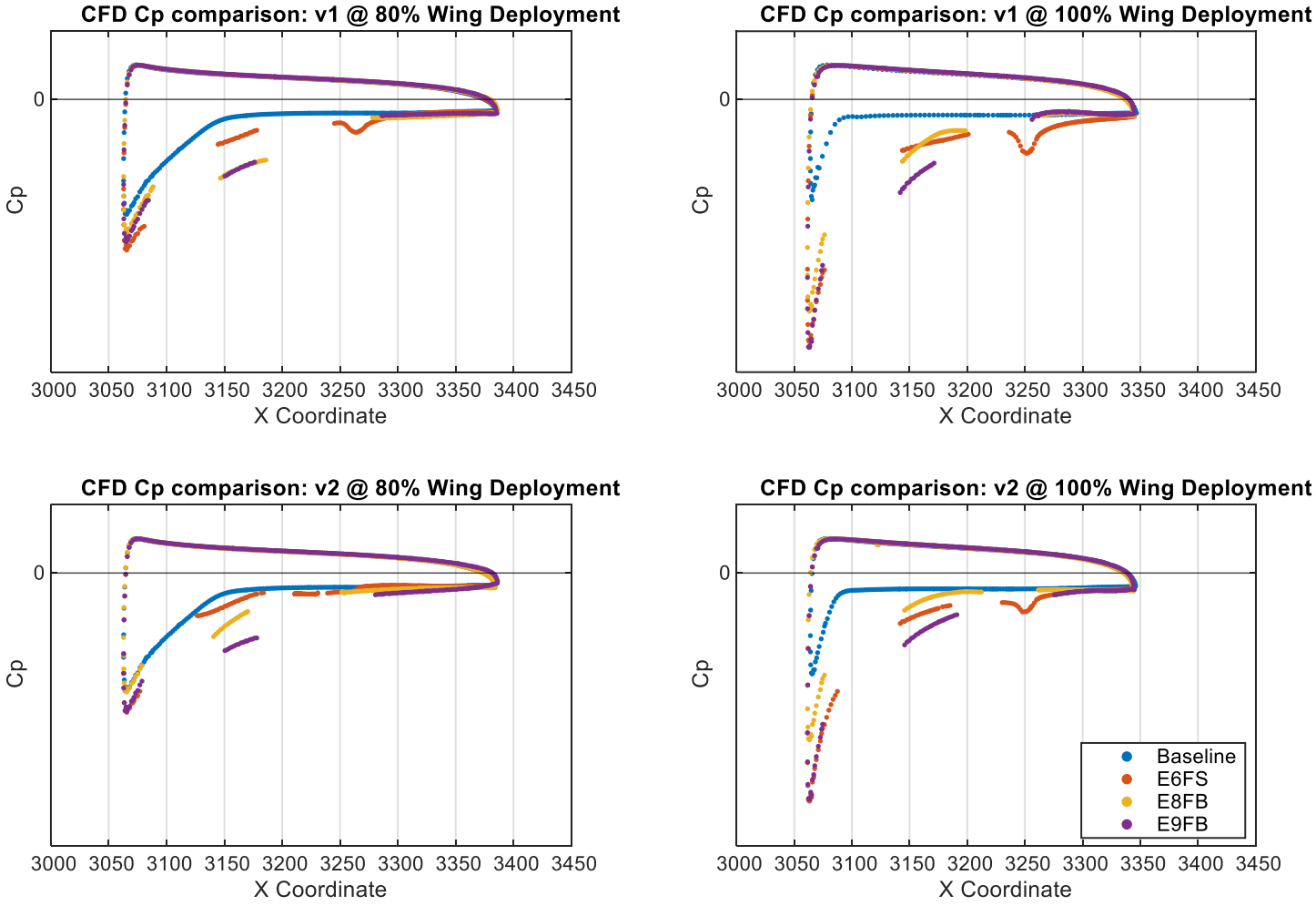

Figure 6.14 Comparison of CFD−predicted local pressure coefficient distributions on the rear wing section (Section 280 mm) for the baseline, E6FS, E8FB, and E9aFB configurations at velocity profiles v1 and v2, 80% and 100% wing deployment, and 100% fan speed.

Among the investigated solutions, E9aFB produces the most pronounced modification of the pressure distribution within the controlled region, whereas E6FS exhibits a less uniform

pressure recovery. In contrast, both E8FB and E9aFB generate smoother pressure distribution trends over the instrumented section. The influence of the Co−Flow system progressively decreases away from the fan centreline, where three−dimensional flow effects and support−induced flow structures become increasingly important. However, the CFD comparison reveals clear differences between the investigated configurations, high-lighting the sensitivity of the pressure−field response to the selected blowing−suction arrangement and to the interaction between the injected flow and the external aerodynamic field. The CFD predictions were subsequently compared against experimental pressure measurements obtained from the instrumented wing section aligned with the fan centreline.

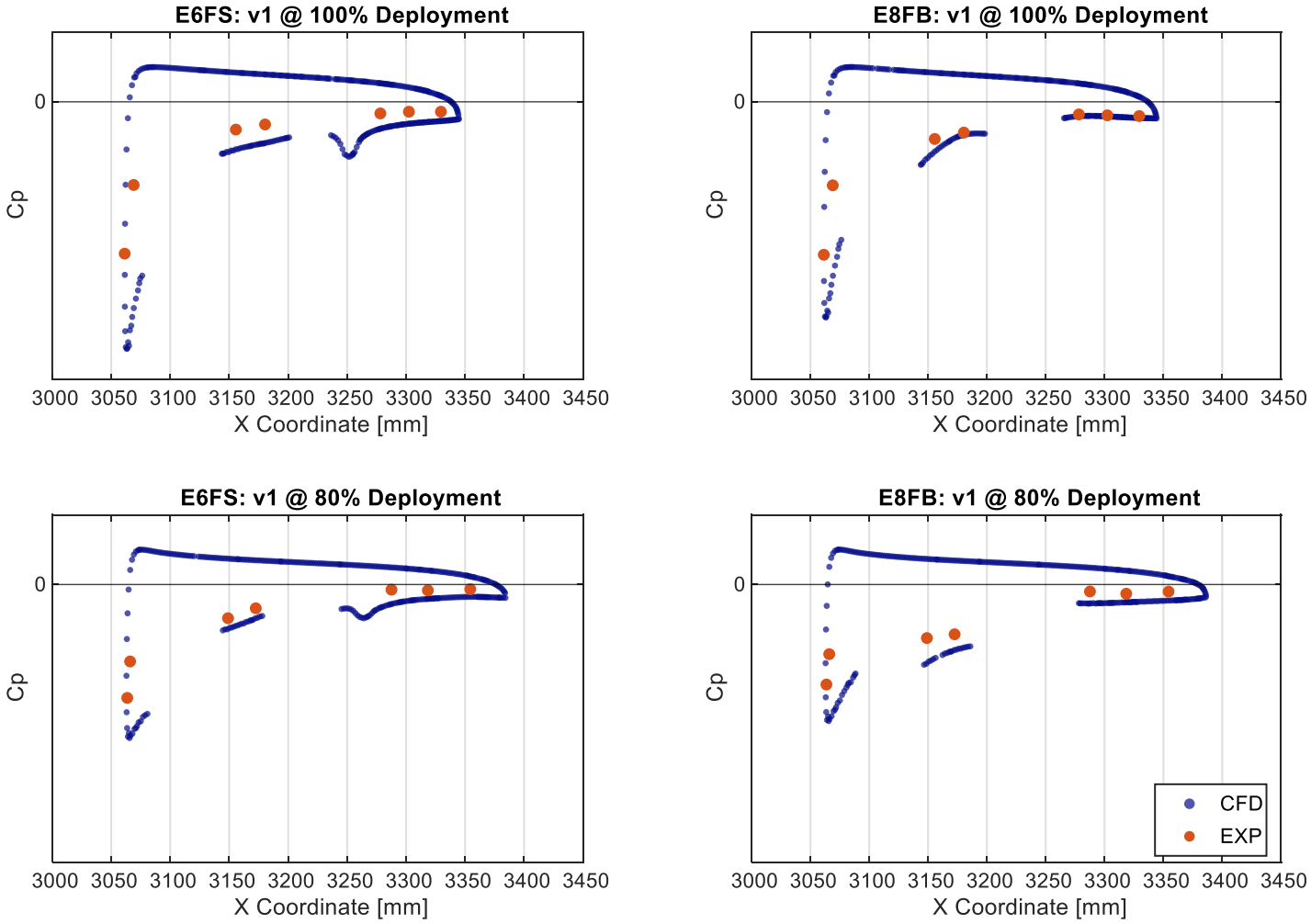

Figure 6.15 Comparison between CFD predictions and experimentally measured local pressure coefficient distributions on the rear wing section (Section 280 mm) for the E6FS and E8FB configurations at velocity profile v1, 80% and 100% wing deployment, with the Co−Flow system operating at 100% fan speed.

Good agreement was observed between numerical and experimental C_p distributions, indicating that the CFD model correctly captures the global pressure trends and the relative aerodynamic behaviour of the investigated configurations (Figures 6.15 and 6.16). The largest discrepancies occur near the leading edge and in regions characterized by strong adverse pressure gradients, where the steady RANS simulations tend to predict a more attached flow than that observed experimentally. This behaviour is particularly evident for the E6FS configuration, whose experimental C_p distributions exhibit localized deviations from the numerical predictions. Conversely, E8FB exhibits a smoother pressure recovery and a closer agreement between CFD and experimental pressure distributions, indicating that the aerodynamic response is captured more consistently by the numerical model than in the E6FS configuration.

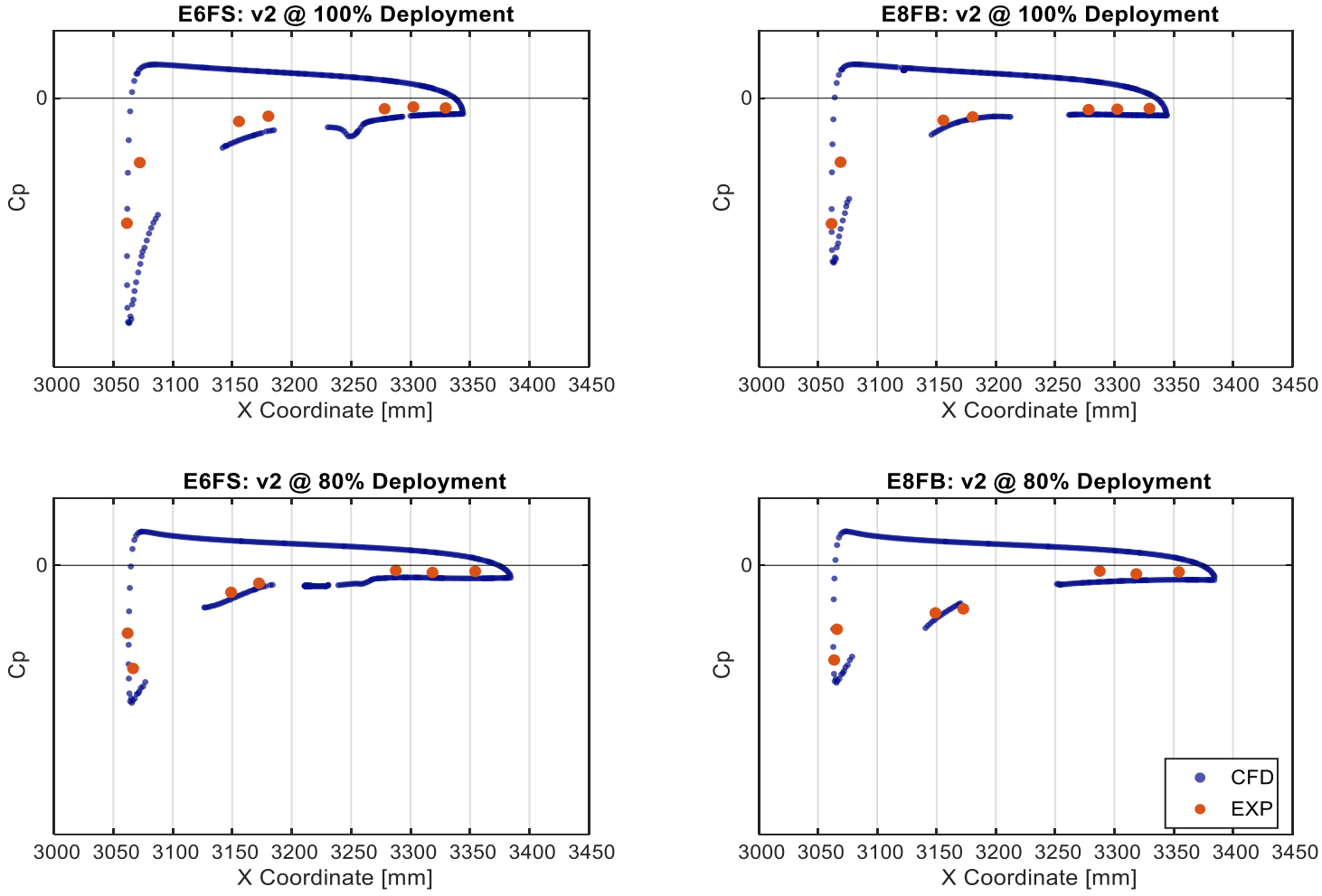

Figure 6.16 Comparison between CFD predictions and experimentally measured local pressure coefficient distributions on the rear wing section (Section 280 mm) for the E6FS and E8FB configurations at velocity profile v2, 80% and 100% wing deployment, with the Co−Flow system operating at 100% fan speed.

Experimental comparisons against the baseline configuration further confirm that the Co−Flow system modifies the pressure distribution over the rear−wing surface. Both E6FS and E8FB generate increased suction levels near the leading−edge region relative to the baseline configuration, with E8FB generally producing the largest deviations from the baseline pressure distributions (Figures 6.17 and 6.18).

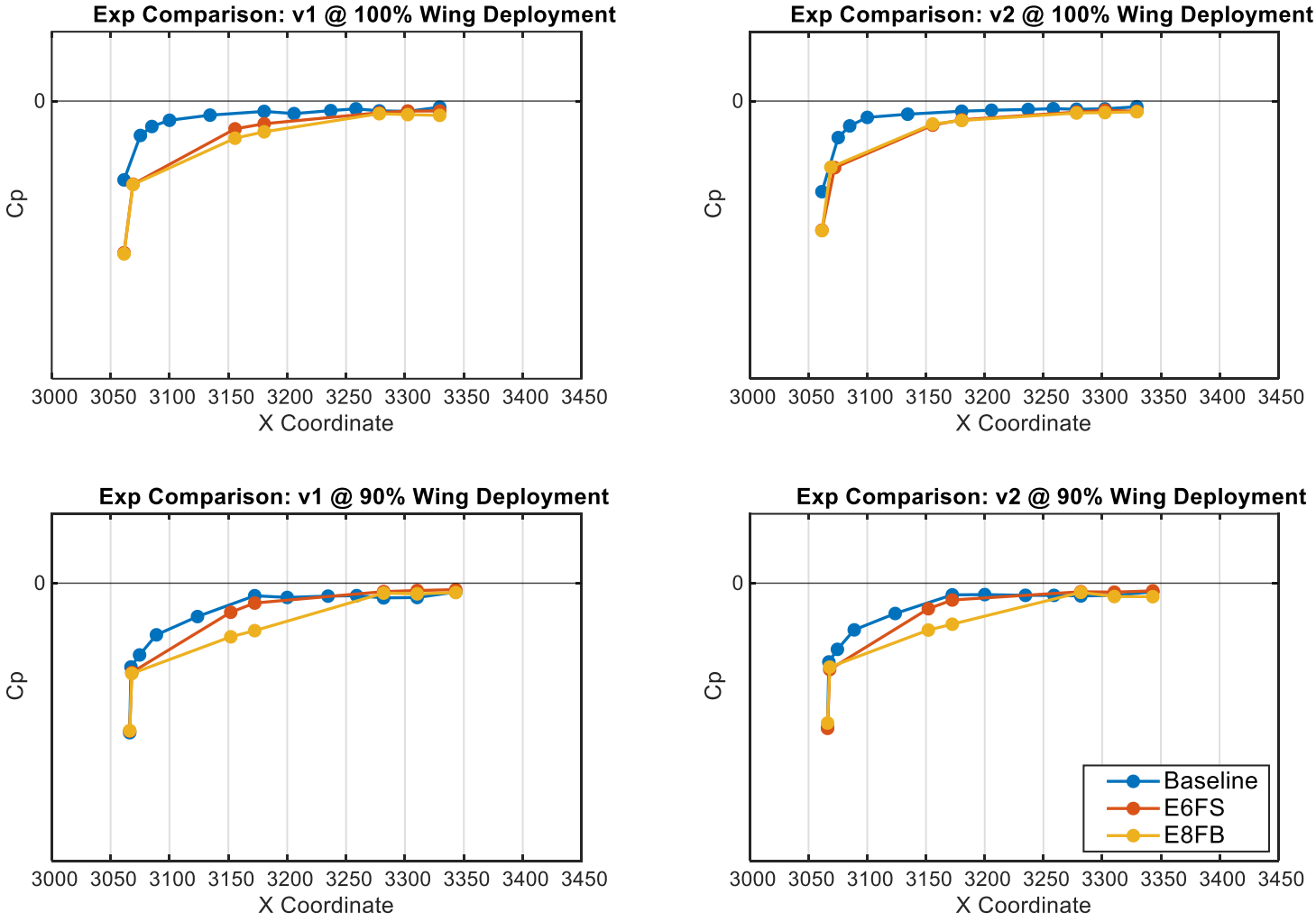

Figure 6.17 Experimental local pressure coefficient distributions measured on the rear wing section (Section 280 mm) for velocity profiles v1 and v2, comparing the baseline, E6FS, and E8FB configurations at 90% and 100% wing deployment with 100% fan speed.

This behaviour indicates that the influence of the Co−Flow system becomes more evident under highly loaded wing conditions. The largest pressure−distribution modifications are generally observed at high wing−deployment settings and low vehicle speeds, which also correspond to the operating conditions associated with the highest momentum−coefficient levels. As vehicle speed increases, the available momentum coefficient decreases due to the increase in freestream

dynamic pressure, and the relative influence of the Co−Flow system on the pressure distributions generally becomes smaller compared to the baseline setup (Figures 6.19 and 6.20).

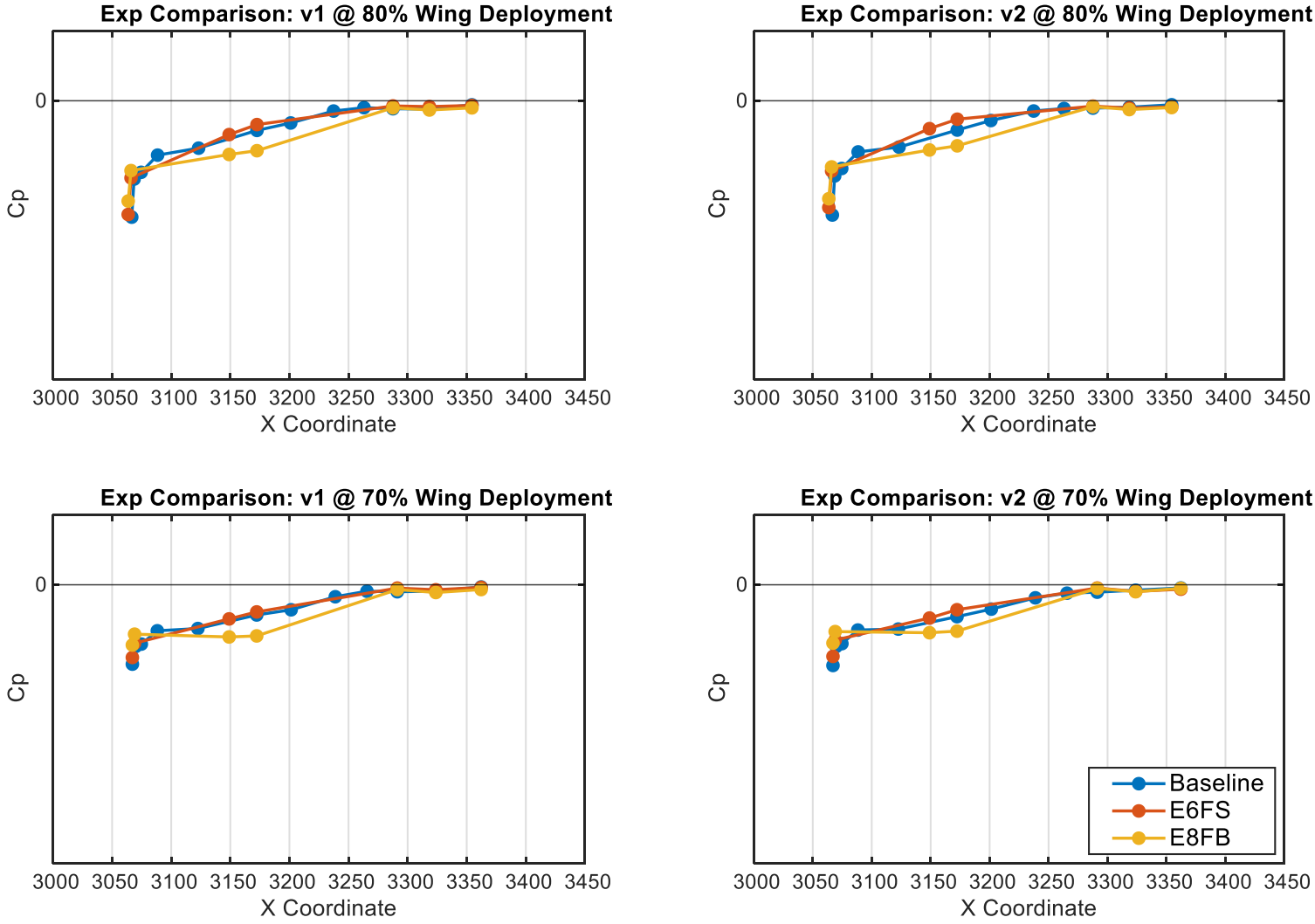

Figure 6.18 Experimental local pressure coefficient distributions measured on the rear wing section (Section 280 mm) for velocity profiles v1 and v2, comparing the baseline, E6FS, and E8FB configurations at 70% and 80% wing deployment with 100% fan speed.

These observations suggest that the achievable mass flow rate and the resulting momentum coefficient influence the pressure−distribution modifications generated by the Co−Flow system. However, consistent with the lift−coefficient analysis presented previously, the present results indicate that the aerodynamic response cannot be described solely in terms of momentum coefficient magnitude. Configurations exhibiting similar momentum coefficient levels may still produce different pressure distributions and different aerodynamic benefits,

indicating that the effectiveness of the actuation also depends on the interaction between the injected flow, the local pressure field, and the wing geometry.

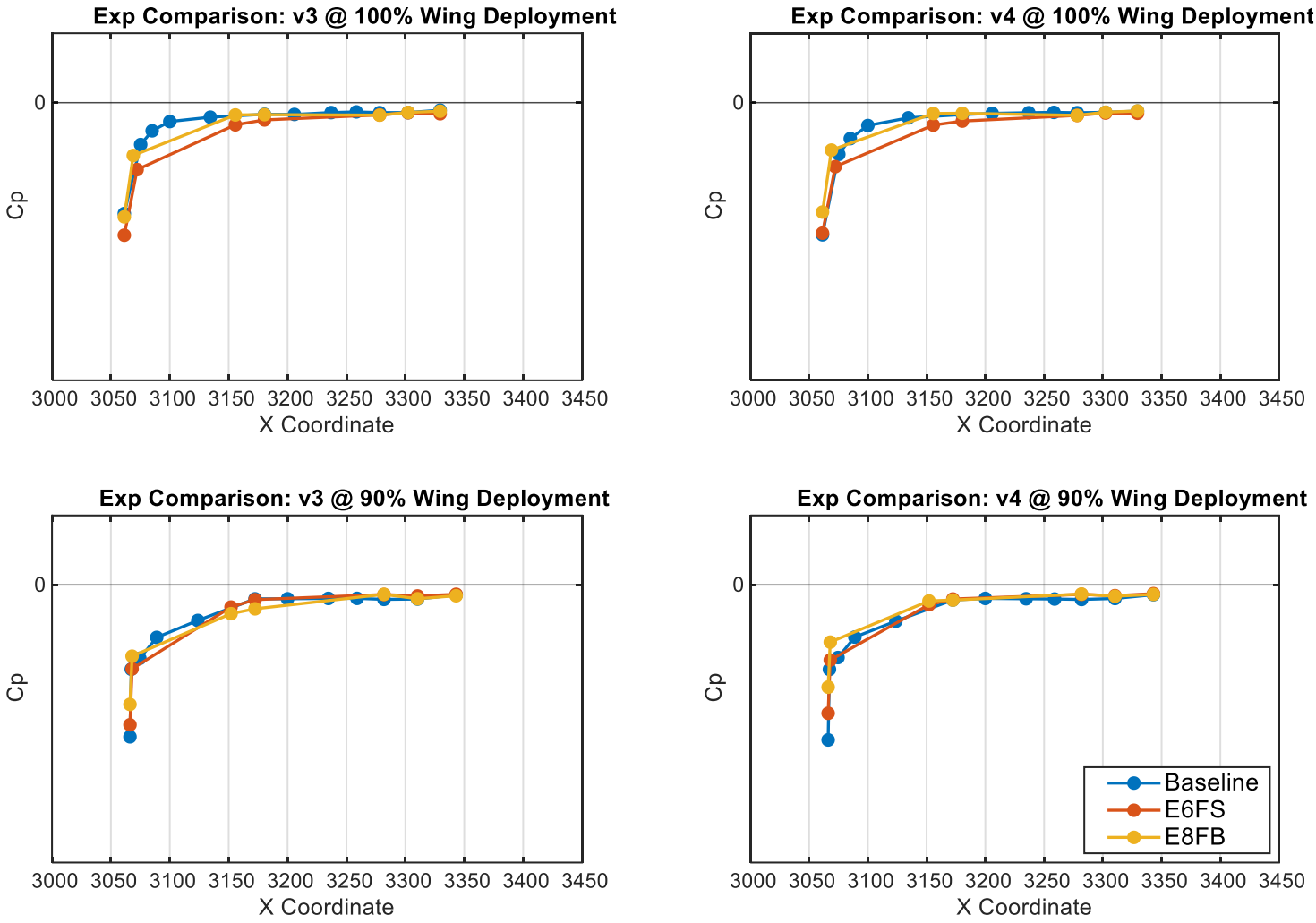

Figure 6.19 Experimental local pressure coefficient distributions measured on the rear wing section (Section 280 mm) for velocity profiles v3 and v4, comparing the baseline, E6FS, and E8FB configurations at 90% and 100% wing deployment with 100% fan speed.

To assess the robustness of the experimental campaign, the coefficient of variation (CV) was evaluated for both the aerodynamic measurements and the monitored Co−Flow operating parameters. The resulting global metrics are summarized in Table 6.3.

Parameter	C_d	C_l	RPM Fan 1	MFR1	MFR2	P_{elec}	PWM Fan 1	PWM Fan 2	Density
Average CV [%]	1.80%	2.83%	0.01%	3.06%	2.29%	0.76%	0.09%	0.24%	0.12%

Table 6.3. Global coefficient of variation (CV) metrics for the aerodynamic measurements and monitored Co−Flow operating parameters, calculated across all investigated configurations and operating conditions.

The low coefficients of variation demonstrate that both the aerodynamic measurements and the Co-Flow operating parameters remained stable throughout the experimental campaign. In particular, the extremely low variability of the fan rotational speed (0.01%) confirms that the control system maintained the prescribed operating conditions with high precision, ensuring that differences observed between configurations are primarily attributable to the investigated geometries rather than to fluctuations in the actuation system.

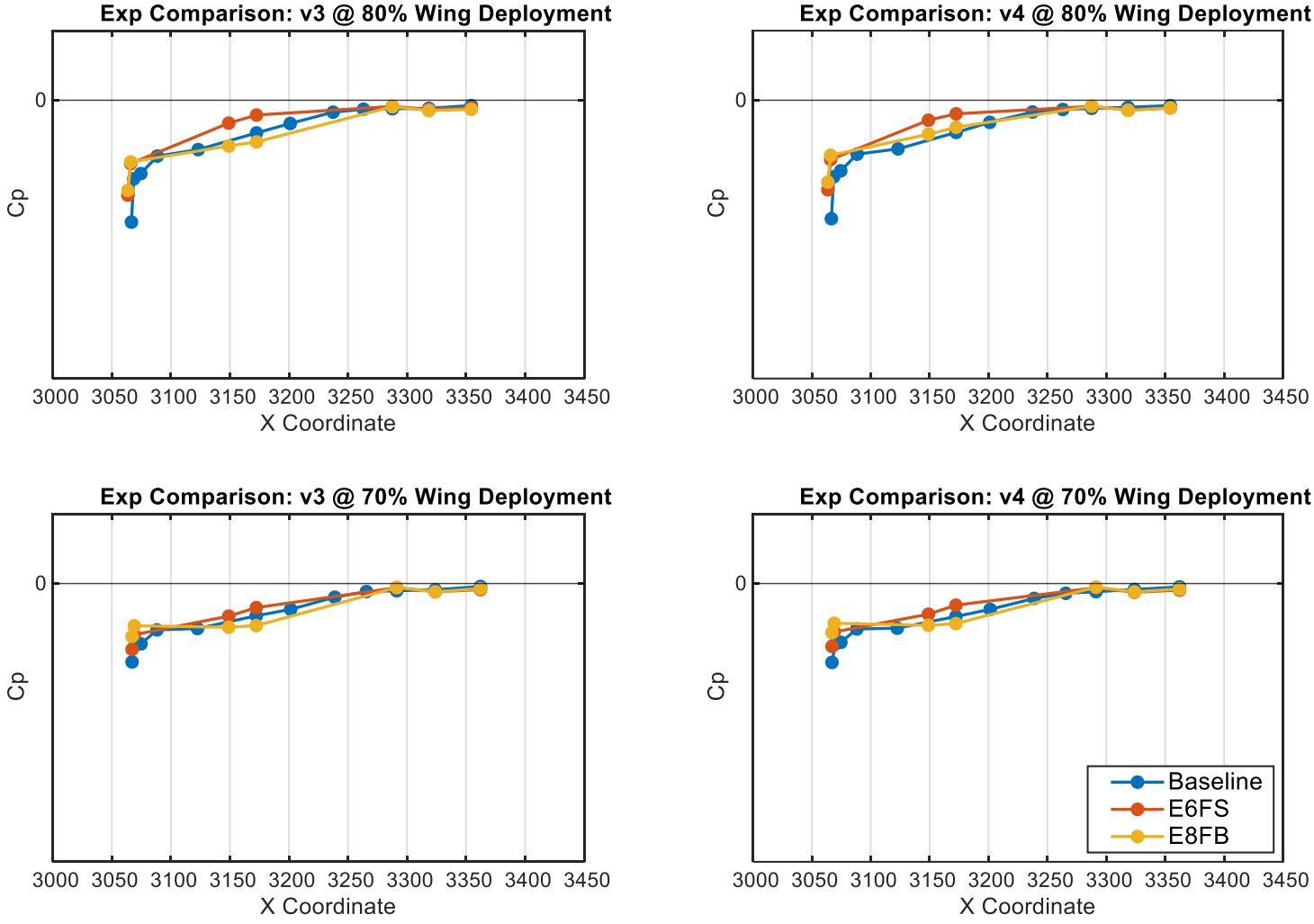

Figure 6.20 Experimental local pressure coefficient distributions measured on the rear wing section (Section 280 mm) for velocity profiles v3 and v4, comparing the baseline, E6FS, and E8FB configurations at 70% and 80% wing deployment with 100% fan speed.

Although the mass flow rate measurements exhibit the highest variability (approximately 2–3%), their coefficients of variation remain below 3.1%, indicating satisfactory repeatability of the Co-Flow operation. The results confirm the robustness of the experimental methodology and provide confidence in the comparison between the investigated configurations.
The low variability observed for the fan operating conditions, control signals, flowrate measurements, and environmental parameters confirms the stability of the actuation system throughout the test campaign. Furthermore, the pressure-coefficient measurements were acquired during the same experimental campaign and using the same instrumentation, operating conditions, and data-processing procedures adopted for the vehicle lift-coefficient measurements. Therefore, the repeatability indicated by the aerodynamic measurements provides confidence in the robustness of the reported pressure distributions. These pressure-coefficient trends are based on spatially coherent variations observed across multiple pressure taps and repeated operating conditions, reducing the likelihood that the reported effects arise from measurement scatter. Detailed repeatability statistics for the vehicle drag coefficient, vehicle lift coefficient, and monitored Co−Flow operating parameters are reported in Appendix A (Tables A1−A3).

6.2.4 Efficiency

The energy efficiency of the Co−Flow system was evaluated by comparing the aerodynamic power savings associated with drag reduction against the electrical power consumed by the ducted fans:

$$\eta = \frac{(Drag_{baseline} - Drag_{CoFlow}) \times V_0}{P_{fans}} \tag{6.4}$$

where $Drag_{Baseline,veh}$ and $Drag_{CoFlow,veh}$ are the measured vehicle drag forces for the baseline and Co−Flow configurations, respectively, P_{fans} is the measured electrical power consumed by the two ducted fans and their associated electronic speed controllers, and V_∞ is the vehicle speed. Values of $\eta > 1$ indicate that the aerodynamic power savings associated with drag reduction exceed the electrical power required by the actuation system.
Although the momentum coefficient C_μ represents the governing aerodynamic parameter of the Co−Flow system and was previously discussed in relation to the lift and pressure distribution results, it is not explicitly included in Equation (6.4). The adopted formulation was intentionally based on directly measured aerodynamic and electrical quantities. In contrast, an explicit formulation in terms of C_μ would require the estimation of additional jet−related quantities, including the effective jet velocity and the corresponding jet power.
The influence of C_μ is nevertheless inherently reflected in both the measured drag reduction and the electrical power required to generate the corresponding momentum injection.
Figures 6.21 to Figure 6.23 summarize the efficiency trends obtained for the investigated Co−Flow configurations as a function of vehicle speed, fan rotational speed, and rear wing

deployment. For all configurations, efficiency generally increases with vehicle speed and wing deployment, indicating that the aerodynamic benefits associated with the Co−Flow system become more significant under highly loaded operating conditions. Conversely, increasing fan speed does not necessarily produce proportional efficiency gains, as the additional aerodynamic benefit may be partially offset by the corresponding increase in electrical power consumption. The E6FS configuration consistently exhibits the lowest efficiency levels throughout the investigated operating range (Figure 6.21). While positive aerodynamic benefits are observed under several operating conditions, the resulting drag reduction remains relatively modest compared with the electrical power required by the actuation system.
Consequently, E6FS provides the least favourable balance between aerodynamic performance and energy expenditure among the investigated solutions.

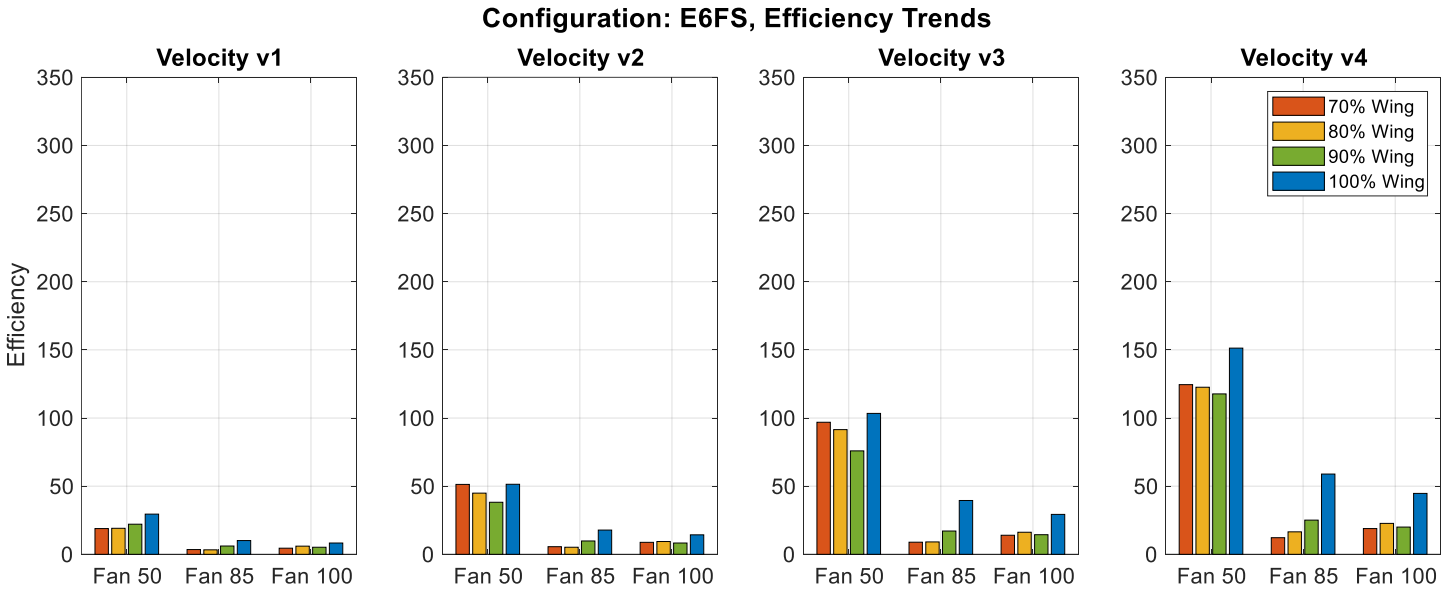

Figure 6.21 Vehicle−level efficiency trends of the E6FS configuration relative to the baseline case, showing the variation in the efficiency metric derived from the complete vehicle aerodynamic response across velocity profiles, wing deployment positions, and fan operating speeds.

The E8FB configuration achieves the highest efficiency and exhibits the most favourable global behaviour (Figure 6.22). Efficiency increases substantially with vehicle speed and reaches its highest values at large wing−deployment angles.

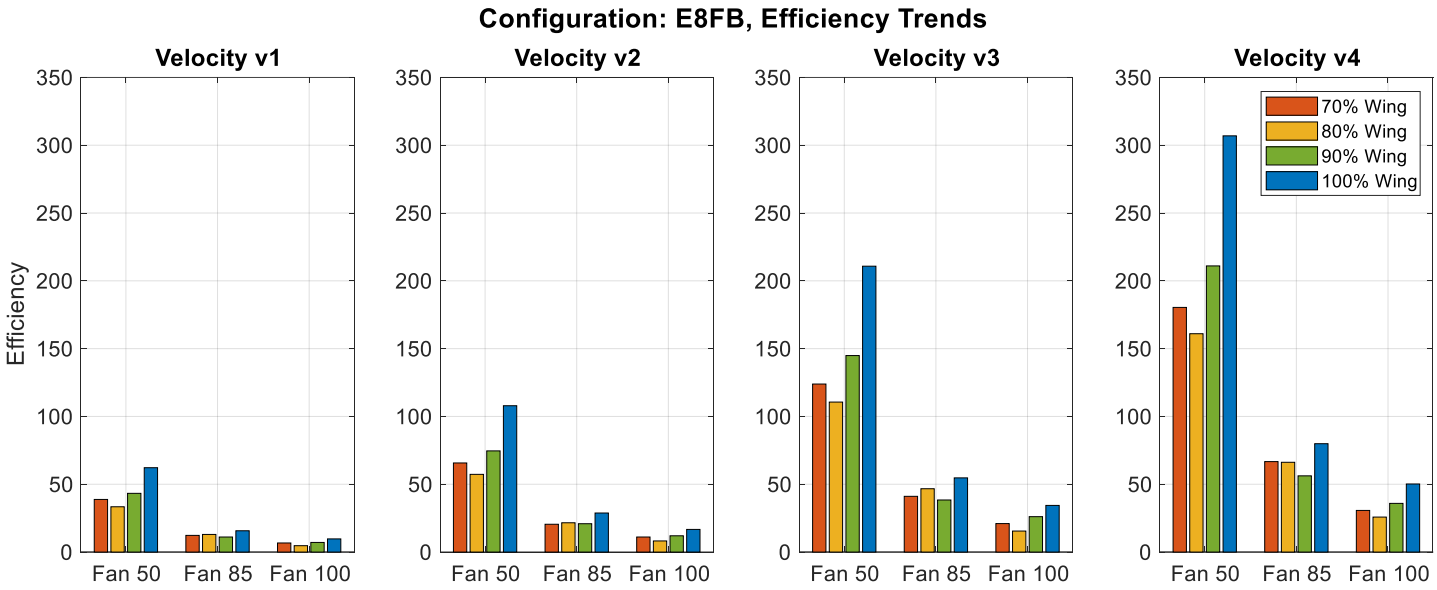

Figure 6.22 Vehicle−level efficiency trends of the E8FB configuration relative to the baseline case, showing the variation in the efficiency metric derived from the complete vehicle aerodynamic response across velocity profiles, wing deployment positions, and fan operating speeds.

The efficiency analysis indicates that the aerodynamic gains obtained with E8FB increase more rapidly than the associated electrical power consumption, resulting in the highest energy return values of the investigated configurations. The E9aFB configuration also achieves substantial efficiency improvements compared with E6FS, particularly at high vehicle speeds and large wing deployment angles (Figure 6.23). However, despite the larger mass−flow capability of this configuration, its efficiency remains generally lower than that achieved by E8FB. This behaviour suggests that the additional momentum injection provided by E9aFB does not translate into proportional aerodynamic benefits over the investigated operating range.

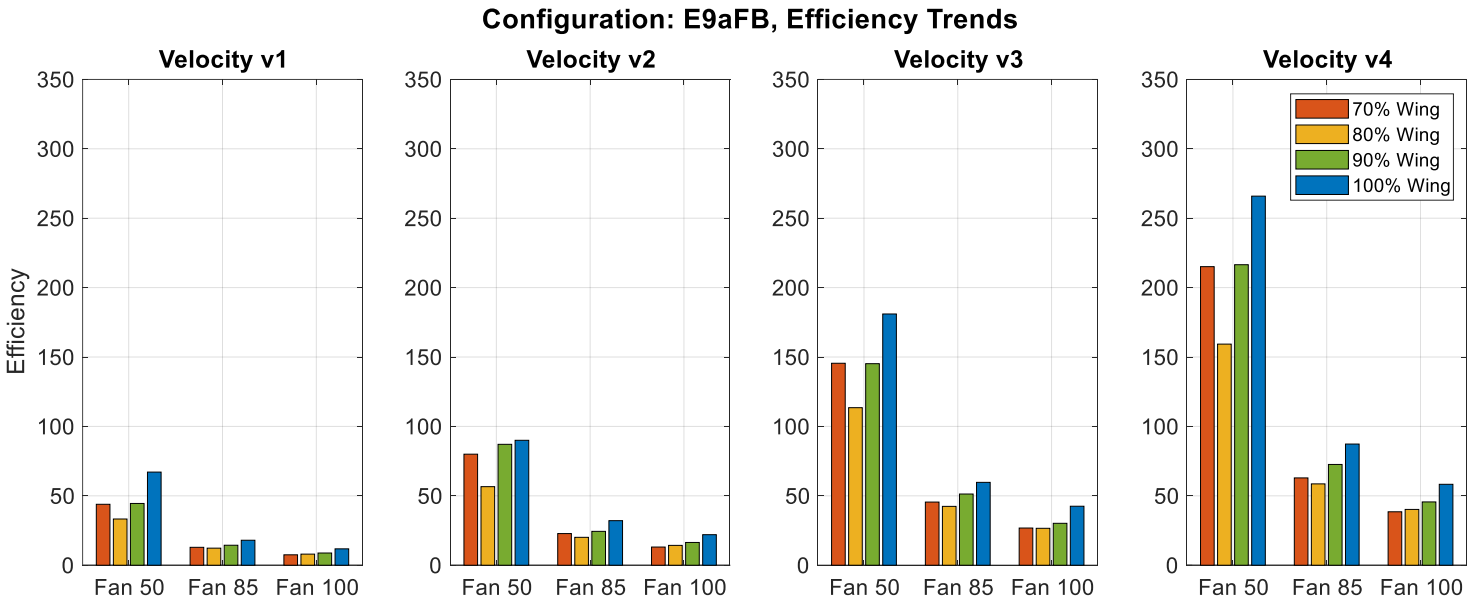

Figure 6.23 Vehicle–level efficiency trends of the E9aFB configuration relative to the baseline case, showing the variation in the efficiency metric derived from the complete vehicle aerodynamic response across velocity profiles, wing deployment positions, and fan operating speeds.

A direct comparison between E8FB and E9aFB further confirms the superior performance of E8FB. As summarized in Table 6.4, E8FB achieves higher efficiency than E9aFB in 37 out of the 48 operating conditions investigated.

Total		Delta Efficiency > 0, E8FB > E9aFB			
E8FB	37				
E9aFB	11				
Veh Speed	% Fan	70	80	90	100
v1	50%	13%	−1%	3%	8%
v1	85%	4%	−6%	29%	14%
v1	100%	12%	69%	23%	22%
v2	50%	22%	−1%	17%	−17%
v2	85%	11%	−7%	17%	12%
v2	100%	18%	73%	37%	32%
v3	50%	17%	3%	0%	−14%
v3	85%	11%	−9%	34%	9%
v3	100%	28%	72%	16%	24%
v4	50%	19%	−1%	3%	−13%
v4	85%	−6%	−11%	29%	9%
v4	100%	26%	56%	27%	16%

Table 6.4. Relative vehicle-level efficiency difference ($\Delta\eta$) between the E8FB and E9aFB configurations for all investigated velocity profiles, wing deployment positions, and fan speeds. Green cells indicate positive efficiency differences ($\Delta\eta > 0$), corresponding to operating conditions where E8FB is more efficient than E9aFB, whereas blue cells indicate negative efficiency differences ($\Delta\eta < 0$), corresponding to conditions favouring E9aFB. The dominance count reports the total number of favourable operating points for each configuration.

E9aFB outperforms E8FB under a limited number of specific conditions, the ultimate results demonstrate that increasing the available mass flow rate alone is not sufficient to maximize system efficiency. Instead, the aerodynamic effectiveness of the injected momentum and the corresponding electrical power required to generate it must be considered simultaneously. The proposed efficiency metric should therefore be interpreted as an aerodynamic power−balance indicator rather than as a complete vehicle−level energy assessment. Its objective is to quantify the aerodynamic benefit obtained from the Co−Flow system relative to the electrical power required for its operation under representative vehicle operating conditions. The metric provides a practical comparison between different Co−Flow configurations by considering the measured aerodynamic response together with the corresponding electrical power demand of the actuation system. As such, it allows the relative merits of the investigated solutions to be assessed on a common basis and highlights the trade−off between aerodynamic performance and energy expenditure. However, the present analysis does not account for vehicle−level considerations such as battery sizing, additional system mass, thermal management requirements, packaging constraints, durability, or long−term operating strategies. These aspects require a dedicated system integration assessment and are therefore beyond the scope of the present investigation. Consequently, the reported efficiency values should be interpreted as a comparative indicator of aerodynamic effectiveness per unit of electrical power consumed rather than as a prediction of the energy efficiency of a production vehicle.

Chapter 7 – Conclusions

This thesis has presented a combined numerical and experimental investigation of a fan-driven Co-Flow system integrated within the rear wing of a full-scale high-performance vehicle. The study focused on the aerodynamic response of three Co-Flow configurations (E6FS, E8FB, and E9aFB) under realistic on-track operating conditions, considering pressure distributions, vehicle drag, aerodynamic load, and actuation-system power consumption. In this framework, the CFD methodology was primarily employed as a comparative design-support tool and was successfully complemented by full-scale experimental testing. The results suggested that the flow-control effectiveness of the investigated Co-Flow systems is strongly influenced by duct architecture, operating conditions, and the balance between blowing and suction. Among the tested configurations, E8FB consistently provided the most favourable compromise between aerodynamic effectiveness and power consumption across the investigated operating envelope. This configuration achieved repeatable drag reductions and downforce improvements while maintaining comparatively robust behaviour over a broad range of fan operating conditions. In contrast, E9aFB has shown that increasing mass-flow capability alone does not necessarily translate into superior aerodynamic performance; although it occasionally achieved larger peak benefits, its response was more sensitive to operating conditions and showed a stronger tendency toward diminishing aerodynamic returns at higher actuation levels. Similarly, E6FS exhibited limited effectiveness, particularly under highly loaded operating conditions, where the front-suction arrangement restricted the achievable flow-control authority. The experimental results further indicate that the aerodynamic benefits obtained from these Co-Flow systems are governed not only by the magnitude of the injected momentum but also by its interaction with the external aerodynamic loading. The pressure-coefficient measurements and aerodynamic-force trends suggest improved pressure recovery for the most effective configurations. However, it should be noted that the underlying flow mechanisms were inferred from the combined interpretation of CFD results and surface-pressure measurements rather than from direct experimental flow-field measurements. Furthermore, while the efficiency analysis has shown that the best-performing configurations can produce aerodynamic benefits that exceed the electrical power required by the actuation system under selected operating conditions, the adopted efficiency metric should be interpreted strictly as an aerodynamic power-balance indicator based on experimentally measured quantities, rather than as a complete vehicle-level energy assessment. The quantitative findings presented in this thesis should be interpreted within the specific vehicle configuration and operating envelope investigated. Because the experimental campaign was conducted on a single production-based vehicle and restricted to three specific architectures, these quantitative results should not be directly generalized to different vehicle geometries or operating conditions. Nevertheless, the present investigation represents a full-scale demonstration of the integration and operation of a fan-driven Co-Flow system on a production-based high-performance vehicle. The combined

numerical and full-scale experimental approach provides a consistent framework for assessing the aerodynamic and energetic performance of active flow-control systems under realistic automotive conditions. While additional investigations are required to extend the applicability of the proposed approach, the methodology developed in this research provide a structured framework for the design, implementation, and experimental evaluation of active flow-control technologies in high-performance automotive applications. Moving forward, future work should address several key areas to expand upon the foundations laid by this research. First, the assessment of additional duct geometries and actuation strategies will be essential to evaluate the scalability and adaptability of the system across different vehicle platforms. Furthermore, future investigations must transition toward broader operating conditions and practical engineering constraints, with a specific focus on packaging limitations, long-term durability, and acoustic behaviour. Finally, aspects beyond the scope of the present investigation, including battery sizing, system mass, thermal management, and advanced closed-loop control strategies should be considered in future studies to enable a more comprehensive vehicle-level assessment of the overall energetic performance and practical feasibility of the proposed approach.

Beyond the aerodynamic results themselves, the principal contribution of this work is the development and experimental validation of an integrated methodology combining CFD-based design, laboratory fan characterization, additive manufacturing, full-scale vehicle instrumentation, and on-track testing.

Published Article

Herberg, M.R.; Bambino, G.L.; De Pinto, S.; Pascazio, G.; de Tullio, M.D. Experimental and Numerical Investigation of an Integrated Fan-Driven Co-Flow Jet System for a High-Performance Automotive Rear Wing. Fluids 2026, 11, 161. https://doi.org/10.3390/fluids11060161

Appendix A. Experimental Repeatability Assessment

To quantify the repeatability of the experimental campaign, the coefficient of variation (CV [%]) was evaluated using repeated acquisitions according to:

$$\mathrm{CV}(\mathrm{C}_{X,\mathrm{veh}})\ [\%] = \frac{\sigma_{\mathrm{C_X}}}{\mu_{\mathrm{C}_X}} \times 100 \qquad \text{(A1)}$$

where $\sigma_{\mathrm{C_X}}$ is the standard deviation of the repeated measurements and μ_{C_X} is the corresponding mean value. The repeatability assessment was performed separately for the vehicle drag coefficient and the vehicle lift coefficient, since the two quantities were obtained using different experimental procedures. For the drag coefficient, repeatability was evaluated from repeated coastdown measurements performed under identical operating conditions. The resulting coefficient of variation was calculated for each investigated Co−Flow configuration, fan−speed setting, and wing deployment condition. For the lift coefficient and the monitored Co−Flow operating parameters, repeatability was evaluated from repeated steady−state measurements performed for each combination of vehicle speed, wing−deployment setting, fan rotational speed, and Co−Flow configuration. The resulting CV values were subsequently averaged to provide representative repeatability metrics for each configuration, while the standard deviation of the calculated CV values was used to quantify the variability of the repeatability across the investigated operating envelope. Table A1 reports the detailed repeatability metrics for the vehicle drag coefficient, while Tables A2 and A3 summarize the average coefficient of variation and the corresponding standard deviation obtained for the vehicle lift coefficient and the monitored Co−Flow operating parameters throughout the experimental campaign.

Design	Wing Deployment	Fan RPM [%]	CV($C_{d,veh}$) [%]
E6FS	70%	50%	2.94%
	80%	50%	3.14%
	90%	50%	0.63%
	100%	50%	1.59%
	70%	85%	1.22%
	80%	85%	1.08%
	90%	85%	1.93%
	100%	85%	1.17%
	70%	100%	2.21%
	80%	100%	2.32%
	90%	100%	0.71%
	100%	100%	1.65%
E8FB	0%	0%	1.57%
	0%	30%	1.20%
	0%	50%	0.89%
	70%	50%	2.36%
	80%	50%	1.05%
	90%	50%	2.77%
	100%	50%	0.88%
	70%	85%	1.33%

	80%	85%	2.71%
	90%	85%	0.79%
	100%	85%	1.78%
	70%	100%	2.92%
	80%	100%	1.63%
	90%	100%	1.61%
	100%	100%	2.68%
E9aFB	0%	0%	2.04%
	0%	30%	2.13%
	0%	50%	1.64%
	70%	50%	1.50%
	80%	50%	1.55%
	90%	50%	2.35%
	100%	50%	1.86%
	70%	85%	2.86%
	80%	85%	1.57%
	90%	85%	1.35%
	100%	85%	1.87%
	70%	100%	1.61%
	80%	100%	1.51%
	90%	100%	1.69%
	100%	100%	3.40%

Table A1. Detailed coefficient of variation (CV) of the vehicle drag coefficient, CV($Cd_{,veh}$), obtained from re-peated coastdown measurements for all investigated Co−Flow configurations, fan speed settings, and wing deployment conditions. The average coefficient of variation across the complete experimental campaign was 1.80%, with a standard deviation of 0.70%.

Design	Fan	Parameter	C_l	RPM Fan 1	MFR1	MFR2	P_{elec}	PWM Fan 1	PWM Fan 2	Density
E6FS	50%	Average CV [%]	3.00%	0.00%	3.97%	4.04%	0.83%	0.05%	0.22%	0.18%
	85%	Average CV [%]	4.51%	0.01%	1.27%	1.54%	1.46%	0.15%	0.51%	0.16%
	100%	Average CV [%]	3.70%	0.01%	1.96%	1.97%	1.39%	0.17%	0.59%	0.08%
E8FB	50%	Average CV [%]	2.16%	0.00%	4.20%	2.69%	0.21%	0.01%	0.03%	0.08%
	85%	Average CV [%]	3.28%	0.02%	8.48%	3.93%	0.54%	0.11%	0.14%	0.15%
	100%	Average CV [%]	1.90%	0.00%	5.47%	3.34%	0.48%	0.08%	0.18%	0.09%
E9aFB	50%	Average CV [%]	1.48%	0.00%	0.68%	1.06%	0.54%	0.03%	0.12%	0.06%
	85%	Average CV [%]	2.82%	0.02%	0.75%	1.17%	0.71%	0.13%	0.19%	0.22%
	100%	Average CV [%]	2.63%	0.01%	0.76%	0.90%	0.64%	0.09%	0.19%	0.08%

Table A2. Average coefficient of variation (CV) of the vehicle lift coefficient, CV($C_{l,veh}$), and of the monitored Co−Flow operating parameters, evaluated from repeated steady−state measurements for all investigated Co−Flow configurations and fan−speed settings. The reported values correspond to the mean CV calculated across the investigated vehicle−speed and wing−deployment conditions.

Design	Fan	Parameter	C_l	RPM Fan 1	MFR1	MFR2	P_{elec}	PWM Fan 1	PWM Fan 2	Density
E6FS	50%	CV Std. Dev. [%]	2.05%	0.00%	5.78%	6.22%	0.53%	0.03%	0.16%	0.37%
	85%	CV Std. Dev. [%]	2.41%	0.02%	0.79%	1.34%	1.21%	0.07%	0.66%	0.10%
	100%	CV Std. Dev. [%]	2.01%	0.01%	3.09%	3.42%	2.32%	0.14%	1.03%	0.07%
E8FB	50%	CV Std. Dev. [%]	3.00%	0.00%	6.97%	7.60%	0.31%	0.02%	0.03%	0.12%
	85%	CV Std. Dev. [%]	1.48%	0.02%	7.56%	4.54%	0.68%	0.09%	0.10%	0.17%

	100%	CV Std. Dev. [%]	1.27%	0.01%	3.53%	2.62%	0.35%	0.06%	0.12%	0.21%
E9aFB	50%	CV Std. Dev. [%]	0.76%	0.00%	0.70%	1.31%	0.54%	0.02%	0.13%	0.08%
	85%	CV Std. Dev. [%]	1.21%	0.02%	0.67%	1.75%	0.71%	0.09%	0.18%	0.25%
	100%	CV Std. Dev. [%]	1.31%	0.01%	0.61%	1.31%	0.60%	0.06%	0.09%	0.10%

Table A3. Standard deviation of the coefficient of variation (CV) of the vehicle lift coefficient, CV($C_{l,veh}$), and of the monitored Co−Flow operating parameters, evaluated from repeated steady−state measurements for all investigated Co−Flow configurations and fan−speed settings. The reported values quantify the variability of the repeatability across the investigated vehicle−speed and wing−deployment conditions.

Appendix B - Accuracy of Measurement Chain

B.1 Introduction

Experimental investigations inevitably involve measurement uncertainties arising from the instrumentation, data acquisition systems, and environmental conditions. Since the aerodynamic performance improvements investigated throughout this work are often of the order of only a few percentage points, a rigorous uncertainty assessment is essential to ensure that the measured variations are physically meaningful and exceed the experimental uncertainty. The uncertainty analysis presented in this appendix follows the principles of the Guide to the Expression of Uncertainty in Measurement (GUM, JCGM 100:2008). The objective is to quantify the confidence associated with every measured quantity used throughout the thesis and to evaluate how these uncertainties propagate into the derived aerodynamic parameters. Whenever possible, the uncertainty budget includes contributions associated with:

- sensor calibration accuracy;
- electronic acquisition resolution;
- analogue-to-digital converter quantization;
- manufacturer specifications;
- repeatability of the measurements (Type A uncertainty);
- systematic effects (Type B uncertainty).

The combined standard uncertainty is evaluated using the root-sum-square (RSS) method,

$$u_c(f) = \sqrt{\sum_i \left(\frac{\partial f}{\partial x_i} u(x_i)\right)^2} \tag{B1}$$

where $\boldsymbol{u_c(f)}$ represents the standard uncertainty associated with each independent input quantity. The expanded uncertainty is then obtained as

$$U\,(f) = k\,u_c(f) \tag{B2}$$

where a coverage factor $k = 2$ is adopted and corresponding to an approximate confidence level of 95%. Unless otherwise specified, all uncertainty values reported in this appendix refer to expanded uncertainties. The uncertainty analysis is organised according to the different measurement systems employed throughout the experimental campaign, including pressure sensors, ambient-condition sensors, suspension displacement sensors, vehicle speed measurements, and the electronic acquisition systems used during laboratory characterization and full-scale vehicle testing.

B.2 Instrumentation and Data Acquisition

The experimental campaign presented throughout this thesis relied on multiple measurement systems operating both during laboratory characterization of the Co-Flow actuation system and during full-scale vehicle testing. The instrumentation was selected to provide accurate measurements of the aerodynamic quantities required for the evaluation of the proposed active flow-control methodology while ensuring compatibility with the harsh operating conditions encountered during on-track testing. The complete measurement chain comprised pressure sensors, suspension displacement sensors, ambient-condition sensors, vehicle dynamics instrumentation, and dedicated electronic acquisition systems. Depending on the specific experiment, measurements were either acquired directly through the vehicle Controller Area Network (CAN) or digitized using dedicated microcontrollers specifically configured for laboratory measurements.

Instrument	Manufacturer	Measurement	Range	Acquisition
Differential pressure sensor	Texense DPS-190	Differential pressure	0–190 mbar	Teensy 4.1
Differential pressure sensor	Texense DPS-90	Differential pressure	0–90 mbar	Arduino R4
Ambient sensor	Bosch BME280	Temperature, humidity and pressure	0° to +65°C, 20% to 80% RH, 300-1100hPa	Teensy 4.1
Suspension displacement sensor	Bosch Rotary Sensor	Angular displacement	Vehicle suspension travel	CAN bus
Vehicle speed and dynamics	Racelogic - VBOX	Speed, acceleration, position	1000Mph, 20g, 1.8m	CAN / VBOX
Ducted fan electrical measurements	Isabellenhütte® IVT−S−100A−U0−I−CAN2−12	Voltage and current	12V, 100A	CAN bus

Table B.1 Main instrumentation employed throughout the experimental campaign.

Pressure measurements constituted the primary experimental quantities used throughout this work. During laboratory fan characterization, differential pressure measurements were acquired using a Texense DPS-190 sensor connected to a Teensy 4.1 microcontroller, whereas full-scale vehicle tests employed a Texense DPS-90 sensor interfaced with an Arduino R4 acquisition system. Ambient conditions were monitored using a Bosch BME280 sensor to account for variations in air density during testing. Vehicle aerodynamic loads were indirectly estimated from suspension displacement measurements acquired through the vehicle CAN network, while vehicle speed and longitudinal acceleration were obtained using a Racelogic VBOX system.

B.3 Uncertainty Evaluation Methodology

The uncertainty associated with each measurement system was evaluated by identifying the individual contributions affecting the measured quantity. Depending on the available information, uncertainty components were classified as either Type A or Type B.
Type A uncertainties were estimated from repeated measurements using statistical analysis. For a set of $n$observations, the corresponding standard uncertainty is

$$u_A = \frac{s}{\sqrt{n}} \tag{B3}$$

where s is the experimental standard deviation. Type B uncertainties were evaluated from non-statistical information, including manufacturer specifications, calibration certificates, sensor resolution, and electronic acquisition characteristics. Unless otherwise stated, manufacturer accuracy specifications were assumed to follow a rectangular probability distribution, yielding

$$u_B = \frac{a}{\sqrt{3}} \tag{B4}$$

where $a$is the half-width of the specified tolerance interval. For measurements acquired through analogue-to-digital converters, an additional uncertainty component associated with signal quantization was considered. Assuming a uniform distribution within one least significant bit (LSB), the corresponding standard uncertainty is

$$u_q = \frac{\mathrm{LSB}}{\sqrt{12}} \tag{B5}$$

where

$$\mathrm{LSB} = \frac{FS}{2^N} \tag{B6}$$

with FS representing the full-scale input range and N the ADC resolution. The uncertainty budgets presented in the following sections identify the dominant contributions for each measurement system and evaluate their influence on the overall measurement uncertainty.

B.4 Measurement System Uncertainty

Differential pressure measurements were performed during both the laboratory characterization of the ducted fan and the full-scale vehicle experiments. Since pressure represents the primary quantity used to evaluate the aerodynamic performance of the Co-Flow system, a detailed uncertainty analysis was carried out for the entire measurement chain.
Two different pressure acquisition systems were employed during the experimental campaign. Laboratory fan characterization was performed using a Texense DPS-190 differential pressure sensor, covering a measurement range of 0–190 mbar. The analogue output signal was acquired by a Teensy 4.1 microcontroller through its 12-bit analogue-to-digital converter operating over a 0–3.3 V input range. During full-scale vehicle testing, pressure measurements were acquired using a Texense DPS-90 differential pressure sensor with a measurement range of 0–90 mbar.

The sensor output was digitized by an Arduino UNO R4, whose 14-bit ADC provided higher quantization resolution for on-board measurements. For both acquisition systems, the overall uncertainty was evaluated by considering the principal contributions associated with:

- sensor accuracy;
- analogue-to-digital conversion;
- ADC quantization;
- sensor repeatability (when available).

Environmental effects such as temperature drift were neglected because the measurements were performed within the operating temperature range specified by the manufacturer, where their contribution is significantly smaller than the intrinsic sensor accuracy. The uncertainty budgets for the two acquisition systems are presented separately in the following sections.

B.4.1 Laboratory Measurements

During the laboratory characterization of the ducted fan, the pressure rise generated by the fan was measured using a Texense DPS-190 differential pressure sensor connected to a Teensy 4.1 microcontroller. The sensor provides an analogue voltage proportional to the differential pressure over a measurement range of 0–190 mbar, while the signal was digitized using the 12-bit analogue-to-digital converter integrated into the Teensy 4.1. The uncertainty associated with the pressure measurements was evaluated by considering the complete measurement chain, including the intrinsic sensor accuracy and the uncertainty introduced by the analogue-to-digital conversion process. According to the manufacturer's specifications, the differential pressure sensor has an accuracy of ±1% of the full-scale output. The accuracy is specified as a percentage of full scale. The corresponding absolute error bound is:

$$a = 0.01 \cdot 190 = 1.9 \text{ mbar} \tag{B7}$$

Assuming a rectangular probability distribution, as recommended by the GUM for manufacturer tolerance specifications, the corresponding standard uncertainty is

$$u_{acc} = \frac{0.01 \times 190}{\sqrt{3}} = 1.10 \text{ mbar} \tag{B8}$$

The digital acquisition introduces an additional uncertainty due to ADC quantization. For a 12-bit converter operating over the entire sensor measurement range

$$\text{LSB} = \frac{Vref}{2^{12}} = \frac{3.3}{4096} = 0.000805 \text{ V} \tag{B9}$$

$$\text{Sensitivity S} = \frac{Range}{Vref} = \frac{190}{3.3} = 57.58 \frac{\text{mbar}}{\text{V}} \quad \text{(B10)}$$

Assuming a uniform probability distribution within one quantization interval

$$u_q = \frac{LSB}{\sqrt{12}} = \frac{0.0464}{\sqrt{12}} = 0.0134 \text{ mbar} \quad \text{(B11)}$$

ADC noise assumed equal to 2 LSB RMS:

$$\sigma_V = 2 * \text{LSB} = 0.00161 \text{ V} \quad \text{(B12)}$$

$$u_{noise} = \sigma_V * S = 0.0927 \text{ mbar} \quad \text{(B13)}$$

The uncertainty associated with ADC quantization is therefore almost two orders of magnitude smaller than the intrinsic sensor accuracy.

The Teensy 4.1 ADC also exhibits additional uncertainties associated with reference voltage stability and integral non-linearity. However, according to the manufacturer specifications, these contributions remain significantly smaller than the pressure sensor accuracy and were therefore considered negligible in the overall uncertainty budget. Assuming independent uncertainty sources, the combined standard uncertainty becomes

$$u_c(p) = \sqrt{u_{acc}^2 + u_q^2} \quad \text{(B14)}$$

which gives

$$u_c(p) = \sqrt{1.10^2 + 0.0134^2} = 1.10 \text{ mbar} \quad \text{(B15)}$$

Finally, adopting a coverage factor of $k = 2$

$$U(p) = 2u_c = 2.20 \text{ mbar} \quad \text{(B16)}$$

corresponding to an expanded uncertainty of approximately ±2.2 mbar at a confidence level of approximately 95%.

Source	**Distribution**	**Standard uncertainty (mbar)**	**Contribution**
Sensor accuracy	Rectangular	1.10	Dominant
ADC quantization	Rectangular	0.013	Negligible
ADC reference voltage	Manufacturer specification	Negligible	—

ADC integral non-linearity	Manufacturer specification	Negligible	—
Combined standard uncertainty	—	1.10	—
Expanded uncertainty (k = 2)	—	2.20 mbar	—

Table B.2 Uncertainty budget for laboratory pressure measurements.

The McLaren PIN16 differential pressure sensor was employed throughout the experimental campaign to measure the pressure difference generated by the Co-Flow system. During the laboratory characterization, the sensor was used to determine the static pressure rise across the ducted fan, while in the full-scale vehicle experiments it was employed to measure the pressure distribution required for the calculation of the pressure coefficient (C_p). Since the same sensor and acquisition principle were adopted in both experimental configurations, a single uncertainty analysis is applicable to all pressure measurements presented in this thesis. According to the manufacturer specifications, the sensor operates over a measurement range of 0–150 mbar with an accuracy of ±1.5% of full scale and provides an 11-bit digital output. The manufacturer's accuracy specification represents a maximum permissible error and is therefore treated as a Type B uncertainty assuming a rectangular probability distribution.
The absolute accuracy limit is

$$a = 0.015 \cdot 150 = 2.25 \text{ mbar} \tag{B17}$$

and the corresponding standard uncertainty is

$$u_{acc} = \frac{a}{\sqrt{3}} = \frac{2.25}{\sqrt{3}} = 1.30 \text{ mbar} \tag{B18}$$

The sensor transmits the measured pressure through an 11-bit digital output. The corresponding quantization interval is

$$q = \frac{Range}{2^{11}} = \frac{150}{2048} = 0.073 \text{ mbar} \tag{B19}$$

which results in a standard quantization uncertainty of

$$u_q = \frac{q}{\sqrt{12}} = \frac{0073}{\sqrt{12}} = 0.021 \text{ mbar} \tag{B20}$$

The combined standard uncertainty is obtained by combining the individual contributions using the root-sum-square (RSS) method,

$$u_c(p) = \sqrt{1.30^2 + 0.021^2} = 1.301 \text{ mbar} \tag{B21}$$

Finally, adopting a coverage factor (k=2), the expanded uncertainty becomes

$$U(p) = 2 \times u_c(p) = 2.6 \text{ mbar} \tag{B22}$$

corresponding to an approximate confidence level of 95%. The uncertainty budget is summarized in Table B.3. The results clearly indicate that the overall measurement uncertainty is almost entirely governed by the intrinsic accuracy of the pressure sensor, whereas the contribution associated with the 11-bit digital resolution is negligible.

Source	**Distribution**	**Standard uncertainty (mbar)**
Sensor accuracy	Rectangular	1.30
Digital quantization	Rectangular	0.021
Combined	—	1.30
Expanded (k = 2)	—	2.60

Table B.3 Summary of the uncertainty contributions associated with the McLaren PIN16 differential pressure sensor.

Therefore, all pressure measurements acquired using the McLaren PIN16 sensor are associated with an expanded uncertainty of $U(p) = \pm 2.60$ mbar (95% confidence level), which was subsequently propagated to the derived aerodynamic quantities presented in this work.
Accurate measurements of the ambient conditions were required throughout the laboratory fan characterization. Ambient pressure, air temperature, and relative humidity were continuously monitored using a Bosch BME280 environmental sensor integrated into the acquisition system. These quantities were primarily employed to determine the thermodynamic properties of air, particularly its density, which was subsequently used in the calculation of the aerodynamic coefficients and in the interpretation of the fan operating conditions. Since the uncertainty associated with the BME280 measurements is considerably smaller than the variability of the atmospheric conditions encountered during testing, only the manufacturer specifications were considered in the uncertainty analysis. For atmospheric pressure, according to the Bosch specifications, the BME280 measures atmospheric pressure with a typical absolute accuracy of ±1 hPa over the operating range considered in this work. Assuming a rectangular probability distribution, accuracy can be calculated as

$$u_{acc}(p) = \frac{1}{\sqrt{3}} = 0.577 \text{ hPa}) = 0.577 \text{ mbar} \tag{B23}$$

For the noise, datasheet propose an accuracy of $\pm 2\%$ RMS

$$u_{noise}(p) = 0.2 \text{ mbar} \tag{B24}$$

The corresponding standard uncertainty is

$$u_c(p) = \sqrt{u_{acc}^2 + u_{noise}^2} = 0.611\ mbar \tag{B25}$$

The expanded uncertainty therefore becomes

$$U\,(p) = 2 \times u_c(p) = 1.22 \text{ mbar} \tag{B26}$$

Although atmospheric pressure contributes to the calculation of air density, its influence on the final aerodynamic coefficients is relatively small because pressure variations during the experimental campaign remained limited. For air temperature, the BME280 provides a temperature accuracy of ± 0.5C within the operating temperature range encountered during testing. The corresponding standard uncertainty is

$$u_{acc}(T) = \frac{0.5}{\sqrt{3}} = 0.29°\text{C} \tag{B27}$$

For the noise, datasheet propose an accuracy of 0.005°C RMS

$$u_{noise}(T) = 0.005\ °\text{C} \tag{B28}$$

The corresponding standard uncertainty is

$$u_c(T) = \sqrt{u_{acc}^2 + u_{noise}^2} = 0.2887\ °C \tag{B29}$$

leading to

$$U\,(T) = 2 \times u_c(T) = 0.58°\text{C} \tag{B30}$$

for $k = 2$.
Since air density varies only weakly with temperature over the relatively narrow environmental range experienced during the experiments, this contribution introduces only a minor uncertainty in the calculated aerodynamic parameters. Regarding the relative humidity, it was monitored to improve the estimation of moist-air density. According to the manufacturer specifications, the sensor accuracy is ± 3 %RH. The standard uncertainty therefore becomes

$$u_{acc}(\%RH) = \frac{3}{\sqrt{3}} = 1.73 \text{ \%RH} \tag{B31}$$

For the noise, datasheet propose an accuracy of $\pm 2\%$ RMS

$$u_{noise}(\%RH) = 0.02 \text{ \%RH} \tag{B32}$$

The corresponding standard uncertainty is

$$u_c(\%RH) = \sqrt{u_{acc}^2 + u_{noise}^2} = 1.76\ \%RH \tag{B33}$$

and

$$U\ (\%RH) = 2 \times u_c(\%RH) = 3.52\ \%\text{RH} \tag{B34}$$

for $k = 2$.

Although humidity influences air density, its effect is considerably smaller than that of atmospheric pressure and temperature under the environmental conditions encountered during the experimental campaign.

Quantity	Manufacturer accuracy	Standard uncertainty	Expanded uncertainty (k = 2)
Atmospheric pressure	±1 mbar	0.611 mbar	±1.22 mbar
Temperature	±0.5 °C	0.2887 °C	±0.557 °C
Relative humidity	±3 %RH	1.76 %RH	±3.52 %RH

Table B.4 Uncertainty budget for the BME280 environmental sensor.

The air density used throughout the full-scale vehicle experiments was calculated from the ideal gas law,

$$\rho = \frac{p}{RT}\ [\frac{kg}{m^3}] \tag{B35}$$

Assuming independent uncertainties in pressure and temperature, the relative uncertainty can be estimated as

$$\frac{u_c(\rho)}{\rho} = \sqrt{\left(\frac{u(p)}{p}\right)^2 + \left(\frac{u(T)}{T}\right)^2} \tag{B36}$$

where p is the atmospheric pressure, T is the absolute temperature, and R is the specific gas constant for dry air. A first-order uncertainty propagation indicates that, under typical atmospheric conditions, the uncertainty associated with the calculated air density is expected to remain below 1% when pressure and temperature are measured using standard meteorological instrumentation. However, during the on-track experimental campaign, the atmospheric data were acquired from the vehicle instrumentation, for which neither calibration certificates nor manufacturer uncertainty specifications were available. Consequently, the uncertainty obtained from the theoretical propagation analysis was considered to represent only a lower-bound estimate of the actual measurement uncertainty. To avoid underestimating the influence of ambient conditions on the aerodynamic coefficients, a conservative relative uncertainty of 3% was therefore adopted for the air-density estimation throughout the uncertainty analysis. For an example of air density

$$\rho = \frac{p}{RT} = 1.225\ \frac{kg}{m^3} \tag{B37}$$

the corresponding standard uncertainty becomes

$$u_c(\rho) = 0.03 \times 1.225 = 0.035\ \text{kg m}^{-3} \tag{B38}$$

The electrical power supplied to the ducted fan was determined from simultaneous measurements of current and voltage using an IsabellenHütte IVT-S current and voltage transducer. These measurements were employed to evaluate the electrical power consumption and the overall efficiency of the Co-Flow actuation system. According to the GUM, the first step of the uncertainty analysis consists in defining the measurement model relating the true value of the measurand to the measured value. Since the IVT-S sensor performs direct measurements and no nonlinear corrections are applied, the measurement model is additive, meaning that each error source contributes independently to the measured value, as reported below:

$$I_{\text{meas}} = I_{\text{true}} + \Delta I_{\text{acc}} + \Delta I_{\text{lin}} + \Delta I_{\text{off}} + \Delta I_{\text{noise}} + \Delta I_{\text{res}} \tag{B39}$$

where

- I_{true} is the true current;
- ΔI_{acc} is the error due to the sensor accuracy;
- ΔI_{lin} is the linearity error;
- ΔI_{off} is the offset error;
- ΔI_{noise} is the electronic noise;
- ΔI_{res} is the quantization (resolution) error.

Similarly, the voltage measurement is described by

$$V_{\text{meas}} = V_{\text{true}} + \Delta V_{\text{acc}} + \Delta V_{\text{lin}} + \Delta V_{\text{off}} + \Delta V_{\text{noise}} + \Delta V_{\text{res}} \tag{B40}$$

The above equations are additive because each error source introduces an independent deviation to the true value of the measured quantity. No multiplicative corrections or nonlinear transformations are applied by the sensor; therefore, the total measurement error is represented as the algebraic sum of the individual error contributions. Because the measurement model is linear and additive, each uncertainty contribution has a unit sensitivity coefficient. Therefore, the combined standard uncertainty is obtained by the root-sum-square (RSS) combination of the individual standard uncertainties.

$$c_i = \frac{\partial x_{\text{meas}}}{\partial x_i} = 1 \tag{B41}$$

where x denotes either the current or the voltage. Consequently, the combined standard uncertainty is obtained by combining the standard uncertainties associated with each error source using the root-sum-square (RSS) method. For the current measurement,

$$u_c(I) = \sqrt{u_{\text{acc}}^2(I) + u_{\text{lin}}^2(I) + u_{\text{off}}^2(I) + u_{\text{noise}}^2(I) + u_{\text{res}}^2(I)} \tag{B42}$$

while for the voltage measurement,

$$u_c(V) = \sqrt{u_{\text{acc}}^2(V) + u_{\text{lin}}^2(V) + u_{\text{off}}^2(V) + u_{\text{noise}}^2(V) + u_{\text{res}}^2(V)} \quad \text{(B43)}$$

The uncertainty associated with each contribution was evaluated according to the manufacturer specifications.
For the current measurement, the IVT-S datasheet specifies an accuracy of ±0.4% of the measured value. For the maximum operating current considered in this work (I = 100A), the corresponding maximum error is

$$\Delta I_{acc}=0.004*100 = \pm 0.40\text{A} \quad \text{(B44)}$$

Assuming a rectangular probability distribution, the associated standard uncertainty becomes

$$u_{acc}(I) = \frac{0.40}{\sqrt{3}} = 0.231 \text{ A} \quad \text{(B45)}$$

The specified linearity is ±0.01% of reading, giving

$$\Delta I_{lin} = 0.0001 \cdot 100 = 0.01 \text{ A} \quad \text{(B46)}$$

$$u_{lin}(I) = \frac{0.01}{\sqrt{3}} = 0.0058 \text{ A} \quad \text{(B47)}$$

The electronic noise is specified by the manufacturer as 5mA RMS. Since an RMS value already represents a standard uncertainty, no additional conversion is required, and therefore

$$u_{noise}(I) = 0.005\ A \quad \text{(B48)}$$

The offset is less than 8mA, so it is possible to calculate the uncertainty with a rectangular distribution as

$$u_{off\ (I)} = \frac{0.008}{\sqrt{3}} = 0.0046\ A \quad \text{[a49]}$$

Finally, the digital resolution of the current measurement is 3 mA. Assuming a uniform distribution over one quantization interval, the corresponding standard uncertainty is

$$u_{res}(I) = \frac{0.003}{2\sqrt{3}} = 0.00087\ A \quad \text{(B50)}$$

The combined standard uncertainty of the current measurement is then obtained as

$$u_c(I) = \sqrt{u_{acc}^2 + u_{lin}^2 + u_{noise}^2 + u_{off}^2 + u_{res}^2} = 0.232\ A \quad \text{(B51)}$$

which corresponds to an expanded uncertainty

$$U\ (I) = 2 \times u_c(I) = 2 * 0.232 = 0.46\ A \quad \text{(B52)}$$

for a coverage factor (k=2).

For the voltage measurement, the IVT-S datasheet specifies an accuracy of ±0.5% of the measured value. For the maximum operating voltage considered in this work (V = 12V), the corresponding maximum error is

$$\Delta V_{acc}=0.005*12 = \pm\ 0.060\ \text{V} \quad \text{(B53)}$$

Giving an accuracy of

$$u_{acc}(V) = \frac{0.060}{\sqrt{3}} = 0.0346\ \text{V} \quad \text{(B54)}$$

The specified linearity is ±0.01%,

$$\Delta V_{lin} = 0.0001 \cdot 12 = 0.0012\ \text{V} \quad \text{(B55)}$$

$$u_{lin}(V) = \frac{0.0012}{\sqrt{3}} = 0.00069\ V$$

[a50]

The voltage offset is specified to be < 100mV
leading to

$$u_{off}(V) = \frac{0.100}{\sqrt{3}} = 0.0577\ A \quad \text{(B56)}$$

The electronic noise is specified to be less than 60mV RMS which directly represents the standard uncertainty

$$u_{noise}(V) = 0.060\ V \quad \text{(B57)}$$

Finally, the voltage resolution with an uniform distribution ± ½v LSB is

$$u_{res\ (V)} = \frac{0.003}{2\sqrt{3}} = 0.0087\ V \quad \text{(B58)}$$

The combined standard uncertainty of the current measurement is then obtained as

$$u_c(V) = \sqrt{u_{acc}^2 + u_{lin}^2 + u_{noise}^2 + u_{off}^2 + u_{res}^2} = 0.090\ V \quad \text{(B59)}$$

which corresponds to an expanded uncertainty (k=2)

$$U\ (V) = 2 \times u_c(V) = 2 * 0.090 = 0.18\ V \quad \text{(B60)}$$

B.4.2 On-Vehicle Measurements

Similarly to the laboratory fan characterization rig, the full-scale vehicle was equipped with a comprehensive measurement system comprising several sensors and electronic devices. Suspension displacement sensors were employed to estimate the aerodynamic downforce in real time, while longitudinal acceleration measurements were used for the evaluation of the aerodynamic drag through the coast-down methodology. The McLaren PIN16 differential pressure sensors and the IVT-S current/voltage transducer adopted during the vehicle experimental campaign are identical to those previously employed for the fan characterization rig; therefore, their uncertainty analyses presented in previous sections remain directly applicable. Vehicle speed was acquired through the onboard wheel-speed acquisition system, while airflow measurements were performed using a Pitot tube connected to a differential pressure sensor. Data acquisition and system management were handled by two dedicated microcontrollers, located inside the vehicle cabin and on the rear diffuser, respectively. These units were responsible for controlling the Co-Flow rear-wing actuation system and for processing the signals acquired from the Pitot pressure sensor. The vehicle Pitot measurements employed a Texense DPS-90 differential pressure sensor specifically selected for its lower measurement range. The sensor operates over a nominal differential pressure range of 0–90 mbar and provides an analogue voltage output proportional to the measured pressure. The analogue signal was digitized using the 14-bit analogue-to-digital converter integrated into the Arduino UNO R4. The combination of a reduced full-scale range and a higher ADC resolution provides a substantially smaller quantization interval than that achieved in the laboratory acquisition system, thereby reducing the uncertainty associated with the analogue-to-digital conversion. According to the manufacturer's specifications, the sensor accuracy is ±1% of the full-scale measurement range. Assuming a rectangular probability distribution, the corresponding standard uncertainty is

$$u_{acc}(p) = \frac{0.01 \times 90}{\sqrt{3}} = \frac{0.90}{\sqrt{3}} = 0.52 \text{ mbar} \tag{B61}$$

The ADC quantization interval is

$$\text{LSB} = \frac{Vref}{2^{14}} = \frac{5}{16384} = 0.000305 \text{ V} \tag{B62}$$

$$\text{Sensitivity S} = \frac{Range}{Vref} = \frac{90}{5} = 18 \frac{\text{mbar}}{\text{V}} \tag{B63}$$

Assuming a uniform probability distribution within one least significant bit,

$$u_q(p) = \frac{LSB \times S}{\sqrt{12}} = \frac{0.00549}{\sqrt{12}} = 0.00158 \text{ mbar} \tag{B64}$$

As observed for the laboratory acquisition system, the uncertainty introduced by ADC quantization is negligible compared with the intrinsic sensor accuracy.

Assuming independent uncertainty sources, the combined standard uncertainty is

$$u_c(p) = \sqrt{u_{acc}^2 + u_q^2} = \sqrt{0.520^2 + 0.00158^2} = 0.520 \text{ mbar} \quad \text{(B65)}$$

The corresponding expanded uncertainty becomes

$$U\,(p) = 2u_c = 1.04 \text{ mbar} \quad \text{(B66)}$$

which corresponds to an expanded uncertainty of approximately ±1.0 mbar at a confidence level of approximately 95%.

Source	Distribution	Standard uncertainty (mbar)	Contribution
Sensor accuracy	Rectangular	0.520	Dominant
ADC quantization	Rectangular	0.0016	Negligible
ADC reference voltage	Manufacturer specification	Negligible	—
ADC integral non-linearity	Manufacturer specification	Negligible	—
Combined standard uncertainty	—	0.520	—
Expanded uncertainty (k = 2)	—	1.04 mbar	—

Table B.5 Uncertainty budget for on-vehicle pressure measurements.

A comparison between the two pressure acquisition systems shows that the on-vehicle setup provides approximately half the expanded uncertainty of the laboratory system (±1.04 mbar versus ±2.20 mbar). This improvement is primarily attributed to the reduced measurement range of the DPS-90 sensor rather than to the increased ADC resolution. In both systems, the uncertainty introduced by the analogue-to-digital conversion is negligible compared with the intrinsic sensor accuracy, confirming that the overall measurement performance is governed by the pressure sensor specifications rather than by the electronic acquisition hardware.

B.4.2.1 Vehicle Drag Accuracy Evaluation

The aerodynamic drag area (C_DA) was determined from the vehicle coast-down tests using the Segers' approach; during the coast-down manoeuvre, the engine torque is negligible, and the longitudinal equation of motion can be rearranged in the followed way

$$C_dA = \frac{2 \times m \times g_{long}}{\rho \times V^2} \quad \text{(B67)}$$

where m [kg] is the vehicle mass, g_{long} $\left[\frac{m}{s^2}\right]$ is the measured longitudinal acceleration, ρ $[\frac{kg}{m^3}]$ is the ambient density and V $[\frac{m}{s}]$ is the vehicle speed. Equation (B67) represents the measurement model adopted for the uncertainty analysis. Since the drag area depends on four independent input quantities, the combined standard uncertainty is evaluated according to the law of propagation of uncertainty

$$u_c(C_DA) = \sqrt{\left(\frac{\partial C_DA}{\partial m}u(m)\right)^2 + \left(\frac{\partial C_DA}{\partial a_x}u(a_x)\right)^2 + \left(\frac{\partial C_DA}{\partial \rho}u(\rho)\right)^2 + \left(\frac{\partial C_DA}{\partial V}u(V)\right)^2} \quad \text{(B68)}$$

Equation (B68) was adopted as the measurement model for the uncertainty analysis. A representative operating point was selected to evaluate the sensitivity coefficients

V= 60 m/s, g_{long} = 1.40 m/s^2, m = 1500 kg, ρ = 1.225 kg/m^3

It is possible to calculate

$$C_dA = \frac{2*1500*1.40}{1.225*60^2} = 0.9524\ m^2 \quad \text{(B69)}$$

The sensitivity coefficients are obtained by differentiating the measurement model,

$$C_DA = \frac{2ma_x}{\rho V^2} \quad \text{(B70)}$$

with respect to each independent input quantity.

Longitudinal Acceleration $\frac{\partial C_dA}{\partial g_{long}} = \frac{C_DA}{g_{long}} = \frac{0.9524}{1.4} = 0.6803$ m*s^2 (B71)

Vehicle Speed $\frac{\partial C_dA}{\partial V} = -2 * \frac{C_DA}{V} = \frac{0.9524}{60} = -0.0317$ m*s (B72)

Air Density $\frac{\partial C_dA}{\partial \rho} = -\frac{C_DA}{\rho} = \frac{0.9524}{1.225} = -0.7775$ m^5/kg (B73)

Vehicle Mass $\frac{\partial C_dA}{\partial m} = \frac{C_DA}{m} = \frac{0.9524}{1500} = 0.006$ m^2/kg (B74)

From Racelogic VBox specifications, the following accuracies can be calculated
Longitudinal acceleration

$$\sigma_a \approx 0.015 - 0.02\ m/s^2 \quad \text{(B75)}$$

This is already variance

$$u_{acc}(g_{long}) = 0.02\ m/s^2 \quad \text{(B76)}$$

Velocity accuracy, considering ±0.1 km/h (on an average of 4 points)

$$0.1 \text{ km/h} = 0.0278 \text{ m/s} \quad \text{(B77)}$$

$$u_{acc}(V) = \frac{0.0278}{\sqrt{3}} = 0.016\ m/s \quad \text{(B78)}$$

Since the uncertainty specifications of the onboard atmospheric sensors were unavailable, the value obtained from the propagation analysis was considered optimistic. A conservative relative uncertainty of 3% was therefore adopted for air-density estimation in the subsequent uncertainty analysis. Finally, the correct value for density uncertainty is calculated to be

$$u_{acc}(\rho) = 3\% * 1.225 = \ 0.03675\ kg/m^3 \quad \text{(B79)}$$

with ρ = 1.225 kg/m^3.

The vehicle mass was restored to the same initial condition before each group of repeated coast-down tests by refuelling the vehicle. During a complete set of repeated measurements, the fuel consumption was approximately 10 kg. Assuming that the nominal vehicle mass corresponds to the average fuel condition within each measurement group, the maximum deviation from the nominal mass is $\Delta m = \pm 5$ kg. Assuming a rectangular probability distribution, the corresponding standard uncertainty is

$$u_{acc}(m) = \frac{\Delta m}{\sqrt{3}} = \frac{5}{\sqrt{3}} = 2.89 \text{ kg} \quad \text{(B80)}$$

Relative uncertainty (k=1, 68%)

$$\frac{u_c(C_D A)}{C_D A} = \frac{0.02867}{0.9524} = 3.01\% \quad \text{(B81)}$$

Relative expanded uncertainty (k=2, 95%)

$$\frac{U(C_D A)}{C_D A} = 2 * 3.01\% = 6.02\% \quad \text{(B82)}$$

At high longitudinal deceleration, the relative uncertainty associated with the acceleration measurement becomes negligible. Under these conditions, the overall accuracy of the drag area estimation is limited by the uncertainty in air density, which acts as a systematic scaling factor and cannot be reduced by averaging.

Input quantity	Standard uncertainty	Sensitivity coefficient	Contribution
Longitudinal acceleration	0.020 m/s²	0.6803	1.85E-06
Vehicle speed	0.016 m/s	-0.0317	2.58E-07
Air density	0.03675 kg/m³	-0.7775	8.16E-04
Vehicle mass	2.89 kg	0.0006	3.37E-06

Table B.6. Uncertainty budget for the coast-down drag coefficient estimation, showing the standard uncertainty, sensitivity coefficients, and individual contributions of the input quantities.

B.4.2.2 Vehicle Downforce Accuracy Evaluation

The aerodynamic downforce was estimated from the suspension displacement measurements using the methodology proposed by Segers. For each axle, the wheel loads were independently estimated from the left- and right-hand suspension displacement sensors. Since

the suspension geometry is symmetric, the same motion ratio and spring rate were adopted for both wheels of the same axle. Accordingly, the aerodynamic load acting on the front axle is obtained as

$$L_F = MR_F \cdot SR_F \cdot (X(FR) + X(FL)) \tag{B83}$$

While the rear axle load is

$$L_R = MR_R \cdot SR_R \cdot (X(RR) + X(RL)) \tag{B84}$$

Where MR is the suspension motion ratio, SR is the spring rate, X is the suspension displacement measured by each displacement sensor. The total aerodynamics downforce is then obtained by summing the contributions of the two axles

$$L = L_F + L_R \tag{B85}$$

Assuming that the three input quantities are mutually independent, the combined relative standard uncertainty is obtained according to the law of propagation of uncertainty

$$\left(\frac{u_c(L)}{L}\right)^2 = \left(\frac{u(SR)}{SR}\right)^2 + \left(\frac{u(MR)}{MR}\right)^2 + \left(\frac{u_c(X)}{X}\right)^2 \tag{B86}$$

The above equation applies independently to both the front and rear axles, using the corresponding motion ratio, spring rate and axle displacement. The suspension motion ratio (MR) was derived from the multibody suspension model developed in MSC Adams. Owing to confidentiality constraints, the detailed suspension geometry, model parameters and validation data cannot be disclosed. Since the aerodynamic tests were performed over a limited suspension travel around the nominal ride height, the motion ratio was assumed to remain constant for each axle throughout the investigated operating range. Although the multibody model accurately reproduces the suspension kinematics, residual discrepancies between the numerical model and the physical vehicle may arise from manufacturing and assembly tolerances, suspension compliance, and modelling assumptions. As no direct experimental quantification of these discrepancies was available, the uncertainty associated with the motion ratio was evaluated as a Type B contribution according to the GUM. Based on the internal vehicle development and model validation process, and adopting a conservative engineering approach, the maximum plausible discrepancy between the multibody model and the physical suspension was assumed not to exceed ±3%. This bound was selected to encompass the combined effects of modelling assumptions, manufacturing and assembly tolerances, and suspension compliance. Assuming a rectangular probability distribution, the corresponding relative standard uncertainty is

$$\frac{u(MR)}{MR} = \frac{3\%}{\sqrt{3}} = 1.73\% \quad \text{(B87)}$$

This relative standard uncertainty was adopted for both the front and rear axle motion ratios and propagated through the uncertainty analysis. The suspension springs were manufactured by Eibach. In the absence of a dedicated specification for the springs installed on the test vehicle, the manufacturer's published spring rate tolerance of ±2% for its motorsport springs was conservatively adopted as representative of the spring rate uncertainty. Since this value originates from the manufacturer's specification rather than from repeated experimental measurements, it was treated as a Type B uncertainty according to the GUM. Assuming a rectangular probability distribution, the corresponding relative standard uncertainty is

$$\frac{u(SR)}{SR} = \frac{2\%}{\sqrt{3}} = 1.15\% \quad \text{(B88)}$$

This relative standard uncertainty was adopted for both the front and rear spring rates and propagated through the uncertainty analysis. The suspension displacement was measured using rotary potentiometric displacement sensors installed on each damper. The analogue sensor output was converted into suspension displacement through the calibration procedure implemented within the vehicle acquisition system. Since the acquisition system does not provide a nominal displacement resolution, the effective quantization step was estimated directly from the recorded vehicle data by observing the minimum distinguishable increment of the measured damper displacement 0.5mm). This approach provides a realistic estimate of the resolution of the complete measurement chain, including the displacement sensor, signal conditioning and data acquisition system. Assuming a rectangular probability distribution, the corresponding standard uncertainty is

$$u_{res}(X) = \frac{\Delta}{\sqrt{12}} = \frac{0.5}{\sqrt{12}} = 0.144 \text{ mm} \quad \text{(B89)}$$

where Δ is the effective quantization step of the displacement measurement chain.
The sensor manufacturer does not provide a specification for the output noise. Therefore, the noise contribution was conservatively estimated from the characteristics of equivalent automotive contactless Hall-effect rotary position sensors [138], assuming an output noise < 1 mV RMS. Considering the nominal sensor sensitivity of 57.1 mV/°, the corresponding angular noise is approximately 0.0175° RMS. During the calibration procedure, the kinematic ratio was approximately 4 mm/°, yielding an equivalent displacement noise of approximately 0.007 mm RMS. This contribution was modelled as a normally distributed standard uncertainty.

$$u_{noise}(X) = 0.07 \text{ mm} \tag{B90}$$

The uncertainty associated with the calibration procedure was evaluated from the specifications of the digital vernier used as the reference instrument during the vehicle setup. The Mitutoyo 500-196-30 digital vernier provides a measurement accuracy of ±0.02 mm. Assuming a rectangular probability distribution, the corresponding standard uncertainty is

$$u_{cal}(X) = \frac{0.02}{\sqrt{3}} = 0.012 \text{ mm} \tag{B91}$$

Assuming that the three uncertainty sources are statistically independent, the combined standard uncertainty associated with a single displacement sensor is

$$u_c(X) = \sqrt{u_{res}^2 + u_{noise}^2 + u_{cal}^2} \tag{B92}$$

$$u_c(X) = \sqrt{0.144^2 + 0.07^2 + 0.012^2} = 0.161 \text{ mm} \tag{B93}$$

Since the wheel load for each axle is obtained from the sum of the left- and right-hand suspension displacements, the corresponding displacement uncertainty becomes

$$X = X_L + X_R \tag{B94}$$

and, assuming independent measurements,

$$u_c(X) = \sqrt{u_c^2(X_L) + u_c^2(X_R)} \tag{B95}$$

which gives

$$u_c(X) = \sqrt{2} \times 0.161 = 0.227 \text{ mm} \tag{B96}$$

A representative suspension displacement of 5 mm was selected, as it is consistent with the typical suspension travel associated with measurable aerodynamic loading during the experimental campaign.

$$\frac{u_c(X)}{X} = \frac{0.227}{5} = 4.549\% \tag{B97}$$

It is possible to calculate the standard uncertainty as per Segers' model (σ =1, 68%)

$$\frac{u_c(L)}{L} = \sqrt{(0.0173)^2 + (0.0115)^2 + (0.04549)^2} = 5\% \tag{B98}$$

Finally, it is possible to calculate the extended uncertainty (σ =2, k=2 95%)

$$\frac{U(L)}{L} = 2 * 5\% = 10\% \quad \text{(B99)}$$

This result is valid for each vehicle's axles.

References

1. Harinaldi, H., Budiarso, B., Warjito, W., Kosasih, E.A., Tarakka, R., Simanungkalit, S.P., Teryanto, L., Fredy, I.G.M. "Modification of flow structure over a van model by suction flow control to reduce aerodynamic drag". Makara J. Technol., 2012, 16. https://doi.org/10.7454/mst.v16i1.1021
2. Cerutti, J.J.; Sardu, C.; Cafiero, G.; Iuso, G. Active Flow Control on a Square-Back Road Vehicle. Fluids 2020, 5, 55. https://doi.org/10.3390/fluids5020055
3. Phan, T.-L., Pham, Q.T., Nguyen, T.K.L., Nguyen, T.T. "A numerical analysis of active flow control techniques for aerodynamic drag reduction in the square-back Ahmed model". Appl. Sci., 2023, 13, 239. https://doi.org/10.3390/app13010239
4. ALA Lamborghini, "ALA Lamborghini". Available online: https://www.autoevolution.com/pdf/news_attachements/640-hp-lamborghini-huracan-performante-looks-big-chinned-on-the-geneva-floor-115944.pdf (accessed on 2026).
5. Dano, B.P.E., Kirk, D., Zha, G.-C. "Experimental investigation of jet mixing of a co-flow jet airfoil". Proceedings AIAA, 2010, 2010-4421. https://doi.org/10.2514/6.2010-4421
6. Connolly, M.G., Ivankovic, A., O'Rourke, M.J. "Drag reduction technology and devices for road vehicles: A comprehensive review". Heliyon, 2024, e33757. https://doi.org/10.1016/j.heliyon.2024.e33757
7. Piechna, J. "A review of active aerodynamic systems for road vehicles". Energies, 2021, 14, 7887. https://doi.org/10.3390/en14237887
8. Modi, V.J., Fernando, M.S.U.K., Yokomizo, T. "Moving surface boundary-layer control: Studies with bluff bodies and application". AIAA Journal, 1991, 29, 1400–1406. https://doi.org/10.2514/3.10753
9. Liu, H. "Racing car aerodynamics: Optimising vehicle drag reduction and downforce control". Proceedings EEIC, 2025, 837–847.
10. Katz, J. "Aerodynamics in motorsports". Proc. IMechE Part P J. Sports Eng. Technol., 2021, 235, 324–338. https://doi.org/10.1177/1754337119893226
11. Piechna, J., Kurec, K., Broniszewski, J., Remer, M., Piechna, A., Kamieniecki, K., Bibik, P. "Influence of the car movable aerodynamic elements on fast road car cornering". Energies, 2022, 15, 689. https://doi.org/10.3390/en15030689

12. Gad-el-Hak, M. “Flow control: Passive, Active, and Reactive Flow Management”. Cambridge University Press, 2000.
13. Ravelli, U., Ravelli, S. “An overview of drag reduction methods in road cars”. Fluid Dyn. Mater. Process., 2026, 22, 1. https://doi.org/10.32604/fdmp.2026.075225
14. Sudin, M.N., Abdullah, M., Shamsudin, S., Faiz, R., Tahir, M. “Review of research on vehicles aerodynamic drag reduction methods”. Int. J. Mech. Mechatron. Eng., 2014, 14, 35–47.
15. Cattafesta, L.N., Sheplak, M. “Actuators for active flow control”. Annu. Rev. Fluid Mech., 2011, 43, 247–272. https://doi.org/10.1146/annurev-fluid-122109-160634
16. Ahmed, S.R., Ramm, G., Faltin, G. “Some salient features of the time-averaged ground vehicle wake”. SAE Trans., 1984, 93, 473–503, https://doi.org/10.4271/840300.
17. Brunn, A., Wassen, E., Sperber, D., Nitsche, W., Thiele, F. “Active drag control for a generic car model”. In Proceedings of Active Flow Control 2006, Berlin, Germany, 27–29 September 2006, pp. 247–259.
18. Jahanmiri, M. “Active flow control: A review”. Chalmers University of Technology, 2010.
19. Maine, M., Oumami, E.M., Bouksour, O., Tizliouine, A. “Review of research on cars wake flow control methods to reduce aerodynamic drag”. Int. J. Innov. Appl. Stud., 2019, 25, 1069–1089.
20. Mukuk, M.I., Abedin, M.Z. “Review on aerodynamic drag reduction of vehicles”. Int. J. Eng. Mater. Manuf., 2019, 4, 1–14. https://doi.org/10.26776/ijemm.04.01.2019.01
21. Heft, A.I., Indinger, T., Adams, N.A. “Introduction of a new realistic generic car model for aerodynamic investigations”. SAE Tech. Pap., 2012, 2012-01-0168. https://doi.org/10.4271/2012-01-0168
22. Heft, A., Indinger, T., Adams, N.A. “Experimental and numerical investigation of the DrivAer model”. Proceedings FDSM, 2012. https://doi.org/10.1115/FDSM2012-72272
23. Varney, M., Passmore, M., Wittere, F., Kuthada, T. “Experimental data for the validation of numerical methods: DrivAer model”. Fluids, 2020, 5, 236. https://doi.org/10.3390/fluids5040236
24. Cho, J., Park, J., Yee, K., Kim, H.-L. “Comparison of various drag reduction devices and their aerodynamic effects on the DrivAer model”. SAE Int. J. Passeng. Cars Mech. Syst., 2018, 11, 225–237. https://doi.org/10.4271/06-11-03-0019
25. Ashton, N., Van Noordt, W. “Overview and summary of the first automotive CFD prediction workshop: DrivAer model”. SAE Int. J. Commer. Veh., 2023, 16, 61–85. https://doi.org/10.4271/02-16-01-0005
26. Ashton, N., Mockett, C., Fuchs, M., Fliessbach, L., Hetmann, H., Knacke, T., Schonwald, N., Skaperdas, V., Fotiadis, G., Walle, A., Hupertz, B., Maddix, D. “DrivAerML: High-fidelity computational fluid dynamics dataset for road-car external aerodynamics”. arXiv, 2024, arXiv:2408.11969. https://doi.org/10.48550/arXiv.2408.11969
27. Ashton, N., Revell, A. “Comparison of RANS and DES methods for the DrivAer automotive body”. SAE Tech. Pap., 2015, 2015-01-1538. https://doi.org/10.4271/2015-01-1538

28. Wang, S., Avadiar, T., Thompson, M.C., Burton, D. "Effect of moving ground on the aerodynamics of a generic automotive model: The DrivAer-estate". J. Wind Eng. Ind. Aerodyn., 2019, 195, 104000. https://doi.org/10.1016/j.jweia.2019.104000
29. Wolf, T. "The aerodynamic development of the new Porsche Cayenne". Proc. IMechE Part D J. Automob. Eng., 2020, 234, 390–408.
30. Ho, H.H., Shirinzad, A., Essel, E.E., Sullivan, P.E. "Synthetic jet actuators for active flow control: A review". Fluids, 2024, 9, 290. https://doi.org/10.3390/fluids9120290
31. Brunet, V., Dandois, J., Verbeke, C. "Recent Onera Flow Control Research on High-Lift Configurations". Aerospace Lab, 2013, 6, 1–12, https://hal.science/hal-01184627v1
32. Rouméas, M., Gilliéron, P., Kourta, A. "Drag reduction by flow separation control on a car after body". Int. J. Numer. Methods Fluids, 2009, 60, 1222–1240. https://doi.org/10.1002/fld.1930
33. Tarakka, R., Salam, N., Jalaluddin, Rauf, W., Ihsan, M. "Aerodynamic drag reduction on the application of suction flow control on vehicle model with varied upstream velocity". IOP Conf. Ser. Mater. Sci. Eng., 2021, 1173, 012045. https://doi.org/10.1088/1757-899x/1173/1/012045
34. Godard, G., Stanislas, M. "Control of a decelerating boundary layer. Part 1: Optimization of passive vortex generators". Aerosp. Sci. Technol., 2006, 10, 181–191. https://doi.org/10.1016/j.ast.2005.11.007
35. Godard, G., Foucaut, J.M., Stanislas, M. "Control of a decelerating boundary layer. Part 2: Optimization of slotted jets vortex generators". Aerosp. Sci. Technol., 2006, 10, 394–400. https://doi.org/10.1016/j.ast.2005.11.006
36. Godard, G., Stanislas, M. "Control of a decelerating boundary layer. Part 3: Optimization of round jets vortex generators". Aerosp. Sci. Technol., 2006, 10, 455–464. https://doi.org/10.1016/j.ast.2005.11.005
37. Radespiel, R., Burnazzi, M., Casper, M., Scholz, P. "Active flow control for high lift with steady blowing". Aeronaut. J., 2016, 120, 171–200. https://doi.org/10.1017/aer.2015.7
38. Mestiri, R., Ahmed-Bensoltane, A., Keirsbulck, L., Aloui, F., Labraga, L. "Active Flow Control at the Rear End of a Generic Car Model Using Steady Blowing". J. Appl. Fluid Mech., 2014, 7, 217–252. https://doi.org/10.36884/jafm.7.04.21752
39. Aubrun, S., McNally, J., Alvi, F., Kourta, A. "Separation flow control on a generic ground vehicle using steady microjet arrays". Exp. Fluids, 2011, 51, 1177–1187. https://doi.org/10.1007/s00348-011-1132-0
40. Littlewood, R.P., Passmore, M.A. "Aerodynamic drag reduction of a simplified squareback vehicle using steady blowing". Exp. Fluids, 2012, 53, 519–529. https://doi.org/10.1007/s00348-012-1306-4
41. McNally, J., Fernandez, E., Robertson, G., Kumar, R., Taira, K., Alvi, F., Yamaguchi, Y., Murayama, K. "Drag reduction on a flat-back ground vehicle with active flow control". J. Wind Eng. Ind. Aerodyn., 2015, 145, 292–303. https://doi.org/10.1016/j.jweia.2015.03.006

42. Zhang, B.F., Liu, K., Zhou, Y., To, S., Tu, J.Y. "Active drag reduction of a high-drag Ahmed body based on steady blowing". J. Fluid Mech., 2018, 856, 351–396. https://doi.org/10.1017/jfm.2018.703
43. Wassen, E., Thiele, F. "Drag reduction for a generic car model using steady blowing". Proceedings AIAA, 2008, 2008-3771.
44. Wassen, E., Thiele, F. "Road vehicle drag reduction by combined steady blowing and suction". Proceedings AIAA, 2009, 2009-4174.
45. Huminic, A., Huminic, G. "Automotive wing with active control of flow". U.P.B. Sci. Bull. Ser. D, 2014, 76, 231–238.
46. Englar, R. "Improved pneumatic aerodynamics for drag reduction, fuel economy, safety and stability increase for heavy vehicles". SAE Tech. Pap., 2005, 2005-01-3627. https://doi.org/10.4271/2005-01-3627
47. Bardera, R., Matías-García, J.C., Barroso-Barderas, E., Fernández-Antón, J., Rodríguez-Sevillano, A.A., Active Flow Control by Coanda Actuators for Aerodynamic Drag Reduction in a European-Type Truck. , Actuators 2025, 14, 556., https://doi.org/10.3390/act14110556
48. Ramadhan, R.D.R., Mat, S., Samin, P.M., Othman, N., Wahid, M.A. "Review on flow controls for vehicles aerodynamic drag reduction". J. Adv. Res. Fluid Mech. Therm. Sci. 2022, 10, 11–36, https://doi.org/10.37934/arfmts.101.1.1136
49. Greenblatt, David & Wygnanski, Israel. (2000). The Control of Flow Separation by Periodic Excitation. Progress in Aerospace Sciences - PROG AEROSP SCI. 36. 487-545, https://doi.org/10.1016/S0376-0421(00)00008-7.
50. Whalen, E.A., Shmilovich, A., Spoor, M., Tran, J., Vijgen, P., Lin, J.C., Andino, M., Flight Test of an Active Flow Control Enhanced Vertical Tail , AIAA Journal, 3393-3398, 56, 9, 2018, https://doi.org/10.2514/1.J056959
51. Pastoor, M., Henning, L., Noack, B., King, R., Tadmor, G., Feedback shear layer control for bluff body drag reduction. , Journal of Fluid Mechanics, 608, 161-196, 2008, https://doi.org/10.1017/S0022112008002073.
52. "Henning, L., King, R., Robust Multivariable Closed-Loop Control of a Turbulent Backward-Facing Step Flow, Journal of Aircraft, 44:1, 201-208, 2007, https://doi.org/10.2514/1.22934"
53. Choi, H., Jeon, W., Kim, J., Control of Flow Over a Bluff Body , Annual Review of Fluid Mechanics, 40, Volume 40, 2008, 113-139, 1545-4479, https://doi.org/10.1146/annurev.fluid.39.050905.110149
54. Pfeiffer, J., Closed-loop active flow control for road vehicles under unsteady cross-wind conditions. , 2016, 10.14279/depositonce-5407.
55. Joseph, P., Amandolèse, X., Aider, J.L., Drag reduction on the 25° slant angle Ahmed reference body using pulsed jets. , Exp Fluids 52, 1169–1185 (2012), https://doi.org/10.1007/s00348-011-1245-5
56. Joseph, P., Amandolese, X., Edouard, C., Flow control using MEMS pulsed micro-jets on the Ahmed body. , Exp Fluids 54, 1442, 2013, https://doi.org/10.1007/s00348-012-1442-x

57. He, K., Minelli, G., Su. X., Huang, N., Krajnović, S., Active wake-flow control for a notchback Ahmed body driven by a genetically inspired optimization. , Journal of Fluid Mechanics., 2024, 1000, https://doi.org/10.1017/jfm.2024.1018
58. Bideaux, E., Bobillier, P., Fournier, E., Gilliéron, P., El Hajem, M., Champagne, J., Gilotte, P., Kourta, A. "Drag reduction by pulsed jets on strongly unstructured wake: Towards the square-back control". Int. J. Aerodyn. 2011, 1, 282–298. https://doi.org/10.1504/IJAD.2011.038846
59. Gilliéron, P., Kourta, A. "Aerodynamic drag control by pulsed jets on simplified car geometry". Exp. Fluids 2013, 54, 1457. https://doi.org/10.1007/s00348-013-1457-y
60. Ja'fari, M., Shojae, F.J., Jaworski, A.J. "Synthetic jet actuators: Overview and applications". Int. J. Thermofluids 2023, 20, 100438. https://doi.org/10.1016/j.ijft.2023.100438
61. Schueller, M., Wiegel, P., Lipowski, M., Schulze, R., Otto, T., Gessner, T., Development and test of synthetic jet actuators based on dual transducer concept, , Proc. SPIE 9059, Industrial and Commercial Applications of Smart Structures Technologies 2014, 905902 (10 March 2014), https://doi.org/10.1117/12.2046204
62. Weigel, P., Schueller, M., Gratias, A., Lipowski, M., Meer, T., Bardet, M., Design of a synthetic jet actuator for flow separation control. , CEAS Aeronautical Journal, 11. 813-821, 2020, https://doi.org/10.1007/s13272-020-00479-2.
63. Kourta, A., Leclerc, C. "Characterization of synthetic jet actuation with application to Ahmed body wake". Sens. Actuators A Phys. 2013, 192, 13–26. https://doi.org/10.1016/j.sna.2012.12.008
64. Park, H., Cho, J.H., Lee, J., Lee, D.H., Kim, K.H. "Aerodynamic drag reduction of Ahmed model using synthetic jet array". SAE Int. J. Passeng. Cars Mech. Syst. 2013, 6, 1–6. https://doi.org/10.4271/2013-01-0095
65. Tounsi, N., Mestiri, R., Keirsbulck, L., Oualli, H., Hanchi, S., Aloui, F. "Experimental study of flow control on bluff body using piezoelectric actuators". J. Appl. Fluid Mech. 2016, 9, 827–838. https://doi.org/10.18869/acadpub.jafm.68.225.24488
66. Edwige, S., Gilotte, P., Mortazavi, I. "Computational analysis of actuation techniques impact on the flow control around the Ahmed body". Fluids 2022, 7, 52. https://doi.org/10.3390/fluids7020052
67. Derghal, I., Mohd Saifuddin, M., Mohd Noh, M.H., Abdul Hamid, A.H. "Optimization of co-flow jet parameters for Ahmed body application". Int. J. Integr. Eng. 2023, 15, 233–243, https://doi.org/10.30880/ijie.2023.15.05.025
68. Jahanmiri, M., Abbaspour, M. "Experimental investigation of drag reduction on Ahmed car model using a combination of active flow control methods". Int. J. Eng. 2011, 24, 403–410. https://doi.org/10.5829/idosi.ije.2011.24.04a.09
69. Modi, V. "Moving surface boundary-layer control: A review". J. Fluids Struct. 1997, 11, 627–663. https://doi.org/10.1006/jfls.1997.0098
70. Modi, V.J., Shih, E., Ying, B., Yokomizo, T. "Drag reduction of bluff bodies through momentum injection". J. Aircr. 1992, 29, 429–436. https://doi.org/10.2514/3.46179

71. Singh, S.N., Rai, L., Puri, P., Bhatnagar, A. “Effect of moving surface on the aerodynamic drag of road vehicles”. Proc. IMechE Part D J. Automob. Eng. 2005, 219, 127–134. https://doi.org/10.1243/095440705X5886
72. Kota, S., Hetrick, J., Osborn, R., Paul, D., Pendleton, Ed., Flick, P., Tilmann, C., Design and application of compliant mechanisms for morphing aircraft structures. , 2003, Proc SPIE. 5054, https://doi.org/10.1117/12.483869.
73. "Sofla, A.Y.N., Meguid, S.A., Tan, K.T., Yeo, W.K., Shape morphing of aircraft wing: Status and challenges Materials & Design, Volume 31, Issue 3, 2010, Pages 1284-1292, ISSN 0261-3069, https://doi.org/10.1016/j.matdes.2009.09.011."
74. Barbarino, S., Bilgen, O., Ajaj, R., Friswell, M., Inman, D., A Review of Morphing Aircraft. Journal of Intelligent Material Systems and Structures, 2011, 22, 823-877, https://doi.org/10.1177/1045389X11414084.
75. Monner, H.P., Realization of an optimized wing camber by using form-variable flap structures , Aerospace Science and Technology, Volume 5, Issue 7, Pages 445-455, ISSN 1270-9638, 2001, https://doi.org/10.1016/S1270-9638(01)01118-X.
76. Li, D., Zhao, S., Da Ronch, A., Xiang, J., Drofelnik, J., Li, Y., Zhang, L., Wu, Y., Kintscher, M., Monner, H.P., Rudenko, A., Guo, S., Yin, W., Kirn, J., Storm, S., De Breuker, R., A review of modelling and analysis of morphing wings. , Progress in Aerospace Sciences 100, 46–62, 2018, https://doi.org/10.1016/j.paerosci.2018.06.002
77. Wang, Z., Sun, X., Yang, Y., Liu, G., Li, D., Xiang, J., Design Optimization and Testing of Seamless Morphing Leading Edge for Large Civil Aircraft. , Engineering Proceedings, 80, 49, 2025, https://doi.org/10.3390/engproc2024080049
78. Sun, J., Guan, Q., Liu, Y., Jinsong, L., Morphing aircraft based on smart materials and structures: A state-of-the-art review. , Journal of Intelligent Material Systems and Structures., 2016, 27, 2289-2312, https://doi.org/10.1177/1045389X16629569.
79. Chu, L., Li, Q., Gu, F., Du, X., He, Y., Deng, Y., Design, modelling, and control of morphing aircraft: A review , Chinese Journal of Aeronautics, Volume 35, Issue 5, 2022, Pages 220-246, ISSN 1000-9361, https://doi.org/10.1016/j.cja.2021.09.013.
80. Zhu, J., Yang, J., Zhang, W., Gu, X., Zhou, H., “Design and applications of morphing aircraft and their struc-tures.” Front. Mech. Eng. 18, 34 (2023). https://doi.org/10.1007/s11465-023-0750-6
81. Cummings, S.B., Smith, M.S., Ali, A., Bui, T.T., Ellsworth, J., Garcia, C.A. “Aerodynamic flight-test results for the adaptive compliant trailing edge”. AIAA Atmospheric Flight Mechanics Conference, 2016, AIAA 2016-3855. https://doi.org/10.2514/6.2016-3855
82. Herrera, C.Y., Flanagan, P., Kapania, R.K. “Aeroelastic airworthiness assessment of the adaptive compliant trailing edge flaps”. NASA Technical Report, 2015, NTRS 20150020900.
83. Cruz, J.R., Cummings, S.B., Perry, B. “Evaluation of load analysis methods for NASA’s GIII adaptive compliant trailing edge project”. NASA Technical Report, 2016, NTRS 20160000871.

84. Miller, E.J., Cummings, S.B., Perry, B. “Evaluation of the hinge moment and normal force loads from a seamless adaptive compliant trailing edge flap in flight”. NASA Technical Report, 2016, NTRS 20160000870.
85. "Parancheerivilakkathil, M.S., Pilakkadan, J.S., Ajaj, R.M., Amoozgar, M., Asadi, D., Zweiri, Y., Friswell, M.I., A review of control strategies used for morphing aircraft applications , Chinese Journal of Aeronautics, Volume 37, Issue 4, 2024, Pages 436-463, ISSN 1000-9361, https://doi.org/10.1016/j.cja.2023.12.035."
86. Kang, S.O., Cho, J.H., Jun, S.O., Park, H., Song, K.S., Kee, J., Kim, K.H., Lee, D.H. “A study of an active rear diffuser device for aerodynamic drag reduction of automobiles”. SAE Tech. Pap. 2012, 2012-01-0173. https://doi.org/10.4271/2012-01-0173
87. Meder, H.D., Wiegand, T.P.M. “Adaptive aerodynamics of the new Porsche 911 Turbo”. ATZ Worldw. 2014, 116, 42–45. https://doi.org/10.1007/s38311-014-0023-4
88. Estrada, G. “Mercedes-AMG GTR: Aerodynamics for the record”. In Progress in Vehicle Aerodynamics and Thermal Management, Springer: 2018, pp. 135–144. https://doi.org/10.1007/978-3-319-67822-1_8
89. McLaren Automotive, “McLaren P1—Design and aerodynamics”. Available online: https://cars.mclaren.com/en/legacy/mclaren-p1/design (accessed on 2026).
90. Wikipedia contributors. “McLaren P1”. Wikipedia, The Free Encyclopedia. Available online: https://en.wikipedia.org/wiki/McLaren_P1 (accessed on 2026).
91. Wikipedia contributors. “List of Nürburgring Nordschleife lap times”. Wikipedia, The Free Encyclopedia. Available online: https://en.wikipedia.org/wiki/List_of_Nürburgring_Nordschleife_lap_times (accessed on 2026).
92. Jani, J.M., Leary, M., Subic, A., Gibson, M.A., A Review of Shape Memory Alloy Research, Applications and Opportunities , Materials & Design, 56, 1078–1113, 2014, https://doi.org/10.1016/j.matdes.2013.11.084
93. Han, M.-W., Rodrigue, H., Cho, S., Song, S.-H., Choi, H., Ahn, S.-H. “Design and performance evaluation of soft morphing car-spoiler”. In Proceedings of ASME 2014 IDETC/CIE, Buffalo, NY, USA, 17–20 August 2014. https://doi.org/10.1115/DETC2014-34915
94. Rodinò, S., Curcio, E., Perrone, D., Castiglione, T., Numerical and experimental analysis of shape memory alloy-polymer composite for aerodynamic morphing applications. , Journal of Intelligent Material Systems and Structures. 37, 302-321, 2025, https://doi.org/10.1177/1045389X251395912.
95. Battaglia, M., Sellitto, A., Giamundo, A., Visone, M., Riccio, A., Shape Memory Alloys Applied to Automotive Adaptive Aerodynamics. Materials, 2023, 16, 4832, https://doi.org/10.3390/ma16134832
96. Post, M.L., Corke, T.C. “Separation control on high angle of attack airfoil using plasma actuators”. AIAA J., 2004, 42, 2177–2184. https://doi.org/10.2514/1.2929

97. Zhang, X., Huang, Y., Wang, X., Wang, W., Tang, K., Li, H. "Turbulent boundary layer separation control using plasma actuator at Reynolds number 2000000". Chin. J. Aeronaut., 2016, 29, 1237–1246. https://doi.org/10.1016/j.cja.2016.08.006
98. Iranshahi, K., Mani, M. "Dielectric barrier discharge actuators employed as alternative to conventional high-lift devices". J. Aircr., 2018, 55, 1–10. https://doi.org/10.2514/1.C034690
99. Choi, K., Jukes, T., Whalley, R., Feng, L., Wang, J., Matsunuma, T., Segawa, T. "Plasma virtual actuators for flow control". J. Flow Control Meas. Vis., 2015, 3, 22–34. https://doi.org/10.4236/jfcmv.2015.31003
100. Boucinha, V., Weber, R., Kourta, A. "Drag reduction of a 3D bluff body using plasma". Int. J. Aerodyn., 2011, 1, 262–281. https://doi.org/10.1504/IJAD.2011.038845
101. Shadmani, S., Mousavi Nainiyan, S.M., Mirzaei, M., Ghasemiasl, R., Pouryoussefi, S.G. "Experimental investigation of flow control over an Ahmed body using DBD plasma actuator". J. Appl. Fluid Mech. 2018, 11, 1267–1276. https://doi.org/10.29252/jafm.11.05.28600
102. Shadmani, S., Nainiyan, S.M.M., Ghasemiasl, R., Mirzaei, M., Pouryoussefi, S.G. "Experimental study of flow control over a standard road vehicle using plasma actuator". Mech. Mech. Eng. 2018, 22, 1047–1059. https://doi.org/10.2478/mme-2018-0083
103. Khalighi, B., Ho, J., Cooney, J., Neiswander, B., Corke, T.C., Han, T. "Aerodynamic drag reduction investigation for a simplified road vehicle using plasma flow control". In Proceedings of ASME FEDSM 2016, Washington, DC, USA, 10–14 July 2016. https://doi.org/10.1115/fedsm2016-7927
104. Roy, S., Zhao, P., DasGupta, A., Soni, J. "Dielectric barrier discharge actuator for vehicle drag reduction at highway speeds". AIP Adv. 2016, 6, 025322. https://doi.org/10.1063/1.4942979
105. Vernet, J.A. "Plasma actuators for separation control on bluff bodies". KTH Royal Institute of Technology, 2017, p. 74
106. Vernet, J.A., Örlü, R., Söderblom, D., Elofsson, P., Alfredsson, P.H. "Plasma streamwise vortex generators for flow separation control on trucks: A proof-of-concept experiment". Flow Turbul. Combust. 2018, 100, 1101–1109. https://doi.org/10.1007/s10494-018-9891-9
107. Kim, D., Do, H., Choi, H. "Drag reduction on a three-dimensional model vehicle using a wire-to-plate DBD plasma actuator". Exp. Fluids, 2020, 61, 135. https://doi.org/10.1007/s00348-020-02961-3
108. Roupassov, D., Nikipelov, A., Nudnova, M., Starikovskii, A., Flow separation control by plasma actuator with nanosecond pulsed-periodic discharge , AIAA Journal, 47(1), 168–185, 2009, https://doi.org/10.2514/1.38113
109. Little, J., Takashima, K., Nishihara, M., Adamovich, I., Samimy, M., High-lift airfoil leading-edge separation control with nanosecond pulse DBD plasma actuators , AIAA Paper 2010-4256, 2010-4256, 2010, https://doi.org/10.2514/6.2010-4256
110. Correale, G., Popov, I., Rakitin, A., Starikovskii, A., Hulshoff, S., Veldhuis, L., Flow separation control on airfoil with pulsed nanosecond discharge actuator , 49th AIAA Aerospace Sciences Meeting including the New Horizons Forum and Aerospace Exposition, AIAA 2011-1079, 2011

111. Adamovich, I., Little, J., Nishihara, M., Takashima, K., Samimy, M., "Nanosecond Pulse Surface Discharges for High-Speed Flow Control," AIAA Paper 2012-3137, 6th AIAA Flow Control Conference, June 2012, https://doi.org/10.2514/6.2012-3137.
112. Saemian, M., Cota, M., Sabidussi, L., Rida, Z., Nabhani, A., Bergada, J., DBD Plasma Actuators for Aerodynamic Flow Control: A Review. 2026, Applied Sciences. 16. 1888, https://doi.org/10.3390/app16041888.
113. Lengers, M., Scholz, U., Bauer, M. "Test and industrial assessment of active flow control integration in order to increase high-lift performance". In Proceedings of DLRK 2011, Bremen, Germany, 2011.
114. Kalarikovilagam Srinivasan, G., Venkatesan, J., Radespiel, R. "Preliminary design and system considerations for an active hybrid laminar flow control system". Aerospace 2019, 6, 22. https://doi.org/10.3390/aerospace6020022
115. PanFeng, Z., Wang, J., Feng, L. "Review of zero-net-mass-flux jet and its application in separation flow control". Sci. China Ser. E Technol. Sci. 2008, 51, 1315–1344. https://doi.org/10.1007/s11431-008-0174-x
116. Daynes, S., Weaver, P.M. "Review of shape-morphing automobile structures: Concepts and outlook". Proc. IMechE Part D J. Automob. Eng. 2013, 227, 1603–1622. https://doi.org/10.1177/0954407013496557
117. Brunton, S.L., Noack, B.R., Koumoutsakos, P. "Machine learning for fluid mechanics". Annu. Rev. Fluid Mech. 2020, 52, 477–508, https://doi.org/10.1146/annurev-fluid-010719-060214
118. Rabault, J., Kuchta, M., Jensen, A., Réglade, U., Cerardi, N. "Artificial neural networks trained through deep reinforcement learning discover control strategies for active flow control". J. Fluid Mech. 2019, 865, 281–302. https://doi.org/10.1017/jfm.2019.62
119. Spalart, P. R., Strategies for Turbulence Modelling and Simulations International Journal of Heat and Fluid Flow, Vol. 21, No. 3, 2000, pp. 252–263, DOI: 10.1016/S0142-727X(00)00007-2.
120. Sagaut, P., Large Eddy Simulation for Incompressible Flows: An Introduction, 3rd ed., Springer-Verlag, Berlin, Germany, 2006, ISBN 978-3540263449.
121. Hucho, W. H., Aerodynamics of Road Vehicles: From Fluid Mechanics to Vehicle Engineering, 5th ed., SAE International, Warrendale, Pennsylvania, USA, 2013, ISBN 978-0768080988.
122. Prause, J., Emmi, Y., Noll, B., Aigner, M., LES/RANS Modelling of Turbulent Mixing in a Jet in Crossflow at Low Velocity Ratios. 54th AIAA Aerospace Sciences Meeting. 54th AIAA Aerospace Sciences Meeting, 2016, San Diego (USA). doi: 10.2514/6.2016-0609
123. Wilcox, D. C., Turbulence Modelling for CFD, 3rd ed., DCW Industries, La Cañada, California, USA, 2006, ISBN 978-1928729082.
124. Pope, S. B., Turbulent Flows, Cambridge University Press, Cambridge, United Kingdom, 2000, ISBN 978-0521598866.
125. Menter, F. R., Two-Equation Eddy-Viscosity Turbulence Models for Engineering Applications AIAA Journal, Vol. 32, No. 8, 1994, pp. 1598–1605, DOI: 10.2514/3.12149.

126. Choi, H., Lee, J., and Park, H., Aerodynamics of Heavy Vehicles Annual Review of Fluid Mechanics, Vol. 46, 2014, pp. 441–468, DOI: 10.1146/annurev-fluid-011212-140616.
127. Akturk, A., Camci, C., Experimental and Computational Assessment of a Ducted-Fan Rotor Flow Model, 2012, Journal of Aircraft 885-897, 49, 3, 10.2514/1.C031562
128. Canape testing software (Version 17.0), computer software, Vector®, 2021.
129. SAE International Recommended Practice, Road Load Measurement and Dynamometer Simulation Using Coastdown Techniques, SAE Standard J1263_201003, Revised March 2010, Issued June 1979, https://doi.org/10.4271/J1263_201003.
130. Segers J., Analysis Techniques for Racecar Data Acquisition (2nd Edition), 2014
131. "BIPM, IEC, IFCC, ILAC, ISO, IUPAC, IUPAP, and OIML. Evaluation of measurement data - Guide to the expression of uncertainty in measurement. Joint Committee for Guides in Metrology, JCGM100:2008. URL: https://www.bipm.org/documents/20126/2071204/"
132. International Organization for Standardization (ISO). ISO 5801:2017—Fans—Performance Testing Using Standardized Airways*; ISO: Geneva, Switzerland, 2017.
133. Zha, G., Gao, W., Paxton, C. D., Jet Effects on Co-flow Jet Airfoil Performance, 2007, AIAA Journal, 1222-1231, 45, 6, https://doi.org/10.2514/1.23995
134. Zha, G., Yang Y., Ren Y., McBreen B., Super-Lift and Thrusting Airfoil of Co-flow Jet Actuated by Micro-Compressors, 2018, Flow Control Conference, https://doi.org/10.2514/6.2018-3061
135. Wang Y., Zha, G., Study of 3D Co-Flow Jet Wing Induced Drag and Power Consumption at Cruise Conditions, 2019, AIAA Scitech 2019 Forum, https://doi.org/10.2514/6.2019-0034
136. Wang Y., Zha G., Super-Lift Coefficient of Active Flow Control Airfoil: What is the Limit?, 2017, 55th AIAA Aerospace Sciences Meeting, https://doi.org/110.2514/6.2017-1693
137. Jha, A. K., and Kudva, J. N., Morphing Aircraft Concepts, Classifications, and Challenges, Vol. 5388, 2004, pp. 213. https://doi.org/10.1117/12.544212
138. Automotive contactless Hall-effect rotary position sensors, https://industrial.curtisswright.com/en-gb/products/sensors/srh220dr-contactless-rotary-sensor-dual-redundant-outputs (accessed on 2026).